Soft x-ray spectroscopy of the Vela supernova remnant

by

Benjamin R. Zeiger

B.A., Physics, Willamette University, 2005

M.S., Astrophysical and Planetary Sciences, University of Colorado, 2009

A thesis submitted to the

Faculty of the Graduate School of the

University of Colorado in partial fulfillment

of the requirements for the degree of

Doctor of Philosophy

Department of Astrophysical and Planetary Sciences

2013

This thesis entitled:
Soft x-ray spectroscopy of the Vela supernova remnant
written by Benjamin R. Zeiger
has been approved for the Department of Astrophysical and Planetary Sciences

Webster Cash

Prof. Andrew Hamilton

Dr. Steve Osterman

Dr. Jeff Forbes

Dr. Randall McEntaffer

Date

The final copy of this thesis has been examined by the signatories, and we find that both the content and the form meet acceptable presentation standards of scholarly work in the above mentioned discipline.

Zeiger, Benjamin R. (Ph.D., Astrophysical and Planetary Sciences)

Soft x-ray spectroscopy of the Vela supernova remnant

Thesis directed by Prof. Webster Cash

The CODEX sounding rocket payload was designed and flown to significantly improve spectral resolution of the Vela supernova remnant (SNR) in the soft x-ray ($0.1 - 1.0$ keV) bandpass. High spectral resolution ($E/\Delta E > 40$) across its $3.25^\circ \times 3.25^\circ$ field of view would disentangle thermal emission from nonthermal or line emission components to constrain the age when SNRs stop emitting nonthermal x-rays. Relatively recent observations have found significant nonthermal emission from remnants up to several kyr old, but CODEX encountered concurrent problems of higher noise and lower signal than expected, leaving the thermal versus nonthermal question unanswered in the 11 kyr-old Vela SNR. This thesis covers the motivation, design, and post-flight analysis of the CODEX instrument and data from its flight.

Dedication

Education is an admirable thing, but it is well to remember from time to time that nothing that is worth knowing can be taught.

-- O. Wilde

In the second scroll of Wen the Eternally Surprised a story is written concerning one day when the apprentice Clodpool, in a rebellious mood, approached Wen and spake thusly: ‘‘Master, what is the difference between a humanistic, monastic system of belief in which wisdom is sought by means of an apparently nonsensical system of questions and answers, and a lot of mystic gibberish made up on the spur of the moment?’’ Wen considered this for some time, and as last said: ‘‘A fish!’’ And Clopool went away, satisfied.

-- T. Pratchett, *Thief of Time*

Acknowledgements

A lot of people have suffered for this thesis. All I did was the work. To you: thank you.

Thanks to my family for making this possible — over the years making my skin thick enough and my head dense enough to put in 120 hour weeks needed to get the rocket ready to launch, or just to get me to Colorado in the first place.

Thanks to Jordan, for putting up with too many nights in the lab and too many days at a keyboard. Perhaps someday, after a long nap, I can make it up to you.

Thanks to Web, for giving me time, money, ideas, and freedom so that I might learn the ropes of rocketry. The Wilde quote in the dedication is a testament to my appreciation for your guidance and faith.

Thanks to the community of scientists at the University of Colorado's Astrophysics Research Laboratory, which supported the general mess of last-minute panic associated with the launch. Particularly, thanks to Mike Kaiser for doing all of the work while I sat in a lawn chair and sipped lemonade, and Ann, who was given far less credit than she deserves in the design section of this thesis and who made sure the payload would not fall apart until at least well after its launch. Also, thanks to Thomas Rogers for help with SolidWorks designs and launch operations and the UV rocket program for accommodation with shared facilities.

Thanks to Phil Oakley and Randy McEntaffer, for building the first editions of this payload but leaving enough unfinished business that there might be something for me to do with it, and to Ted Schultz for cleaning up the rat's nest.

Thanks to the many folks at the NASA Wallops Flight Facility and Orbital Sciences Corp.,

who actually made this payload fly.

Thanks to Adrian Martin and Sensor Sciences, LLC, for the time and ideas that pushed data through our old electronics.

Thanks to my friends for distractions and entertainment, and for showing me that there are things more tedious than running 100 miles. And to my dog, for preserving my sanity by occasionally dragging me out of the door.

And lastly, thanks to NASA for funding graduate student joyrides into space. Or more realistically, thanks for supporting the sounding rocket program that is a proving ground where technologies and graduate students grow up together.

Contents

Chapter

Tables

Table

Figures

Figure

Chapter 1

Introduction

‘‘Questions do not have to make sense, Vincent,’’ said Miss Susan. ‘‘But answers do.’’

-- Terry Pratchett, *Thief of Time*

The soft x-ray sky ($0.1 - 1.0$ keV; $15 - 150$ Å) is understood poorly on large angular scales. Soft x-rays have a short mean free path through the interstellar medium (ISM), giving a very shallow depth of field for telescopes looking in the plane of the Galaxy (Figure 1.1). As a result, sources that are discernible from the ubiquitous soft x-ray background are either very close or out of the plane of the Galaxy and very distant extragalactic targets. The former encompasses nearby supernova remnants (SNRs) and other $>10^6$ K gas, as well as local phenomena correlated with the solar wind. The latter encompasses stars, compact objects, and extragalactic targets such as active galactic nuclei and galaxy clusters (some of these are slightly extended).

Astronomical x-ray spectroscopy has generally — and rightly — been optimized for the broadest range of targets, namely point-like and harder (>1 keV, which have a much longer mean free path through the ISM than that of soft x-rays) sources. Efficient spectrographs for point-like sources are easier to build than spectrographs for diffuse sources because a dispersive optic requires light to be collimated, and collimation over a wide field of view is difficult because x-rays can only be reflected at grazing incidence, redirecting them by a few degrees per reflection. Spectrographs based

on detector response functions increase the efficiency of the optical system because fewer optics are needed, and both energy and spatial resolution of energy-sensitive detectors have improved drastically in the past few decades from proportional counters to CCDs to microcalorimeter arrays.

An additional complication of astronomical x-ray instruments is that soft x-ray telescopes must be above the vast majority of the atmosphere to be effective, so experiments are expensive and designs are limited by launch requirements. Orbital telescopes such as the Chandra X-ray Observatory (CXO) and XMM-Newton are fantastic spectrographs for point sources, with resolution ($E/\Delta E$) approaching 10^3 for CXO, but for diffuse sources they are limited both by the natural energy resolution of their CCD detectors (CXO cannot collimate light from a diffuse source) and by the small fields of view ($<30'$) of the instruments.

Microcalorimeter detector arrays provide energy resolution across a focal plane and are approaching the ability to provide soft x-ray spectral resolution of 10^3 across an entire focal plane, but they are also approaching the theoretical limit imposed by quantum noise. The ASTRO-H mission, scheduled to launch in 2014, will employ a microcalorimeter array to achieve spectral resolution of $50 - 100$ above 0.4 keV. Once the theoretical limit is reached, a new technology will be needed, or older dispersive optics will need to be improved. This thesis is the story of a sounding rocket payload designed around the use of off-plane reflection gratings for spectroscopy of diffuse sources.

The soft x-ray bandpass is typically defined as $0.1-10$ keV because of experimental constraints (above 10 keV the penetration depth of hard x-rays requires different detector technologies); for this thesis, I will use "soft x-rays" to refer only to the ultra-soft $0.1 - 1.0$ keV region. The state of the art for soft x-ray observations of diffuse sources was set by the ROSAT position-sensitive proportional counter (PSPC), which offered spectral resolution of $\frac{E}{\Delta E} = 0.43 \left(\frac{E}{0.93\mathrm{keV}}\right)^{-1/2}$ and built up maps of the entire sky with $12'$ spatial resolution (Briel and Pfeffermann 1985; Freyberg and Egger 1999). The ROSAT PSPC bandpass covered $0.1 - 2.4$ keV. Although very low in both spatial and spectral resolution compared to what the Chandra and XMM-Newton observatories would provide a decade later, the PSPC's 2° field of view gave the first integrated look at the diffuse soft x-ray sky. The improved resolution unraveled some mysteries but presented others as

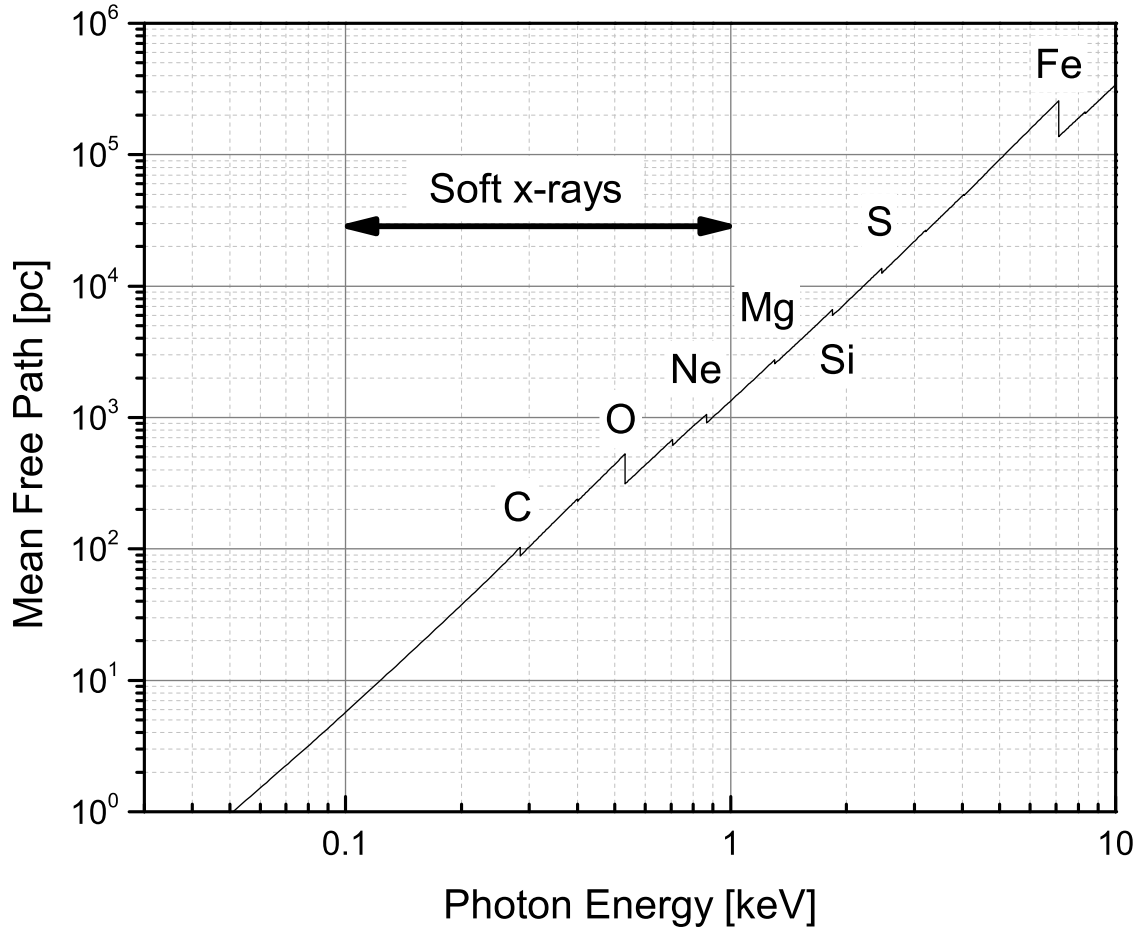

Figure 1.1 Mean free path of photons as a function of energy as they travel through the ISM, using data from Morrison and McCammon (1983). The interstellar mean free path of soft x-ray photons includes neutral species only and a hydrogen density of 1 cm^{-3}.

supernova remnants, the soft x-ray background, and large-scale structures in the Galaxy (Figure 1.2) were brought into clearer focus.

The diffuse soft x-ray sky maps hot gas, encompassing the thermal peak of $2-20\times10^5$ K gas and highly relativistic (TeV) electrons accelerated in magnetic fields. Anomalies in the emission trace shock fronts and supernova remnants, mostly. More mysterious, however, was that those emission regions themselves were anomalies: the ROSAT All Sky Survey showed a background in all locations, with a component tracing Galactic structures overlaid on a nearly uniform component.

The soft x-ray background, a nearly ubiquitous x-ray flux, was first discovered in 1962 by a $2-6$ keV proportional counter on a sounding rocket (Giacconi et al. 1962). The same flight also observed the first x-ray point source, Sco X-1. The isotropic signal suggested two interpretations: that it was extremely local, such that the solar environment dominated the signal; or that it was extremely distant, such that cosmological distributions lead to an isotropic sky. Galactic flux was ruled out because of the general clumpiness of the Galaxy, particularly with a focus near the disk. Since 6 keV photons have mean free paths easily capable of passing through the 1 kpc Galactic disk (Figure 1), the extremely-local hypothesis was ruled out for them, and thus it was determined that the x-ray background had a large contribution from unresolved extragalactic sources. The local environment (Local Hot Bubble, solar neighborhood) contributes a large fraction of the lower-energy soft x-ray flux, where the mean free path is much lower. The CyXESS (Cygnus X-ray Emission Spectroscopic Survey; flight 36.224; McEntaffer and Cash 2008)/EXOS (Extended X-ray Off-plane Spectrometer; flight 36.252; Oakley et al. 2011a)) lineage of sounding rocket payloads from the University of Colorado was designed to eventually measure the contribution of solar wind charge exchange to the local component of the soft x-ray background.

Prior to targeting the background, however, the new CyXESS and EXOS spectrographs targeted the Cygnus Loop SNR twice as instrument tests before the design was built to the full sensitivity required to detect the background. The Cygnus Loop is the brightest extended soft x-ray source in the sky, and the fields of view of the CyXESS/EXOS payloads were designed explicitly to measure the integrated soft x-ray output of the entire remnant at high resolution

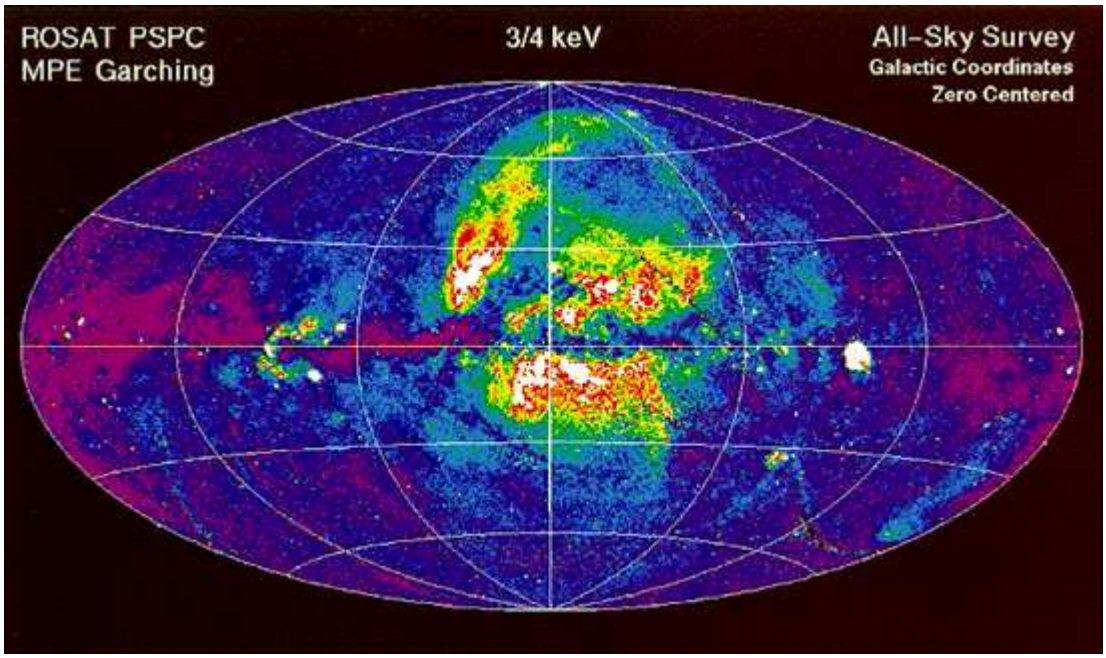

Figure 1.2 ROSAT All Sky Survey at 3/4 keV projected into Galactic coordinates (Snowden et al. 1997). Spatial resolution is $12'$, and the full bandpass is, nominally, $400 - 900$ eV.

$(50-100)$. Although the lack of spatial resolution precluded identifying emission with particular components of the SNR (i.e., a hot shock front, a cool knot, the interior of the SNR, etc.), the high spectral resolution would resolve dominant emission lines and determine the cooling mechanisms dominating the evolution of the remnant and the "average" state of the plasma. CyXESS detected several spectral lines, but problems with detector noise inhibited the payload from determining the full soft x-ray spectrum of the SNR (McEntaffer and Cash 2008). The troubles of CyXESS inspired EXOS to target the Cygnus Loop again, but a higher-than-expected count rate made its spectrum difficult to interpret (Oakley 2011).

The EXOS results inspired more questions than they answered, because the results indicate either a noisy instrument or nonthermal x-ray emission that would shift our understanding of how supernova remnants evolve and cool. The cooling and evolution of SNRs drives the evolution of the ISM. Due to the limits of instrumentation on spectroscopy of evolved SNRs, however, these are not well constrained observationally.

1.1 Supernova remnants

Each supernova injects $\sim 10^{51}$ ergs into the ISM. A Galactic supernova rate of several per century (e.g., Diehl et al. 2006) gives a mean energy deposition of $\sim 5\times10^{41}$ erg s^{-1}, one thousandth of the stellar output but capable of driving shocks that heat and sculpt the ISM. Since their explosions are local deposits of large amounts of kinetic energy, they create rarefied bubbles in the ISM that make the Galaxy reminiscent of a wheel of Swiss cheese, and the density variations driven by the shock fronts have consequences for the evolution of the ISM. The state of the ISM after these explosions is still quite unclear, since the rarefied (10^{-2} cm^{-3}) gas left in the wake of the shocks is too tenuous to be easily detected and measured in mature remnants. For the same reason, the actual amount in warm (10^4 K) and hot (10^6 K) components is poorly quantified (see Table 1.1). In a fantastic example of natural recycling or of happy coincidence, the x-ray flux expected from supernova remnants is consistent with the total x-ray flux of the soft x-ray background (Cox 2005).

The question of how SNRs evolve as a population is a nonlinear problem, since the porosity of

the ISM — the fraction of the ISM filled by rarefied bubbles created by other SNRs — determines the rate of expansion of SNRs. Lower densities impede the shock front of an SNR less than higher densities. Slavin and Cox (1993) describe the porosity q as the product of the supernova rate S_{-13} (in units of 10^{-13} pc^{-3} yr^{-1}), the mean kinetic energy of a supernova E_{51} (in units of 10^{51} ergs), the mean ISM density n_0, and the ISM pressure p due to magnetic fields, cosmic rays, and thermal pressure thus:

$$q = 0.176 S_{-13} E_{51}^{1.17} n_0^{-0.61} (10^{-4} p/k_B)^{-1.06}, \tag{1.1}$$

with k_B being Boltzmann's constant and neglecting the effects of any ordered magnetic field. The already complex problem of porosity is exacerbated because the regions where porosity is highest are also the regions where density is lowest, and x-ray emitting plasmas are already short on diagnostic lines for determining the various parameters that might lead to a solution. That supernovae often occur in groups as clusters of stars co-evolve makes the problem even more daunting, and the potential for overlapping SNRs is emphasized by the large spatial scales: older SNRs can reach 100 pc to 150 pc in diameter (Badenes et al. 2010).

ROSAT made significant progress in elucidating the contribution of supernova remnants to the Galactic structure, but its low spectral resolution in the soft x-ray bandpass — where much of the energy of 10^6 K gas and of SNRs generally is emitted — only allowed for broad fitting of thermal models and guessing at the dominant spectral lines that propped up the spectrum. Although the spatial mapping and census of SNRs and the overall flux of SNRs provided many insights about their evolution, the state of SNR plasmas and their emission mechanisms are still poorly understood.

Canonical supernovae occur in one of two observationally-distinguished types according to the Minkowski-Zwicky classification system: Type I (no hydrogen lines) and Type II (hydrogen lines), with a ratio of about 1:3. The former are thought to be white dwarfs, usually with binary companions transferring mass to the dwarf, pushed over the 1.4 $M\odot$ Chandrasekhar mass limit, beyond which the atomic structure of the white dwarf collapses into a neutron star and releases 10^{51}

Table 1.1. Ferrière (2001): Phases of the ISM

Component	Fractional volume	Scale height [pc]	Temp. [K] [K]	Density [cm^{-3}]	State of hydrogen	Obs. notes
Molec. clouds	<1%	80	$10^2 - 10^6$	molecular	molec.	[a]
Cold neutral	$1 - 5\%$	$100 - 300$	$50 - 100$	$20 - 50$	neutral	[b]
Warm neutral	$10 - 20\%$	$300 - 400$	$(6 - 10) \times 10^3$	$0.2 - 0.5$	neutral	[c]
Warm ionized	$20 - 50\%$	1000	8000	$0.2 - 0.5$	ionized	[d]
H II regions	<1%	70	8000	$10^2 - 10^4$	ionized	[e]
Hot ionized	$30 - 70\%$	$1000 - 3000$	$10^6 - 10^7$	$10^{-4} - 10^{-2}$	ionized	[f]

[a]Primary observation technique: radio and infrared molecular emission and absorption lines

[b]Primary observation technique: H I 21 cm line absorption

[c]Primary observation technique: H I 21 cm line emission

[d]Primary observation technique: Hα emission, pulsar dispersion

[e]Primary observation technique: Hα emission, pulsar dispersion

[f]Primary observation technique: x-ray emission; absorption lines of highly-ionized metals, primarily in the ultraviolet

ergs of photons and energetic particles. Vink (2012) provides a good review of the classification scheme, including its finer divisions.

Type II supernovae are thought to be the core collapse events of the deaths of massive stars, after they exhaust their silicon-burning shells. The total energy of a Type II SN is in the vicinity of 10^{53} ergs, with neutrinos carrying 99% of that away without transferring the energy to other particles or fields. The remaining energy in the SN is then 10^{51} ergs, although this remains an empirical statement as the transfer of energy into a shock front, either from processes occurring during the collapse or from confinement of neutrino momentum, is not presently understood. The assumption, which has not yet worked in modeling, is that about 1% of the neutrino flux is absorbed in the outer mantle of the star while the core is opaque to neutrinos, accelerating the shell into the ejecta seen as an SNR. Simulations show this inelastic collapse to stall before it becomes a blast wave, but astronomers have found that the resulting shock waves are still generally consistent with a 10^{51} erg explosion once the neutrinos have carried away their 99% of the energy. That it is mysteriously identical to the Type Ia value is at once beautiful and upsetting.

Regardless of the mechanism of neutrino energy transfer (or the possibility that models have yet to get it right because of a flaw in estimates of the energetics), a supernova generates a shock wave that evolves into the ISM as a supernova remnant. This much, at least, is well supported by the "historical supernovae" observed by humans hundreds of years ago, notably the well-studied supernovae SNe 1006, 1054, 1572, 1604, and SN 1987a. The overconcentration of energy from converting a large star into kinetic energy evolves as a blast wave into the ISM, and the expansion can be approximated rather well as four distinct phases of evolution, described below. Within each phase, the expansion of the remnant is self-similar, differing only by a scaling parameter of time if the medium into which it is expanding is uniform.

(1) Free expansion. The explosion dominates the surrounding medium so completely that there are no significant energy losses, and the ISM, at a density of $\sim$1 cm^{-3} (less if it is a cavity explosion), cannot slow the ejecta appreciably. At this point, the SNR has all of the

energy it will ever have, and what is left is to trace the evolution of that energy. Due to the high temperature, the blackbody spectrum peaks in the x-ray regime but the remnant is optically thick. The free expansion of SN 1987a is shown in Figure 1.3 in a series of observations spanning 6 years. The 300 yr old Cas A remnant is shown in Figure 1.4.

(2) Adiabatic/Sedov-Taylor expansion. When the ejected mass is roughly equivalent to the swept-up mass, the momentum transfer to the swept-up ISM material is significant enough that the SNR begins to slow. Energy and momentum are both conserved in this phase. Magnetic field formation becomes significant as the $\sim$3 μGauss field of the ambient ISM is compressed in the shock wave. As the remnant grows in size and slows in velocity, the shock front becomes less turbulent. Remnants also begin to encounter other structures in the ISM, brightening some regions of the shock front. The $r \propto t^{2/5}$ dependence, which can be derived analytically from conservation equations, was verified experimentally in nuclear bomb tests in the late 1940s (Taylor 1950). The Cygnus Loop and Vela SNRs are shown as examples of this phase in Figure 1.5, where the filamentary instabilities seen in Figure 1.4 have mostly died away.

(3) Radiative/pressure-driven snowplow. Significant line emission occurs when the energy drops enough for the plasma to recombine, and the system can no longer be approximated as having a constant energy, although momentum is still conserved. The expanding shell (<1 pc thick) has a density of $10^6 - 10^8$ cm^{-3} while the interior of the remnant is still in the vicinity of 10^6 K. An example of one such older remnant is Simeis 147, shown in Figure 1.6.

(4) Confusion. SNRs continue to grow and cool, eventually either merging with the ISM or with other SNRs to form a superbubble. The confusion rate depends on the density of evolved supernova remnants and the rate of expansion. The last traces will disappear as the shocks approach the turbulent speed of the ISM, generally of order 10 km s^{-1}. This stage is the death of the SNR, essentially. For an isolated SNR it reaches an equilibrium

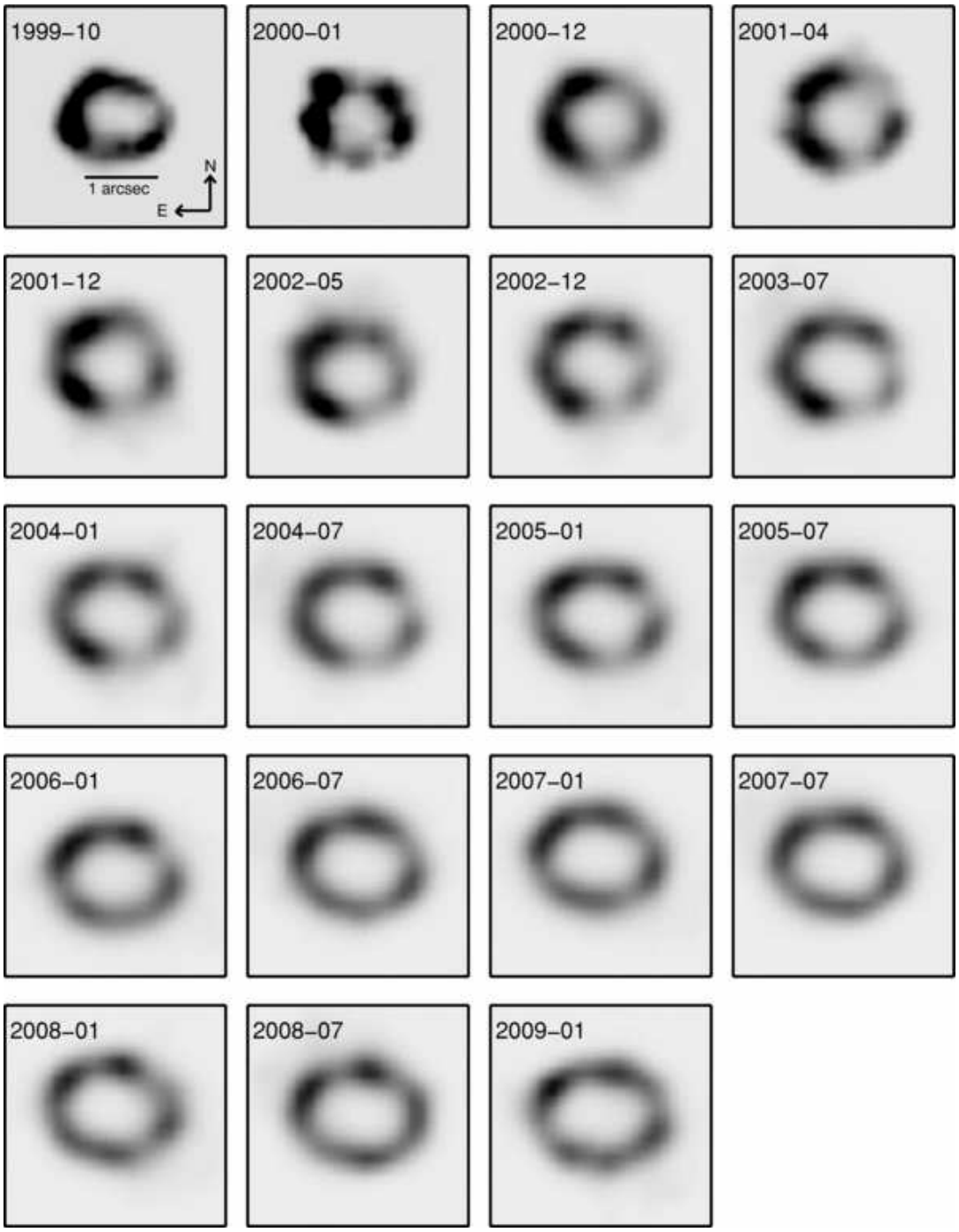

Figure 1.3 Supernova 1987a expansion, chronicled in x-ray emission ($0.3 - 8.0$ keV broadband) by the Chandra X-ray Observatory from 1999-2007 (Racusin et al. 2009). Images are all on the same spatial scale, shown in the image at top left).

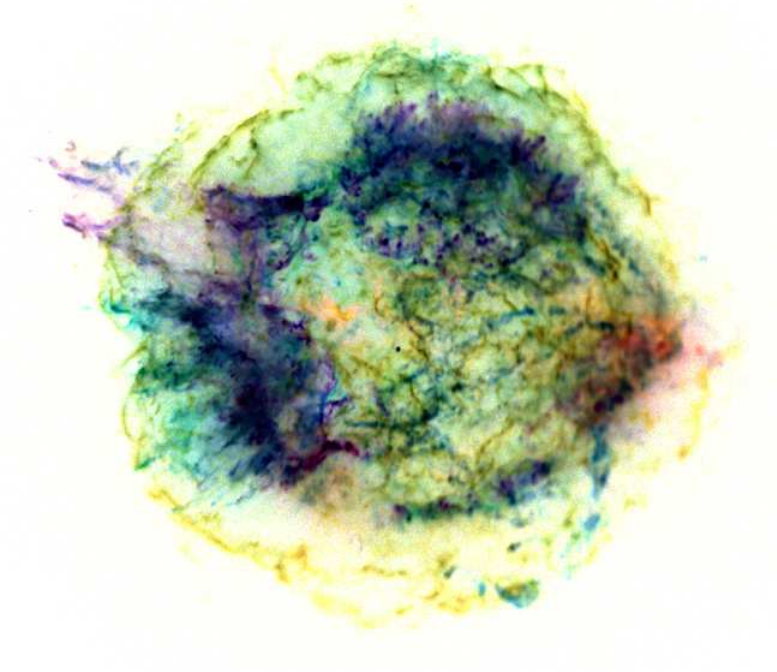

Figure 1.4 X-ray map of the Cas A supernova remnant. The remnant is about 3.3 kpc away, spans $7.3' \times 6.4'$ (roughly 3 pc in diameter), and is approximately 300 years old. Yellow is 4.0-6.0 keV, blue is 1.5-2.5 keV, and red is $0.5 - 1.5$ keV (image credit: NASA/CXC/MIT/UMass Amherst/M. D. Stage et al., unpublished).

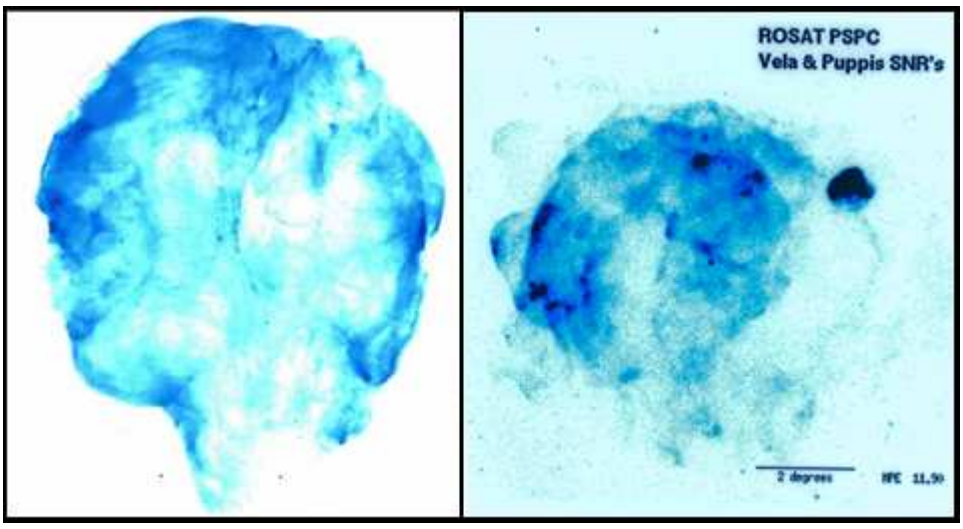

Figure 1.5 ROSAT images of the Cygnus Loop (*left*, Levenson et al. 1999)) and Vela (*right*, Aschenbach 1998) supernova remnants. The images have different scales, with the Loop roughly 3° in diameter and the Vela SNR spanning $5^\circ \times 8^\circ$.

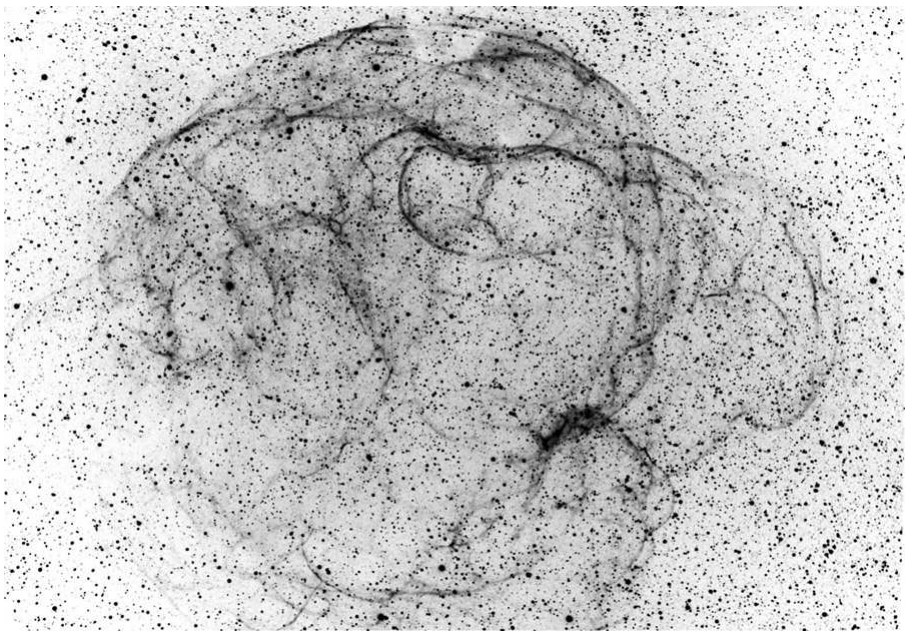

Figure 1.6 Hα image of Simeis 147, an SNR $\gg 10^4$ years old (image credit: S. Mandel, unpublished).

in $\sim 10^6$ yr, but the time could be shorter in a complicated environment (other nearby supernovae, dense star cluster, etc.). Figure 1.7 shows the Galaxy in Hα emission, tracing shock fronts and showing how densely packed the SNRs can be in the plane.

The phases, summarized graphically in Figure 1.8, describe the evolution of an energy overdensity in the ISM regardless of the explosion mechanism and the "bouncing" magic act of the neutrinos. Observationally, the free expansion phase has weak emission due to its paucity of available electronic transitions and low surface area. As it enters the adiabatic phase, the shock interaction with the ISM produces a textured bremsstrahlung ("braking radiation" of charged particles accelerated by interactions with other charged particles) surface with a synchrotron emission (from nonthermal relativistic particles accelerated in a magnetic field) shell forming on the outside. As the remnant evolves (growing older than a few kyr), canonical theory describes the high energy radiation as coming from bremsstrahlung processes and the synchrotron emission fading away because the lower shock velocity can no longer drive the necessary nonthermal population of electrons.

Remnants spend much of their lives in the adiabatic stage, and they become mostly unobservable before they reach the radiative stage because they are too diffuse and the surface brightness is too low for easy detection. This thesis will focus on adiabatic remnants from henceforth.

The adiabatic expansion of the remnant, as noted above, can be described in a fairly simple fashion. After its initial impulse, the shock drifts (internal pressure is negligible as a shock driver when it is still traveling at speeds >100 km s^{-1}. The "jump" conditions for a fast-moving shock describe the transition from the unshocked medium to the shock front. A fast-moving shock is >50 km s^{-1}, such as a supernova blast wave; these are traditionally called "J-shocks" for the jump of density, temperature, and velocity within the shock, but hereafter they will be referred to simply as "shocks" since the weaker "C-shocks" (continuous shocks) do not fall within the scope of this paper. Evolution of an adiabatic shock, assuming that radiative losses in all forms are negligible,

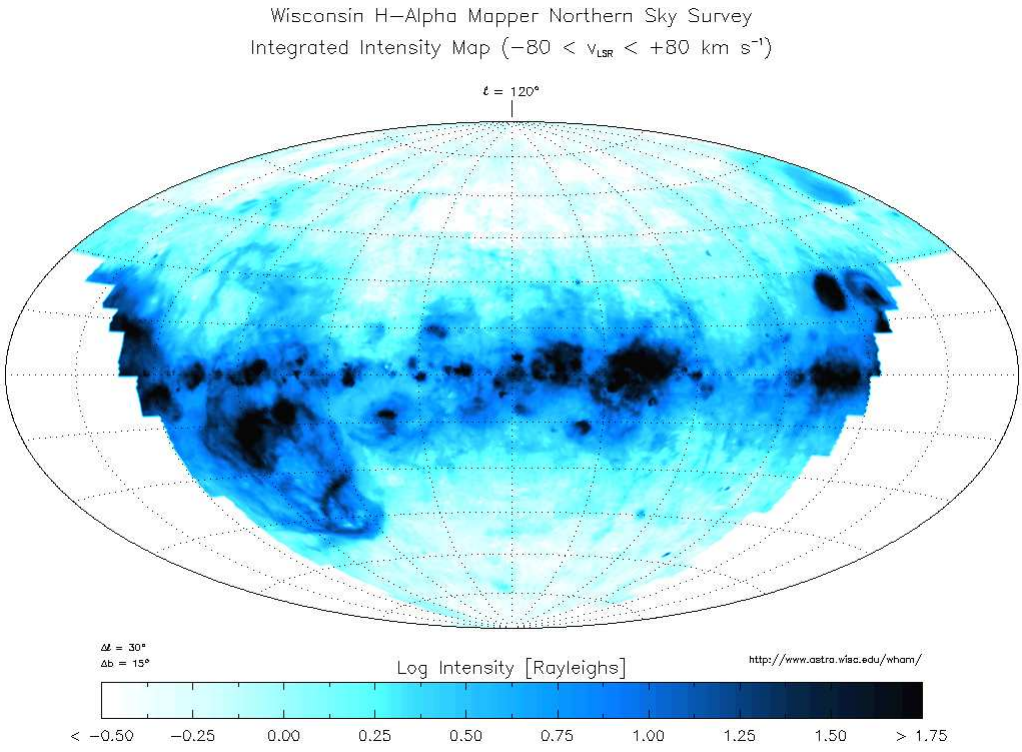

Figure 1.7 Wisconsin Hα Mapper (WHAM) Northern Sky Survey, showing the confusion of hot gas in the ISM along the Galactic plane. The map is centered at $b = 0°$ and $l = 120°$ (Haffner et al. 2003).

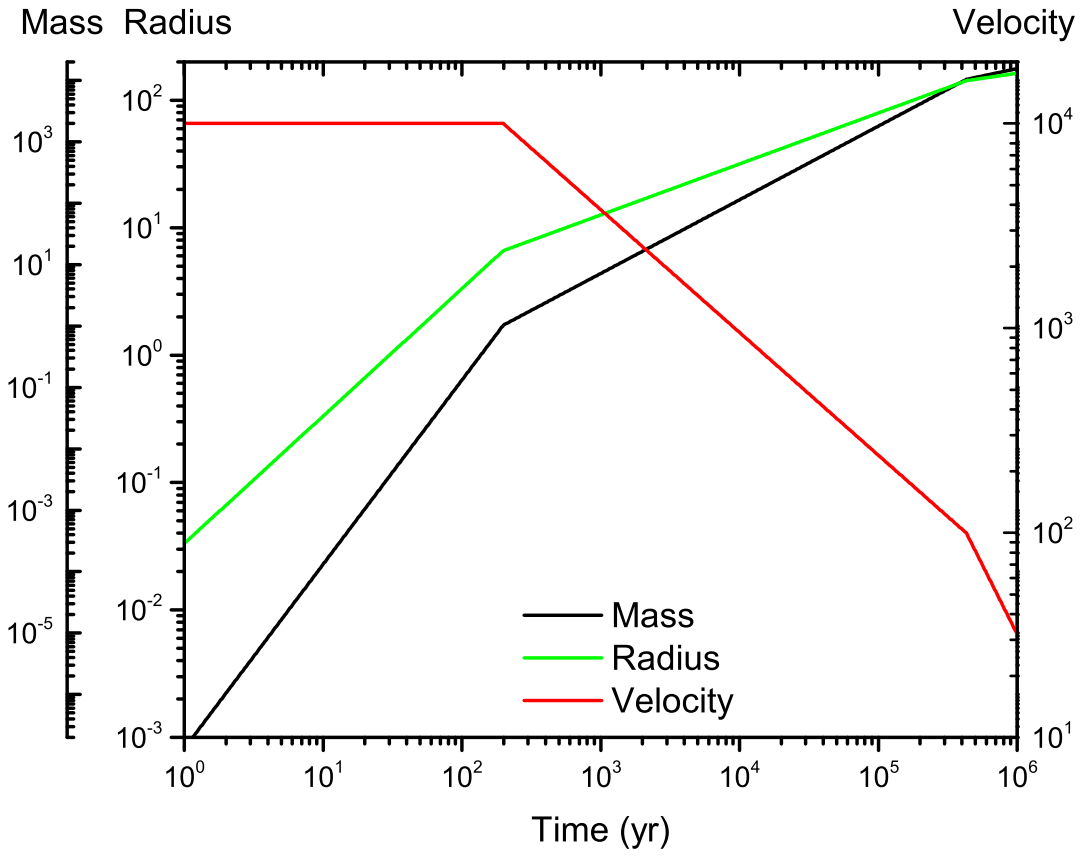

Figure 1.8 Evolution of an isolated supernova remnant according to the first three stages of the traditional four-stage model of SNR evolution, determined by scaling relations and assuming an ISM density of 1 cm^{-3}, inconsequential magnetic fields, and 10^{51} ergs of initial energy driving a 1 $M_\odot$ initial shock (this is low for a core-collapse supernova, but good for visual scaling). The y axes are labeled at the top, with mass in units of $M_\odot$, radius in pc, and velocity in km s^{-1}.

conserves mass flux,

$$\rho_0 v_0 = \rho_1 v_1, \tag{1.2}$$

momentum,

$$\rho_0 v_o^2 + P_0 = \rho_1 v_1^2 + P_1, \tag{1.3}$$

and energy

$$\tfrac{1}{2} v_0^2 + \frac{u_0}{\rho_0} + \frac{P_0}{\rho_0} = \tfrac{1}{2} v_1^2 + \frac{u_1}{\rho_1} + \frac{P_1}{\rho_1}. \tag{1.4}$$

Collectively, these are known as the Rankine-Hugoniot (RH) relations, and they describe the jump at the leading edge of the shock; they do not encompass the dynamics of the entire shock (which is broader than just the leading edge) or of the SNR interior behind that. Variables in these relations are v (velocity), ρ (density), P (pressure), and u (internal energy), with a subscripted 0 indicating the upstream region and a 1 indicating the post-shock or downstream region. Per the traditional treatment of shock propagation, the shock is taken in its own reference frame with a velocity of 0. The pre-shock gas, in the rest frame of the shock, flows into the shock front and is considered "upstream" while the post-shock interior of the remnant is "downstream." Accordingly, v_0, the velocity of the unshocked ambient medium, represents the velocity at which ambient material from the ISM is swept up by the shock front. Few philosophers have ever accused tradition and intuition of agreeing, and at least in this case the discrepancy makes the math easier.

The RH relations can be further massaged to give additional properties of the shock in relation to the upstream medium. Defining a strong (supersonic) shock as having a Mach number M much greater than 1, viz.,

$$M = v_0 / C_{s,0} = v_0 / \sqrt{\gamma \frac{P_0}{\rho_0}} \gg 1, \tag{1.5}$$

where C_s is the speed of sound, and γ is the ratio of specific heats ($\gamma = C_p/C_V$[$= 5/3$ for a monatomic gas such as that which would be found in an SNR]). In the adiabatic phase of evolution, the shock velocity is proportional to $t^{-2/5}$. Under these conditions and assuming an ideal gas where the internal energy $u = P/(\gamma - 1)$ and pressure $P = \rho k_B T/\mu$ (μ is the mean molecular mass), the pressure behind the shock (P_1) is equal to $\frac{3}{4}\rho_0 v_0^2$ and the velocity v_1 is $\frac{1}{4} v_0$. The shock temperature

T_1 is given in terms of the mean ion mass μ and the shock velocity as

$$k_B T_1 = \frac{3}{16}\mu v_0^2, \tag{1.6}$$

where the shock velocity accelerates cold ISM and randomizes the energy into a thermal temperature. The compression ratio of the shock is a constant: $\rho_1/\rho_0 = 4$ (see Tielens 2008 for a derivation). The compression ratio describes the density jump immediately behind the shock front, and for obvious reasons (n.b., conservation of mass) does not fill the entire SNR at this increased density or even the shock region behind the front, where densities can be >4 times ambient.

The electron temperature and the shock temperature are not necessarily equal, since the mass and collisional cross sections vary from the ion population and they have, at the very least, different thermalization timescales as a result. Additionally, electrons are accelerated more rapidly in magnetic fields and are more prone to losing energy via radiation. Nonetheless, Masai (1994) has shown that, in the adiabatic phase of evolution, the electron population swept up by the passage of the shock will be thermalized to energies of a few keV in only a few thousand years. The calculation only considered Coulomb interactions to heat electrons swept up from the cold ISM, and it neglected any acceleration mechanism that would produce superthermal electrons.

It is interesting to note that both temperature and pressure are unbounded in strong shocks (in the sense that they are set by the physical conditions of an individual shock and have no intrinsic limit), yet the compression ratio is constant. A gas can be compressed by more than a factor of 4, but this will occur farther downstream than the leading edge, and the shock can have a compression ratio in its interior in the hundreds. In the shock frame, the high-velocity particles of the ISM impact the shock and the ordered flow is randomized as the particles are thermalized.

1.2 Fermi acceleration processes

Magnetic fields throw wrenches into otherwise-beautiful Rankine-Hugoniot SNR evolution. This is "the great tragedy of science — the slaying of a beautiful hypothesis by an ugly fact" (Huxley 1894). Magnetic fields provide an additional pressure term to the description of the gas. The altered

dynamics of charged particles can decrease the compression ratio due to the increased pressure in the shock and or increase the compression ratio by increasing the diffusion rate. Additionally, the effects on charged particles produce radiation that changes the energy budget of the evolving remnant, albeit in a relatively small fashion at first.

Magnetic fields can pump a population of energetic charged particles by Fermi acceleration, the repeated reflection of the charged particles between magnetic fields. The turbulent shock front of a young SNR presents numerous structures ordered only on a small scale; if two of these clumps progress toward each other, a particle will be reflected back and forth between their magnetic fields, each time taking a small amount of energy for itself. (The converse is also true: a particle trapped between receding structures will lose energy to the magnetic fields.) Small numbers of ions can thus be driven up to $\sim$4 PeV and electrons into the 100 TeV regime within $500 - 1,000$ yr, producing both cosmic rays from high energy ions and synchrotron x-rays from the electron population (Fermi 1949). The resulting population follows a power law distribution of energies. This process is called "second-order Fermi acceleration" because the energy gained per bounce is proportional to the square of the relative velocity of the structures.

Second-order Fermi acceleration is straightforward in a qualitative sense, relying simply on the well-known behavior of charged particles in magnetic fields and momentum transfer in collisions. In fact, a reasonable conceptualization can be built strictly from introductory physics: imagine a perfectly elastic billiard ball bouncing between two approaching massive walls on a frictionless surface. The ball will start at the first wall, W_1, which defines the rest frame of the system, and travel toward the other, W_2. The ball has a positive velocity $v_{b,0}$ while W_2 approaches with a velocity $-v_w$. When the ball hits W_2, it is reflected as though it hit with $v_{b,1} = v_{b,0} + v_w$, and travels back toward W_1 with a velocity $v_{b,1}$. It is then reflected (W_1 is at rest) and the process repeats, with the ball gaining v_w each time such that the final velocity (whenever one gets bored of watching the perpetual motion machine) after N cycles will be $v_{b,f} = v_{b,0} + Nv_w$. Since energy is proportional to the square of the velocity (and the acceleration goes from keV to TeV energies, so the $v_{b,0}$ term is negligible), energy is proportional to N^2 and the second-order designation becomes

apparent.

In this particular example, the collisions were elastic and the wall was essentially unchanged by the collisions, either in its structure or in its momentum. For interactions of charged particles and magnetic fields in a plasma, the collisions are inelastic (bystander particles are accelerated by the passing electrons) and the walls are actually compressed as the collisions drive the field lines closer together. Thus the above example would be improved with a coefficient describing the inelasticity as a function of number of collisions, but the example still provides a reasonable conceptual understanding of the mechanism.

In a young SNR, second-order DSA is relevant only when the shock fronts are highly turbulent. A first-order process can also occur between plane-parallel shocks such as a supernova blast wave and its radiative precursor in an environment where density is not constant — a clumpy ISM can drive the precursor closer to the shock front — as in the conceptual example above. First order Fermi acceleration, or "diffusive shock acceleration" (DSA) in its astrophysical application, is not as intuitive as second-order Fermi acceleration. Charged particles diffuse (hence the "diffusive" in the name) into the shock front and then get accelerated back out from it. The particles are reflected back into the shock by magnetic fields. At each crossing of the shock, it gains energy due to its acceleration from the shock boundary, with the energy gain proportional to the number of times it crosses the shock boundary. A numerical simulation of first order DSA is shown in Figure 1.10. Experimental physicists are starting to look to the possibility of creating shocks in a laboratory that are capable of the first-order Fermi process, which will greatly improve our understanding of the efficiency of acceleration (both in number and in time scale) and distributions of particle energies (Reville et al. 2012).

1.3 Cosmic rays and synchrotron x-rays

There is a natural limit to the maximum energy of the particles accelerated by Fermi processes, as the higher energy particles become too energetic to be confined by the magnetic fields (the gyroradii become larger than the clouds/SNR, so the product of the structure and the magnetic

field strength defines the cutoff). This is the reason for the PeV limit to cosmic ray energies that describes quite well the observed "knee" in the cosmic ray spectrum where the power law index changes from -2.7 to -3.1 around 4 PeV (Figure 1.9). However, this process is thought to die out after a few kyr (Aharonian and Atoyan 1999).

Galactic observations show the thermal pressure, the magnetic field pressure, and the cosmic ray pressure to be roughly balanced (e.g., Cox 2005). This is an odd situation, since cosmic rays and thermal pressure both describe motions of particles and cosmic rays represent a definitively nonthermal population. In an equilibrium state, the equipartition theorem can adequately explain the particle and magnetic field energy equality, but when cosmic rays are included it is a statement that there are clearly distinct (cosmic rays will not be generated in an equilibrium plasma at any reasonable temperature) but somehow related populations. Cosmic rays are generally thought to be generated by DSA in supernova shocks and other strong shocks in the ISM, which points to shocks as the likely culprits for including cosmic rays in the equipartition.

Supernova remnants provide much of the thermal and the cosmic ray pressures of the ISM, but that they also could provide the magnetic field structures is at once logical and perplexing, since it requires relic fields to remain after the SNR has mingled with the ISM. Additionally, to maintain the equipartition of these three energies, they must remain coupled for much of their "lives": the cosmic rays must be produced rapidly, sapping one third of the energy from supernova remnants during the first few kyr in the common interpretation of the DSA lifespan; or the cosmic rays are produced for much longer than the few kyr DSA picture would have us believe.

Since the cosmic ray population and the $\sim$100 TeV electron population that produce x-ray synchrotron emission are tied together by the same acceleration mechanism, the above quandary of rapid or sustained cosmic ray production can be tested by observing the synchrotron contribution to the emission from supernova remnants greater than a few kyr old. Without a method for accelerating the nonthermal population, the synchrotron lifetime of an electron is tens of years (Parizot et al. 2006).

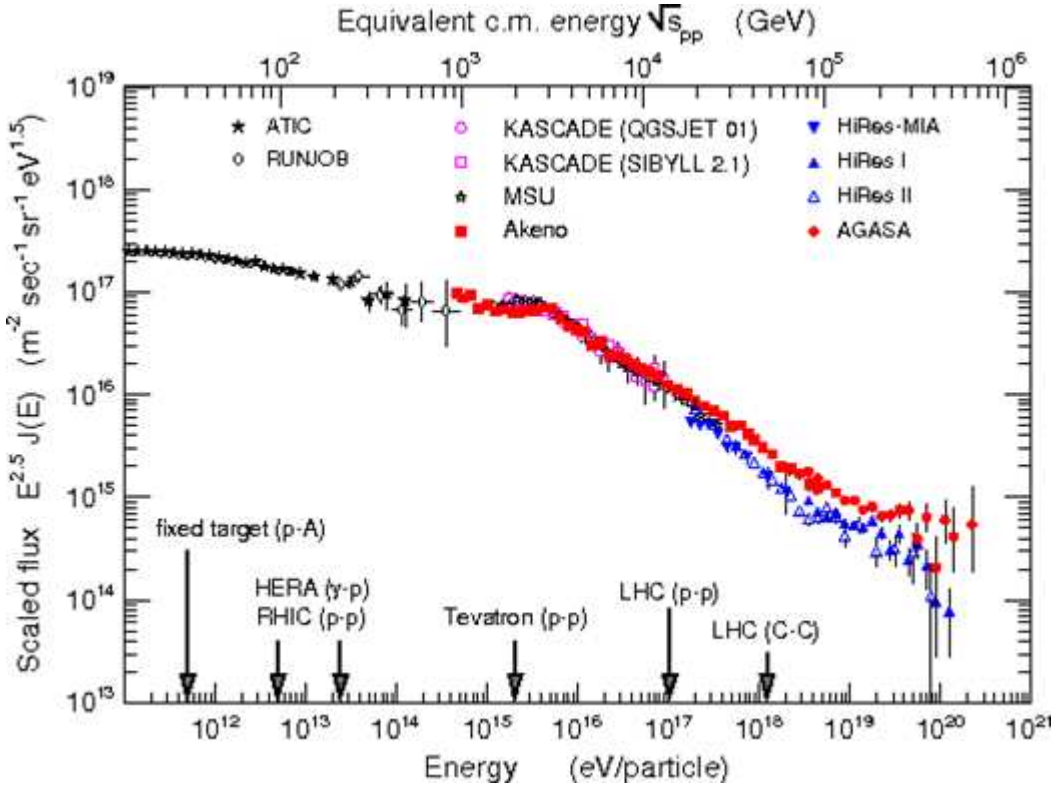

Figure 1.9 The cosmic ray spectrum, showing the "knee" at 4 PeV. It also has a second knee at ∼200 PeV and an ankle above 2 EeV (Blümer et al. 2009). The x axis is marked with the human achievements in the field of particle acceleration.

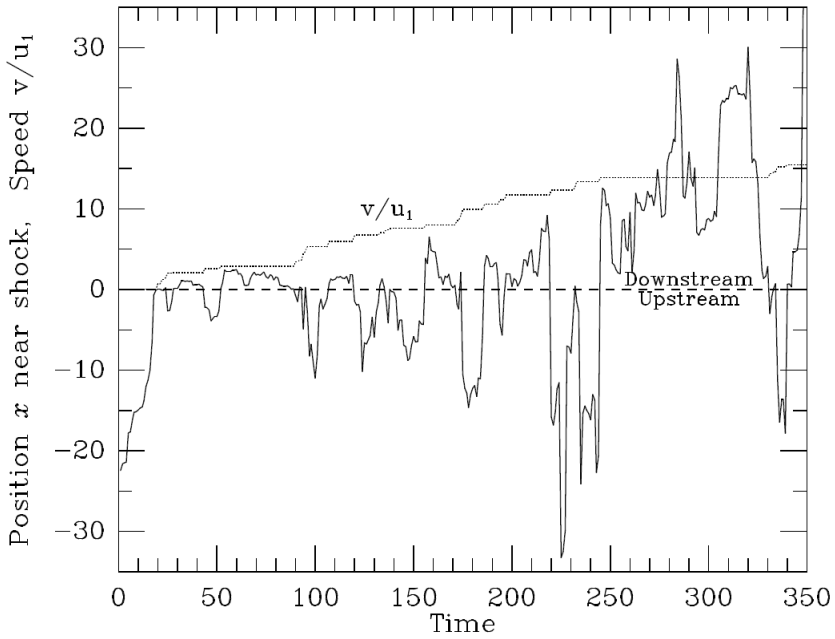

Figure 1.10 Monte Carlo simulation of a particle crossing back and forth across a shock front, plotted with its position (solid) and velocity relative to its input velocity (dashed). The energy climbs monotonically (Baring 1997).

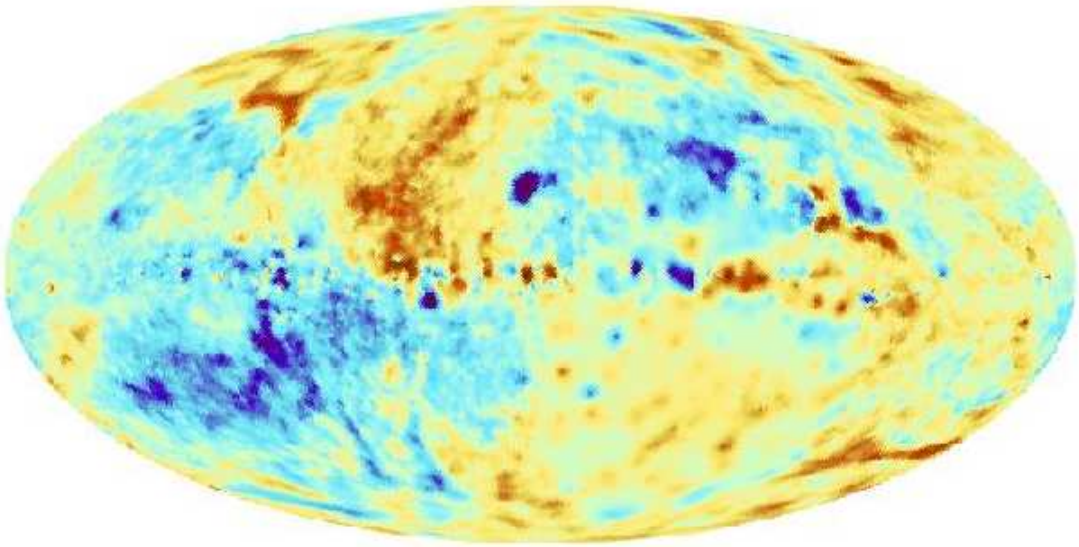

Figure 1.11 Dimensionless map of the Faraday rotation signal, tracing Galactic magnetic fields by their effect on the polarization of background light (Oppermann et al. 2012). The plane itself has been removed since it dominates the faint signal from the likes of the North Polar Spur (mid/top center of the image).

1.4 Diffusion rate

Both forms of Fermi acceleration are coupled to the transport of particles through a plasma, which is usually of order $\sim(1/16)k_BT/eB$, the empirically-determined Bohm diffusion coefficient for a particle in a plasma of temperature T and magnetic field strength B (Bohm, D. 1949). The magnetic field of a young SNR can be $10-100$ times the ambient several-μG magnetic field of the ISM, and the diffusion coefficient can be up to 10 times the Bohm coefficient (Parizot et al. 2006). According to simulations, the amplification of the magnetic field, driven by the DSA process, is required to steepen the spectrum of cosmic rays, observed as $E^{-2.7}$, while efficient acceleration without converting kinetic energy into magnetic field energy produces spectra flatter than E^{-2} (Caprioli 2012).

Although fluid advection carries matter from the pre-shock upstream region to the post-shock downstream, the diffusion rate also describes the rate at which particles counterstream via diffusion in either direction from the shock. A more efficient DSA mechanism implies a higher diffusion, which in turn implies a higher rate of recycling of hot thermal electrons from the interior of the remnant to the shock. The transport of energy via diffusion and the transfer of energy into hot electrons also make the shock front more compressible, with hydrodynamical simulations indicating that the standard shock solution of a compression ratio of 4 can be several times that, depending on efficiency of the acceleration process (Ellison et al. 2004). The diffusion rate, although with different variables, also defines how far in front of the shock the charged particles will advance, with the distance proportional to the diffusion rate divided by the shock velocity, D/v_s. Since the forward diffusion affects the strength of the precursor shock that in turn affects the efficiency of the DSA, this is another way in which the acceleration and the accelerating mechanism are coupled.

The Ellison et al. (2004) simulations show the shock compression ratio decaying to the more-traditional value of 4 over some 10^4 years (the simulation goes to 5 kyr, at which time the compression ratio for efficient acceleration cases is $\sim$5). Temperatures are considerably lowered — up to an order of magnitude — because of the loss of thermal energy into the DSA process. Others

estimate that $10\% - 30\%$ of the kinetic energy of the shock is lost to the DSA process and cosmic ray acceleration within the first several kyr after the SNRs birth (Morlino and Caprioli 2012).

1.5 Emission processes

The shift of temperatures shifts the balance of types of emission. Historical remnants (those observed by eye over the past 1 kyr or so, and thus well-dated, if nothing else), which are small enough to be relatively easy targets for the likes of Chandra, have a combination of thermal and nonthermal emission. The nonthermal component is generally accepted as synchrotron emission (Reynolds 1998) and requires high energy (tens of Tev) electrons to emit in the x-ray regime, while the thermal component is bremsstrahlung from collisions of hot particles in the plasma.

The acceleration of one charged particle in the electric field of another creates bremsstrahlung, or free-free emission, essentially from the collisions of particles in a plasma. For a hot plasma in thermal equilibrium, this will be the dominant emission mechanism. In the thermal case (a Maxwellian electron velocity distribution) the emissivity (power emitted per volume per time per Hz) is given by

$$\epsilon_\nu \equiv \frac{dW}{dV\ dt\ d\nu} = \frac{2^5 \pi e^6}{3mc^3} \left(\frac{2\pi}{3k_B m}\right)^{1/2} T^{-1/2} Z^2 n_e n_i e^{h\nu/kT} \overline{g}_{ff} \tag{1.7}$$

Rybicki and Lightman (c.f., 2004), where the $\overline{g}_{ff}$ factor is the velocity-averaged Gaunt factor. The Gaunt factor accounts for the probability of interaction of two particles and the integrated power across all frequencies is proportional to $T^{1/2}$ (the particle velocity), which scales the collision rate. Bremsstrahlung is dominated by electrons, which are accelerated more rapidly than ions due to their lower mass and travel at a higher velocity. The electrons collide with ions because the collisional cross section of an ion is much larger than that of an electron. Since n_e and n_i are close (electrons come from the ions, so the balance will be skewed toward n_e because the majority of the heavy ions will be multiply ionized and differ only by a coefficient), bremsstrahlung is an n^2 cooling process. A nonthermal distribution of electrons produces a spectrum dependent on the particular

velocity distribution of the electrons, with a peak corresponding to the temperature.

The acceleration of charged particles in an ordered magnetic field such that the Lorentz force

$$\overrightarrow{F} = q(\overrightarrow{E} + \overrightarrow{v} \times \overrightarrow{B}) = m\overrightarrow{a} \tag{1.8}$$

drives the particles with charge q in circles and creates cyclotron emission, or for relativistic velocities synchrotron emission. For the case of particles exiting radially from the SNR center, a swept-up tangential magnetic field (such that $\overrightarrow{v}$ is always perpendicular to the magnetic field $\overrightarrow{B}$), and an electric field $|\overrightarrow{E}|$ of 0, the acceleration is perpendicular to the magnetic field and velocity vectors as described by the cross product, and, after substituting in the mean kinetic energy

$$\frac{1}{2}\mathrm{K}E_{avg} = \tfrac{1}{2}mv^2 = \tfrac{3}{2}k_B T, \tag{1.9}$$

of a magnitude

$$a = \sqrt{3k_B} \cdot q \cdot T^{1/2} \cdot B \cdot m^{-3/2}. \tag{1.10}$$

Heavier ions will be accelerated far less per charge than electrons. Since the mass of an electron is ∼1800 times less than the mass of a proton, the acceleration of electrons will be ∼80,000 greater than a proton (and more for heavier ions). With a nod to Larmor's formula for power emitted from an accelerated charge, namely

$$P = \frac{2q^2a^2}{3c^3}, \tag{1.11}$$

the power emitted by a charged particle goes as the cube of both charge and mass. Even in science fiction, no one has discovered an ion with a charge/mass ratio greater than 1800, and in a highly-ionized plasma the number of electrons exceeds the number of protons.

The proton versus electron emission was quietly discussed in a non-relativistic form. The frlativistic version of Larmor's formula is

$$P = \frac{2q^2}{3c^3}|\overrightarrow{a} \cdot \overrightarrow{a}| = \frac{2q^2}{3c^3}\gamma^4 a^2, \tag{1.12}$$

where $\gamma = (1 - v^2/c^2)^{-1/2}$ is the relativistic Lorentz factor (see Rybicki and Lightman 2004, for a derivation). With some simple algebra, this shows that the synchrotron power emitted by a single

charged particle traveling in a magnetic field is proportional to $\gamma^4 T B^2$. The power is broadband, even for a single electron, up to a cutoff energy determined by the velocity and magnetic field. The cutoff is defined by the maximum frequency of observation (the window Δt where emission from two points in the orbit could produce a coherent photon signal at an observer) for which the electron is sufficiently accelerated to produce a photon of energy $h\nu_c$. For a velocity perpendicular to the magnetic field, the cutoff frequency is

$$\nu_c = \tfrac{3\pi}{4}\gamma^3 \omega_B, \tag{1.13}$$

where $\omega_B = \frac{qB}{\gamma mc}$ is the frequency of gyration for a relativistic particle.

Per the discussion of DSA above, the population of highly-energetic particles accelerated by the Fermi process follows a power law that is a function of the momentum p such that $f(p) \propto p^{-b}$, where b is the power law index. For a synchrotron power law with intensity $I_\nu \propto E^{-\alpha}$, the indices are related by $b = 2\alpha + 3$. Furthermore, the acceleration of electrons due to DSA produces a power law with a slope proportional to the compression ratio r of a shock ($r = 4$ in a strong nonrelativistic shock without magnetic fields or diffusion). The shock compression relates to the electron population by $b = 3r/(r-1)$ (Melrose and Crouch 1997). For $r = 4$ this gives $\alpha = 0.5$; diffusion effects that raise the compression ratio will steepen the spectrum. If the population mimicked the cosmic ray spectrum ($b = 2.7$), then $I_\nu \propto \nu^{+0.15}$. Melrose and Crouch (1997) shows that, for this case, $b \approx 3$ (a flat continuum), at least for energies well below the synchrotron cutoff.

Bremsstrahlung emission needs only a tail of a velocity distribution at high energies to produce x-rays (10^6 K gas has a thermal peak in the 100 eV range, and even old SNRs meet that requirement). Synchrotron emission requires extremely high energies just to produce soft x-rays, with Parizot et al. (2006) estimating that the electron energy E_e required to produce an electron of a particular energy $E_{\gamma,\mathrm{keV}}$ in keV units in a magnetic field B_{100} (scaled to a 100 μG field) is

$$E_e \approx (22\mathrm{TeV}) B_{100}^{-1/2} E_{\gamma,\mathrm{keV}}^{1/2}, \tag{1.14}$$

with >5 TeV electrons required to produce soft x-rays at 0.5 keV. Parizot et al. also used diffusion and advection rates to estimate magnetic fields of 250 to 500 μG in the $300 - 400$ yr old Cas A,

Kepler, and Tycho SNRs, and ∼100 μG in SN 1006, based on the shock widths of the nonthermal shells.

Studies of diffuse shocks are difficult because of their angular extent and their (generally) low surface brightness. Nonetheless, there is evidence that large-scale structures in the Galaxy are produced by synchrotron emission. Compare Figure 1.2 to Figure 1.12: polarized radio emission and x-ray emission trace the same features. There are two explanations for this: (1) the radio map could be dominated by weak and old magnetic fields at the edges of remnants (or other bubbles), while electrons from the hot interior diffuse into the old shock front and produce keV bremsstrahlung photons; or (2) that the magnetic fields and shock fronts of the older, extended remnants are still capable of emitting synchrotron radiation in the x-ray bandpass. The former is the usual hypothesis, but soft x-ray spectrometry of these sources, as mentioned above, has thus far been incapable of definitively separating the models.

The coupling of diffusive shock acceleration and the magnetic field strength makes it difficult to predict the time dependency of the nonthermal component. In young remnants, the magnetic field amplifies the cosmic ray energies, and the cosmic rays in turn amplify the magnetic fields. Particles are accelerated to a maximum energy of

$$E_0(t) \approx 20 B_{10} t_{1000} v_{s,2000}^2 \eta^{-1} \mathrm{TeV}, \tag{1.15}$$

with the magnetic field B_{10} in 10 μG units, the time t in kyr, the velocity v_{2000} in 2,000 km s^{-1}, and the gyrofactor η defined as the mean free path divided by the gyrofrequency. The maximum electron energy which can be sustained (balancing DSA and synchrotron emission), however, is dependent on shock velocity:

$$E_0 \approx 45 B_{10}^{-1/2} v_{s,2000} \eta^{-1/2} \mathrm{TeV}. \tag{1.16}$$

The mean energy of the synchrotron photons is proportional to the square of the cutoff energy and the magnetic field (n.b., $\langle E \rangle \propto B E_0^2$), so the magnetic field curiously cancels out of the mean energy of synchrotron emitting electrons, leaving only a velocity dependence that spells an early doom for

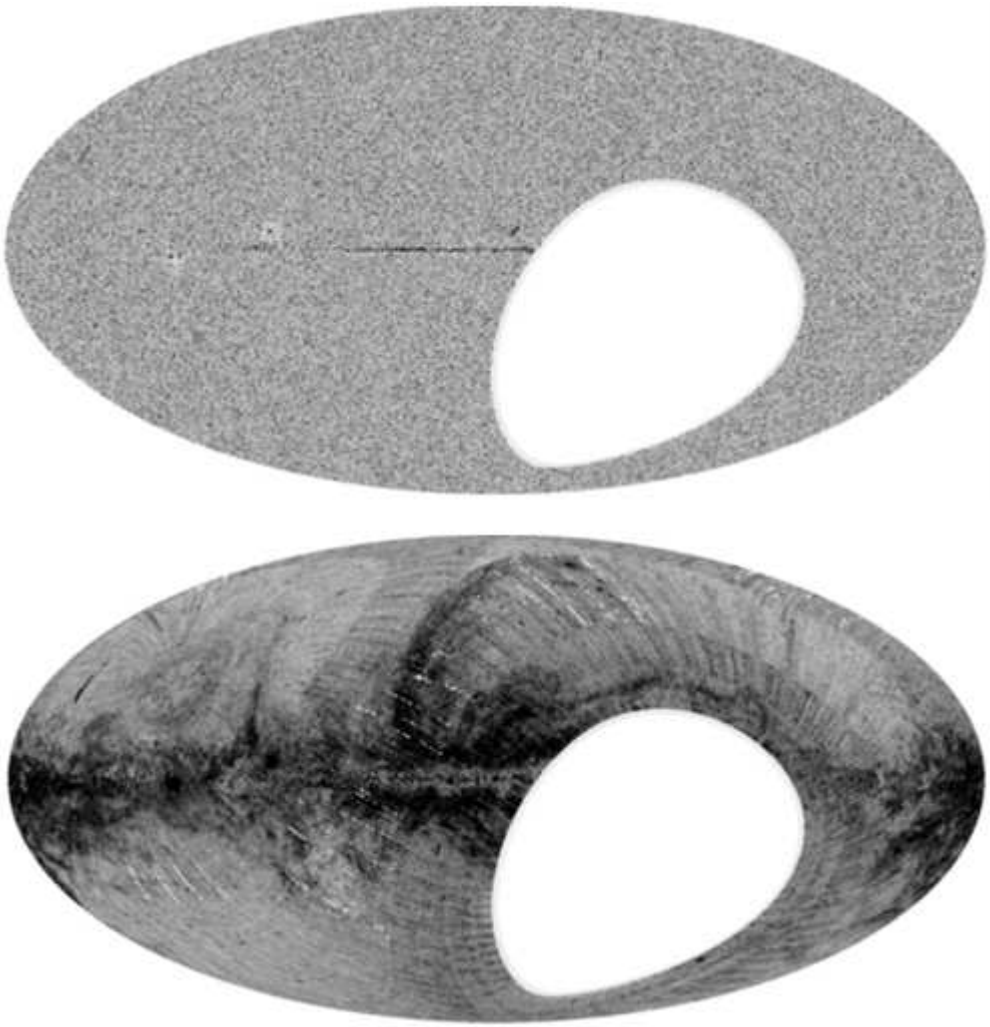

Figure 1.12 Total intensity (*top*) and polarization (*bottom*) in the 1.4 GHz NRAO VLA Sky Survey (NVSS) plotted in Galactic coordinates. Note the strength of the NPS in polarized emission, generated from synchrotron processes. Dramatic arcs emanate from the Galactic plane in the polarized image, spatially correlated with similar looking features in the ROSAT All Sky Survey. The central arc is "Loop I" containing the northern feature dubbed the North Polar Spur. The Vela SNR is too far south to show up in the NVSS image. Radio synchrotron emission only requires tens of GeV, compared to the tens of TeV for soft x-rays (Rudnick and Brown 2009).

the population that would emit soft x-rays from older remnants with slower shocks (Figure 1.8):

$$\langle E \rangle \approx 0.5 v_{s,2000} \eta^{-1/2} \mathrm{keV} \tag{1.17}$$

(Aharonian and Atoyan 1999). In a practical sense, this is the cutoff below which the electrons will radiate energy more quickly than they gain it from DSA because the shock is no longer traveling fast enough to energize the electrons sufficiently with its reflection.

The early cutoff of diffusive shock acceleration translates to a maximum age of the nonthermal population of a few kyr because the synchrotron lifetime of an un-accelerated particle is of order tens of years. The limit on acceleration assumes Bohmian diffusion, however, and as stated above, observational evidence from young SNRs suggests that the diffusion rate could be low by as much as a factor of 10 (Parizot et al. 2006). The more efficient diffusion would make diffusive shock acceleration more efficient. If it is a linear change of E_0, it still has a quadratic effect on the mean energy or, conversely, on the necessary shock velocity needed to sustain first-order DSA. Applying this to Figure 1.8 shows that the synchrotron emission could be sustained well beyond the lifetime of the supernova remnant (when it becomes indiscernible from the ISM), and even a nonlinear effect on DSA that reduced the diffusion coefficient to a linear term would carry the synchrotron lifetime of the remnant to 100 kyr.

According to the conventional model — which does not account for the increased diffusion and increased DSA efficiency — as the shock slows with time, the magnetic field will dissipate, releasing the higher energy particles that previously helped to amplify the field and fading further. The nonthermal electron population could not be sustained past a few kyr.

Observations have confirmed the DSA process in SNRs by showing the strength of the nonthermal component in young SNR shells (e.g., Koyama et al. 1995), as well as through agreement with the cosmic ray spectrum. The oldest known x-ray synchrotron emitter is RCW 86. Calculations based on the strength of the synchrotron emission give a shock velocity of $\sim$2,700 km s^{-1} and an age of 2.2 kyr (Vink et al. 2006) that is consistent with RCW 86 being the product of SN 185, while optical observations of a different part of the remnant give velocities closer to 600 km s^{-1}

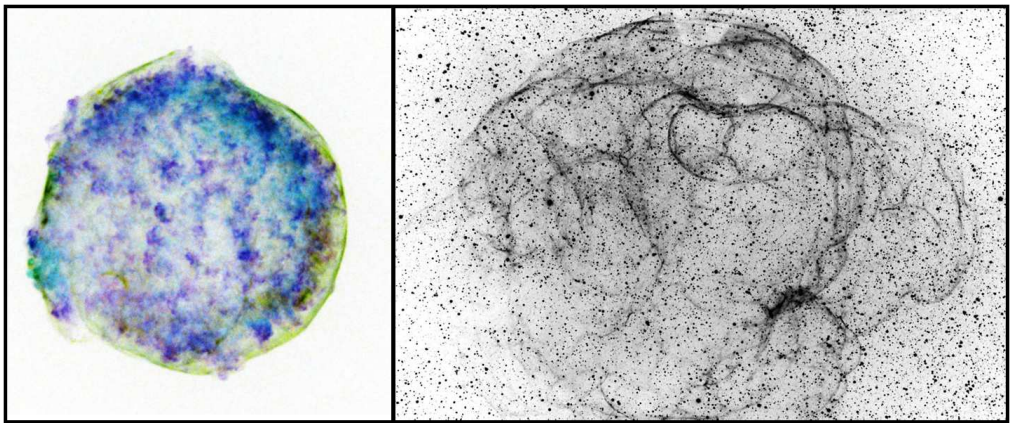

Figure 1.13 The Tycho remnant (340 yr old, *left*, image credit: NASA/CXC/Rutgers/J.Warren & J.Hughes et al.) and the Simeis 147 remnant ($\gg 10^4$ yr old), *right*, image credit: S. Mandel.. The synchrotron shell (green) on the Tycho remnant resembles the Simeis 147 Hα shell structure far more than the thermal (blue) emission does, and although Hα preferentially traces shocks, anyway, the image shows that the smooth and ordered shock fronts persist from young to old remnants.

and an age of 10 kyr (Ghavamian et al. 2001). To reconcile x-ray synchrotron emission with the Aharonian and Atoyan (1999) result (Equation 1.17) required deviating from the spectroscopically-measured velocity by a factor of 4.5 to produce TeV electrons capable of x-ray synchrotron emission. There is an increasing number of supernovae in the age range of hundreds to a few thousand years where emission is predominantly nonthermal (1.15; Koyama et al. 1995, 1997; Slane et al. 1999, 2001), but what happens to the bremsstrahlung/synchrotron ratio as they evolve is an open question.

The above discussion is a hybrid of theory and observations, suggesting that restricting synchrotron emission to young remnants with very high (>2,000 km s^{-1}) shock velocities might not be accurate. Perhaps the simplest argument that synchrotron emission persists is the appearance of young remnants and old ones. Older remnants are difficult to image because of their large angular size and low surface brightness, but the features are often more similar to the shell-like synchrotron emission of young remnants than to the filled-in, turbulent bremsstrahlung emission (for example, see Figure 1.13).

1.6 Tests of thermal versus nonthermal emission

Even if the theory that thermal emission dominates the x-ray emission of older remnants is not entirely consistent with recent observations, any proposed alternative (such as nonthermal synchrotron emission) needs to be observationally supported to gain credibility. One cannot simply declare the presence of synchrotron emission on the grounds that some observations have opened the door to its possibility. One of the crowning achievements of ROSAT was defining the global soft x-ray budget, and the integrated flux of any SNR is a known quantity un ROSATs bandpass and thus must remain fixed in any model. Adding synchrotron emission to the model requires explaining away at least a fraction of the bremsstrahlung, perhaps because of the ordered advection in the shock front or a larger fraction of the particles being trapped in the nonthermal population. This needs to be observationally motivated, as the bremsstrahlung certainly will not disappear entirely and the relative contributions need to be understood.

One test of the consistency of synchrotron emission with observations might be through a survey of old supernova remnants. Cosmic ray dominated shocks have a thermodynamic $\gamma = 4/3$, while a classical shock has a ratio of specific heats of $\gamma = 5/3$. This should produce different expansion rates as kinetic energy is converted to thermal energy at different rates. This method might even escape the troubled soft x-ray bandpass because the evolutionary structure of remnants can be traced in other bandpasses. However, old SNRs have a complicated history of interactions with the ISM and of emission, and obtaining their expansion history from a snapshot is daunting at best.

Another method would be to look in the radio regime, where synchrotron emission can be seen in very old remnants, dating back $10^4 - 10^5$ yr, approaching the regime where the SNR begins to blend into the ISM. The selection of supernova remnants that can be seen in the soft x-ray regime is very small due to the short mean free path of soft x-ray photons, and the large angular sizes and low surface brightnesses of diffuse SNRs make them observational challenges. However, as seen in the comparison of the soft x-ray ROSAT All Sky Survey (Figure 1.2) and the

1.4 GHz NVSS data (Figure 1.12), the large-scale structures show significant similarities. Figure 1.11 shows magnetic fields that align with the radio synchrotron and x-ray maps. The flaw with this test is that hot electrons could produce x-ray bremsstrahlung emission and radio synchrotron emission. The emission frequency cutoff could be well before the x-ray regime, and the cutoff would be imperceptible at radio wavelengths because the electron population still follows a comparable energy distribution at lower energies. Although scarcely definitive proof that they represent the same population of particles, the colocation of radio and x-ray emission both in the all-sky images and in the images of individual SNRs at least is consistent morphologically with them being tied by the same process.

A third possibility is to search for analogs to supernova shocks that might be easier to observe due to smaller angular extents. Planetary magnetospheres and galaxy clusters offer comparable situations, although admittedly their bow shocks are driven by massive bodies. In both cases of shocks, DSA has been at least a statistically adequate description of the observed spectra (Baring and Summerlin 2005; Siemieniec-Ozieblo 2004). In galaxy clusters, in particular, there is a large continuum contribution in the soft x-ray band (Figure 1.14). While this can be described with thermal models, the weak line emission does not definitively argue for thermal over synchrotron emission scenarios. In the end, this does not strongly argue one way or another on the case of emission mechanisms in older supernova shocks, but it is at least qualitatively not inconsistent.

1.7 Reasons synchrotron emission might not persist

This assessment of SNR emission theory would not be complete without addressing the counterarguments to persistent synchrotron emission, however. First, the spectrum of Vela Jr. (Figure 1.15) shows a thermal continuum as well as a synchrotron one, distinguished by the energies with which they dominate. Vela Jr. is a young remnant (^{44}Ti dating places it around 680 yr; Aschenbach 1998)) and still in its free expansion stage. Velocity drops as $t^{-2/5}$ in the Taylor-Sedov phase, and the shock thermal temperature is proportional to the square of the shock velocity (Eq. 1.6). For a 10 kyr remnant, the velocity will have slowed by a factor of $\sim$300 and the thermal peak

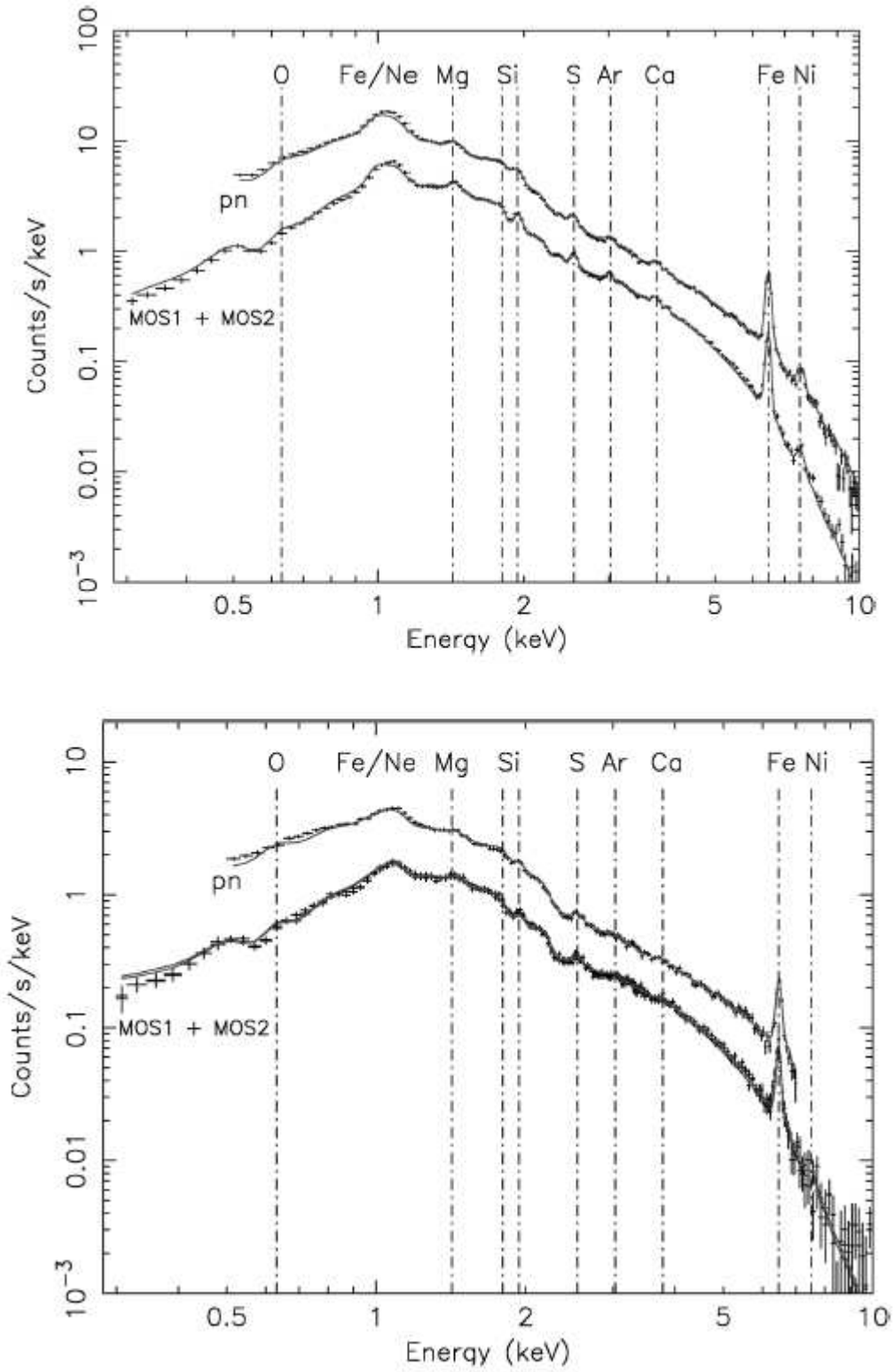

Figure 1.14 Spectra of the inner $3'$ and $3' - 9'$ of the galaxy cluster 2A 0335+096 (Werner et al. 2006). The XMM–Newton spectra (with different lines for each detector) show weak spectral lines of oxygen around 0.5 keV and iron around 1 keV.

drops as the square of the velocity, leaving the synchrotron continuum in the soft x-ray bandpass.

A second counterargument comes from the new methods of measuring magnetic fields in young remnants via the diffusion length of the synchrotron electrons (Vink and Laming 2003; Parizot et al. 2006). In young remnants, the synchrotron shocks are very thin (<0.25 pc for the five studied by Parizot et al. 2006). The only nonthermal x-ray emission seen from shocks in young remnants comes from thin features, yet the likes of the North Polar Spur are decidedly not thin, with features ranging in widths from 0.4 pc up to nearly 20 pc (Salter 1983). With observed SNR nonthermal shocks being so thin, it is unconfirmed that a broader shock could sustain DSA for accelerating TeV electrons and the requisite magnetic fields for their confinement. Parizot et al. (2006) show the magnetic fields monotonically declining with age in young remnants, with the nonthermal shock width growing with age (a linear fit to Table 1 of Parizot et al. 2006 gives the time-evolution of the synchrotron shock width with an intercept of essentially 0 [5×10^{-4} pc] and a slope of 0.17 pc kyr^{-1}). The jury is still out on older remnants, however, as there are no good spectroscopic measurements of them. In the Cygnus Loop, a remnant $5 - 8$ kyr old, shocks have been observed with widths in the 0.1 pc range, comparable to the nonthermal shock widths in younger remnants (Raymond et al. 2003), but Fermi-LAT observations of the Loop from $0.2 - 100$ GeV argue against a pure power law description with 3.5σ significance. Spectra of the North Polar Spur and the Vela SNR (Figure 1.16) both show considerable continuum emission, although at low spectral resolution it is usually considered strictly a thermal continuum with overlaid spectral lines. This seems to be a reasonable argument against a significant contribution of synchrotron emission from older remnants, but it is not decisive.

Third, the injection of particles into the DSA process from the thermal population is already an issue of debate. Particles need to be well above the thermal population's mean energy to begin the acceleration process or they will be simply scattered back into the thermal hodgepodge. Without the turbulence of a young remnant to drive electrons to higher energies, the synchrotron population might not be sustainable in old remnants. High diffusions rates, however, allow the hot gas from the interior of the remnant to diffuse into the shock region and provide a higher energy

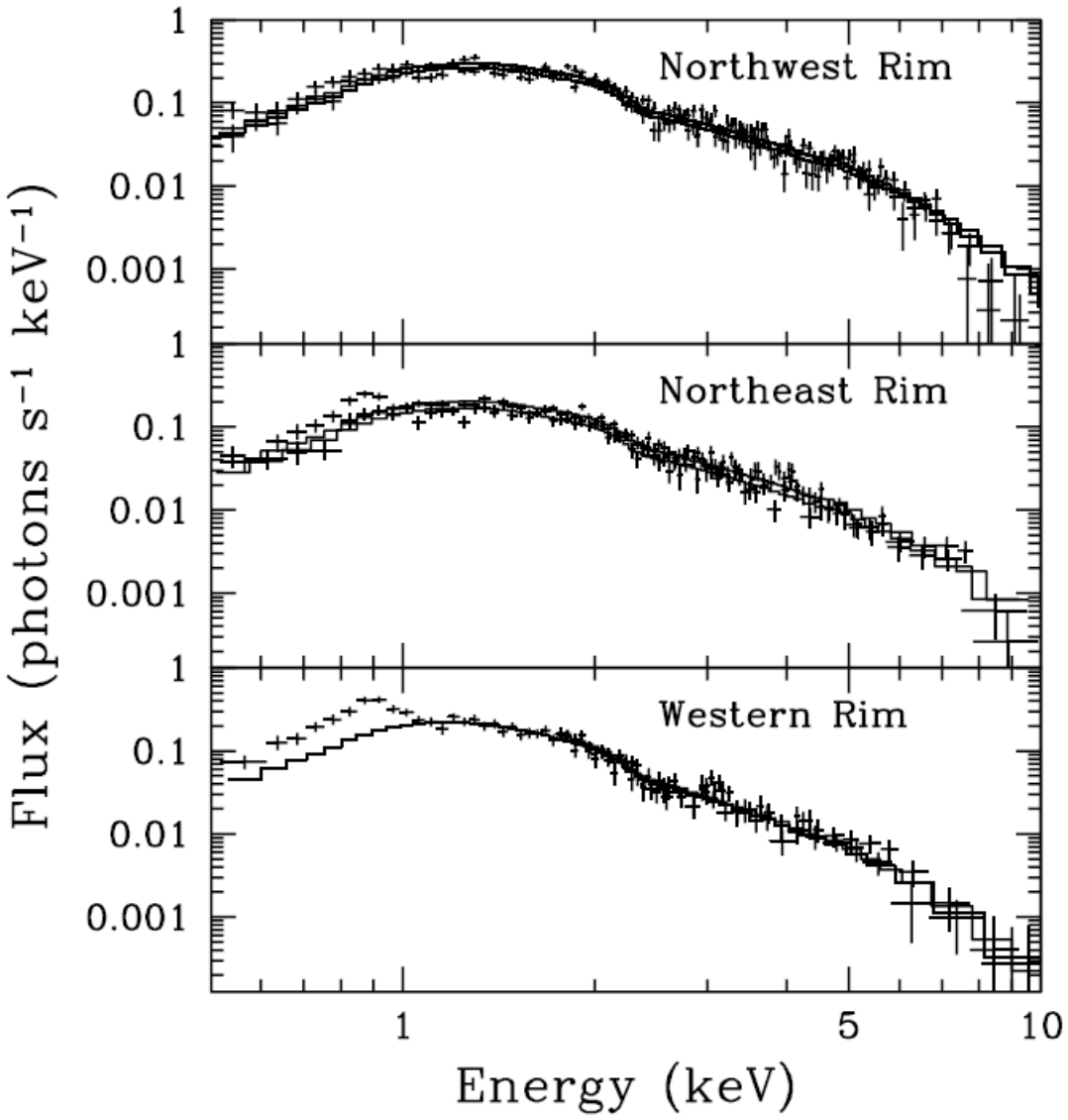

Figure 1.15 Nonthermal spectra of Vela Jr. (RX J0852.0−4622). The broad peak around 1.2 keV is thermal, and the power law above ∼2.5 keV is synchrotron. The excess flux below 1 keV is due to the Vela SNR along the same sight line (Slane et al. 2001). The remnant is ∼200 pc distant and ∼680 yr old (Aschenbach et al. 1999).

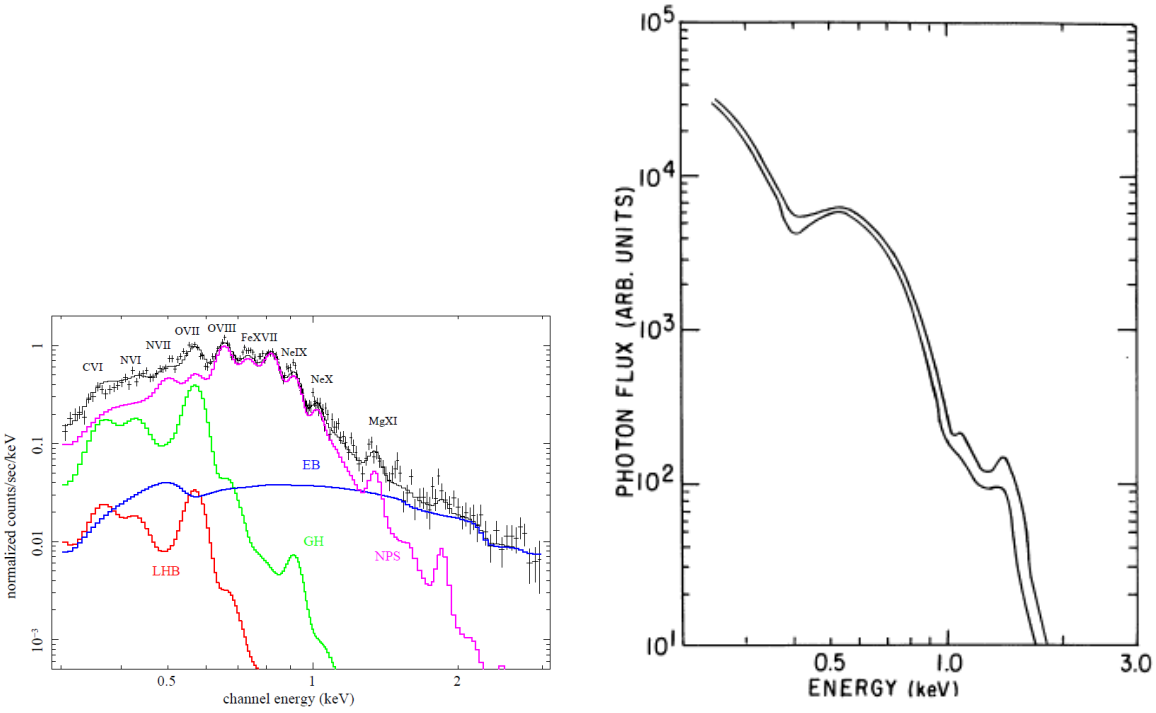

Figure 1.16 Spectra of the North Polar Spur (*left*; Willingale et al. 2003) and Vela SNR (*right*; Kahn et al. 1983). Spectral resolution of both are too poor to determine if a proper fit is thermal continuum and lines or if there is an underlying nonthermal power spectrum contributing to the soft x-ray flux. A higher resolution spectrograph could make this distinction.

population.

Lastly, the argument for synchrotron emission is based, in part, on high diffusion rates that result in compressed shocks. Compressed shocks result in steeper power laws, and a compression ratio as high as 10 would produce a power law index of 3.5 that could be impossible to disentangle from a thermal spectrum without an exquisite instrument. Since the discussion hinges on continuum distributions, a broader bandpass will increase the chances of distinguishing between the types of emission. Difficulty of observation is not a counter to a scientific case.

That the knee of the cosmic ray spectrum is fairly well defined would also seem to indicate that processes of a particular size and energy scale cause it, such as young SNRs in a free expansion stage that have a tightly-constrained size. However, the containment of charged particles is dependent on the radius of the SNR being larger than the gyroradius ($r \propto B^{-1}$). As the remnant ages and the magnetic fields weaken, the radius of the remnant also grows. As long as both processes occur at nearly the same rate, the particles will continue to be confined in the shock.

Perhaps the best answer to theoretical counterarguments is observational evidence: an observation demonstrating clearly whether the emission is synchrotron or bremsstrahlung in remnants older than a few kyr. The soft x-ray bandpass is ideal for determining the emission mechanisms present in old supernova remnants, aside from the difficulty presented by needing to observe in space with an instrument that does not exist. It will catch the bremsstrahlung thermal peak, and the higher energy tail will show if the spectrum has a nonthermal component.

`Quaerendo invenietis.`

1.8 Motivation for a sounding rocket flight

Normally, an observation of a diffuse SNR is a challenging scenario because the soft x-rays generated by 100 TeV electrons have such a short mean free path through the galaxy, meaning that observable old remnants must be nearby and therefore occupy large solid angles on the sky. Obtaining a spatially-integrated, high-spectral resolution observation of a diffuse remnant is nor-

mally daunting because of the expense of many pointings required to build up a picture of the entire remnant and because of the difficulty of dispersing a spectrum from a diffuse object. The CyXESS/EXOS sounding rocket payload design, however, was developed to do exactly that.

The EXOS and CyXESS payloads both targeted the Cygnus Loop when they flew in 2007 and 2009, trying to provide the first high-resolution ($R \approx 50 - 100$) soft x-ray spectra of the entire remnant. CyXESS had considerable trouble during its flight due to gas discharge from the detectors and electronics trouble, producing very strong noise from arcing within and in front of the detectors before settling down in the final 65 seconds of the flight. McEntaffer and Cash (2008) reports detection of the O VII, Mg X, and several Si and S lines near the short-wavelength edge of CyXESS's $44 - 143$ Å bandpass.

EXOS mimicked the design of CyXESS, with a rebuilt but essentially similar wire grid collimator. The most significant change in the second generation payload was that the targeted bandpass was shifted to slightly higher energies, capturing 17-106 Å, primarily to get the oxygen lines at 23 Å. EXOS flew with less obvious noise — no large discharge events, at least — but it detected a factor of 5 more photon events than expected. The reported signal agreed with the CyXESS results, and again there were possible detections at either edge of the bandpass where O VII and O VIII lie (Oakley 2011). The background level was high, however, with no apparent source of noise but also significant arguments against it being an astronomical signal. The line emission results of both flights are consistent with previously published detections, but the continuum (Figure 1.17) possibly detected by EXOS is not.

The large field of view and high resolution of the CyXESS/EXOS instrument is ideal for differentiating between the two scenarios of the temporal extent of DSA. Additionally, the continuum observed by EXOS could be described by synchrotron emission, if it were real. The higher-than-expected count rate detected by EXOS made the spectrum difficult to interpret, however, and a nonthermal explanation could not be firmly established with the data available even though the continuum made such an interpretation very tempting.

The EXOS flight results presented two obvious choices: repeat it but do it better (go back

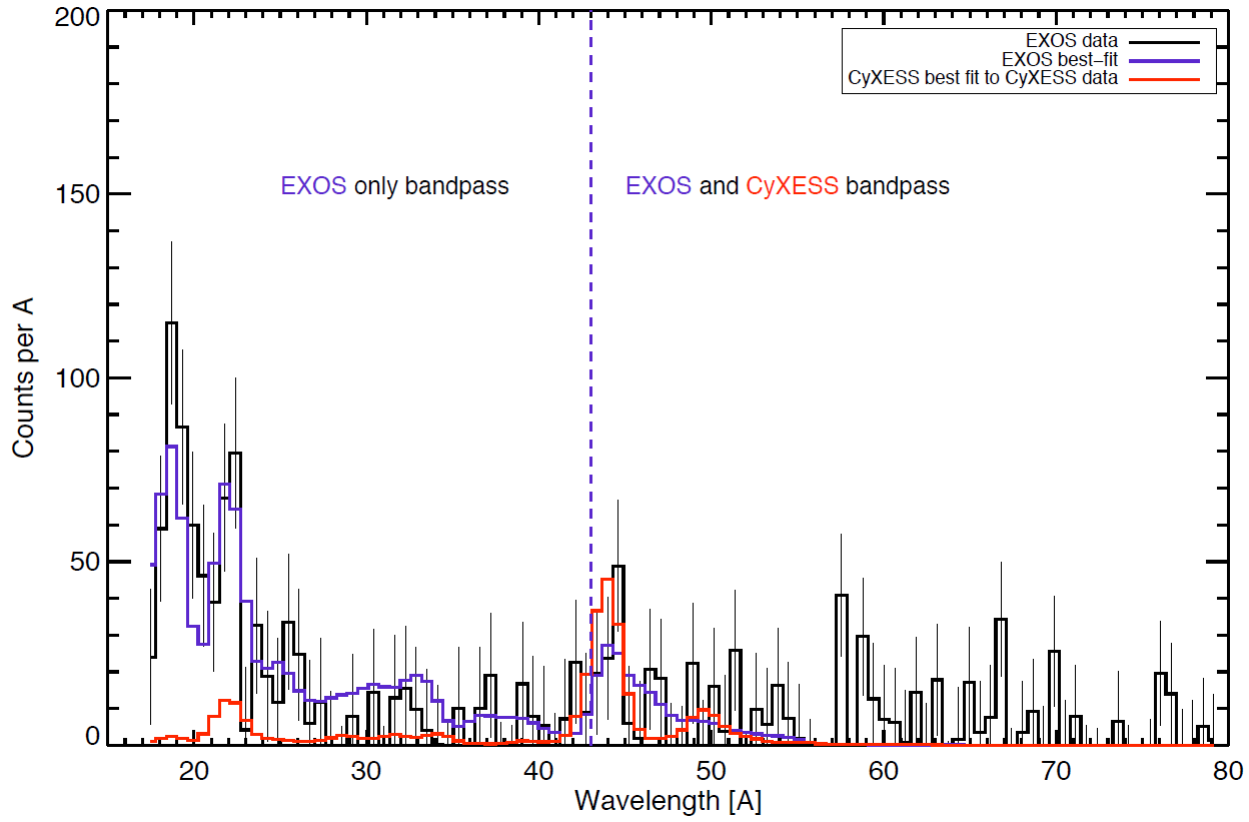

Figure 1.17 Final data from the EXOS and CyXESS flights (Oakley 2011) The EXOS spectrum has had a continuum of several hundred counts per bin removed because its validity could not be confirmed.

to the Cygnus Loop but design the experiment to distinguish better between astronomical signal and systemic noise), or find a comparable target where a similar result would act as confirmation of the Cygnus Loop (and still improve the experiment as much as possible). Targeting a different remnant could confirm the Cygnus Loop results while making them more robust, if the nonthermal interpretation holds up in the different target. The target chosen was the Vela supernova remnant, slightly older and larger than the Cygnus Loop, but the most similar observable object. The payload to make the observations would follow the design heritage of CyXESS and EXOS. It would be called CODEX (Zeiger et al. 2011).

The list of bright targets for CODEX to choose from was short. CyXESS/EXOS expected ∼5,000 counts in a 300 s rocket flight, assuming a thermal plasma. Scaling strictly off of those estimates and a comparison of surface brightnesses of the ROSAT all sky survey maps centered on 1/4 keV and 3/4 keV, the targets that presented themselves strictly in terms of brightness were M87, the full Moon, relatively bright regions of the North Polar Spur and the Monogem Ring, and the Vela SNR. The first two were considered only for calibration targets, since they are decidedly not supernova remnants.

The Spur and the Monogem Ring are comparable to each other. Both are large Galactic structures with strongly polarized radio emission. The Spur presents a particularly tempting target. It is a northern target with a large launch window. It is tempting in that its identity is not known. It has been suggested that it is everything from a single SNR (Cruddace et al. 1976) to a mixture of stellar winds from an OB association (Wolleben 2007) to a jet from the Galactic center (Miroshnichenko 2010). Aside from the Galactic jet hypothesis, most authors agree that it is close, at roughly 100 pc, and some (Frisch 1981; Crutcher 1982) have suggested that it is a supernova with a shock front that has already interacted with the Local Bubble. At its brightest, it is ∼1/12 the Cygnus Loop in the 1/4 keV band, and weaker at 3/4 keV.

The spectra from select regions of the Spur also make it an intriguing candidate for testing the DSA hypothesis. Figure 1.18 shows an emission line spectrum of sufficiently poor resolution that it could be anything from a handful of lines overlaid on a strong continuum to a pure line

emission spectrum to emission lines with a thermal peak on a synchrotron power law. If the Spur is an old remnant with a notable synchrotron component, it could test the contribution of DSA to the emission from old SNRs. The virtue of its mystery and the possibility of perhaps finally resolving its identity through spectroscopy is also its bane, in that its uncertainty makes it a poor check on the Cygnus Loop results. If they agreed, then the results and their motivating theory of old synchrotron emission were probably both right. If they differed, then both results could be called into question.

The Vela supernova remnant is the best target in terms of brightness, similarity to the Cygnus Loop, and historical measurements (as well as its beauty — see Figure 1.19). In the 1/4 keV band it is fully as bright as the Cygnus Loop, and roughly 60% of the surface brightness in the 3/4 keV band. The Vela SNR has a long history with soft x-ray sounding rockets, dating to its discovery as an extended soft x-ray source (Palmieri et al. 1971). As the picture evolved over time with higher resolution instruments, the 5° blob seen by Seward et al. (1971) was resolved into clumps in the NE and SW and further into a filamentary shock structure by the Einstein (HEAO-2) Observatory (Kahn et al. 1983). The thermal peak is also low enough (∼0.22 keV, Figure 1.20) that a soft x-ray spectrometer could snag the nonthermal distribution splitting off from the thermal one at the upper end of the soft x-ray bandpass. The best measurements of some relevant physical properties listed below in Table 1.2.

Recent hydrodynamical modeling of the structure of the Vela SNR places it in the Sedov phase of evolution (contrary to the older view of it being radiative, which relied on a distance estimate of 500 pc rather than the current measurements in the 290 pc range) and best described by evolution in a clumpy ISM (Sushch et al. 2011). With an age of 11.4 kyr nicely determined by the pulsar spin-down rate, the remnant is quite comparable to the Cygnus Loop and old enough to push the boundary of "acceptable" age for synchrotron emission a little further, if the EXOS continuum is supported.

ROSAT spectra exist of the Vela SNR (Figure 1.20). They show a clear thermal peak in the ∼0.2 keV range. The XMM-Newton, Chandra, and Suzaku observatories have all targeted the

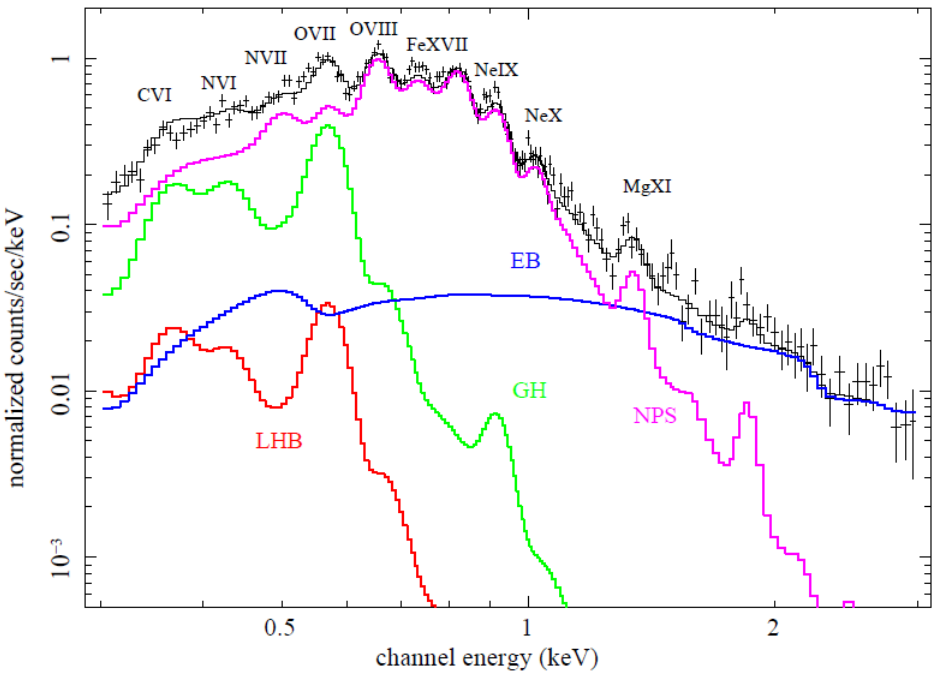

Figure 1.18 Suzaku spectrum of a southern region of the North Polar Spur. The Spur dominates at all energies, although the Galactic halo approaches within a factor of ∼2 below the O VII line, and the extragalactic background dominates at energies above 1.5 keV (Miller et al. 2008). The models fit to the data are: the Galactic halo (GH, green) model; the local hot bubble (LHB, red), the Spur (NPS, purple), and the extragalactic background (EB, blue).

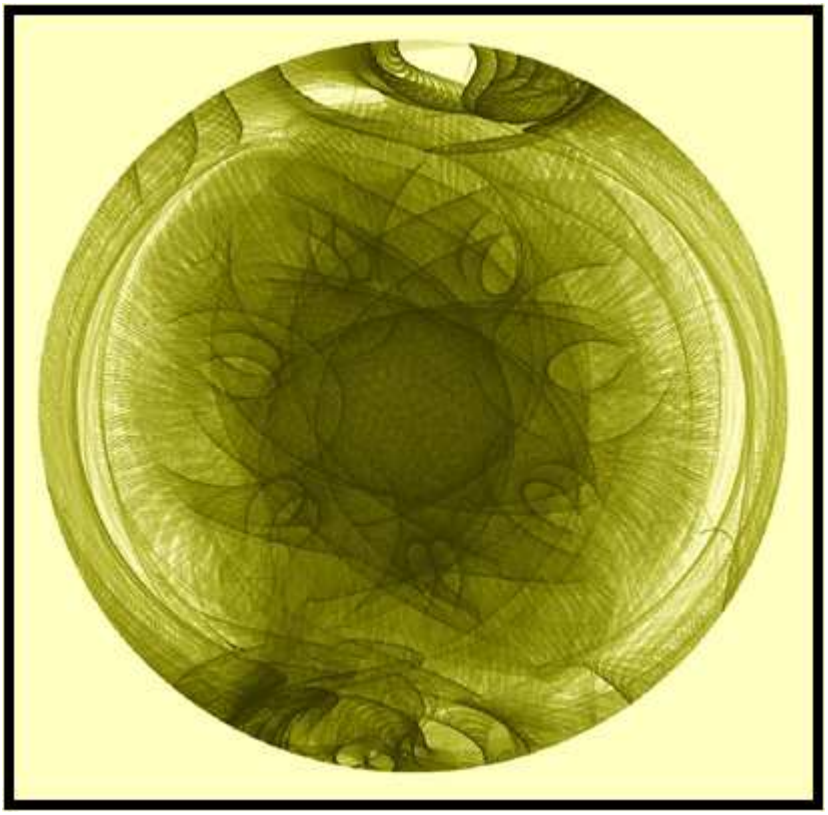

Figure 1.19 Perhaps one of the prettiest images ever produced by high energy astronomers, this is the Fermi Large-Angle Telescope (LAT) image of the Vela pulsar. The spirograph pattern is because of the steradian field of view, which traces the location of the point-like pulsar as Fermi tumbles through its orbit on its all-sky survey mission (image credit: NASA/DOE/International Fermi LAT Collaboration].

Table 1.2. Measured properties of the Vela SNR.

Property	Value	Reference
Location	08h35m21s, $-45°10'35''$	Aschenbach et al. (1995)
Radius (∼circular)	$\sim 4.2°$ with ejecta to $5.2°$	Aschenbach et al. (1995)
Distance		
Optical absorption	250(30) pc[1]	Cha et al. (1999)
HST pulsar parallax	294(+76,−50) pc	Caraveo et al. (2001)
VLBI pulsar parallax	287(+19,−17) pc	Dodson et al. (2003)
Inferred physical diameter[a]	41(+3,−2) pc	Rhind Math. Papyr. (1650 BC)
Age		
Pulsar spin-down	11.4 kyr	Reichley et al. (1970)
Pulsar, filament proper motion	18(9) kyr	Aschenbach et al. (1995)
Relative metallicity (solar = 1)	∼1	Sankrit et al. (2003)
Intervening column density	$5.0 - 60. \times 10^{19}$ cm^{-2}	Lu and Aschenbach (2000)
N/NE	$<2.0 \times 10^{20}$ cm^{-2}	
SW	$\sim 6.0 \times 10^{20}$ cm^{-2}	
Electron temperature		
Shock front, NE	5×10^6 K	Sushch et al. (2011)
Interior, NE	9×10^6 K	
X-ray flux (0.1-2.4 keV)	1.3×10^{-8} erg cm^{-2} s^{-1}	Lu and Aschenbach (2000)
Other details	Pulsar and wind nebula	Large et al. (1969)
	Overlaid with Puppis A and Vela Jr.	Iyudin et al. (1998) Aschenbach (1998)

[a]Assumed central distance of 287 pc from pulsar parallax

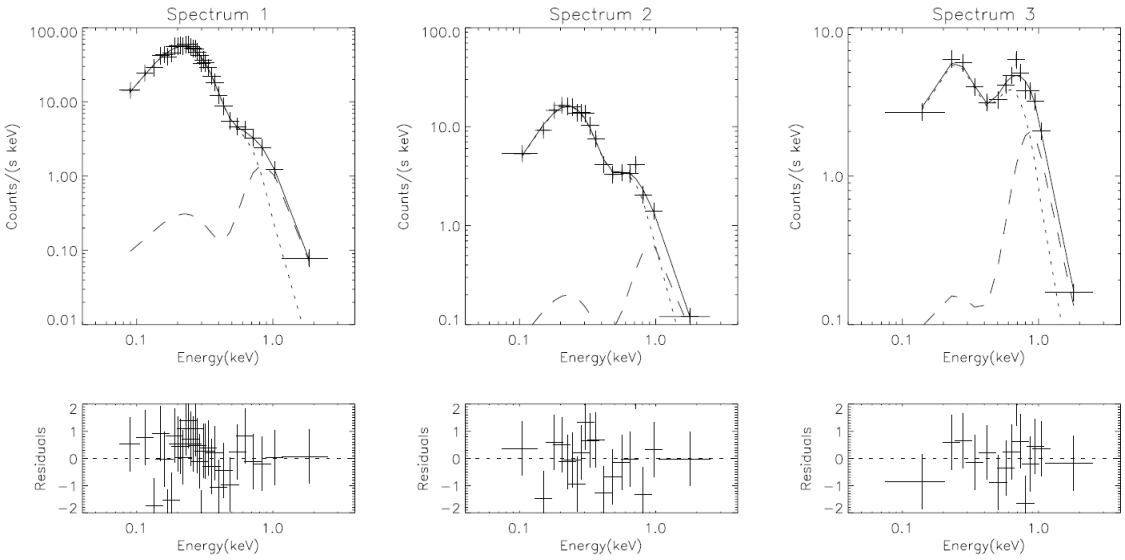

Figure 1.20 Three spectra of ROSAT PSPC pixels (Lu and Aschenbach 2000). The authors do not specify the spatial location of the pixels, but the four plotted components are the observed data (crosses represent errors), the cool thermal component (dotted), the hot component (dashed), and the sum of the components (solid). There are two points to be taken from these data: the spectra are well-fit by the two-temperature thermal model, and the hot component is insignificant to the soft x-ray flux. Although individual photon events may be localized quite well, the true energy resolution of the PSPC is $0.43 \cdot (0.93 \text{ keV}/E)^{1/2}$.

bright regions shown in Figure 1.21. Yoshii et al. (2010), observing shrapnel E, found a thermal tail and a strongly nonthermal head of the shock. Yamaguchi and Katsuda (2009) successfully fit a non-equilibrium plasma model to the Suzaku spectrum of shrapnel B, but were unable to resolve spectral lines (noting, in fact, that they could find a good fit by arbitrarily jumping the oxygen abundance to 10× solar), which is still consistent with other observations that show wildly varying abundances attributed to being the product of an asymetric supernova explosion. Spectra of shrapnel B are shown in Figure 1.22. An XMM-Newton spectrum of shrapnel D, fit with enhanced O, Si, and Ne lines, is shown in Figure 1.23. Shrapnel A, observed with Chandra and with the same inability to resolve spectral lines, is shown in Figure 1.24. (Additional spectra can be found in Miceli et al. 2005a,b; Plucinsky et al. 2002).

Higher spectral resolution is needed to resolve the contribution of line emission, which is indistinguishable from a continuum at low resolution. The existing low-resolution spectra are not inconsistent with a synchrotron component, at the very least. Additionally, the existing spectra are of bright and isolated features only and do not show the diffuse interior and the integrated energy budget of the remnant; they serve only to measure local conditions. With higher resolution in the $0.5-1.0$ keV range (where the continua of Figures 1.22, 1.23, and 1.24 turn downward), the relative contributions of line emission, bremsstrahlung, and synchrotron emission could be separated. That is the hope of CODEX payload.

The Vela SNR profile is filled in more than that of the Cygnus Loop, although both are shell-type remnants. The stronger interior signal from the Vela SNR might, however, increase the contribution from the thermal interior relative to the (possibly) synchrotron exterior. The other potential complication is that the Vela SNR line of sight is more complicated than the line of sight to the Cygnus Loop, although the other remnants along the line of sight, Puppis A and Vela Jr., are harder and smaller x-ray sources than the Vela SNR. The brightest soft x-ray region for the CODEX field of view, at the northern rim of the remnant, successfully dodges those two potentially confusing remnants (Figure 1.25).

An *xspec* model provided an indication of what to expect from the flight. The model comprised

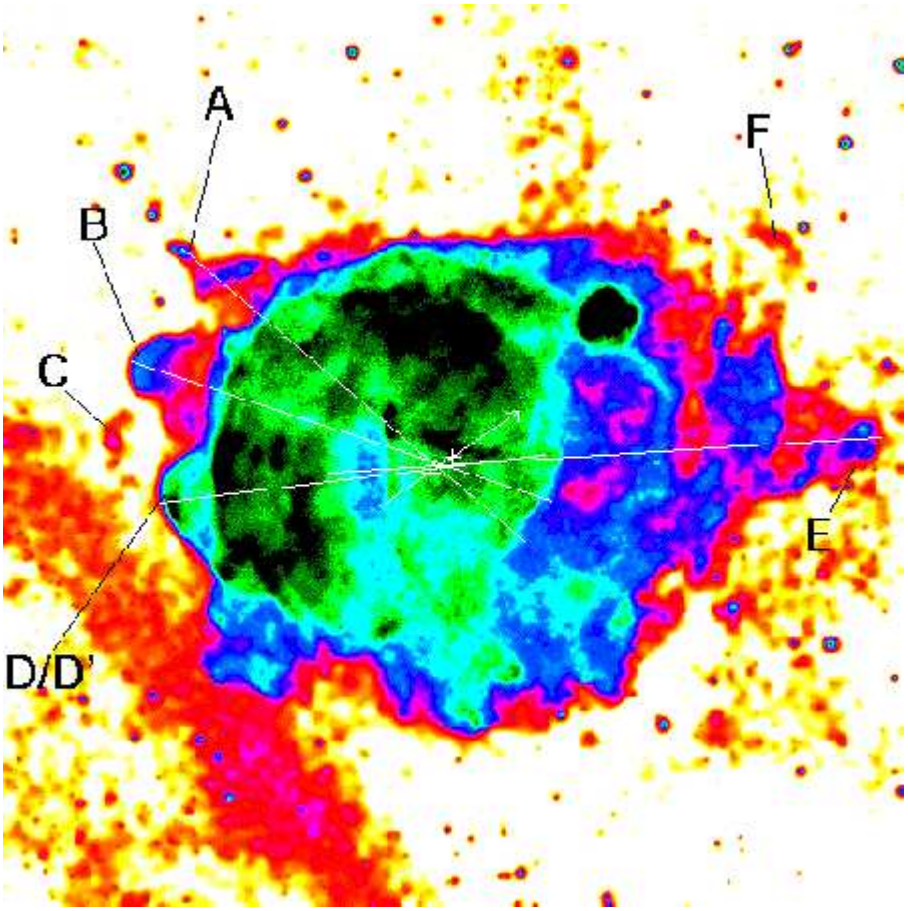

Figure 1.21 The Vela remnant, as seen by ROSAT, with the "shrapnel" blowout regions marked (Aschenbach et al. 1995)

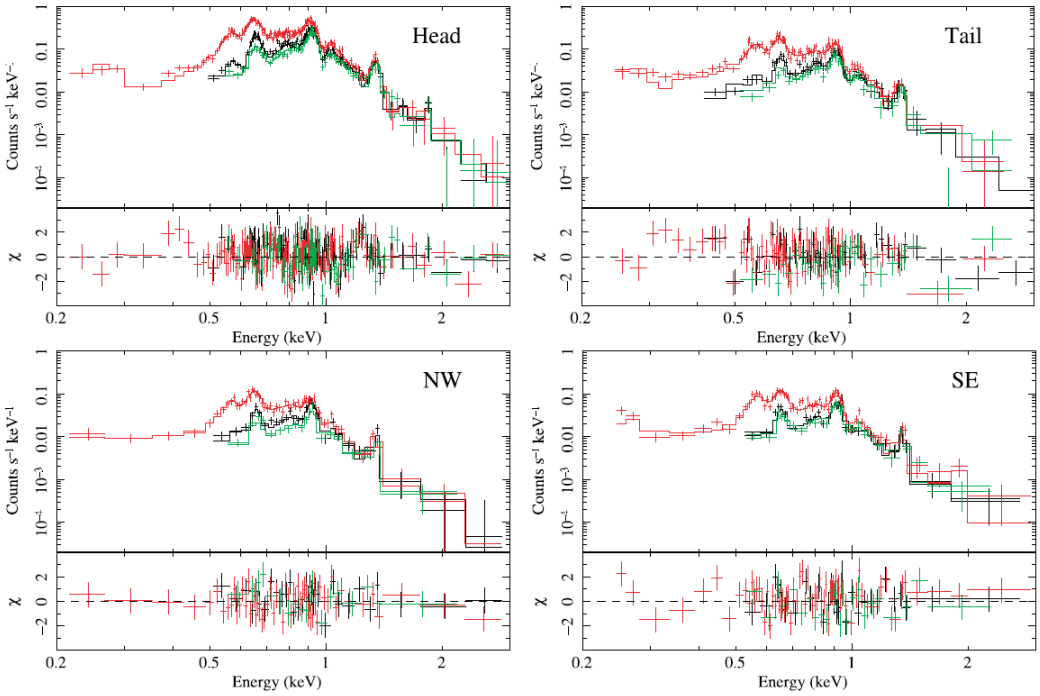

Figure 1.22 Spectra from regions around the ejecta shock front of shrapnel B (Yamaguchi and Katsuda 2009). Colors represent different Suzaku detectors. The inability to resolve spectral lines in the soft x-ray bandpass allows a thermal model to fit the data with abundances that vary by a factor of 10.

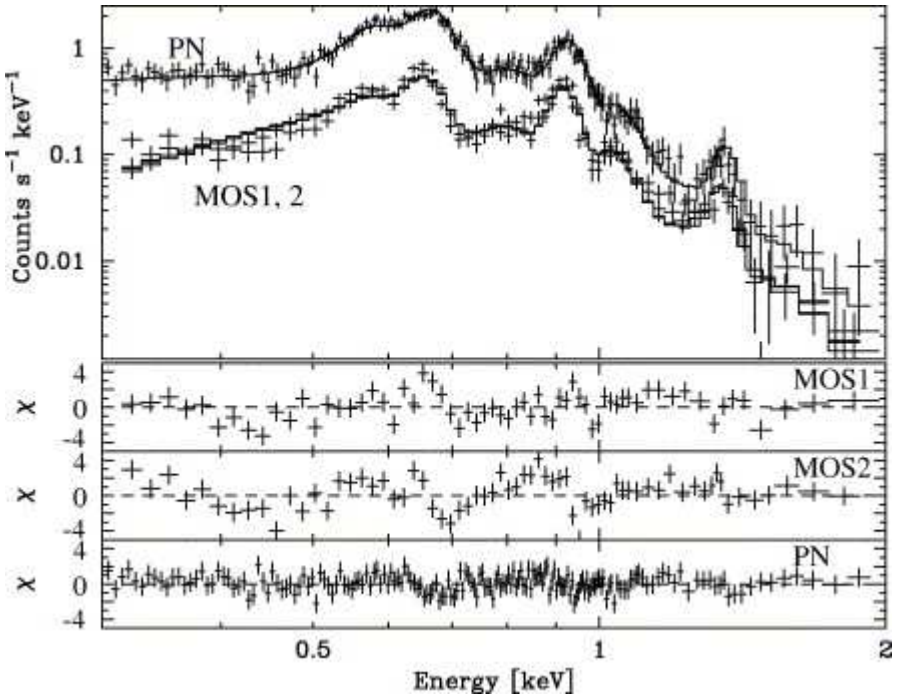

Figure 1.23 XMM-Newton spectra of shrapnel D (Tsunemi and Katsuda 2006).

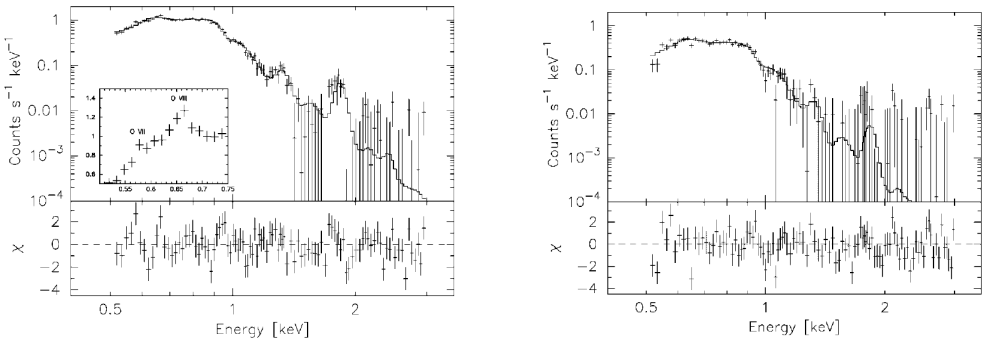

Figure 1.24 Chandra ACIS spectra of the head *left* and tail *right* of Vela shrapnel A (Miyata et al. 2001). The inset at left is to emphasize the oxygen emission.

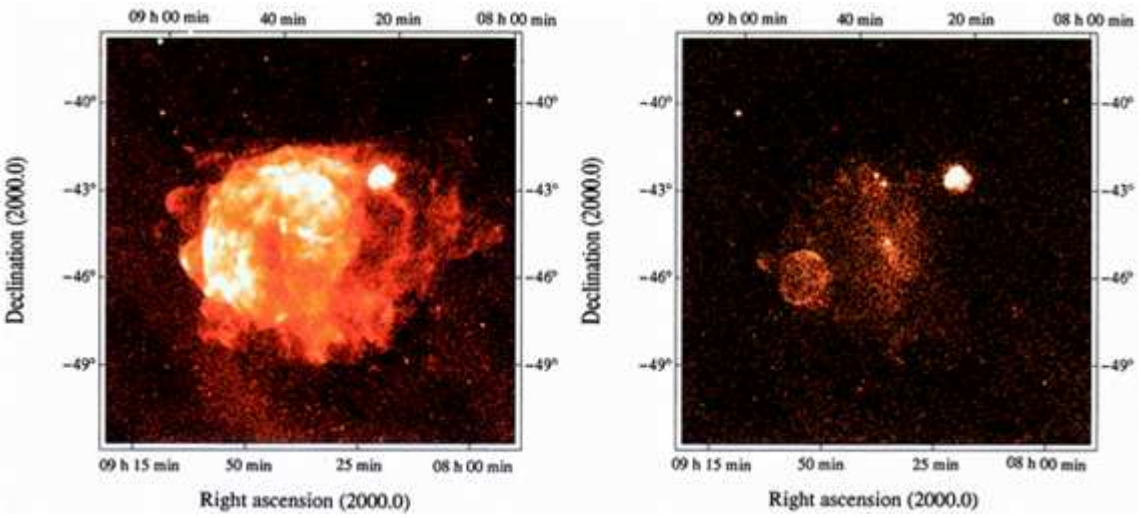

Figure 1.25 Low energy ($0.1 - 0.4$ keV; *left*) and high energy ($0.4 - 2.4$ keV; *right*) images of the Vela SNR, with the high-energy image showing the Puppis A (bright, 08h20m, $-43°$) and Vela Jr. (dimmer, 08h50m, $-46°$) supernova remnants along the line of sight. CODEX, with its 3.25 field of view, pointed toward the top center and dodged both of these confusing sources. (Aschenbach 1998)

a two-component Raymond-Smith plasma, per the ROSAT results and using the parameters in Table 1.2. The source was taken as uniform and beam-filling (there are variations across the beam, but the resolution of existing data is poor), which is not a great assumption as the NE and SW regions (1.5° square) differ in brightness by a factor of 11 (Lu and Aschenbach 2000), but it is at least a reasonable first step. The plasma code (in the black box of *xspec*) determines line ratios based on the temperature, intervening column density, and relative elemental abundances, and the total flux is scaled to the integrated luminosity of 1.3×10^{-8} erg cm^{-3} s^{-1} between 0.1 and 2.4 keV (Lu and Aschenbach 2000). CODEX's field of view will catch roughly half of the remnant (weighted by intensity at 1/4 keV, where the Vela SNR is brightest; Figure 1.26). Convolution with the system response uses measured alignment errors from the collimators and theoretical efficiency values for the gratings and detector windows, and assumes ∼100% quantum efficiency of any photon that makes it inside the detectors (generally a reliable assumption for an optimized proportional counter, but gain variations and other arguments contend that this assumption might not be valid — this is discussed further in §4 and §5).

Accounting for all components of the throughput except detector gain, CODEX should receive ∼1500 counts of diffracted light across its bandpass for 170 s on the Vela supernova remnant. Depending on the emission model (thermal and nonthermal will invoke different response functions because of their different photon energy distributions), undiffracted 0 order light will have $\sim 350 - 700$ counts (10-12 Hz). If the EXOS count rate is correct for the Cygnus Loop, then the count rate could scale upward by a factor of ∼5.

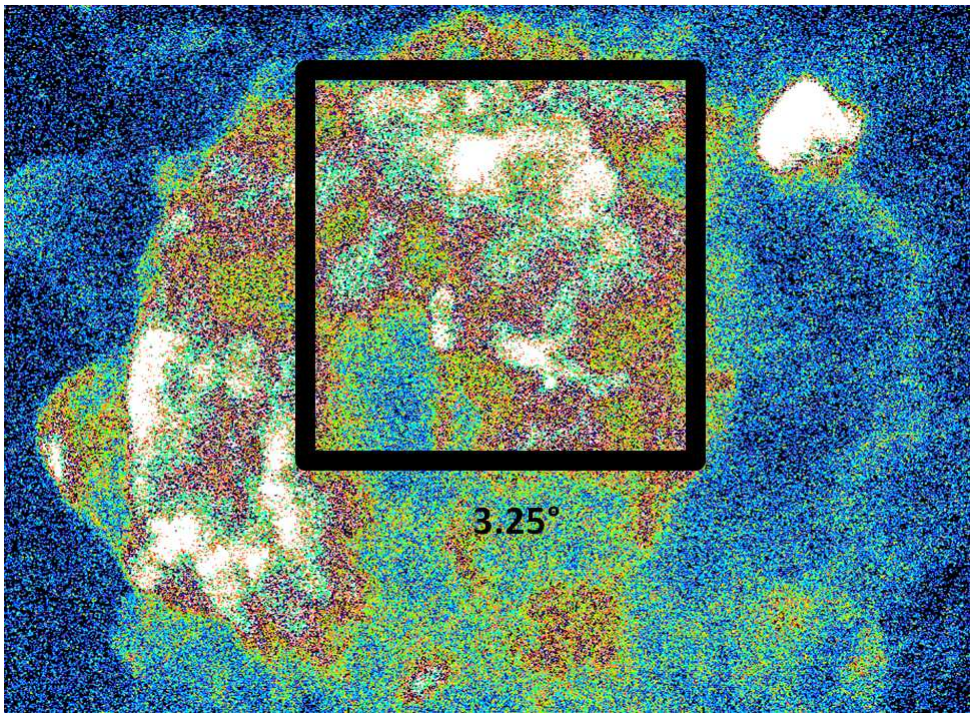

Figure 1.26 The Vela SNR at 1/4 keV, imaged by ROSAT with the CODEX field of view superimposed. The pointing was determined by smoothing the image with a 2-dimensinoal top-hat function matching the field of view of CODEX and finding the peak brightness.

Chapter 2

Design and Construction

If I had stayed for other people to make my tools and things for me, I had never made anything.

-- Attributed to Sir Isaac Newton[1]

CODEX was designed, built, and launched between mid-2010 and December 2011. It is the third generation of the Center for Astrophysics and Space Astronomy's wide-field soft x-ray spectrographs designed as sounding rocket payloads, previously flown as the CyXESS and EXOS payloads. Additional discussions of the instrument can be found in McEntaffer (2007), McEntaffer and Cash (2008), Oakley (2011), and Oakley et al. (2011b). The mechanical design of the payload is optimized for cheapness and robustness (required for a sounding rocket flight), while the scientific requirements demand optics capable of high spectral resolution ($E/\Delta E \approx 50 - 100$) observations of diffuse sources (3.25° square field of view, no spatial resolution) in the soft x-ray bandpass.

CODEX abandoned the six-channel design that was to be the destiny of the CyXESS/EXOS payloads, and the mechanical structure was redesigned for only two. Six channels, necessary to achieve the sensitivity required to detect the line emission spectrum of solar wind charge exchange during a sounding rocket flight, would not work well for observing a continuum spectrum, anyway: due to the unblazed gratings and the close proximity of the channels (six detectors, each 10 cm ×

[1] More (1934)

10 cm, placed on a bulkhead of 25 cm in radius), spectra from neighboring spectrographs would overlap. Relative angles of focus and dispersion would disentangle spectral lines, but they would not be as effective for distinguishing continuum spectra. Since CODEX was designed to detect a bright continuum spectrum, redesigning it for only two channels was consistent with the scientific goals and it also allowed for more precise construction and alignment of the spectrograph components.

The payload design, in broad brush strokes, is simple. A dispersive spectrograph, such as CODEX, has three basic elements: a collimating mechanism, a dispersing optic, and a detector. The CODEX design is shown in Figure 2.1 and described below, tracing the path of light through the payload. CODEX has two channels with identical components, differing only in their bandpasses. CODEX uses wire grid collimators and off-plane diffraction grating arrays to define a 3.25° square field of view with no spatial resolution. The spectrographs give resolution up to 100 (wavelength-dependent) across their overlapping bandpasses, between them spanning $\sim 10-144$ Å and collecting 0 order (undiffracted specular reflection) light as a flux and wavelength calibration reference. All components must fit within a 22 inch outside diameter rocket skin (∼21.5 inches interior, but 20.5 inches to account for joints in the skins), while being robust within alignment tolerances to 12.7 g_{rms} launch vibrations and, ideally, to the impact of landing.

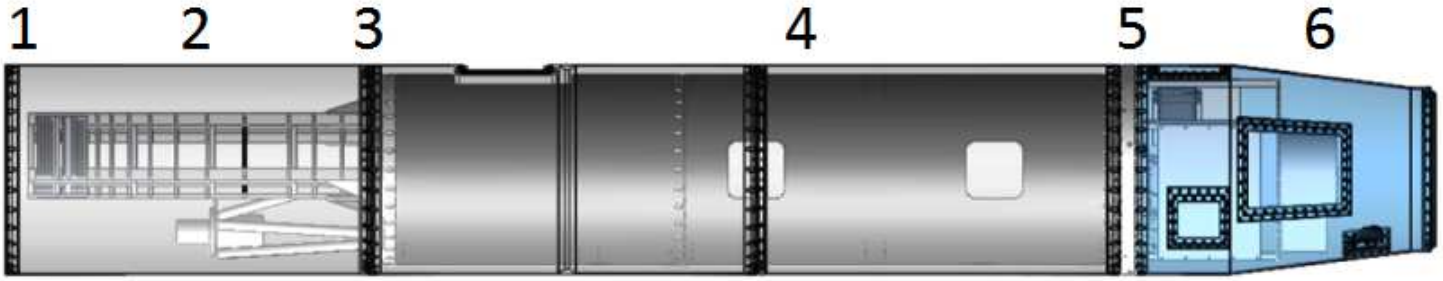

Figure 2.1 Following the light from left to right, the photons enter the shutter door [1] and pass almost immediately into the collimators [2]. Traveling 0.9 m through the collimators brings the photons to the off-plane diffraction grating arrays [3]. The optical bench [4] provides empty space for the photons to come to a focus and for the spectrum to disperse before the photons hit the GEM detectors [5]. Electronics for conversion of the detector time-delay signal into x/y/pulse height digital bits and the gas supply system for the detectors is located behind the detectors at [6]. The payload itself is made almost exclusively of 6063 aluminum alloy to minimize thermal distortions and to provide a lightweight and rigid structure.

The entire payload is an aft-facing instrument: after jettisoning the booster and sustainer fuel stages of its Black Brant IX launch vehicle, the payload is the aft-most object on the rocket. The forward end still has the celestial attitude control system (ACS), S-19L launch guidance system, and recovery parachute. A shutter door at the aft end swings open to expose the payload to space.

Pointing of the instrument is done by the ACS, guided by gyroscopes for rough pointing and for fine pointing by a ST5000 star tracker, provided by NASA's Wallops Flight Facility and mounted near the collimators. After the shutter door opens, the ST5000 camera acquires an image of the sky in its $5^\circ \times 7^\circ$ field of view and fits triangles formed by triplets of 4^{th} to 8^{th} magnitude stars within that field (casting out anything brighter or dimmer). The triangles are fit to a catalog of the sky, a process that takes at most a few seconds, and the ACS changes the pointing accordingly via argon gas jets. The star tracker is usually able to point and remain stable to about an arcsecond.

2.1 Collimators

In order to disperse light coherently from diffraction gratings, it must be collimated. Failure to control the incident angles results in a failure to control the output angles, which results only in specular reflection rather than in a dispersed spectrum. Most spectrographs use a focusing telescope and a slit to produce a collimated beam from a point source or a narrow region of the sky. The slit is not necessary if a single point source illuminates the telescope, and this is how both the Chandra and XMM-Newton x-ray telescopes were designed, but this limits spectroscopy of extended sources because of the overlap of spectral lines from different regions of the object.

The CODEX field of view is a legacy of the CyXESS and EXOS flights, although the structure for holding the plates was significantly redesigned to increase structural stability. The CyXESS/EXOS field of view was designed to be slightly larger than the 3° radius of the Cygnus Loop. While the Vela supernova remnant is significantly larger ($8^\circ \times 5^\circ$), the line of sight contains several undesirable features: the harder, older, and more distant Puppis A SNR, the younger and closer Vela Jr. SNR, and a pulsar wind nebula. Maintaining the 3.25° field of view allows CODEX to avoid these potentially confusing sources. Since CODEX has no spatial resolution, cutting out

the other objects along the line of sight is more advantageous than enlarging the field of view (due to the wire grid design – discussed below —, enlarging the field of view does not increase the number of photons received, either), and the large fraction of the Vela SNR observed would still be sufficient to determine the energetics of one of the two bright regions of the SNR.

CODEX collimates light in a very simple fashion, using a series of wire plates to define collimated channels instead of using focusing optics, shaping the beam by vignetting rays that do not travel along the collimated path to the focus (Shipley et al. 2011). This is shown schematically in Figure 2.2.

The two collimators, one for each spectrograph, have identical designs. They stand 0.9 m in height and are built around 24 wire plates, each 0.005 inches thick, which define a converging beam. Each plate has 184 wires ranging in thickness from 114 μm to 167 μm. As the plates approach the focus of the instrument, the wires converge from their initial spacing of 891 μm to 624 μm (center-to-center; Figure 2.3 shows the first plate). The minimum slit size between the wires is 500 μm, while the maximum is 724 μm; the slits comprise 80% of the plate aperture. The dimensions are legacy from the CyXESS design, when acid-etching of the plates set a minimum feature width; CODEX's electroformed plates maintained the flight-proven structural design. Changing these dimensions would have required redoing the modeling and tensile strength analyses done for CyXESS (McEntaffer 2007) for, at best, only a very small gain in throughput; time constraints due to the launch schedule did not permit this.

At the base of the collimators, the product of these plates is a set of 185 beams of light, collimated along one axis (along the dispersion axis of the diffraction gratings) and unconstrained along the other. The 1-dimensional collimator does not really collimate the light but destroys light that is not already collimated; it might better be termed a "destroyer" than a "collimator," but this thesis will use the latter because of both historical precedent and its place in the optical path. The optical system is equivalent to 185 slit spectrographs (the number of slits in each plate) operating in parallel along each of CODEX's two channels. Since the collimators only accept converging beams, the system is very inefficient for detecting planar waves from point sources, which would only pass

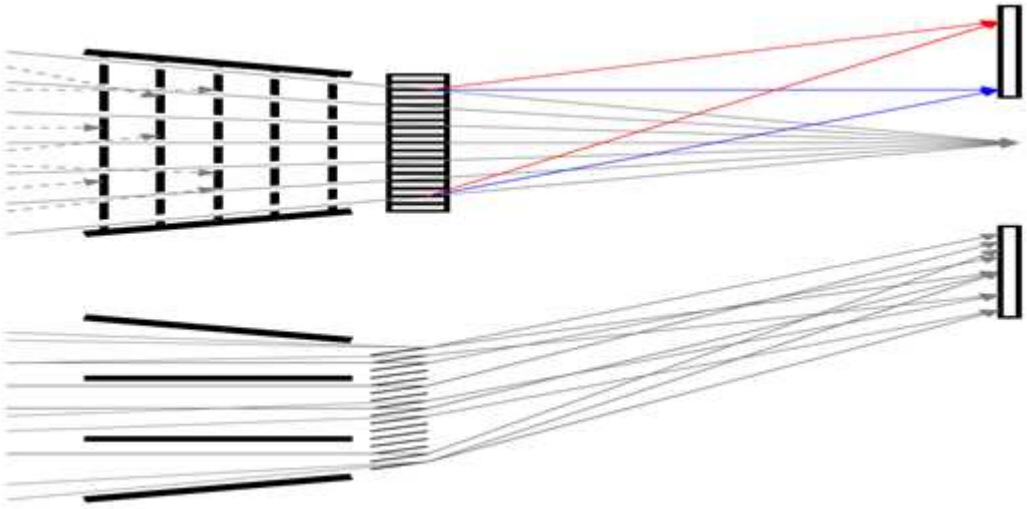

Figure 2.2 Simplified schematic of the collimators (McEntaffer 2007). They each produce a one dimensional focus by blocking light along one axis that does not come to a focus (*top*); the orthogonal axis is unfocused (*bottom*). Photons diffract off the gratings (red and blue lines) and away from the 0 order specular reflection (gray lines).

Figure 2.3 The first collimator plate of 24 in the stack. *Left*: Full plate, showing the 184 wires and 185 slits. *Right*: Zoomed in image of a corner of the plate to show the wires more clearly. In discussions that follow, the x axis is perpendicular to the wires but in the plane of the plate, the y axis is parallel to the wires, and the z axis is perpendicular to the plate.

light along several of the 185 slits.

The wire plates were spaced to minimize scattered light. Ray tracing (using W. Cashs Interactive Ray Trace IDL routines) indicates that the 24 plates limit light outside of the focus to 1.3(1)% of the light in the focus (McEntaffer 2007). Blocking all light outside the focus would require 46 of the 0.005 inch plates at impossible machining and assembly tolerances; thicker plates would require fewer plates but allow more reflections and scatter from the walls of each slit. Plate positions are listed in Table 2.1. Light comes to a focus at the detectors if it passes through all 24 plates without encountering a wire (3 m from the entrance aperture; f/17.6 effective optical speed, although not truly a focusing system); light not already traveling to the focus hits wires and is efficiently absorbed.

Each of the 185 slits in the collimator has a field of view of 1.45×10^{-4} sr and the minimum open aperture of the plates is 105 cm^2, giving the collimators a wavelength-independent grasp of 0.0152 cm^2 sr in an ideal case, or 0.0132 cm^2 sr when including the reduced throughput from alignment errors. The grids have, ideally, about 80% efficiency (ratio of wires to open spaces), while being much lighter and cheaper than nested mirror designs to achieve comparable fields of view and effective area.

The each wire plate was mounted with epoxy to a water jet-cut (cheap, low-stress manufacturing to prevent twisting from relaxation) frame, providing supporting edges roughly 6 mm thick. The epoxy was mixed with 0.0025 inch glass beads in a 20:1 (by volume) ratio to provide uniform spacing and optimal strength for the bond line (McEntaffer 2007). Additionally, the epoxy was applied in spots rather than in lines to prevent peeling of the entire bond line if the epoxy were to fail at one location.

The frames support the wires against launch vibrations and gives mounting points for #4-40 screws in every corner and potted pins in two corners. The plates are mounted to L-beam supports at each corner to position the plates vertically. The L-beams are then supported by load-bearing braces similar to the plate frames, but thicker and with potted pins in all four corners. The four-cornered clamping is not ideal for maintaining the figure of the plates and would not be viable

if they presented an optical surface, since only three points are required to define a plane and a fourth will cause distortion if any machining or handling error produces a deviation from the theoretical design. However, since the plate is defined in terms of rotation and x and y translation (z translation has a much looser tolerance), the benefits of a four-corner attachment configuration was worth the risk of small z distortions. Shims as large as 50 μm were applied in several cases to allow clamping with minimal distortions.

Table 2.1. Collimator plate positions

Plate	Position from first plate [mm]
1	0.00
2	5.84
3	11.66
4	17.47
5	23.28
6	29.14
7	36.12
8	44.78
9	55.50
10	68.74
11	85.16
12	105.35
13	130.34
14	161,03
15	198.60
16	245.02
17	301.30
18	369.96
19	453.07
20	552.26
21	670.70

Table 2.1 (cont'd)

Plate	Position from first plate [mm]
22	738.11
23	812.27
24	900.00

Each collimator plate is electroformed nickel and only 125 μm thick. The thinness of the plates approximates a knife edge, making grazing incidence reflections through the collimator negligible. Normal incidence reflections are not a concern for x-rays, since the reflection efficiency is 0.

As noted above, the CyXESS/EXOS design envisioned a future configuration where there would, eventually, be six channels — six spectrographs operating in parallel. The six-fold increase in collecting area would have obvious advantages in sensitivity and robustness. However, the changed scientific goal from its initial (CyXESS/EXOS) design precluded the realization of the 6-channel dream. The design required to fit six channels was impractical as well as imprecise, as the plates were all connected via a welded superstructure in a 6-fold symmetric radial pattern around a central position for the star tracker (Figure 2.4). The superstructure prevented definition of positions along any axis with high accuracy.

CODEX abandoned the problems and the dream of six channels, embracing the two channels that flew on CyXESS and EXOS and trying to improve on that basic design. CyXESS and EXOS used hexagonal collimator plates positioned to accommodate the six channels. CODEX used square plates, increasing the ease of assembly and the mechanical strength, with the added benefit of increasing the per-channel collecting area by 17%. (If higher sensitivity is needed in the future, CODEX retains the ability of doubling its throughput by incorporating additional detectors or blazed gratings, as the currently-unblazed produce equal spectra on either side of the 0 order reflection.)

The square, isolated collimator towers, as opposed to the monolithic CyXESS/EXOS superstructure that linked all six channels together, allowed more precise machining of the support

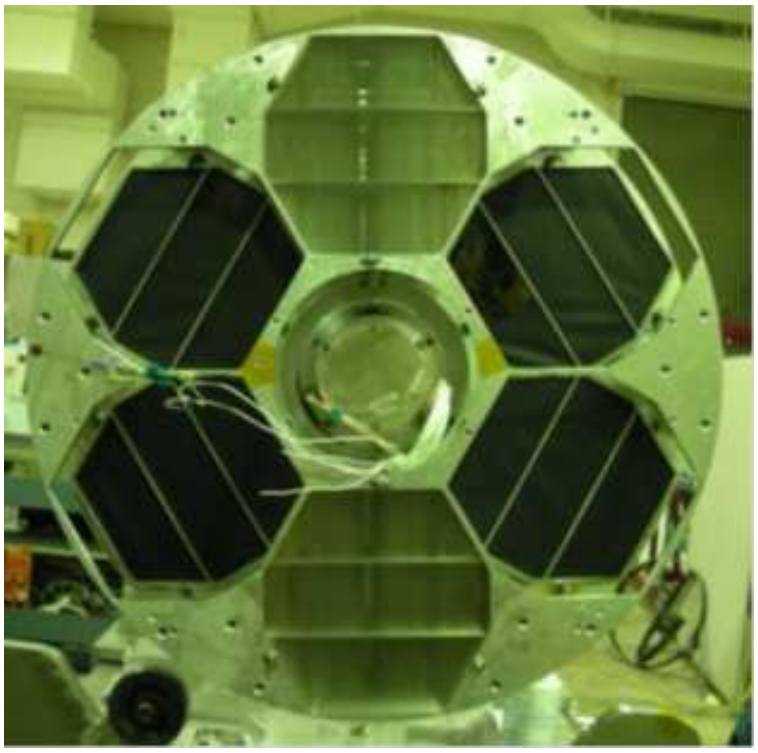

Figure 2.4 Front end of the CyXESS rocket. The top and bottom channels hold the spectrographs; the two on either side are baffled to block stray light and were designed for additional modules in future flights. The star tracker (in this picture, a mass model for testing purposes) sits in the open central region (McEntaffer 2007).

structures. Although the collimator is relatively insensitive to errors in the z axis, the square support structure did far better in this respect than the welded superstructure of the six-channel design. The individual stacks also meant that the edges of the collimator plates were accessible before the tower was enclosed in sheer panels. We added a 508 μm protrusion along the x direction of the plates and assembled the towers independently in an alignment fixture.

The alignment fixture was simple: two aluminum plates bolted at right angles, and attached to those were three solid steel cylinders, toleranced to a flatness of 13 μm variation per meter (Figure 2.5). In the ideal case, the 500 μm alignment edge rests on two of the bars, aligning the plates in x-translation and in rotation. Unfortunately, the fixture was made on a short deadline and either poor production by the manufacturer or warping from the construction of the alignment fixture enlarged the errors to about 375 μm. Alignment at that level would cost CODEX some 70% of its throughput. The fixture was re-machined by flattening the bars with a mill, creating a flat surface within about 38 μm variation peak-to-peak. Since the cylinders were no longer cylindrical, the rotational alignment of the bars became an important factor in constructing the alignment fixture: a plane does not have a constant radius from the center of a cylinder. The 38 μm figure includes errors in rotation of the bars, measured with a precision height gauge that was precise to $\sim$2.5 μm. The maximum deviation from the alignment fixture was 25 μm, and although the standard deviation is a nice number to use and for 24 plates is quite small, the maximum plate-to-plate difference is what defines the obscuration of the desired light path. The combined error of 63 μm reduces the throughput of a collimator by 13% from ideal; both collimators had comparable alignment errors mostly due to twisting induced by bolting the plates to the collimator structure and thermal expansion of the frame during construction.

Delays in the launch schedule due to Orbital Science's issues with the flight termination system would soon push the launch deadline out by most of a year and would have allowed for another attempt to match better the specifications for the fixture, but the collimators were constructed before these delays were known. Since the "optic" works by blocking rather than focusing light, peak-to-peak variations in plate alignment correspond directly to a loss of throughput.

Figure 2.5 Alignment fixture showing the two bars that provided the y alignment edge along the bottom and the x alignment edge along the side. The two bars along the y edge defined the plate rotation such that, between the three plates and the corners of the collimator structure, every plate position was fully defined. The fixture was flat to within 38 μm (measured as 0.0015 inches) relative to a flat granite table, and alignment of plates to the fixture could be done to 25 μm (0.001 inches).

The CODEX collimator assembly began with the four L-beams defining the corners and extending 25 mm on either side, and these were supported by the five braces that were both screwed in place and held by potted pins. The braces, significantly thicker than the collimator plates and their support frames, were designed to carry most of collimators' share of the mechanical load of launch. Plates were inserted one at a time in slots in the corner braces and screwed into place — a process that often caused the frame to rotate about the z axis. After adding each plate, feeler gauges were inserted between all attached plates and the alignment fixture. The collimators were within several plates of completion numerous times before tightening one plate sent a torque to the others that knocked many of them out of position. When all were inserted, they were potted in place and sheer panels were added to the outside to strengthen the structure (Figure 2.6). A view down a fully-constructed collimator is shown in Figure 2.7.

Figure 2.6 *Left*: Collimator stack, lacking the 12 densely-stacked plates at the top (image left) of the collimator. The five wide braces spaced at both ends and evenly in the middle carry the majority of the load between the precision-machined corner L-beams. Collimator plates slide into the slots in the corners before being fixed into place with potted sheer pins and #4-40 screws. *Right*: Fully assembled collimator stack, with 0.125 inch thick aluminum sheer panels affixed to the side to strengthen the tower. Light will enter at image left, and the mount to the grating bulkhead will attach at image right.

Since the new collimator structures were not flight-tested, as the old one was, we tested it on the Sierra Nevada, Inc., shake table. The sine sweep ($5 - 2{,}000$ Hz) shake test revealed two things: that the sheer panels supporting the collimator structure sing very loudly — essentially just aluminum drums — and that the resonant peaks were not as sharp as expected. The latter was fixed by making new precision pins to mount the collimator structure to the feet that mounted to the shake plate (the same mounting that would be used in the payload). Small flat mirrors on the collimator tops, on the star tracker mount, and reference ones on the shake plate itself were used to measure the effects of the shake test on the collimator alignment. Changes in angles of the mirrors on the collimators were a few arcseconds, comparable to the shifts of mirrors attached directly to the shake plate: any motion of the collimators was less than the measurement error. A motion of 1 arcsecond from the top plate to the bottom corresponds to a shift of 4.8 μm, or a decrease in throughput of $<1\%$. Mirrors were placed only on the ends of the collimators and could not detect warping in the middle of the collimators, although most deformations should have shown on the mirrors. We were unable to test translation of individual plates within the collimator structure after the shake test, aside from later measurements of overall throughput.

When fully assembled, the two collimators were ready for attachment to the grating bulkhead. (In the actual assembly sequence, the gratings were added to the underside of the bulkhead first before the collimators were added to the top.) The low-density collimators were positioned such that they countered the denser star tracker to produce a rotationally-balanced payload (Figure 2.8). The star tracker mount was sturdier than the collimators — three angled triangular braces of 1 inch diameter aluminum tubing, and only half of the height — and the three structures were tied together halfway up the collimators (at the height of the star tracker; Figure 2.1) to minimize the primary bending mode of the collimators during launch.

Testing the collimators is tricky, since they are designed for observing diffuse x-ray sources. X-rays are, by definition, high energy, and accordingly hard to produce in laboratory situations. Optical light will reflect and scatter through the collimator structure (Figure 2.9), making it a poor test of collimator alignment and ability to block scattered light. Radioactive iron is a convenient

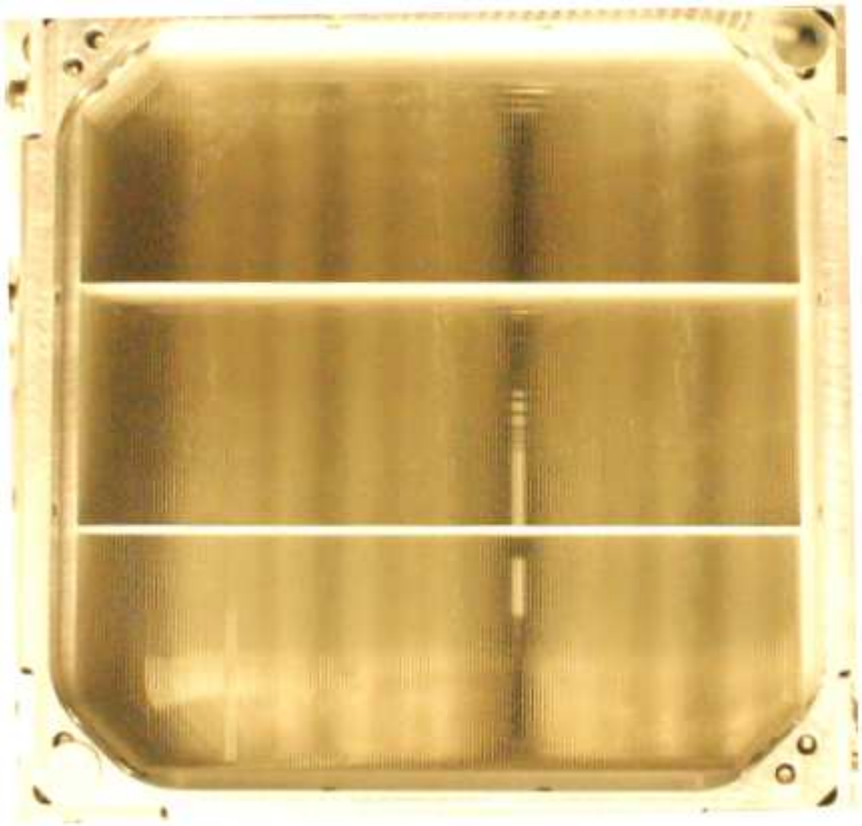

Figure 2.7 Photograph down one collimator stack. Note the wave-like dark spaces on the front: depending on the angle of incidence, light is blocked at various depths of the stack (up to 0.9 m, at the last plate), but only one path, spanning three slits in the wire plate, admits light all the way through the collimator. Note the several wires in the bottom left that reflect light differently than the others. These are warped toward the camera. Many plates acquired errors similar to this in the mounting process due to stresses from mounting the plate to its frame or from mounting the frame into the collimator, where the four-point mount distorted the figure. As long as the wires were perturbed strictly in the z direction, the system is relatively insensitive to the errors; perturbations in the x direction (perpendicular to the wires) were corrected to assembly tolerances.

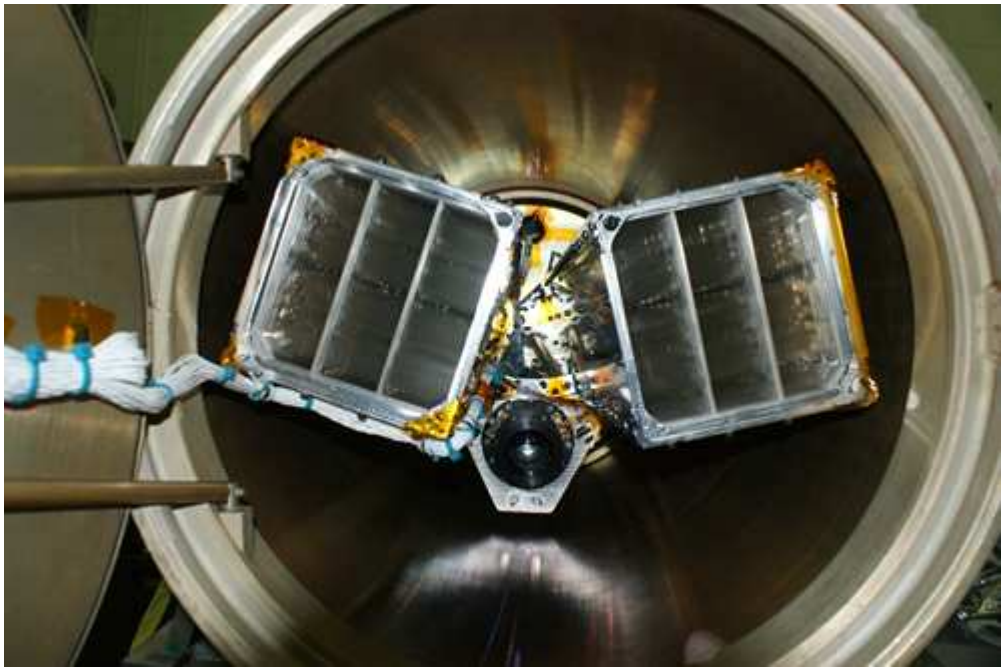

Figure 2.8 Collimators in place, facing aft out of the shutter door (at image left). Note the location-dependent light path through the collimators, appearing in a different location on each. The ST5000 star tracker is below the collimators, and all three structures are secured to the grating bulkhead. The collimators and ST5000 are placed to keep this section of the rocket nearly perfectly rotationally balanced.

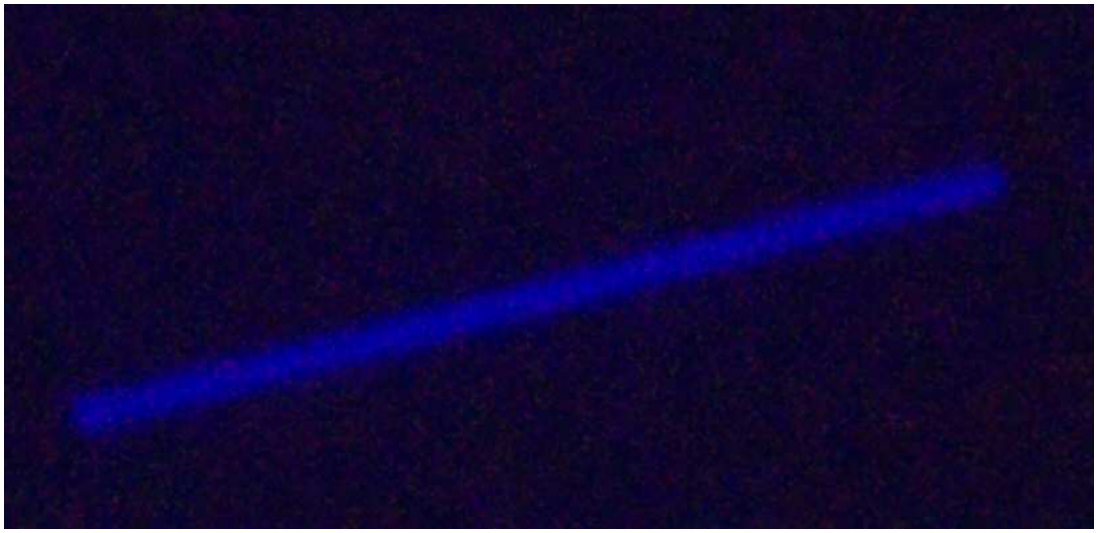

Figure 2.9 Blue light sent down one of the collimators, testing for unblocked optical paths. The line is roughly 8 mm across, while x-ray lines should be ∼2 mm. The additional width is due to scattering and reflections within the collimator.

x-ray source for laboratory testing of detectors, where the 6 keV photons only need to travel a few inches through the air. Sealed radioactive sources should not be put in a vacuum, however, and the emission rate would be too low for detection 3.0 m from the detectors without evacuating the collimators. Additionally, the ^{55}Fe source is small and would not map the entire field of view. Larger radiation sources are available, but they are expensive and more hazardous to handle. The higher-output, vacuum-safe alternative is the Manson Model 2 Ultra-soft X-ray source, which sends a focused beam of electrons across a potential difference (usually $0.5-5$ keV) before slamming them into an anode with the desired composition (e.g., a carbon anode will produce lines at 23 and 44 Å from oxygen and carbon K-lines). Although this produces a strong signal and was used for much of our testing, it is still a point source.

Our solution to the problem was to use the Manson as a primary photon source (Figure 2.10) and aim it at a carbon-coated aluminum plate (Figure 2.11). The Manson photons were absorbed by the carbon sheet, exciting atoms that re-emitted soft x-rays (carbon K lines) from a large (∼22 inch) area. The count rate was vastly lower at the detectors than when the Manson shone directly down them, but the diffuse source showed the collimators' ability to exclude randomly-directed

light and leave only the focused light.

The diffuse source tests showed that the collimators efficiently blocked light not coming to a focus (Figures 2.12 and 2.13). The tests were not exhaustive. Another use for the diffuse source, which was not done due to time constraints prior to launch, would be to block portions of the aperture. Testing outer regions would verify the machining tolerances of the collimator plates (an error in the replication of the collimator plates would propagate and increase toward the edges of the collimator beam) and the rotation of the plates from assembly tolerances. Aside from intensity, light passing down only one of the 185 slits is indistinguishable from light passing down all of them, and without a partially-obscured aperture it is impossible to differentiate regions of the aperture. Testing with a point source was also done close to the central axis (again, not a full test of the optics); relative throughput across the aperture of the collimators was tested only by eye. All subsequent tests described in this thesis used the Manson source as a point source in the field of view because the higher signal reduced the amount of time the detectors had to be turned on, thus prolonging the lives of the sensitive GEM plates inside.

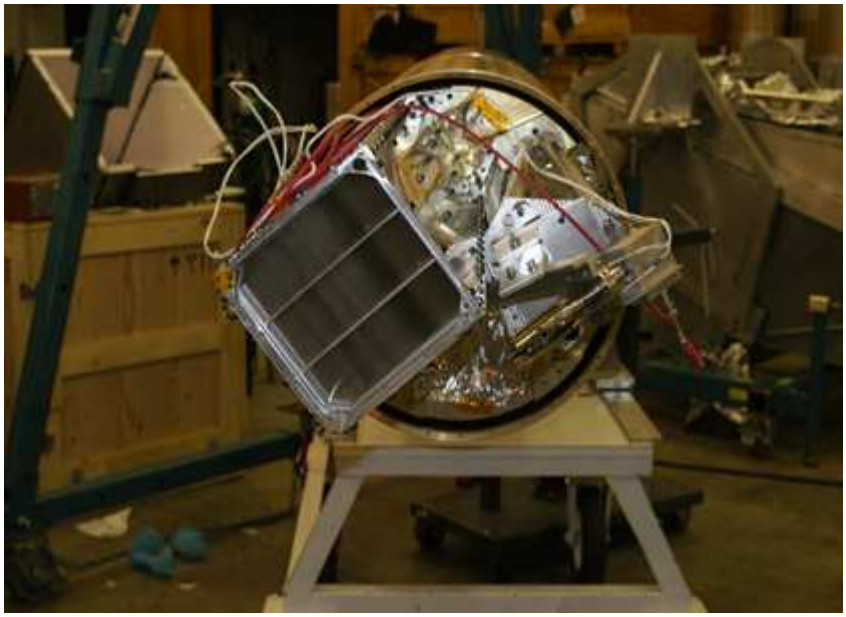

Figure 2.10 Configuration of the payload for testing a collimator with the diffuse source. The Manson electron impact x-ray source is the tube-like object attached to electrical wires at image right, and the collimator is opposite. The Manson sends photons toward the location of the camera, where they excite carbon K lines on a carbon-coated sheet of aluminum (Figure 2.11). The detector is positioned directly behind the collimator, which is not its flight configuration.

Figure 2.11 The diffuse source itself: a sheet of aluminum coated in carbon. The Manson x-ray (point) source bombards it with photons, kicking out K-shell electrons that allow the carbon atoms to fluoresce from all parts of the sheet, creating a diffuse source of soft x-rays. To my knowledge, and despite its simplicity, this is the first practical (non-radioactive, low budget) design of a diffuse x-ray source.

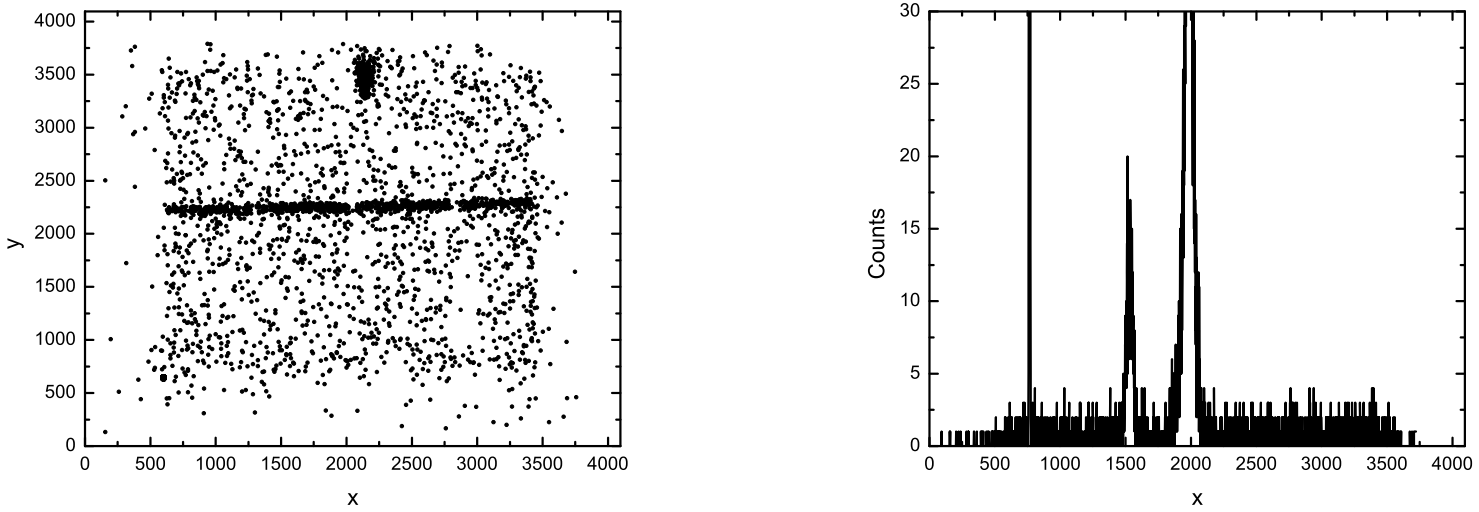

Figure 2.12 Analysis of collimator quality for one collimator. The axes, x and y, are merely detector bin designations, with a scale of 28 pixels per mm. Tests were done before optimizing the detector, operating it at -4.3 kV and 13.7 psia Ar/CO_2, with the collimator illuminated by the carbon-coated diffuse source excited by the Manson x-ray source with a magnesium anode held at 5.00 kV and a heating current of 0.20 mA illuminating the carbon-coated diffuse source. Light not coming to a focus was <5% of the total, consistent with ray traces and indistinguishable from electronic noise. A hot spot dominates the top of the detector. Vertical shadows (white spaces) visible in the one dimensional collimator focus image, where the focus is rotated 88.12° from vertical (*left*), are shadows of the window bars supporting the thin polyimide detector window. The shadows are not evident in the summed image (*right*) because the summation was perpendicular to the focus. The bright spot in the bottom left corner (600, 700) is the 12 Hz stim signal. Counts outside of the apparent active area are either noise pickup from the lab or misanalyzed bits, with the former more likely than the latter because there is no feature consistent with misanalyzing bits from the concentrated counts of the hot spot or the focused line. The line has Gaussian full width half maximum of 61.4 pixels, or 2.2 mm. The image was collected over 504 seconds and has 11,094 counts, of which the uniform background is ∼1,508 and the line is 831(13); the balance comprises the stim and the hot spot. No signal aside from the focus is detectable as a concentration of scattered light.

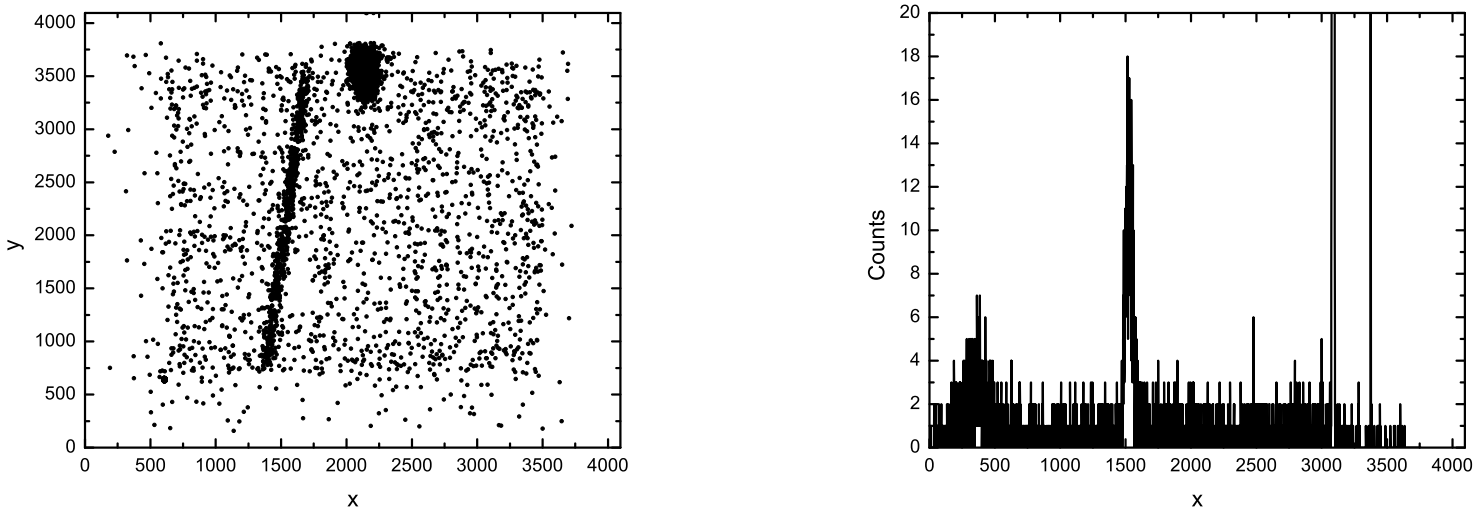

Figure 2.13 Analysis of the quality of the other collimator, akin to Figure 2.12 above. It creates a focus rotated 6.15° from vertical. The line has a full-width half-maximum of 56(1) pixels or 2.0 mm, with 690(16) counts on a background of ∼1,466. The three prominent features of the image summed along the direction of the focus (*right*), from left to right, are the stim, the line focus, and the hot spot. The stim and the hot spot were excised from the fit describing the line profile. Scattered light was indistinguishable from noise for this 500 s exposure. This test used the same configuration, electronics settings, and detector as the test shown in Figure 2.12 above.

Strict translational errors of collimator plates are difficult to find and correct. Translations of distances that are integer multiples of a wire plus a spacing (such that space N aligned with space $N + 1$) are nearly impossible to discern via throughput (comprising only a 0.5% drop due to the one out of 185 slits that gets blocked at the edge). Fractional translations would uniformly decrease the throughput across the face of the collimator by a maximum of 20% for a single plate in an otherwise perfect collimator, but the cumulative error could be as high as 100% for sloppy construction. Relative throughput tests (putting the collimator in place, then removing it and replacing it with the same aperture sans collimators) or tests with an absolute calibration source would measure the translational errors. These tests were also not conducted prior to flight. The collimators were found to be functional, and time constraints presented by the launch schedule prevented further testing.

The diffuse source mimics a diffuse astronomical target like an SNR, and it is a fantastic tool for measuring stray and focused light fractions. The collimator-only tests have a severe shortcoming, however. The payload is designed to focus light not just over the distance from the collimators to the detector, but over the distance from the collimators to the reflection gratings, where the light reflects at an average of $\sim 8.8^\circ$. The reflection elongates the path, but it was not present in the collimator tests. To detect the light, the detectors had to be repositioned directly behind the collimators, where the path length differs from the flight configuration by $\sim$2.8 cm. Since the beam converges from 16.5 cm to its focus over 3.0 m, the beam converges at a rate of 0.55 mm/cm. The focus is worsened by 1.5 mm (to $\sim$3.5 mm) from its full construction. The measured result is $2.0 - 2.2$ mm, which is consistent with the expected $\sim$2 mm line width of the fully constructed system but only makes sense in this configuration if the optics bench is slightly too long. Sadly, this seems to be the case (see §2.2). These tests were done before optimizing the pressure and voltage of the detectors, and this can also be responsible for poorer focus than the theoretical 1.7 mm (see §2.3).

2.2 Gratings

The gratings[2] were manufactured by HORIBA Jobin-Yvon, Inc., from a straight-ruled master grating in 104 mm square sheets, with a groove density of 5670(10) grooves/mm etched sinusoidally and without a blaze. The gratings were imprinted into an epoxy layer on a nickel substrate, electroformed for flatness with a thickness of 0.0050(3) inches. The electroforming process was done on a $\sim\lambda/2$ mandrel, ensuring a flat reflective surface to one part in 2000 (McEntaffer 2007), as is necessary for the gratings to achieve their desired resolution. The epoxy layer was then coated with nickel, which has a high reflectivity ($\sim$70%) longward of 20 Å. The nickel/epoxy/nickel grating minimizes bimetallic bending and subsequent delamination or deformation.

X-ray optics must operate at grazing incidence (several degrees at most from parallel to the light) to maintain reflectivity. To prevent groove shadowing and to reflect efficiently (Figures 2.18, 2.19, and 2.20), the gratings were placed in an off-plane mount, meaning that the grooves were quasi-parallel to the light (see Figure 2.14; Neviere et al. 1978). The familiar normal incidence grating equation requires additional terms to account for the three-dimensional nature of the problem:

$$\sin\alpha + \sin\beta = \frac{n\lambda}{d\sin\gamma}, \tag{2.1}$$

with the terms defined pictorially in Figure 2.14. Light diffracted from an off-plane mount is diffracted into an arc, rather than into a line as it would with a normal incidence grating. An example of this arc of diffraction is shown in Figure 2.15, and one must trace the arc to form a spectrum (Figure 2.16). With a line focus, this has the effect of dispersing the spectral lines along one axis while in the other the brightest region of those lines traces an arc.

CODEX's gratings are mounted 4.4° from the rocket's vertical axis, with their dispersion direction being tangential to the radius such that light reflects across the payload to a detector on the opposite side of the rocket cylinder. The gratings must be kept short or the difference between diffraction from the front and backs end of the grating limits the instrument's resolution. For a

[2] The gratings and their mounting fixture have not been modified since the CyXESS payload, and they were flown successfully on both the CyXESS and EXOS payloads. For greater details on design decisions and construction, see McEntaffer (2007).

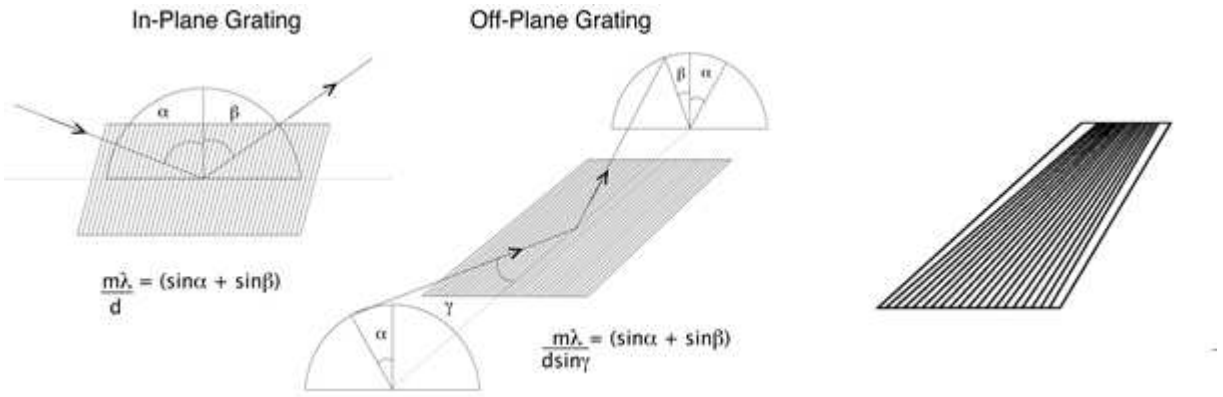

Figure 2.14 Comparison of the two grazing-incidence mounts for diffraction gratings. Note how the in-plane mount (*left*) produces a line spectrum perpendicular to the grooves of the grating, while the off-plane mount (*center*) produces an arc of diffraction. The off-plane mount will blur proportional to the length of the gratings due to the differing throw from the point of incidence, a problem which can be cured by making a grating with a groove density that increases as the beam of the spectrograph converges (*right*). The latter design has been tested extensively at the University of Colorado (Zeiger et al. 2010) and further testing is underway at the University of Iowa.

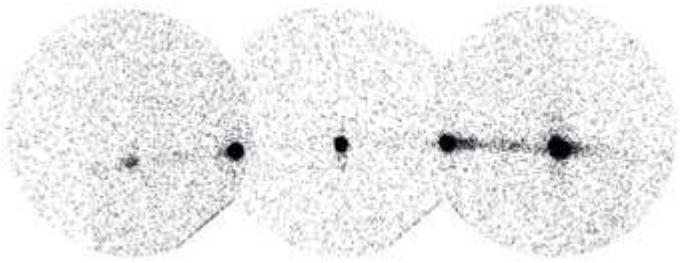

Figure 2.15 Three images of the carbon K line spectrum (44.7 Å) taken with a Ranicon microchannel plate detector in the University of Colorado x-ray beamline, demonstrating the arc of diffraction produced by an off-plane grating. The grating that dispersed this spectrum was much lower density (300 grooves mm^{-1}) than the CODEX gratings. The central spot (a two dimensional focus rather than CODEX's one) is the undiffracted 0 order, with two orders on either side and a visible streak of continuum emission across the blaze of the grating (between first and second order). Exposure times for the three images vary, as is evident by the relative noise levels (Zeiger et al. 2010).

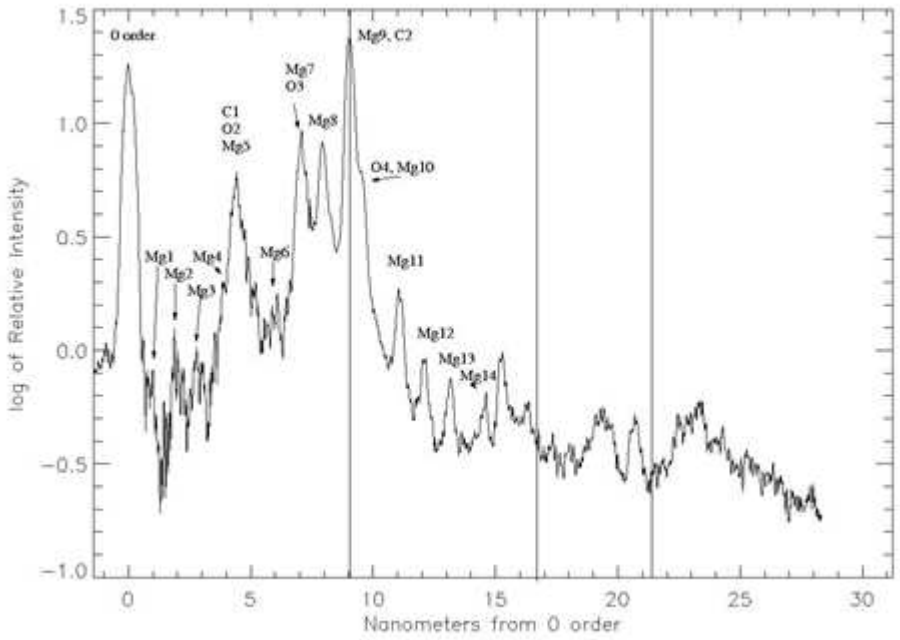

Figure 2.16 Off-plane grating tests of a low-resolution (300 groove mm^{-1}) grating — the same used to generate Figure 2.15 in the University of Colorado x-ray beamline, using the Manson soft x-ray source with a magnesium anode (Zeiger et al. 2010). The x axis is in nanometers for a first order reflection. The carbon and oxygen lines are contaminants on the surface of the anode, while the strong increase at $7 - 9$ nm is due to the blaze of the grating. Vertical lines indicate where the spectrum was stitched together from multiple detector images, akin to Figure 2.15.

goal resolution of ∼100 and a throw distance of 2.0 m, this required keeping the gratings to 2.0 m/100 or 20 mm in length; at 4.4° this gives a cross section of only 1.53 mm. (Rays can pass through the system at roughly ±2° from the central graze angle.) Thus, the gratings had to be mounted in a tightly-packed array to fill the 10 cm × 10 cm aperture at the base of the collimators, requiring 67 diffraction gratings per array (Figure 2.17). Making the gratings longer would change the dispersion distance too much for light incident at the leading and trailing edges of the gratings, and the resolution would degrade proportional to the length of the grating. The gratings were laser-cut to the proper length with a pulsed laser, keeping the pulses short enough that heating did not distort the gratings.

The gratings were thin because, in the off-plane mount, their leading edge blocks light rather than reflecting or diffracting it. For robustness, they were mounted in a titanium flexure, holding a constant force of 5 lb to increase their fundamental frequency and decrease the displacement of the gratings during launch vibrations (Shipley et al. 2006).

Alignment of the gratings relative to the collimators was coarse. Although a precise alignment could have been done with a diffuse source (reflected optical light forms a line translated solely in the direction of reflection of the gratings), instrument tolerances did not require that level of painstaking detail for the gratings.

With some algebra, the grating equation can be manipulated from describing an arc to describing a linear dispersion across a small portion of the spectrum, giving a dispersion of 0.90 Å/mm (Oakley 2011). Small changes in α, the relative rotation of the optics from the grating equation (Equation 2.1), result in a proportional change in the output angle β, which is an approximately linear translation for small $\Delta\alpha$. Effects of a misalignment of the collimators as a tilt of the collimator axis relative to the grating depend on the direction of the tilt: if it is a rotation of the collimators around its x axis results only in a change of throughput due to the change in aperture caused by the tilt. A rotation around the y (non-focusing) axis will have a comparable effect to a rotation around z and will produce an error corresponding to $\Delta\langle\alpha\rangle$, a change of the average incidence angle on the grating. Misalignment of the collimators and gratings via translation rather

Figure 2.17 Diffraction grating array, showing the 67 off-plane mounted reflection gratings in their titanium flexure mount. The mount holds the gratings uniformly tensioned at 5 lb to reduce their deflection during launch.

than rotation would reduce throughput but not change the diffraction pattern.

The gratings themselves are also old, mounted in their frame more than half a decade before the CODEX flight, flown twice before, shipped across the country, boxed, handled, and mounted to a bulkhead and unmounted twice. Several have been bent slightly over the years, and others show signs of wear, such as grating edges that are starting to delaminate or discoloration of the surface. In a practical sense, this means that their efficiency (Figures 2.18, 2.19, and 2.20), should have been verified independently of the rest of the system with laboratory tests. Time constraints did not allow for isolated testing or even for their absolute calibration; the entire system was tested in a relative sense, comparing its quality to that of the CyXESS and EXOS payloads. The gratings were calibrated prior to the CyXESS flight, but only at the 44 Å carbon line due to difficulties with the laboratory monochromator and only at a 4.4° graze angle. The limited testing of the gratings and collimators in previous flights was motivation for developing our diffuse calibration source.

The entire collimator and grating structure is separated from the outer skin of the rocket and tied directly to and only to the detector bulkhead via a 2.0 m optics bench. The separation from the skin decouples the vibrational modes of the entire rocket from the aligned optical components. The optics bench is a hollow 20.5 inch diameter cylinder with several cutout access ports and a port through it for a vacuum pump to attach to the payload during laboratory testing. The optics bench is connected to both the grating and the detector bulkheads with radax joints. The only other component in this entire section of the rocket — the majority of CODEX's length — is a bundle of wires leading to the star tracker.

A post-flight discovery by Thomas Rogers was that the length of the optics bench was incorrect. Although CODEX used a new bench, dimensions from CyXESS were used because the design had been empirically vetted by using the same collimator design to achieve near-theoretical resolution. The proper length of the optics bench is necessary for the 3.25° to come to a focus, and the length appears to have been defined such that the converging beam of a collimator focused directly behind the collimator on the detector bulkhead. The optical path, however, is deflected 4.4° by the gratings, elongating the path by 2.0sin(8.8°) m, more than 2 cm out of focus. Since

the beam convergence is linear, the 1-dimensional focus will be broadened by $\sim 2.4 \sin(3.25^\circ) = 1.3$ mm. A 50% broadening is severe indeed, and it decreases the resolution by the same factor. With a dispersion of 0.9 Å/mm, a line becomes 2.7 Å in width. With our bandpass of $\sim 10 - 140$ Å, the error in finding the focus results in a resolution that ranges from 4 to 52, which is respectable but causes CODEX to lose much of its groundbreaking edge.

This explains why the collimator tests were close to the theoretical focus of the entire instrument despite not being redirected by the gratings (which is why the problem was not identified during CODEX testing). The collimator tests showed full-width half-maxima (FWHM) of $2.0 - 2.1$ mm, compared to the 1.7 mm theoretical line width, while the adapters placed on the detectors would have defocused the instrument by ~ 0.4 cm, which should correspond to a $0.2 - 0.3$ mm increase in size of the focus. Both the CyXESS and EXOS collimator resolutions were tested and met their design specifications, however. My best explanation for the difference between collimator focus results is that collimator alignment of the previous payloads cut the size of the collimator slits, decreasing the range of angles that could transmit light through each slit in the collimator. The alignment of the collimator plates was improved for the CODEX payload.

2.3 Detectors

After traveling and dispersing over the 2.0 m length of the hollow optics bench, photons terminate on either the detector bulkhead or on the detectors themselves. The 1-dimensional focus of the collimators results in a large portion (>20%) of the lines missing the detectors.

To get higher resolution, a longer throw from the gratings is desirable as it gives more distance for the spectrum to disperse. Additionally, the beam of the 1-dimensional focus of the collimators is large in the unfocused directions. Large-format, high-efficiency CCD or microchannel plate detectors (requiring the tiling of multiple detectors) are very expensive and were not used. Instead, CyXESS, EXOS, and CODEX have been flight tests of gaseous electron multiplier detectors (GEMs), an innovative hybrid of microchannel plates and proportional counters shown in Figure 2.21. (The recent development of large-format microchannel plates could change the

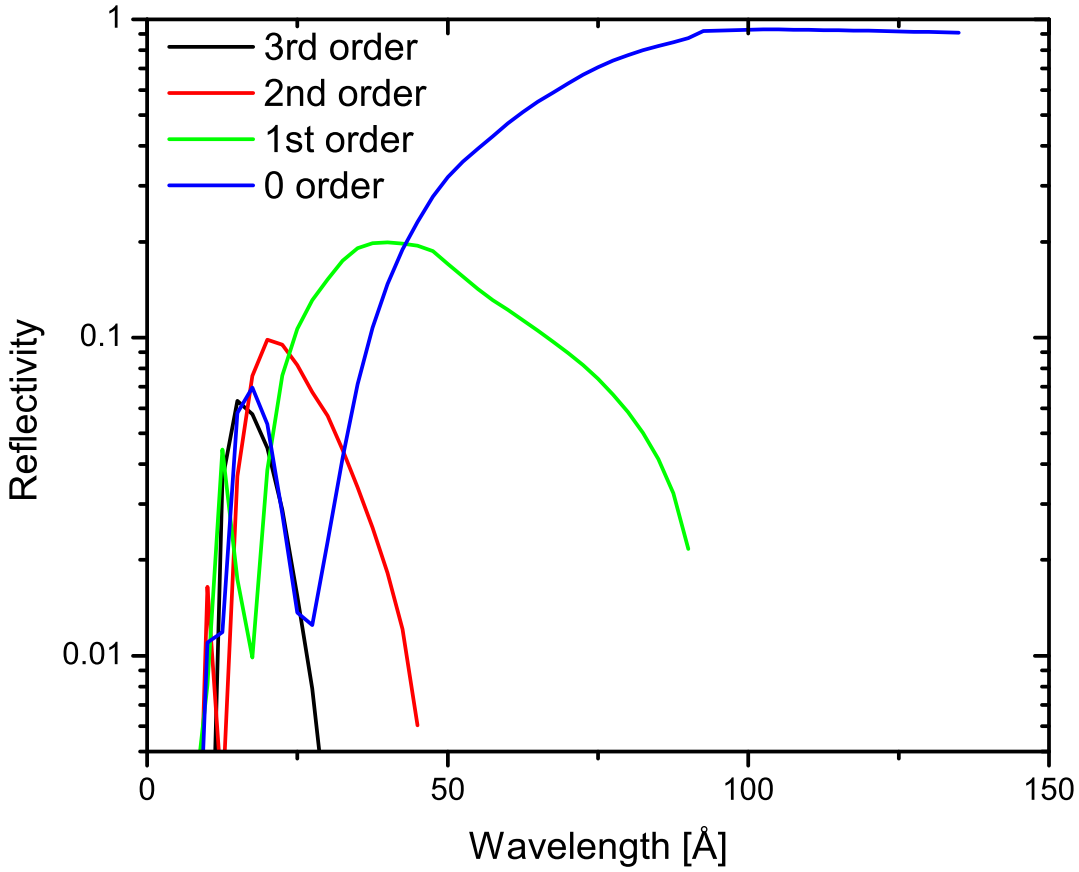

Figure 2.18 Grating diffraction efficiency as a function of wavelength and order, for a 3° reflection angle, representative of the low-angle reflections that can pass through the CODEX grating arrays and still land on the detectors. Theoretical efficiency data was provided by HORIBA Jobin-Yvon.

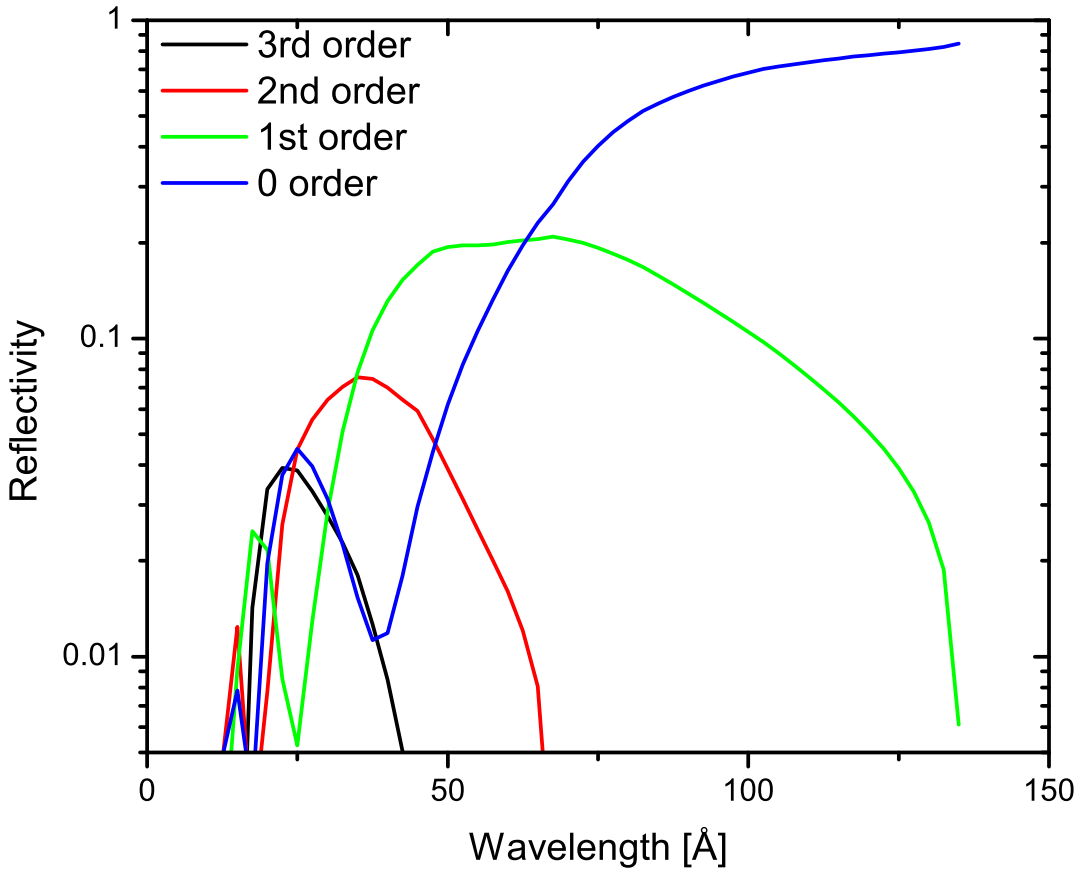

Figure 2.19 Grating diffraction efficiency as a function of wavelength and order, for the nominal 4.4° graze angle from the CODEX gratings. The curves represent the fraction of incident light diffracted into each order, not the fraction of reflected light in each order. Theoretical efficiency data was provided by HORIBA Jobin-Yvon.

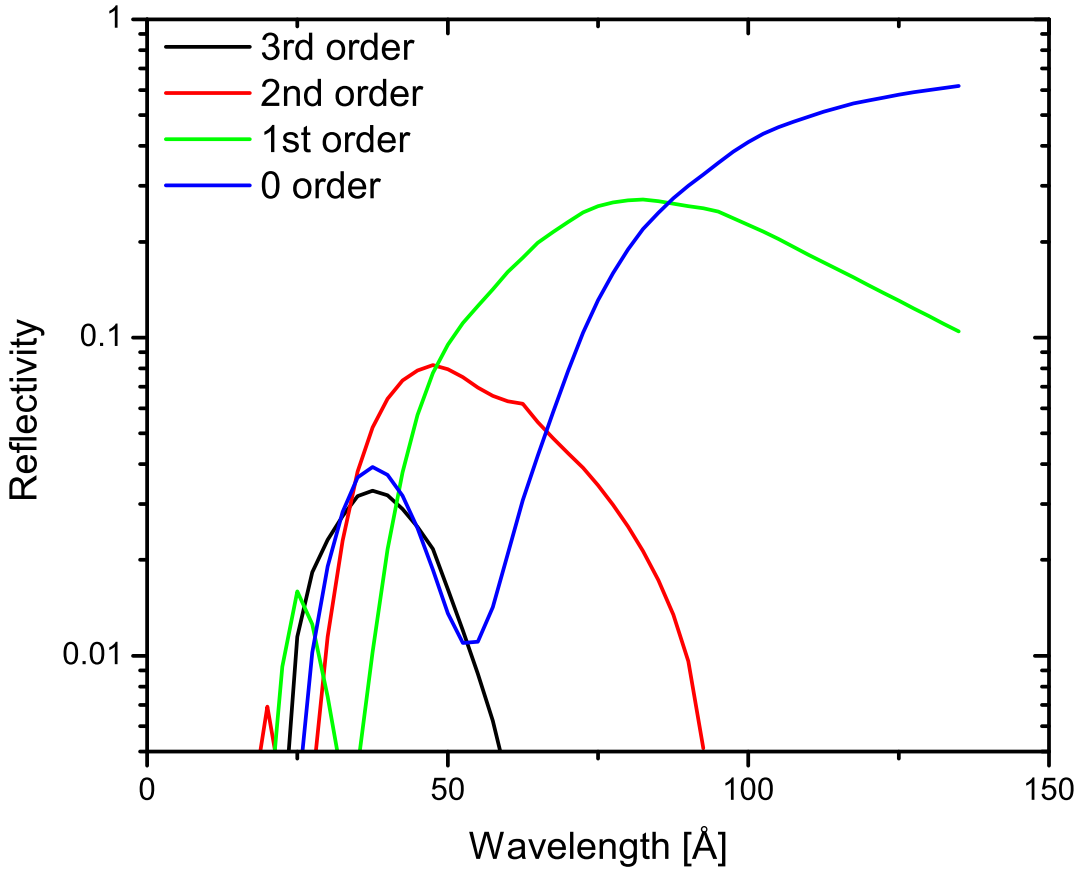

Figure 2.20 Grating diffraction efficiency as a function of wavelength and order, for a 6° reflection angle, representative of the highest-angle reflections that can pass through the CODEX grating arrays in a single reflection. Theoretical efficiency data was provided by HORIBA Jobin-Yvon.

optimal detectors for future flights, although the plates would need to be supported against launch vibrations; Siegmund et al. 2011.) The detectors on CODEX were identical to those on EXOS, and had the same design as those that flew on CyXESS (using the same body but differing in anode, GEM plates, and window, all described below).

Incident x-rays pass through a thin polyimide window before freeing an electron from the gas contained inside the detector. The freed electron is accelerated away from the window and toward a grounded anode by an electric potential of roughly -4 kV. As it passes through and is accelerated by the electric field within the Ar/CO_2 gas (75% argon, 25% carbon dioxide, 13.0 psia) that fills the detectors, the electron frees additional electrons via collisions. The electron shower is magnified by the concentration of the electric field in four porous copper/insulator/copper plates between the window and the anode. The detectors are capable of a gain of $\sim 10^4$ electrons per photon (as calibrated when they were originally built at Sensor Sciences, LLC), delivering this electron shower onto a cross-delay line anode, where snaking, independent x and y lines detect the electron shower as a charge signal. The signal arrival times are compared to determine the position of the impact.

To contain the gas, the detectors are sealed on all sides, with a 500 nm polyimide window separating the gas-filled interior from the vacuum of the payload. (For reference, the ROSAT proportional counters had 1 μm polypropylene windows.) A 30 nm carbon coating applied to the polyimide makes it conductive, so that it can be held at -4000 V. The two flight windows are the same that flew on EXOS, but $\sim$40% thicker than those that flew on CyXESS. The CyXESS windows burst too easily under launch stresses, while the thicker window sacrificed $5 - 10\%$ absolute transmission. The relative loss in transmission form the thicker window is nearly 50% just longward of the 44 Å carbon line, but less severe elsewhere. We considered coating part of the detector window with another medium (i.e., a thin boron coating) to firmly establish the energies of overlapping lines, but we devised the experiment to aqcuire the same information by designing CODEX's bandpass to extend continuously from 139 Å to 0 order specular reflection. The bandpass measures the contribution of high energy photons (the window cutoff would definitively determine whether a feature was a repeated higher-order spectrum or a lower-energy feature, an

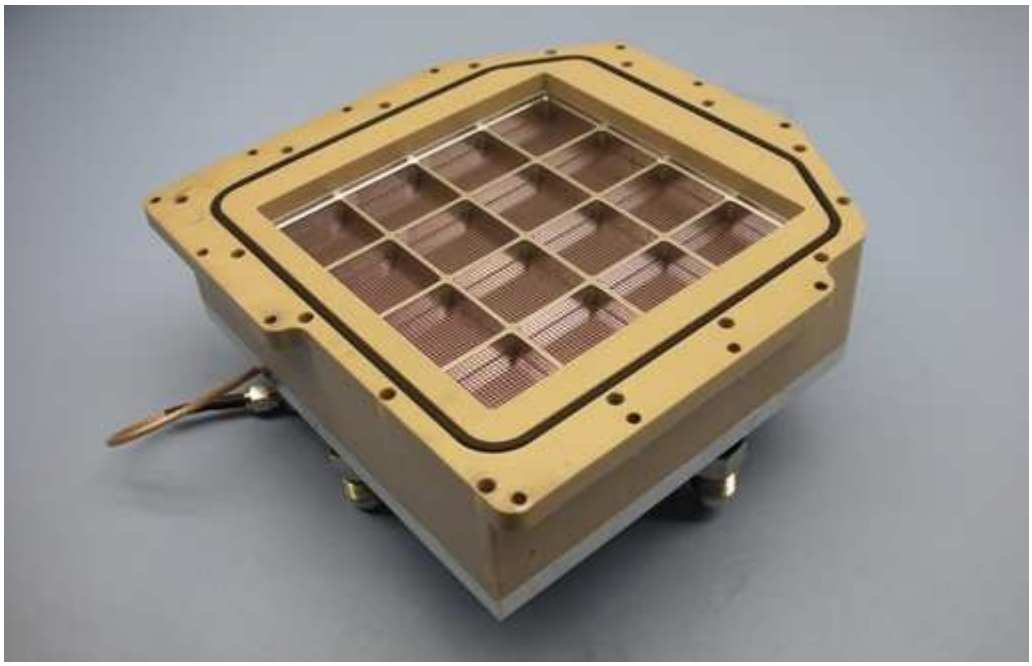

Figure 2.21 One of the flight GEM detectors. The window and its stainless steel support structure face upward (McEntaffer 2007). The light brown housing is an insulating plastic.

issue discussed extensively as an explanation for the EXOS results; Oakley 2011).

The thin window requires a supporting mesh to withstand launch vibrations. The mesh is a 0.005 inch stainless steel square grid with 20 lines/inch spacing, divided every inch by large stainless steel bars (these visibly shadow the detector) into a 4 inch square aperture. The structure blocks 42.2% of the light outright, for a fully-illuminated detector. The burst pressure differential of the windows is ∼90 psi.

Inside the detector is a stack of four GEM plates (Figure 2.22), each composed of 100 μm sheets of liquid crystal polymer (LCP) sandwiched between 8 μm layers of copper, manufactured by SciEnergy, Inc. The stack holds the plates ∼3 mm apart. The plates have a 10 cm square active area, perforated with $\oslash$70 μm holes with a 140 μm pitch and roughly a 50% filling factor (Figure 2.23). The GEM plates are the same as the ones flown on EXOS, an upgrade over the chemically-etched Kapton® sheets flown on CyXESS because of the reduced water absorption and negligible warmup time (compared to a $10-80$% gain increase over several hours for the Kapton® sheets; Simon et al. 2007; Tamagawa et al. 2009)).

The copper/LCP GEM plates are large (∼12 cm on a side), and held only at the edges. Thus, launch vibrations are a concern. The sheets were attached to custom-made alumina (Al_2O_3) frames while heating them. Alumina is an easily-machined insulator, and it has a low thermal expansion coefficient. Under heat, the copper/LCP sheet expanded significantly more than the frame; after cooling, the sheet was tensioned within the frame and capable of withstanding launch vibrations. (The detectors are not turned on until well after the launch vibrations have died out — the booster stops firing at 44 s after launch, and the detector turns on at 110 s). The plates can be seen mounted on the detector (but still missing the window and polyehtylethylketone — PEEK — housing) in Figure 2.24.

All copper plates are held at high voltage relative to the grounded anode, with the voltage climbing from -4000 V at the window in roughly 500 V steps across each sheet (with the LCP insulating the sides from each other) and $200-300$ V between the sheets. Drops between the last sheet and the anode and the window to the first sheet are $500-1,000$ V (see Table 2.2 for measured

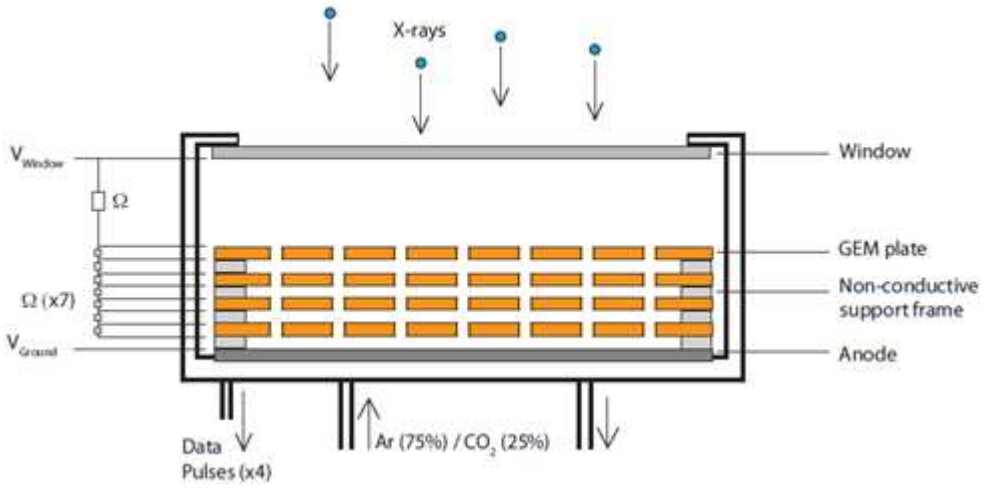

Figure 2.22 Schematic of a GEM detector (Oakley 2011). X-rays enter from the top, at the polyimide window held at roughly −4 kV. The four porous copper/LCP/copper GEM plates are held at voltages that progress toward 0 V at the anode, accelerating any electrons freed from the filling Ar (75%)/CO_2 (25%) gas by incoming x-rays and producing a gain of order 10^4 electrons per photon. The time delay of the data pulses from the start to the end of the x and y lines of the cross-delay line anode define the location of the electron shower.

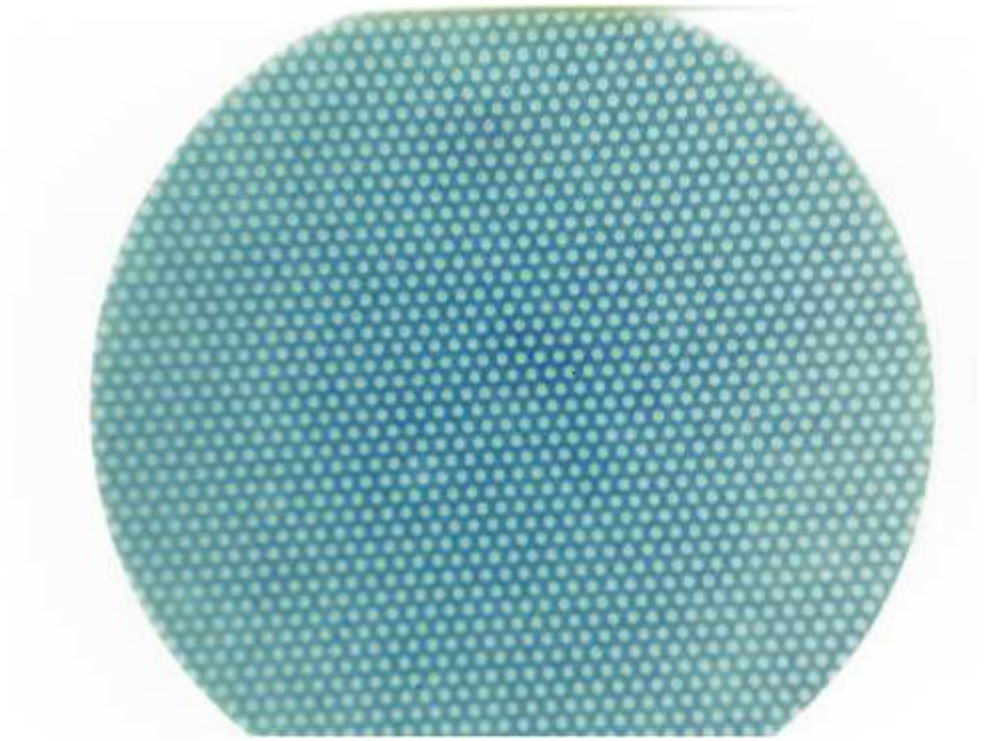

Figure 2.23 Magnified image (photographic negative) of a region of a GEM plate, showing the pores through which the electron shower propagates (Oakley 2011). The plates have a 10 cm square active area, perforated with 70 μm holes with a 140 μm pitch and roughly a 50% filling factor of holes.

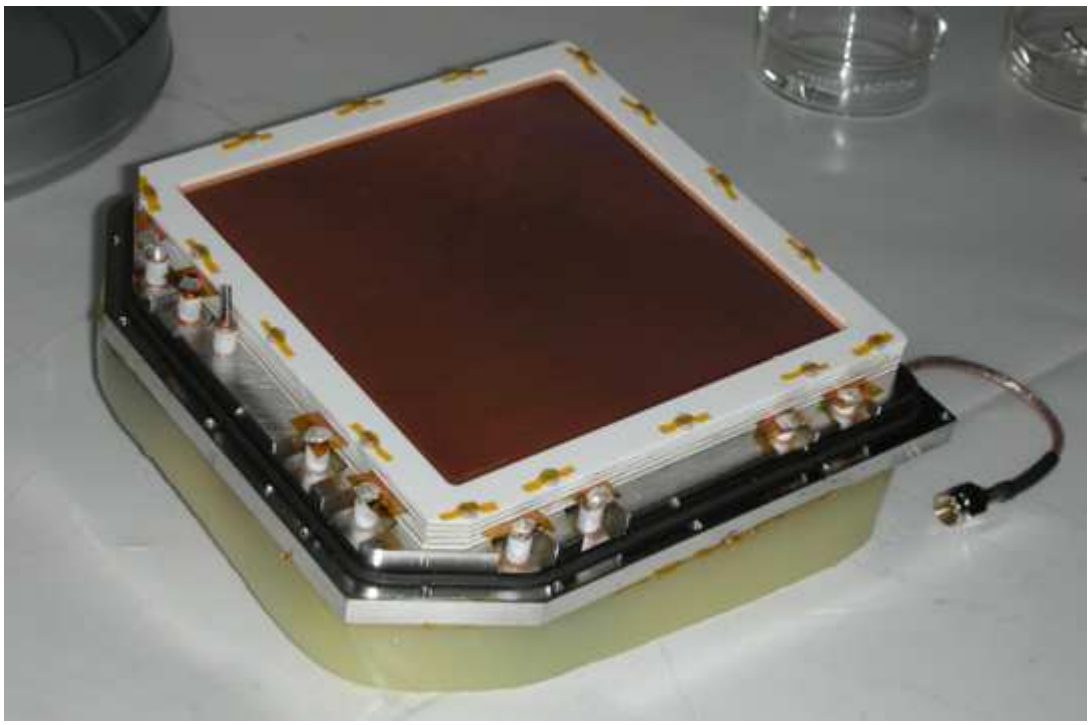

Figure 2.24 The guts of a GEM detector, showing the stack of copper/LCP plates held in a stack of alumina frames. The alumina frames are held in place with insulating PEEK screws, which have the heads taped with Kapton® tape to hold the screws in place during launch vibrations (ScotchWeld 2216 epoxy is the standard for this elsewhere in the rocket; tape was used here to allow easier removal of the screws and because of the outgassing of 2216 epoxy while it cures, which could have deposited small amounts of organic residue on the sensitive copper/LCP GEM plates). The yellowish backing to the detector is an arathane potting surrounding the high voltage chain that delivers voltage to the eight posts (seen on the closer edges of the detector) and to the copper sheets.

values).

The electron shower (also known as a "Townsend avalanche") generated by the incident photon is accelerated toward each successive GEM plate, where the electric field lines from the sandwiching copper plates are concentrated in the pores. The acceleration through the pores creates a concentrated, high-gain electron shower proceeding toward the anode. The voltage limit across the plates, which significantly defines the gain (along with the gas pressure), is defined by the stability of the GEM plates. At high voltages, the thin insulator separating the copper plates can become unstable, or contaminants can bridge the insulating gap. Making the insulator thicker is a potential cure for this instability, although the detector would then be required to operate at a very high voltage, and the gas itself might undergo a dielectric breakdown.

The electron shower lastly hits the anode, which is composed of independent x and y cross delay lines and an insulating layer separating them. The serpentine palladium lines have resistances of $50 - 100\ \Omega$, and a signal line goes from each of the two ends of each of the two delay lines to the amplifiers. The y line lies atop the x line and is held at roughly -60 V to keep it from absorbing all of the electrons. This is done by splitting the resistor chain from the last of the GEM plates, where the voltage is still $500 - 700$ V, and sending one side to ground and the other to the y anode line, with additional resistors in between. This is a convenient but potentially hazardous design, because although the high voltage power supplies are generally very stable, ripples in the power line are transferred directly along the signal line. By virtue of the delay line anode, this should not cause problems: comparing arrival times of charge signals along each line and requiring a minimum charge signal to be associated with the signal allows discrimination between real and spurious signals. However, in a noisy environment such as laboratory testing or during flight, it is conceivable that this increased noise could couple with RF noise external to the system and increase the likelihood of spurious signals.

The signal itself is processed in four different places on the payload. After being received in the detector, it travels along 30 cm lines from each terminus of the delay line anode to amplifiers, where each of the four signals (two each for x and y) being amplified and an overall charge for the

Table 2.2. GEM plate voltages

Plate position	Measured voltage [kV]	Designed voltage [kV]
Window	-3.620^a	-3.620
Top of plate #1	-3.165	-3.169
Bottom of plate #1	-2.756	-2.777
Top of plate #2	-2.528	-2.552
Bottom of plate #2	-2.194	-2.101
Top of plate #3	-1.971	-1.875
Bottom of plate #3	-1.522	-1.425
Top of plate #4	-1.303	-1.199
Bottom of plate #4	-0.945	-0.825
Anode	0.000	0.000

[a]Measured and theoretical values for the GEM detector that straddled 0 order (operating voltage is -4.23 kV). This is below the operating voltage of -4.23 kV. The measurement probe is calibrated to 1%.

event is measured. These five signals are sent to the adder, which combines the signals from the two detectors into a single signal. The signal is then passed to the time/digital converter (TDC), where the arrival of the signal must match closely with a positive charge pulse (integrated value, so consistently high noise or charge with noise overlaid both register as signals, if the integrated value exceeds the threshold). The signal is sent through a discriminator (minimum x, y, and charge) and an analog-to-digital converter (converting to 12 parallel bits each of x and y, and 8 of charge). Based on which line received the charge signal, the detectors are differentiated by the least significant bit (0 or 1) of the charge data pulse after conversion from an analog signal to a digital one. The least significant bit is unimportant for the signal as the charge resolution is very poor. The signal arrival times are also compared to determine the position of impact on the anode. The solution, coupled with the charge information that also identifies the receiving detector, is sent to the telemetry interface board and passed to the Wallops telemetry section at a rate of 10^5 Hz (consequently, that is the maximum count rate for a perfectly periodic source; random arrival times will see some overlap that results in misanalyzed counts).

The integrated charge signal, which lags behind the position signal by several microseconds, is noteworthy: if another signal arrives before the previous one is fully processed (separation of signals of less than a few microseconds), the charge from the first pulse could define which detector apparently "saw" the signal, and for high count rates there is often significant detector confusion.

We built two new detectors at the University of Iowa with intent to fly them on CODEX, duplicating the high voltage resistor chains of the CyXESS/EXOS detectors made by Sensor Sciences. The detectors are elegantly simple in their design; the readout electronics are the tricky bit. The new design, shown in Figure 2.25, was not an improvement in any quantifiable aspect, as it had the same collecting area, theoretically the same quantum efficiency, and even used many of the same parts (anodes, windows, and GEM plates). The improvements of the new detectors were in the mechanical aspects — symmetric bolt patterns to allow rotation of the detectors, larger screws for more robust threads, assembly screws on the back rather than on the face of the detector, and stronger gas feedthroughs to prevent leaks. Using BNC instead of SM-A connections on signal

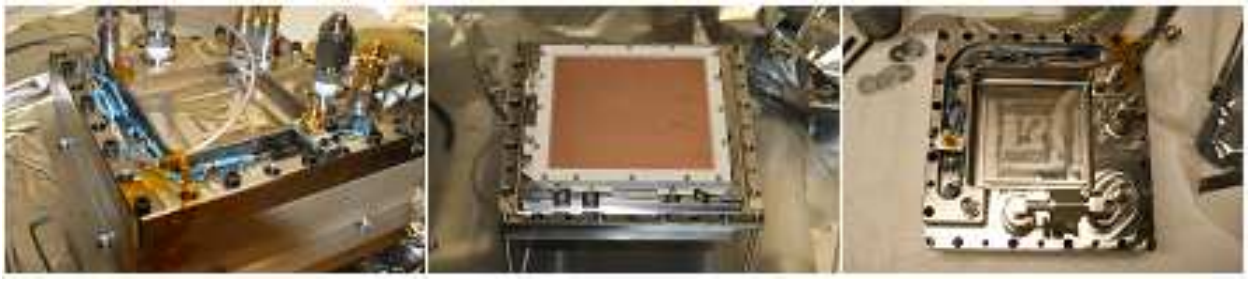

Figure 2.25 The new design of the GEM detectors, as built at the University of Iowa. *Left*: The fully-constructed GEM, viewed from the back. The high voltage resistor chain (blue resistors) is exposed; it was later potted in arathane for safety and durability. *Middle*: The interior of the GEM, revealing the GEM plates. The window and the PEEK housing, which hold the Ar/CO_2 gas, have been removed. *Right*: The back side of the detector, with a clearer view of the high voltage resistor chain and the gas feedthroughs.

cables also increased the durability and reliability of the connections.

The new design omitted a crucial electrical detail, namely the voltage split from the end of the high voltage resistor onto the y anode line. The omission would have prevented any real signal from being passed through the detectors because the electron shower would hit a grounded y line first (it lies on top of the x line) and all signal would show up on the y line. The TDC would then discriminate against it as noise because the x line could not corroborate it. Biasing the y line repels some of the electron shower so that part of it reaches the x line. This was fixed after discovering the flaw.

Done properly, a detector's resistor chain (Figures 2.26 and 2.27) should be optimized along with the gas pressure. The best design for this would be to use individually-tunable high voltage power supplies or variable resistors for each of the eight copper sheets in the sack of GEM plates. However, the CODEX detectors have fixed resistor chains potted with arathane. The detectors were optimized for the hardware of the CyXESS payload, but testing of the EXOS payload with new GEM plates and anodes revealed that the detectors had sufficient gain without optimizing the entire resistor chain. We rebuilt the resistor chain of one old detector and built two new detectors, but modeled them as clones of the CyXESS/EXOS detectors.

Although the resistor chain was tested and stable above 4 kV, when fully assembled the new GEM detectors arced in the 3 kV range. Time constraints prevented tracing down and correcting

Figure 2.26 Part of the high voltage resistor chain, carrying −4,000 V at its start, in the new GEM detectors built for CODEX. The close-packing of the resistors was ameliorated by an arathane insulator potting the channel around the detectors to prevent arcing.

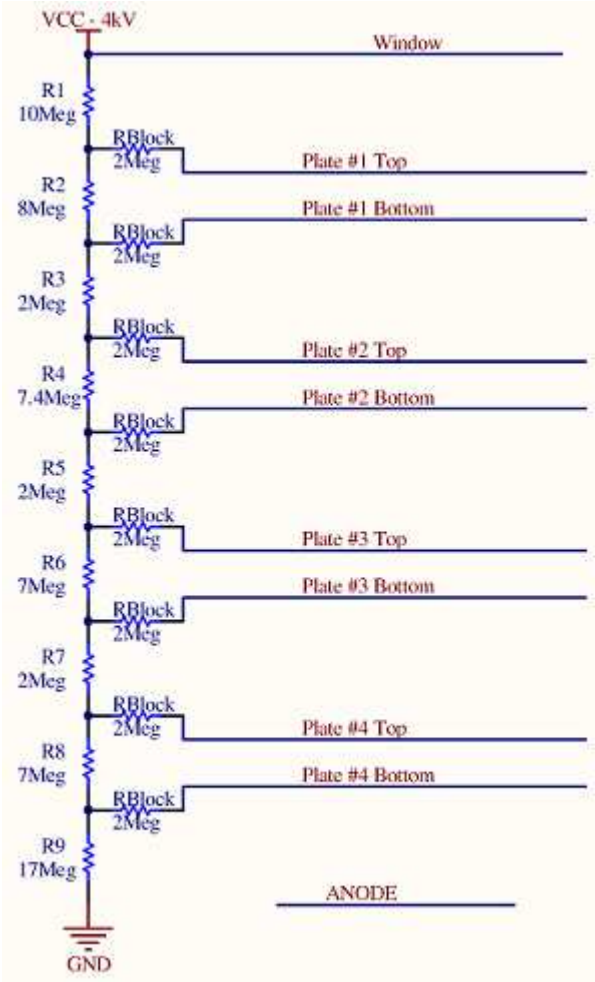

Figure 2.27 Schematic of the resistor chain of the new GEM detectors as initially constructed at the University of Iowa and the University of Colorado. Note the resistors separating the plates from the main resistor chain. Because these resistors carry no current, they do not create a voltage drop. They exist to protect the rest of the detector in the case of a top-to-bottom arc across one detector, which would bypass an entire $7 - 8$ MΩ resistor and jeopardize expensive (in both money and lead time) GEM plates; the 2 MΩ shunt resistors do not affect performance and will not maintain detector functionality in the case of a fused GEM plate. This schematic is erroneous, however, in that the R9 resistor separates Plate #4 Bottom from the ground and the anode is separated entirely, while to function correctly the R9 resistor must split to ground and the anode to bias the y anode line with -50 to -60 V to prevent the top line from absorbing the vast majority of the electron shower. The CODEX detectors, which are the original ones flown by CyXESS and EXOS and manufactured at Sensor Sciences, LLC, do not have the 2 MΩ shunt resistors and will fry an entire stack of GEM plates if one plate fuses. Due to limited time and money for testing with the new design, whether the shunt resistors would actually serve their purpose of sparing the other three GEM plates when one fuses has not been experimentally verified. (Image credit: T. Schultz)

the problem, and instead the old GEM detectors flew on CODEX. The detector that straddled 0 order was disassembled as a model for the high voltage resistor chain, and so it was rebuilt from the initial Sensor Sciences, LLC, handiwork that flew on CyXESS and EXOS.

After transporting the electronics and new detectors back from Iowa, the electronics no longer functioned correctly. The electronics are fickle: slightly bad connections can garble a signal too much to be recognized as a photon event, a daunting thought for a sounding rocket payload. Prior to flight, connections were torqued and then staked with either epoxy or urethane; neither method of securing connections was used prior to transporting the electronics section from Iowa to Colorado. To recover functionality, tests were first conducted with the old GEM detectors, which were known to have worked for CyXESS and EXOS. Due to time constraints, CODEX eventually flew the old detectors and never fully tested the new ones, although the failure points identified were cable connections independent of the detectors.

Testing the detectors required a variety of mechanisms. A first-order liveliness test comes from a "stim" pulse generated by the adder, which sends a signal into the amplifiers that returns as an event with a timing delay that places it just outside of the corner of the active area of the detector. The stim checks connections, essentially. A second accidental test was achieved by laboratory noise. This is shown in Figure 2.28 and is worrisome, because pickup on the signal lines was interpreted by the electronics as vertical and horizontal lines; the CyXESS and EXOS spectral lines were both vertical relative to the detectors. The noise signal test was accidental, and its periodicity would not be seen in the case of random interference.

The most desperate attempt to make the electronics work, at a time when it looked like the TDC had stopped correctly passing data — it acknowledged viable data but did not output a signal, a problem which, to repair, would have been expensive in both time and money — came from Adrian Martin at Sensor Sciences, who suggested using a signal generator to charge a small capacitor. Testing with just a signal generator (sans capacitor) producing a simulated signal for the TDC did not work, but charging and discharging the 20 pF capacitor was the necessary step to send a charge signal that would actually register as data. By using this technique, CODEX's electronics

gradually passed functionality checks. The electronics troubles were due to several worn-out cables and connectors.

Testing then moved on to the easiest real signal: the decay of ^{55}Fe. The 6 keV line is well beyond the <1 keV upper end of the CODEX bandpass, but the signal is strong and can be used to test detectors at atmospheric pressure if the source is placed close to the detectors. The signal will frequently result in misanalyzed counts (counts registering as outside of the active area). Since the TDC determines the position of a photon event based on comparison of signal arrival times, it is unclear what causes the misanalyzed counts. The ^{55}Fe source is only used for liveliness tests of the active surface, however, and the error is not a concern for the overall instrument performance because the payload is unresponsive above 1 keV due to the reflection efficiency of the gratings. With x-rays below 1 keV, the fraction of counts that is misanlayzed is insignificant.

When it was confirmed that all components were working correctly, the electronics and the detectors were installed on the rocket for further testing.

2.4 Bandpass

Although the components of CODEX's two spectrographs mimic closely those of the CyXESS and EXOS payloads, a key component of the spectrograph is its bandpass. Dispersion from the grating equation gives a scale of 0.90 Å/mm (for a derivation, see Oakley 2011, Eq. 2.12), and the positive and negative orders from the unblazed reflection gratings are equal. Placing the detectors is simply a matter of putting them at the focus of the collimator (the distance is defined by the optics bench) and positioning them in the part of the spectrum desired. This requires mounting them as close to the rocket skins as possible, since that is the brightest part of the spectrum.

The CODEX detectors were positioned with a different philosophy than those of the EXOS and CyXESS rockets. The original motivation for CyXESS was to target the soft x-ray background, with six redundant spectrographs (each with the throughput of roughly one of CODEX's two spectrographs). The faint background requires all six spectrographs to have identical bandpasses to build up enough collecting area. That vision, however, has yet to be realized, and CODEX and

its ancestors have targeted the two brightest diffuse soft x-ray sources in the sky: the Cygnus Loop and Vela supernova remnants.

CODEX was designed to confront two possibilities:

(1) that the EXOS results were correct, which would indicate the exquisite sensitivity of this payload design. In this scenario, CODEX would detect some 10,000 counts from diffracted photons. The noise level would be a few hundred counts across each entire detector. The carbon and oxygen lines should still be expected, as well as a strong 0 order, on the shorter wavelength detector, while the flux should increase strongly in the continuum on the longer wavelength detector. If the arguments in §1 and the interpretation of the EXOS results as a synchrotron continuum are indeed correct, then the spectrum will be dominated by a continuum with some overlaid spectral lines; or

(2) that the EXOS results were fundamentally flawed or at least misunderstood and the arguments in §1 regarding nonthermal emission are either not valid or not relevant to the Vela SNR. CODEX should still expect a line-dominated thermal spectrum, with the strongest handful of lines (oxygen, carbon, iron, possibly a few other species) carrying >100 photons per detector per line relative to a detector noise level of several hundred Hz across the entire detector (giving a conservative signal-to-noise ratio of ∼25). In this interpretation, EXOS detected a large quantity of noise.

In either case (line or continuum), the signal was strong enough that overlapping the detectors was unnecessary and the $\sqrt{2}$ improvement in the signal-to-noise ratio was not necessary. Instead, the CODEX detectors were offset but overlapping across the carbon and oxygen lines to allow for bootstrapping relative calibration between the detectors. To further extend the bandpass and to misalign spectral lines from characteristic detector noise signals (Figure 2.28), as well as to place them in an optimal part of the payload's throughput, the CODEX detectors were rotated -6.206° and 36.000° relative to the collimators and gratings (Figure 2.29). This gave continuous coverage from 30 Å on the negative side of 0 order to 139 Å on the positive side. See Figure 2.30 for the

collecting area as a function of wavelength.

The detector area on CODEX is equivalent to that on EXOS and CyXESS, but the positioning on the spectrum creates a more complicated bandpass. EXOS and CyXESS both had square bandpasses in terms of collecting area (window and reflection efficiencies made the effective areas very much not square). The CODEX bandpass is shown relative to the EXOS one in Figure 2.31.

Positioning the detectors thus gave CODEX a detector that would receive coverage of both the $+1$ and -1 order oxygen lines at 22 Å, the 0 order specular reflection, and $+1$ order carbon, while the second detector would overlap the carbon and oxygen lines light on one detector, and carrying out beyond 100 Å where Oakley (2011) observed a steeply climbing spectrum, concurrent with the Cash et al. (1976) result for the spectrum of the diffuse ISM. The overlapping detectors allow for bootstrapping relative calibration of the detectors with lines that show up in both detectors. An alternative positioning would have placed 0 order on the edge of one detector, and extend the bandpass farther out toward the long wavelength part of the spectrum. Due to the reflectivity of the poor efficiency of the payload at short wavelengths, the region shortward of $\sim$10 Å (roughly 9 mm on either side of 0 order), is wasted; putting 0 order on the edge of a detector would restore $8-9\%$ of the detector as a viable collecting area.

The detectors were fitted into positions on the detector bulkhead (Fgire 2.32), but the bulkhead was designed for the screw pattern of the new but unsuccessful GEM detector design. To fit the old detectors on the payload for flight, we made an adapter plate. The plate was 0.4 cm thick, but since the rate of convergence of the beam is very slow (effective speed of f/17.6), the spreading of the 1.7-2.0 mm focus will be $\sim$10%. This worsens the resolution of the instrument, but it does not compromise its overall objectives.

2.5 Gas system, electronics, and housekeeping

The detectors require an Ar/CO_2 gas mixture as the photo-absorptive and electron-producing medium inside the detectors; the GEM plates and high voltages are merely for accelerating electrons produced in this gas. Proportional counters require gas flow, albeit at a low rate, to replenish the

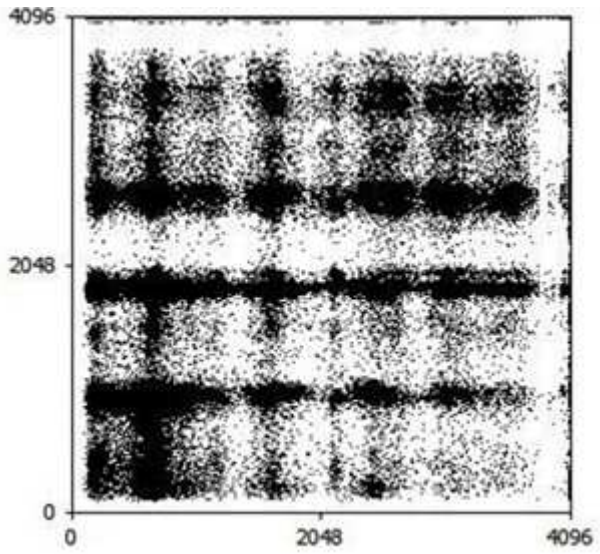

Figure 2.28 Laboratory noise image, showing the tendency of a noise to spread along the cardinal axes. Noise has also been seen to spread at a 45° angle, but axial noise is more common. Strong signals can spread similarly, including the stim pulses, although no line produced in the laboratory (up to 300 Hz per line) exhibited this bleeding. It is also noteworthy that this image of laboratory noise is not constrained to the active area of the detector and the anode. The non-uniformity is probably due to periodic RF pickup, although the cause of the noise in this image is unknown. CODEX detectors were rotated relative to the spectrum, which would only be focused in one dimension and so detected as a line the length of the detector. A line corresponding to the angle of the detectors relative to the optics would be a clear indication of a spectral line.

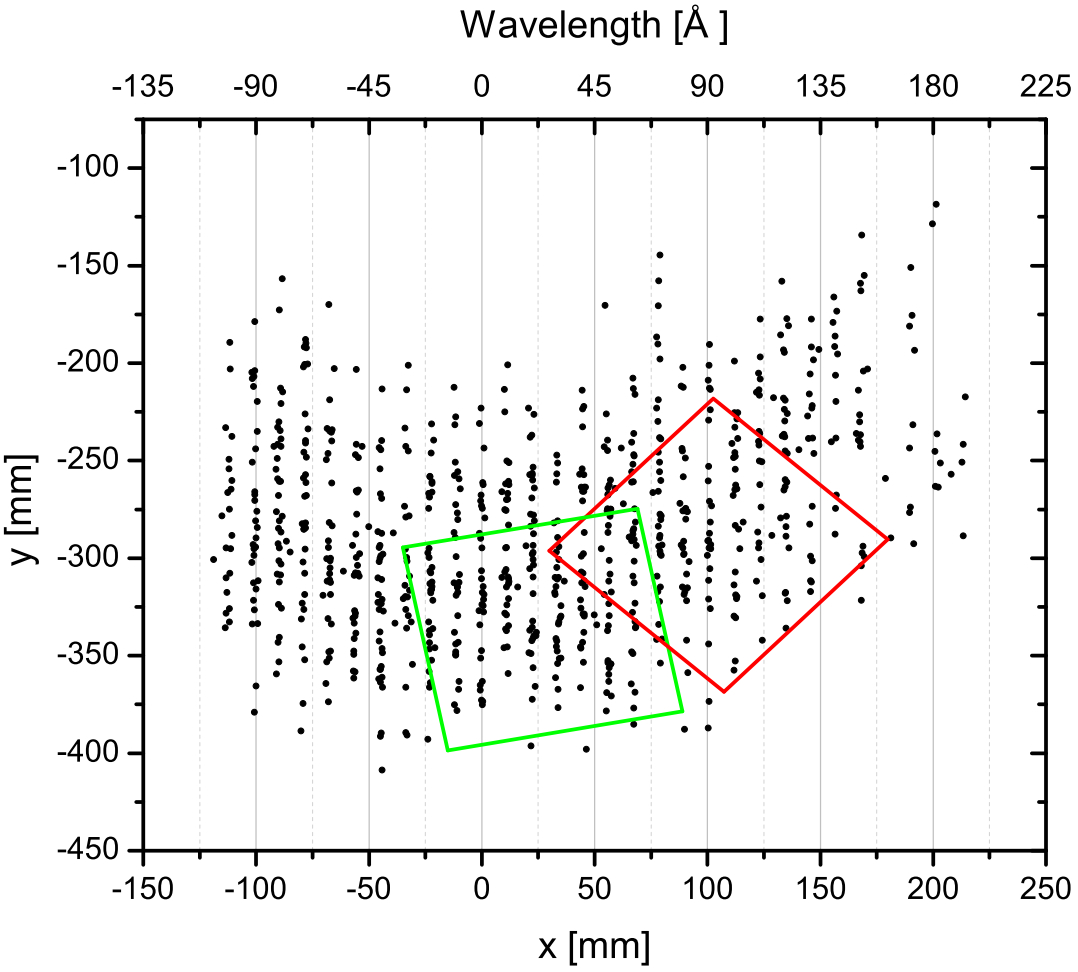

Figure 2.29 Detector placement relative to a spot diagram from a ray trace of the CODEX spectrograph, with positions relative to a photon passing through the center of a collimator. Since the detectors back different spectrographs, they can overlap on the spectrum without overlapping in space. Specular reflection ("0 Å" diffracted light) falls at $x = 0$. Lines are traced in 10 Å intervals. Some rays fall beyond the detectors, both along the dispersion direction (outside of the bandpass of a particular detector) or perpendicular to the dispersion. These photons will be lost.

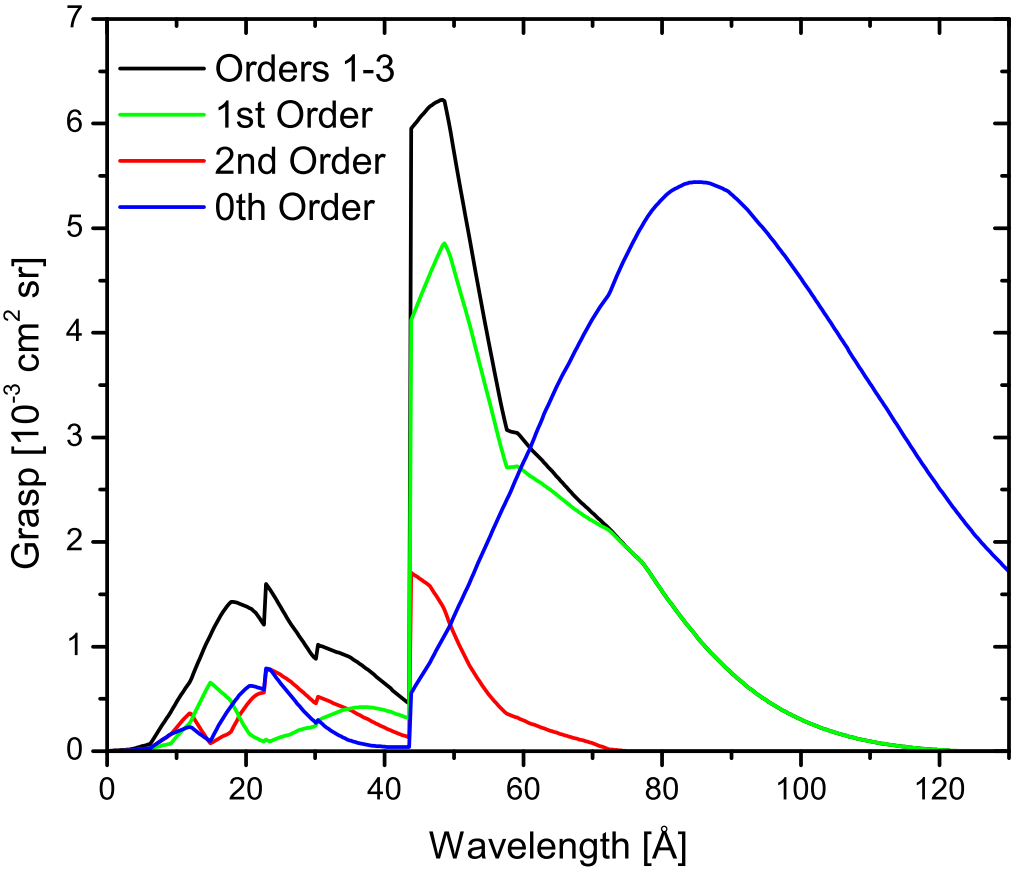

Figure 2.30 Theoretical grasp as a function of effective area for CODEX (uses an incidence angle of 4.4°). Grasp is the relevant figure of merit for a large-area telescope; for a spectrograph, an additional figure for resolution is also important, but since the resolution is already defined by the grating array and the length of the rocket, they are not optimized for CODEX and can be neglected from a figure of merit analysis for this payload. This figure does not include shadows of window bars.

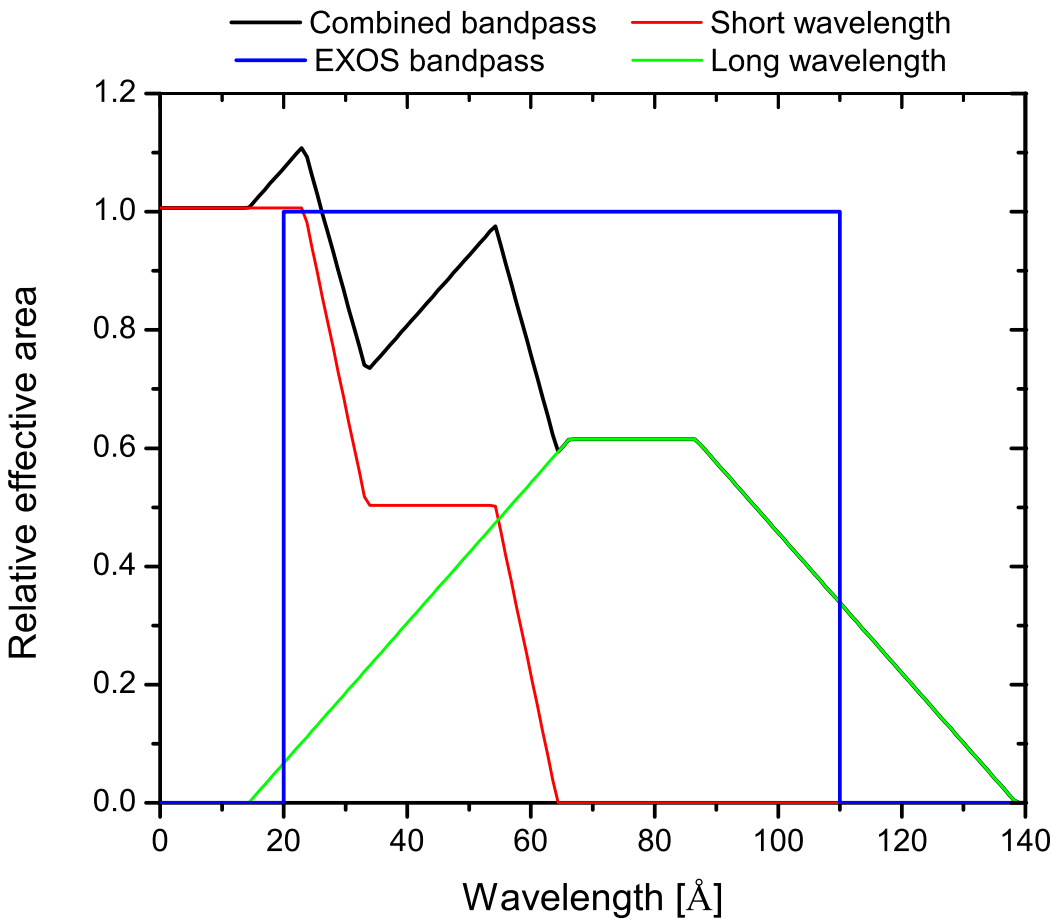

Figure 2.31 The CODEX bandpass, with the collecting area compared to that of EXOS. The physical collecting area of the instrument is the width of the line (∼2 mm) times its extent across the two 10 cm square GEM detectors, with unity defined in this figure as each detector receiving a 2 mm × 10 cm line. Deviations from unity are due to non-overlapping detectors and rotation of the detectors relative to the spectral lines. EXOS's 20-110 Å bandpass is plotted for comparison.

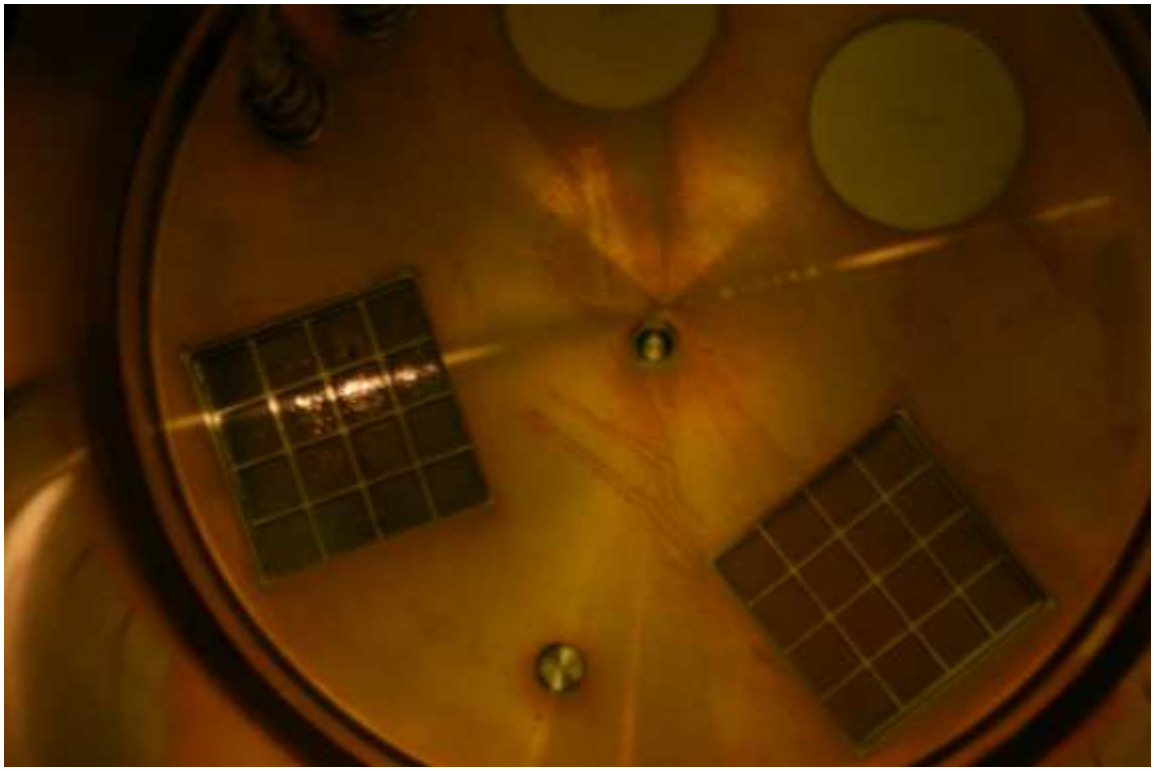

Figure 2.32 Photograph of optical light (white LED flashlight) shone down the collimator. The picture was taken post-flight. Visible light is not diffracted by the CODEX gratings; the visible line is the 0 order specular reflection. A light shone down the other collimator would not fall on either grating. The tremendous length of the line is deceptive. All light in the line to the right of the center of the image comes from multiple reflections in the grating array. The nickel gratings are highly reflective to visible light, but x-rays will not survive a second reflection in any significant quantity, effectively killing the stray light to the right.

neutral gas that is the supply of electrons for the detector gain, and the windows have a low but intrinsic leak rate that fulfills the gas flow requirement. This gas flow requires a gas delivery system (for a schematic, see McEntaffer 2007; Oakley 2011). Gas is stored in a 1 L high-pressure bottle, regulated via a manual regulator down to 35 psia, and then sent to two proportional valves, one for each detector. The proportional valves are set electronically via a variable resistor (pressure is proportional to the voltage) to deliver 13.0 psia to each detector. Neither the regulator nor the proportional valves reference pressure to the atmosphere, and thus they function well in a vacuum. The manual regulator has a high-tension spring inside of it, but in its two preceding flights the internal diaphragm was not affected significantly by launch vibrations. The system provides a constant 13.0 psia gas delivery to the detectors, with the inflow/outflow set by the leak rate of the windows and o-ring seals in the detectors.

The gas system is very similar to the CyXESS/EXOS design, although several components were improved. Tubing was rebuilt to allow for better fastening to reduce the detrimental effects of launch vibrations and a pair of pressure relief valves (low-probability but potential failure points) were removed in favor of just unscrewing a connection.

Also, we removed a latching solenoid valve from the CyXESS/EXOS design, originally included to shut off gas flow if a detector window blew, which would drain the gas reservoir into the payload and make the payload opaque to x-rays. Although the latching solenoid would have allowed the detectors to continue to operate at a rapidly-decreasing gain, it also provided a failure mode where the gas flow could have been shut off to functioning detectors. Having a safe mode that simply makes the detectors non-functional is not worth the risk of including the solenoid on the payload. In retrospect, however, the low leak rate eventually achieved with the CODEX detectors would have allowed one detector to keep functioning if the solenoid had triggered due to a failed detector window. The solenoid would then have prevented the payload from flooding with gas and obscuring the other detector. The leak rate was low enough that the undamaged detector would have continued to operate at high efficiency. However, this level of stability was not achieved until three weeks prior to launch. The low leak rate might have obviated most of the gas delivery system

except for a small reservoir of tubing and proportional valves, but again this level of stability was not achieved until too close to the launch date to make the changes.

The proportional valves, although modified explicitly to work under vacuum for the EXOS flight, did not function correctly during laboratory tests. The payload was tested under vacuum (including the electronics section), and at low pressures one of the flight gauges and one spare gauge did not maintain their output pressure when under vacuum. They did not appear to be continuously leaking (pressure did not rise in the vacuum chamber where they were being tested), but pressure rapidly dropped to about 3.5 psia over $1 - 2$ minutes. This was interpreted as the pressure gauge being affected by the vacuum, likely due to a leak in the gauge; potting the sensor inside of the proportional counter with arathane was sufficient to restore its functionality. The flight proportional valve that did not have this trouble was not modified in the spirit of "If it ain't broke, don't fix it." Both flight proportional valves worked for the EXOS flight and during laboratory testing for CODEX, and both the potted and unpotted proportional valves appeared to function during CODEX's flight.

CODEX also flew a pair of MKS MicroPirani 925C vacuum transducers, one monitoring the pressure inside the instrument and the other monitoring the pressure in the electronics section. 925C gauges are stable and reliable under launch vibrations and from atmospheric pressure down to 10^{-5} Torr. Since the vacuum gauge relies on passive thermal conductivity of the gas to measure the pressure rather than generating ions via high voltage measurement devices, the detectors can operate throughout the flight – including while the detectors are operating. Previous vacuum gauges flown on CASA sounding rockets had to be turned off during detector operation. This was the first flight test of the 925C, although MKS has tested their vibrational stability, and they are now flying on other Colorado payloads.

2.6 Testing and optimization

2.6.1 Detector pressure and voltage optimization

Detector optimization was done with a fully-configured rocket (collimators, gratings, detectors) and a Manson Model 2 Ultra-Soft X-ray Source. The Manson source provided point-source illumination, which is a less accurate simulation of in-flight performance than the diffuse source used for collimator testing, but it has a higher count rate that is good for statistics and short testing times.

As constructed, the GEM detectors have two easily optimizable parameters: Ar/CO_2 gas pressure, and overall high voltage supply. The voltage drops across individual plates and the gas composition are also optimizable, but the former was not configured for easy optimization (defined by a potted resistor chain rather than by individually-tunable power supplies or variable resistors). The primary criterium for optimization was count rate in the spectral lines. Detector background, a flat response function across the face of the detector, and gain per photon were secondary.

Detector pressure was constrained to be greater than atmospheric pressure at the White Sands Missile Range, as $P < P_{atm}$ would allow backflow into the detectors that would bring in ambient gas and decrease the gain. Testing at $P < P_{\mathrm{atm}}$ was never done for CODEX, and this is an acknowledged deficiency of the optimization, especially considering that the optimal pressure was found to be the lowest tested (Figure 2.33). Testing by Phil Oakley (Oakley 2011) showed that the detector became unstable below 12.0 psia, although this was likely due to the fixed operating voltage of -3.8 kV during EXOS pressure optimization tests; the same EXOS tests showed that lower pressures produced higher count rates (Figure 2.34). The optimal voltage and pressure are correlated, and voltage must decrease with lower pressure to prevent arcing.

The optimal voltage was the highest non-arcing voltage possible. This voltage dropped with pressure, and since CyXESS and EXOS both flew at 14.5 psia while CODEX flew at 13.0 psia, CODEX flew at about 400 V lower detector voltages than EXOS and CyXESS. The optimized images are shown in Figures 2.35 and 2.36, with both detectors in the short wavelength spectrograph

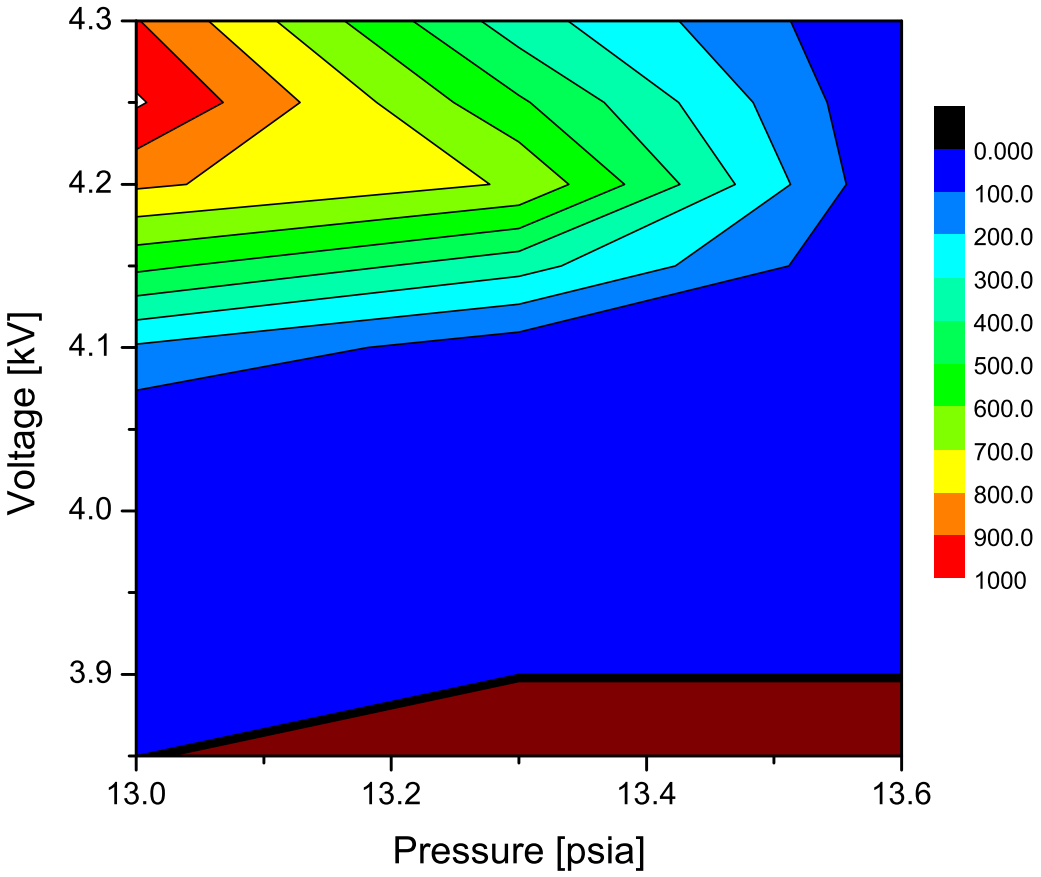

Figure 2.33 Optimization of the detector placed across 0 order, based on count rate (contours) received in the 0 order and spectral lines of a predominantly oxygen and trace carbon (less than a few percent) spectrum. The y axis is the absolute value of the voltage, as it is in fact negative. The parameter space was sampled at 13.0, 13.3, and 13.6 psia and every 50 V from 3.9 kV (3.85 at 13.0 psia) to 4.3 kV, where the detector arced; the brown region at low voltages was not tested. Colors represent count rates. The test at 4.3 kV and 13.0 psia was too unstable to be a viable data point. Background counts of a few Hz were assumed to be part of the signal (lost in the noise). 13.0 psia was chosen as a minimum pressure to keep the detector pressure above atmospheric pressure, and 4.3 kV was the upper voltage limit due to arcing within the detectors. Generally, higher pressures produce more even gain but lower overall quantum efficiency. The highest count rate was deemed the optimal location, regardless of gain variations or background level (within reason; and major events such as arcs were excised from the data). The detector was flown at 4.23 kV and 13.0 psia.

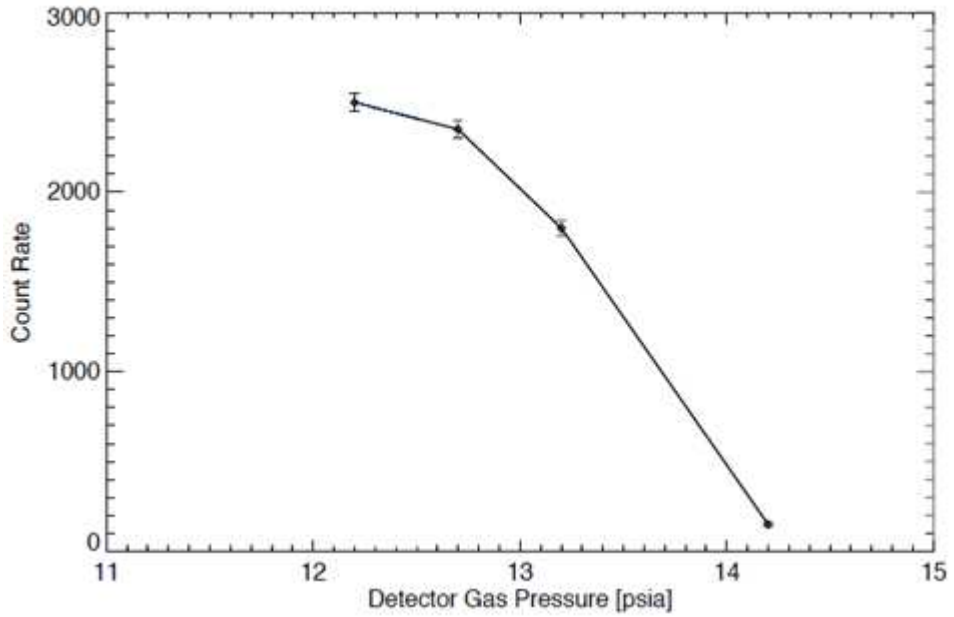

Figure 2.34 Count rate as a function of pressure, measured for the EXOS payload (Oakley 2011). Tests were conducted strictly at 3.8 kV, although the voltage must change along with the pressure for optimal gain. The detector became unstable below 12 psia, although this might be due to the high voltage. EXOS flew at 14.5 psia, but also at 4.5 kV.

for easier comparison. The lower voltage resulted in a more uneven gain distribution but also in fewer hot spots. Due to the high voltage across thin insulating sheets, the GEM detectors are highly susceptible to arcing, and arcing events dominated the CyXESS flight and were problematic for EXOS testing and parts of the flight. CODEX did not have similar problems in laboratory testing or in flight, although the lower voltage resulted in a more uneven gain across the CODEX detectors. CODEX detectors operated at 50 V below optimal, reducing their quantum efficiency by $\sim$10%.

One detector was tested more thoroughly than the other; the best detector was placed on the shorter wavelength spectrograph to ensure a strong calibration signal from the 0 order specular reflection line. The reduced testing of the second detector was due to a bad tee connection on the y signal line that was difficult to diagnose. When the detector was fixed, three days before deployment to the White Sands Missile Range, there was insufficient time to do more than start with the first detector's optimization as a baseline and optimize from there.

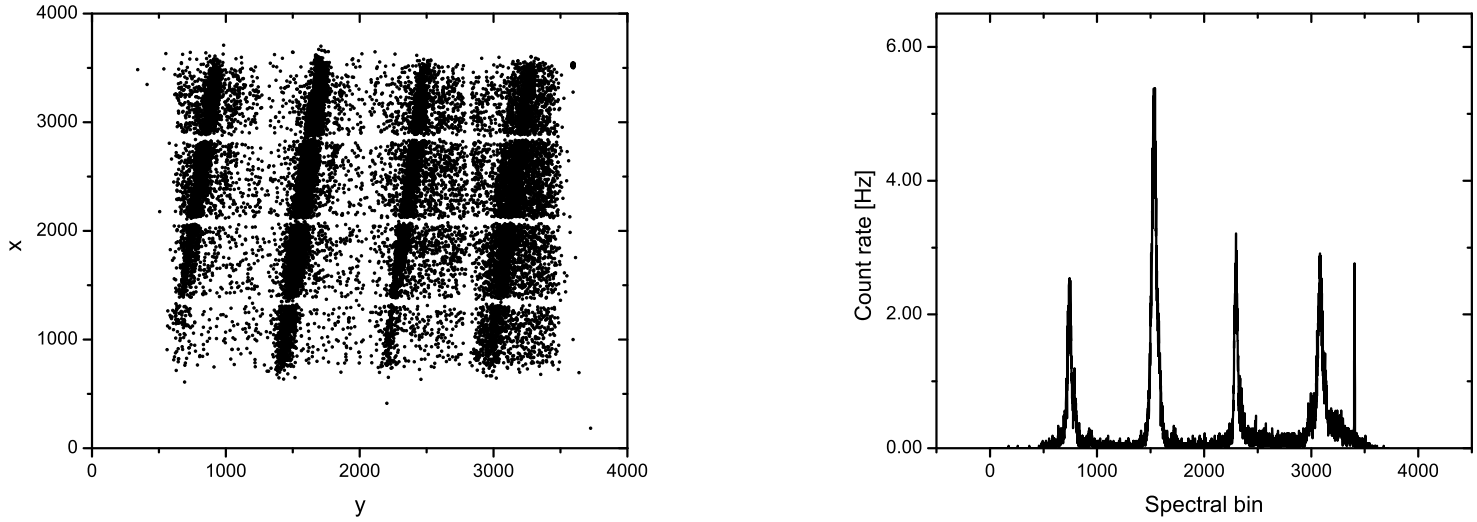

Figure 2.35 Optimal image (*left*) and spectrum (*right*) for the detector that straddled 0 order, operating at 4.25 kV. The highest peak clearly identifies 0 order, while the narrow peak on the far right is the stim pulse. The Manson x-ray source was 3.9 m from the detectors, operating at 2.0 kV and 20 μA with an aluminum anode. Exposure time was 26.8 s. The three spectral lines are the -1, $+1$, and $+2$ orders of oxygen, and the $+2$ oxygen line is broadened by the $+1$ order carbon line. A small blip can be seen to the right of every feature, as well. Since the blip is to the right side of the lines regardless of whether the line is to the left or right of 0 order, this feature is due either to slightly bent grating in the grating array or to a light path in the colimator that is not entirely blocked. Scatter around 0 order is still $<5\%$, as it was for the collimator-only tests with the diffuse source. This test was conducted with a point source, but the diffuse source is nothing more that a collection of point sources, and the scattered light in the above image shows that photons from a point source and a diffuse source pass similarly through the system. These data have not been rebinned to increase the signal to noise ratio, although the resolution allows smoothing by a factor of 18 without compromising the spectral lines. The result of $+1$ and $+2$ order oxygen lines being comparable in strength and 0 order being twice their strength contradicts the theoretical grating efficiency values used to generate Figure 2.30 and strongly suggests the need for more thorough grating calibration. The theoretical values would place $+1$ order oxygen as nearly non-existent and 0 and $+2$ orders at comparable strengths. 0 order, however, could be gaining significant flux from carbon (or possibly lower energy photons).

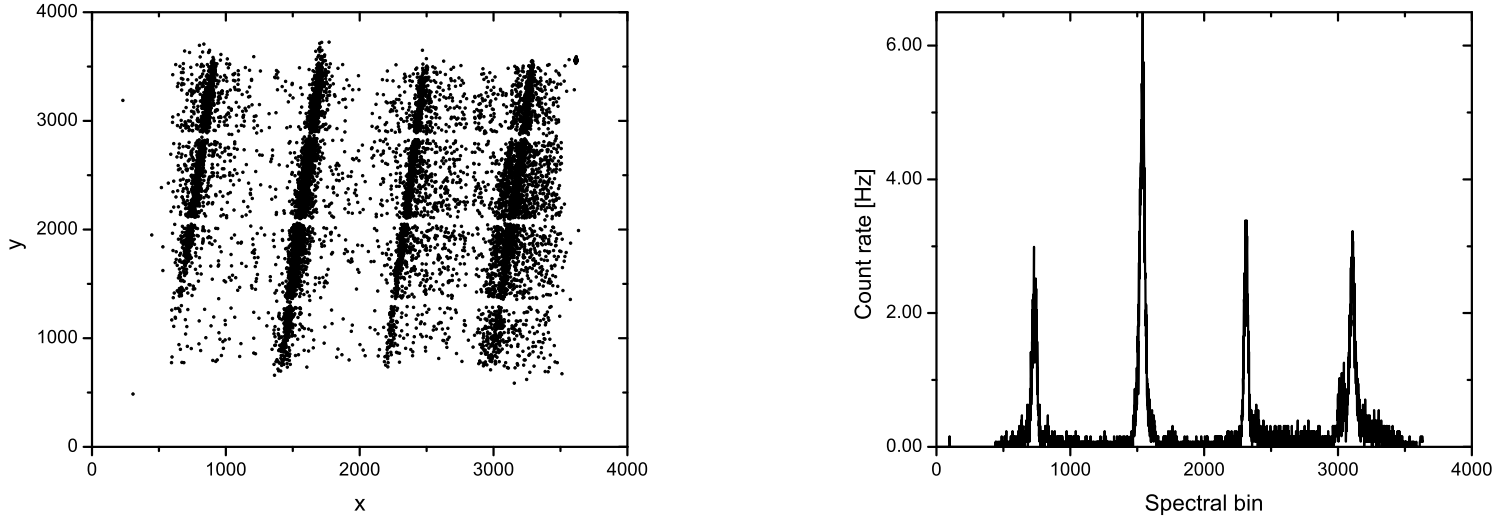

Figure 2.36 Same as Figure 2.35, but for the longer wavelength detector (still positioned over 0 order), operating at 3.90 kV. Exposure time was 12.7 s. All configurations outside of the detector were identical to those for Figure 2.35: same collimator, same gratings, same amplifiers. Any difference is due to the detectors alone, although the performance of the detectors is comparable despite their different operating parameters (13.0 psia for both, but 3.90 kV for this detector and 4.25 kV for the other).

Changing the voltage of a detector also changes the charge pulse received by the electronics, since it affects the amplitude of the electron shower (Figures 2.37 and 2.38). For a fixed pressure, a higher voltage will increase the charge signal received from each photon, because a freed electron will have a greater acceleration than in a lower-voltage detector. Interestingly, the increased voltage does not improve the low quality of the charge signal, as the increased value of the charge signal (and thus a wider separation of charge pulses of different energies) is accompanied by an increased FWHM of the charge pulse, as shown in Figure 2.38: the detector pulse height resolution, which provides a small amount of energy resolution to the detectors, does not improve with voltage.

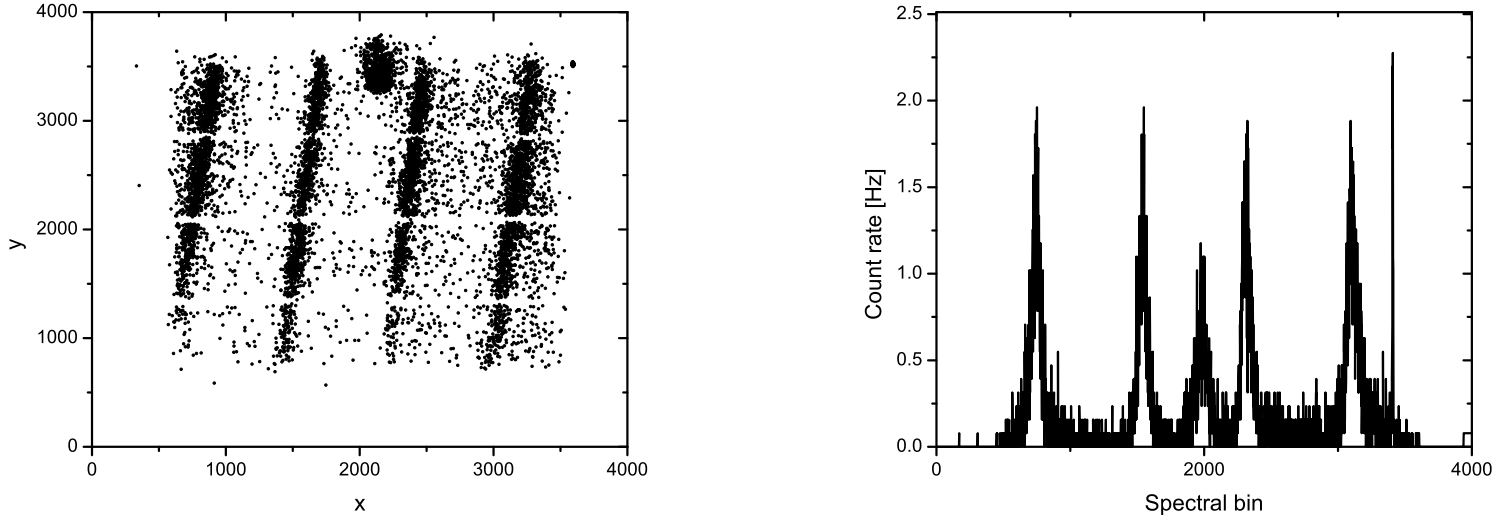

Figure 2.37 Same as Figure 2.35 and 2.36, but for the short wavelength detector operating at non-optimal conditions, with the voltage at 4.20 kV and the pressure at 13.3 psia. Note the decreased 0 order flux, and the oxygen lines that are ∼1/3 weaker. The exposure time is 12.7 s. Since no lines higher in energy than oxygen are present (readily apparent because there is no flux around 0 order), the higher pressure and lower voltage clearly reduce the longer-wavelength quantum efficiency that is coupled to 0 order. Additionally, the detector's resolution has degraded. A hot spot, visible at $(x, y) = (2100, 3500)$, shows up at spectral bin ∼2,000.

If the intrinsic GEM resolution could be improved by a factor of a few, charge resolution would provide a second dispersion axis and make CODEX (or a similar dispersive spectrograph design) into an x-ray echelle spectrograph, with dispersion along one spatial and one charge axis instead of the traditional two spatial axes. This is actually more efficient than a traditional echelle spectrograph because, in theory, there is no decrease of signal-to-noise ratio usually found by dispersing a spectrum across an additional spatial axis. The same regions of the detector are active regardless of where the incident photon will fall along the energy axis, and no noise is gained in exchange for the additional information about the signal. Coupling dispersive optics with detectors that have moderate energy resolution (position-sensitive proportional counters, GEMs or, with exquisite energy resolution, microcalorimeters) could lead the way to higher resolution x-ray spectrographs.

CODEX was optimized for count rate and not for intrinsic spectral resolution, relying on the spectrograph for energy resolution. The pulse height data was sufficient to distinguish charge from stim pulses, but the important gain was to optimize the quantum efficiency of the detector first, and use the pulse heights if such an optimization produced degenerate solutions. As shown in Figure 2.33, the solution is unique. However, optimization for a different line (oxygen was used for CODEX optimization) might yield a different result due to differing depths of penetration of the photons before initiating an electron shower.

The background levels for the two detectors are in the vicinity of $1 - 2$ Hz each across the entire (100 cm^2) active area, randomly distributed. The stims provide $12 - 14$ Hz of additional signal, but localized to corners of the detectors. By flying at lower voltages and pressures than EXOS and CyXESS, CODEX avoided much of the arcing trouble that plagued its predecessors, but the pulse height distributions were lower and the gain was less even.

An important parameter that was not tested was the stability of the high voltage power supplies, although the GEMs should be fairly insensitive to high voltage variations aside from that which comes along the y anode line to bias it to -60 V ($\sim$1.5% of operating voltage) via a split from the high voltage line. The readout electronics require the x, y, and charge pulses to all pass

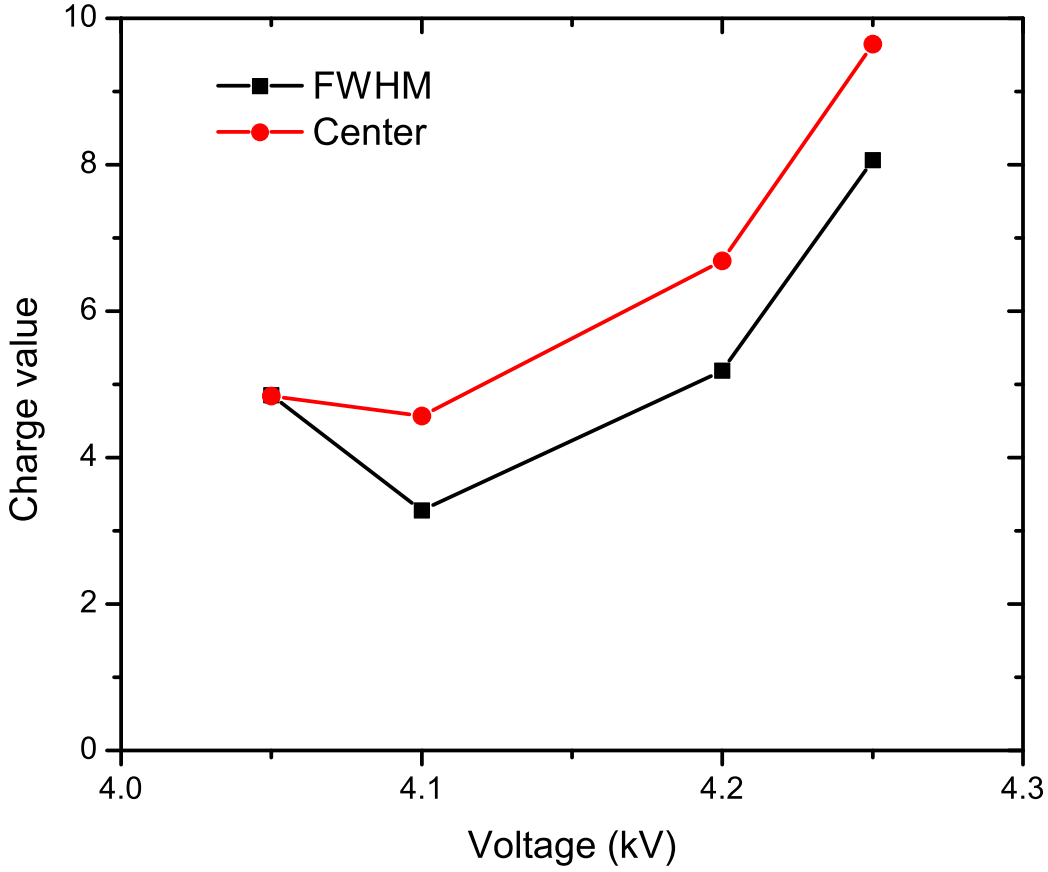

Figure 2.38 The effect of voltage on the charge pulse (raw value of the detector signal) from the +1 order oxygen line. The black line is the FWHM of the distribution of pulses received with photons from the line, while the red line is the center of the pulse, both determined by Gaussian fits to the data. Errors are $\sim 1 - 8\%$ of the reported values.

a threshold check, and the x and y lines must do it doubly because the signal is passed from each end of the anode and then compared in the TDC for a reasonable time delay between the signals. The threshholds in both time and amplitude of a signal reduce the danger of noise from the high voltage power supply masquerading as a photon. An externally generated electromagnetic signal (radio frequency noise), however, could affect all signal lines.

2.6.2 Wavelength calibration

As CODEX is a dispersive spectrograph, the dispersion of the spectrum must also be calibrated. As mentioned above regarding optimization, only one detector functioned for much of CODEX's calibration. Wavelength calibration was done with only the detector that eventually landed on the short wavelength spectrograph. The longer wavelength detector was placed on the short wavelength spectrograph for its optimization tests so that the detectors could be readily compared.

Calibrating two spectrographs with one detector requires repositioning the detector after testing, so this wavelength calibration is accurate for plate scale only and not for actual position on the detector. The second detector was placed in its spectrograph and checked for functionality only, not for thorough calibration. This is not ideal, since different time delays on the signal, either internal to the detector or along the signal lines, will lead to different positions in the digital output. It was sufficient to determine that the rocket was functioning as designed prior to flight, however. Additional calibration was to be done post-flight, if needed.

Figure 2.35 shows the wavelength calibration image for the short wavelength spectrograph. Figure 2.39 shows the wavelength calibration for the long wavelength spectrograph, using the detector from the short wavelength spectrograph because it was the only one working at the time that the testing needed to be done. The test shown in Figure 2.39 did not use the optimal detector settings (13.3 psia and 4.25 kV instead of 13.0 psia and 4.25 kV) because the additional tests were used to simultaneously check detector parameter space. The test was conducted strictly for wavelength calibration and not for spectrograph efficiency. Gain calibration was to be bootstrapped

from flight data from the better-tested detector (detectors overlap on the spectrum specifically to allow for relative calibration) and post-flight testing.

Gaussian line profiles were fit to the spectra in Figures 2.35 and 2.39 to determine the locations of each line. Table 2.3 shows the fit locations and measured FWHM. The mean FWHM for the shorter wavelength detector was 56(1) detector bins and a scale of 33.49(6) bins Å^{-1}, giving a resolution of (0.62(2) $\times$ wavelength [Å] $\times$ order), so on that detector the maximum resolution is 40.4(7). Spectra from this detector can be rebinned into spectral bins encompassing 18 detector pixels while still leaving three channels per line (16 is more convenient and used later on because of the binary pixel count of $2^{12} - 1$ in each axis).

A grating spectrograph maintains its line width (in geometric/dispersion space, not in energy). As long as the detector follows the focal plane — which the CODEX detectors do not — across its dispersion, so with a linear dispersion and a constant FWHM, the resolution increases as the spectrum progresses from 0 order. At the farthest reaches of the spectrograph (139 Å), the resolution, extrapolated from the short wavelength spectra, climbs to 90 (due to the lack of detector optimization for the tests of the long wavelength spectrograph, the numbers reported in Table 2.3 do not reflect its in-flight performance). In actual performance, that is an upper limit because the instrument defocuses farther from 0 order due to the flat detector bulkhead and the curved focal plane of the collimators.

Table 2.3 gives a tight correlation between wavelength and spectral bin of 33.1(2) bins Å^{-1} for the short wavelength spectrograph. Despite having only three easily distinguished lines (+1 order oxygen was not used) instead of five and having the considerably worse line widths (and poor centroiding of the fit as a result of blending oxygen and carbon lines), the long wavelength spectrograph has a consistent dispersion of 33.8(6) bins Å^{-1}.

Using an image generated post-flight, as it is the deepest exposure taken at 494 s and with the x-ray source turned up higher than during pre-flight tests, the spatial scale of the detector can be easily determined by comparing the observed shadows of the window bars to the physical spacing of the bars on the face of the detector, spaced at 26.63(51) mm. With the deep image in

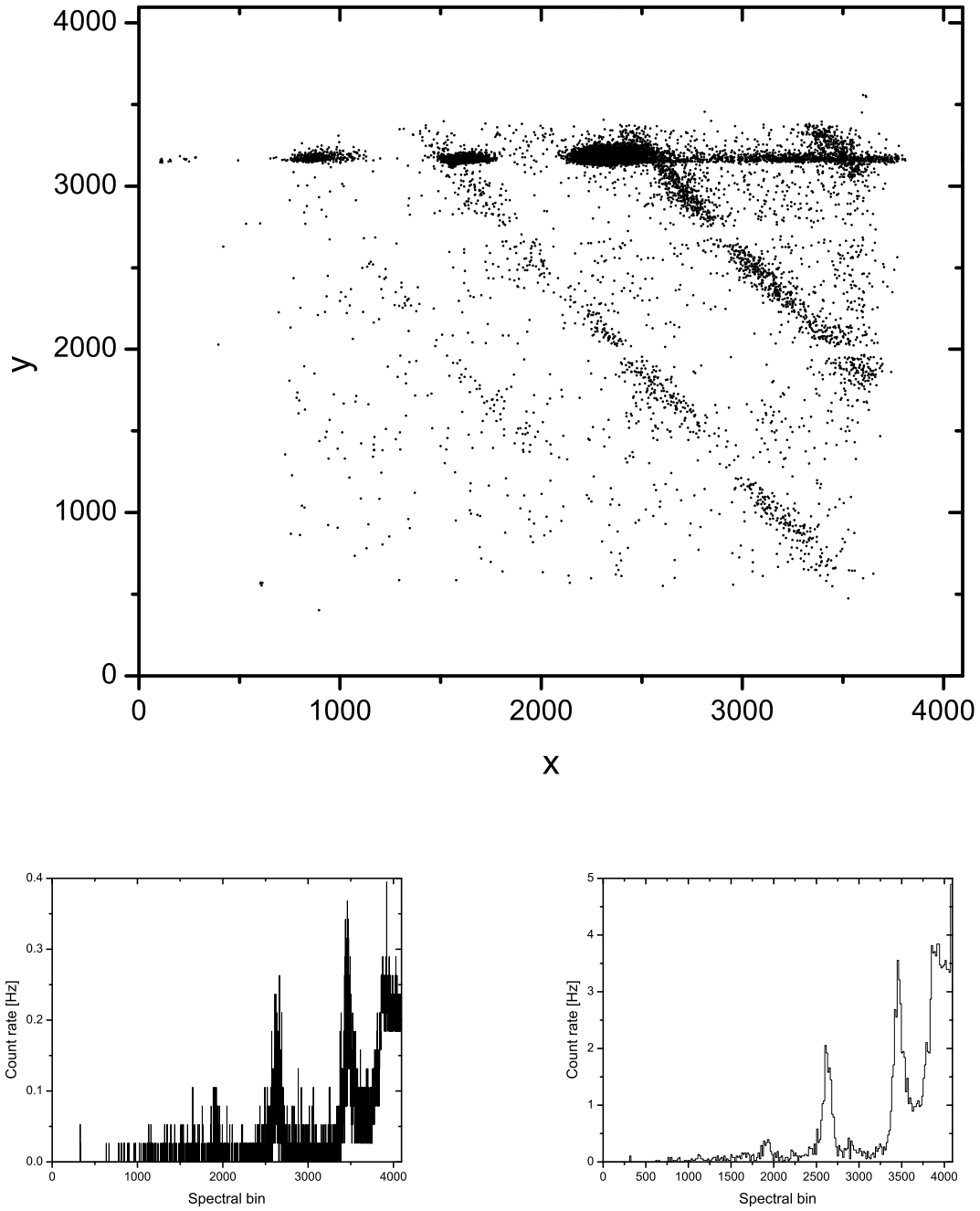

Figure 2.39 Wavelength calibration of the long wavelength spectrograph, with the short wavelength detector placed in the long wavelength spectrograph. The detector was set at 13.3 psia and 4.25 kV, and the Manson x-ray source was set at 2 kV and 0.020 mA with an aluminum anode. Top: Full detector image, unsmoothed and plotted by detector coordinates. In the top right +1 order oxygen, and cascading to the left and down are +2 order oxygen and +1 order carbon (blended), +3 order oxygen, +4 order oxygen and +2 order carbon (blended). *Bottom left*: Raw (unsmoothed) spectrum going from the top right to bottom left of the detector surface, with the spectral axis perpendicular to the lines. *Bottom right*: Same as the image at left, but rebinned with 16 detector bins per bin, placed on the same axis for reference. +5 order oxygen peaks above the noise at detector bin 1120.

Table 2.3. Wavelength calibration lines

Spectrograph	Line	Å/order	Position[a]	FWHM
Short wavelength	Oxygen	23.6/−1	743.9(5)	55.5(11)
Short wavelength	Specular reflection	All/0	1533.8(2)	61.1(5)
Short wavelength	Oxygen	23.6/+1	2298.7(3)	43.4(8)
Short wavelength	Carbon	44.7/+1	2992.7(23)	52.6(56)
Short wavelength	Oxygen	23.6/+2	3086.8(5)	69.5(13)
Long wavelength	Carbon; Oxygen blended	44.7/+1; 23.6/+2	3459(6)	125(24)
Long wavelength	Oxygen	23.6/+3	2630(2)	106(6)
Long wavelength	Carbon; Oxygen blended	44.7/+2; 23.6/+4	1921(6)	84(15)

[a]Location of spectral lines in the wavelength calibration images (Figures 2.35 and 2.39). The long wavelength spectrograph was tested with a detector operating away from its optimal parameters, hence the significantly larger FWHM, and +1 and +5 order oxygen were omitted because of their low statistical significance. Spatial units in this table are in spectral bins.

Figure 2.40, the window bar shadows become Gaussians that are easily fit, giving x and y plate scales of 28.87(6) and 29.2(4) bins mm^{-1}, respectively, consistent with a square detector response. Assuming they are in fact square, this gives a plate scale of 29.0(4) bins mm^{-1} and a a spectral plate scale of 0.87(1) Å mm^{-1} in any direction, slightly less than the Oakley (2011) calculation of 0.90 Å mm^{-1} even after including the $\sim$1% optics bench error. Higher dispersion for a fixed line width means higher resolution, so achieving less than the theoretical dispersion means that the resolution is below optimal.

2.6.3 Gain map

Figure 2.40 is also useful as a gain map for the y axis, by tracing the signal that falls in the four regions between the three window bar shadows (Figure 2.41). The gain map is not perfect, since the light is bichromatic and the gain is likely energy-dependent, and this spectrum is oxygen and carbon only. Additionally, the region $x < 1,200$ cannot be viably mapped because the line is truncated by the edge of the detector while, by eye, it is dropping in strength and making extrapolation worthless. A reasonable substitute for the first quarter can be made by borrowing the profile from the second quarter and rescaling the brighter 0 order data. Although borrowing neighboring data is onerous, the four regions (including the first quarter) display similar profiles below $y = 2,000$. After normalizing to a maximum value of one within each quarter, the $y < 2,000$ region of the second quarter was borrowed and rescaled to the first quarter such that the full profile of the first quarter had a continuous (no sudden drop) gain profile. A very similar result can be obtained by simply scaling up the data from the $y < 2,000$ region of the first quarter to account for what is lost at the edge of the detector. The image carries no value for relative scaling in the x direction, aside from the symmetry of $+1/-1$ orders of oxygen, and these were consistent with a uniform gain along the x axis. Window bar shadows were added in the positions determined during plate scale calculations, as inverted Gaussian features of unit amplitude.

The map made by this method is shown in Figure 2.41, smoothed by a factor of 16 to reduce noise from pixilation. The map shows that the gain is far from uniform, dropping by a factor of

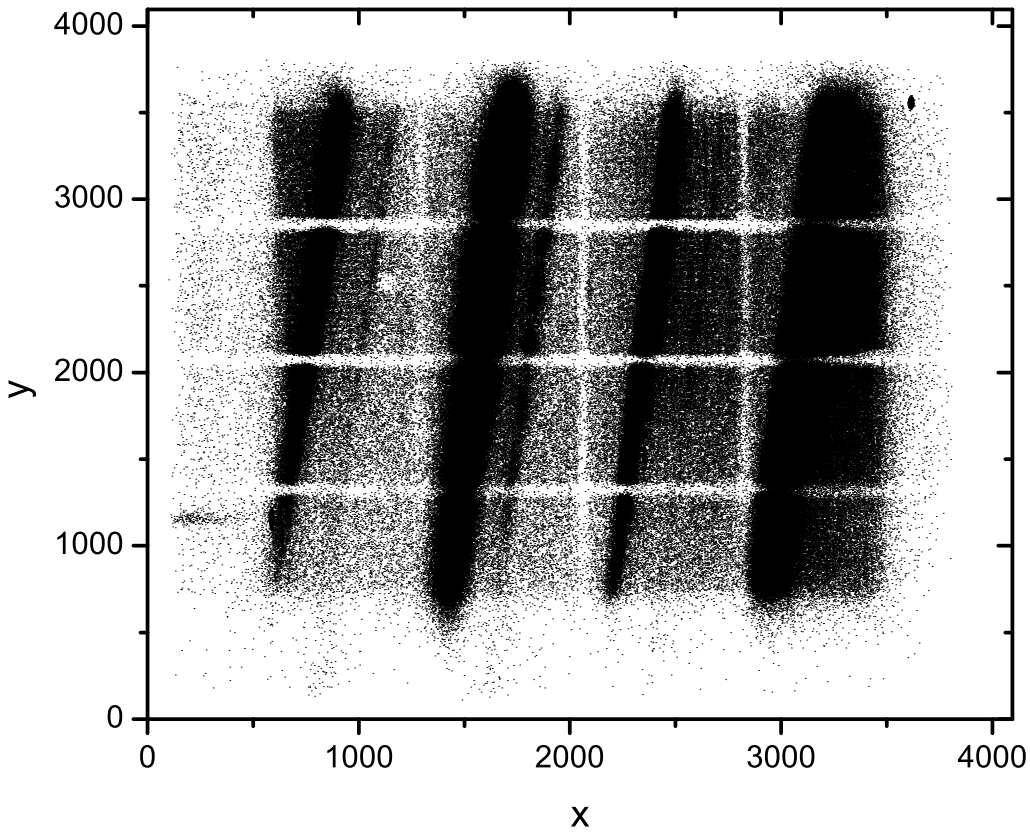

Figure 2.40 Short wavelength detector, run for 497.258 s in front of a magnesium anode in the Manson x-ray source, which was operating at 1.00 kV and 0.10 mA and placed 3.9 m from the detector. In this image, one can see the window bar shadows in both x and y dimensions, as well as the fine support grid between the window bars. The faint line duplicated to the right of the -1, 0, and $+1$ oxygen lines is a glitch in the gratings, causing some light to be uniformly reflected to the right of each order (a spectral order would place it on the same side relative to 0 order, and it would not exist near the 0 order feature at $x \approx 1500$). There are nearly 1.5 million counts in this image; the erroneous reflection represent $\ll 1\%$ of the signal. The carbon line is much more pronounced on this magnesium anode than on the aluminum one used for most calibration; carbon is a surface contaminant on the anode itself, usually due to running the Manson source at <0.5 W, which allows surface contamination to build up. The contamination can be cured with sandpaper, but in this particular case the contamination is beneficial, as it provides an additional line and a signal. The oxygen line is also technically a contaminant, but preventing a magnesium oxide coating from forming on the surface is not feasible. Full-system scattered light in this image is $2.5 - 5\%$, depending treatment of the bright regions near spectral lines.

100 across some vertical regions of the gain map. Normalized to a peak value of unity, the map has a median and a mean value of 0.44. Since this is a relative normalization, that number means that >56% of all photons that enter the detector are lost, as a lower limit. CyXESS and EXOS gain maps were flatter due to higher operating voltages and pressures. The gain map conveniently kills noise beyond the active area of the detector.

Although the method described above is a reasonable approximation of the detector's performance, a better gain map could be made (but was not) by illuminating the entire detector. This is readily done by removing the optics or putting the source between the optics and the detectors, although the Manson source produces too high of a count rate for the electronics to handle with only a short separation. Without restrictions placed by time and budgets, the proper way to build a gain map is to fully illuminate the detector with a variable monochromatic light source, stepping between energies to build a 3-dimensional (x, y, energy) gain map, complete with pulse height data for every position and energy.

2.6.4 Pulse height distribution

In addition to the "mechanical" resolution of the spectrograph, the intrinsic energy resolution of the detectors was also considered, although not heavily weighted, when optimizing the detectors. An incident photon frees a number of electrons proportional to its energy, and thus the charge pulse received by the anode varies in height according to the incident photon's energy.

Resolution in the pulse height dimension is too poor for the detector energy resolution to notably improve the resolution of the CODEX spectrographs, but the charge signal can only realistically be used to differentiate between confused lines of different orders of diffraction from photons with energies differing by factors of a few (Oakley 2011). A comparison of the pulse height distributions (PHDs), the variations in the charge measured on the anode that are the source of the GEM's energy resolution, is shown below in Figures 2.42, 2.43, and 2.44.

.

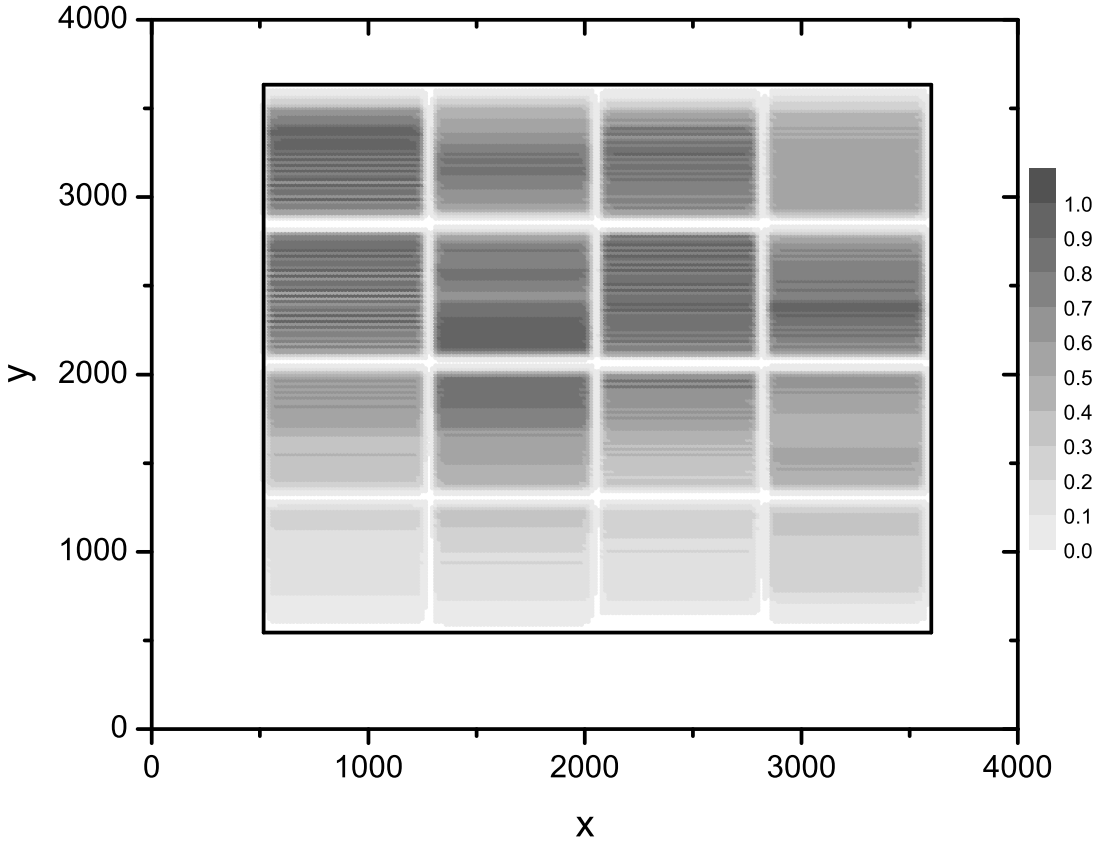

Figure 2.41 Gain map for the short wavelength detector on the CODEX payload, generated from Figure 2.40. The gain map scale is given by the color bar, with a maximum value of unity by virtue of normalization. The black rectangle is the nominal active area of the detector. The map was constructed with nearly monochromatic (oxygen K-line) light.

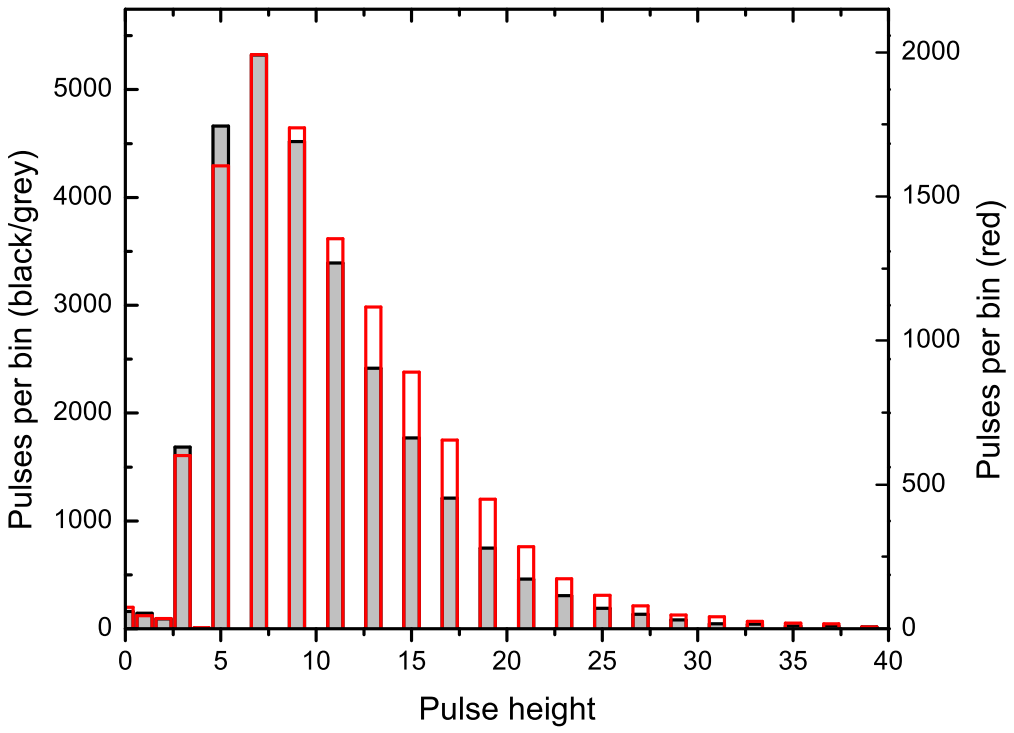

Figure 2.42 Comparison of the pulse height distributions from the data sets collected for Figures 2.35 and 2.36. Pulse height is given as a raw, unscaled detector output. The two detectors compare favorably. When normalized to the peak intensity (approximately scaling for different exposure times and slightly differing quantum efficiencies), one can see that the detector destined for the long wavelength spectrograph (red) produces pulses with slightly higher energies than the short wavelength one (black). Detector testing was insufficiently comprehensive to determine if this difference should be interpreted as a differing quantum efficiency or just a differing description of the same photon population. The strictly odd binning is due to the detector identification bit that occupies the least significant bit of the charge information.

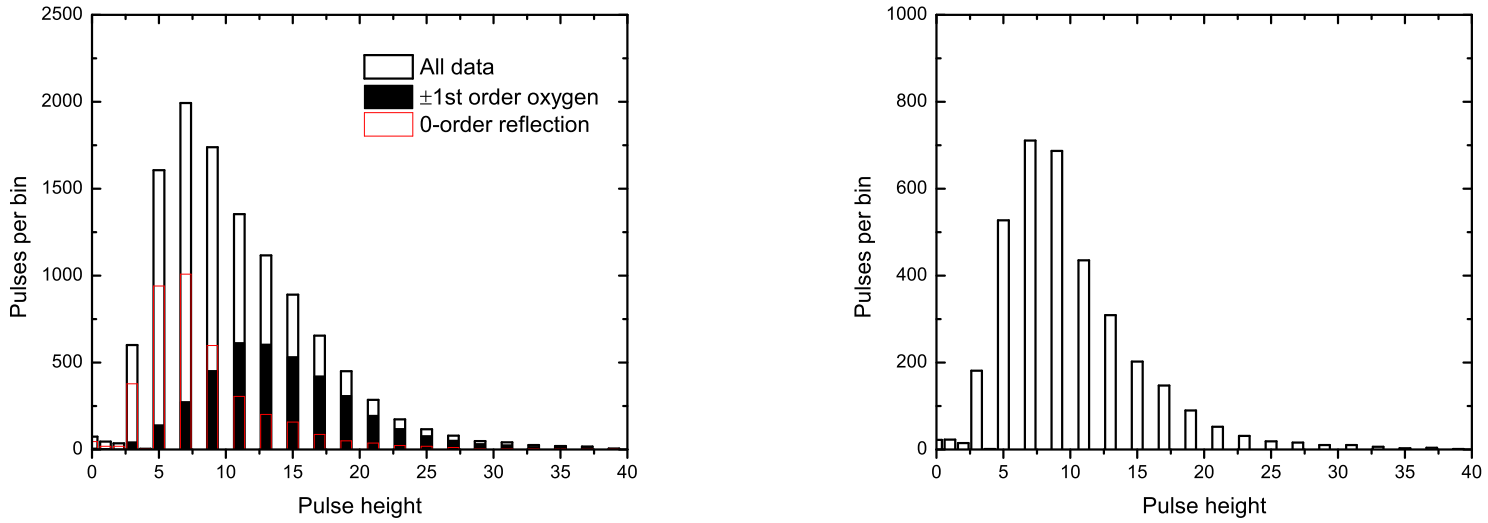

Figure 2.43 Three regions of the longer-wavelength detector's PHD (from the image in Figure 2.36). *Left*: A comparison of the 0 order specular reflection, the combined PHDs of the ±1 order oxygen lines, and the PHD of the entire image. Bars are absolute and not stacked. Although comparison of the three spectra shown in Figures 2.36 and 2.37 clearly indicates that the detector is picking up low-energy photons, perhaps even far-UV, the PHD provides a very clear confirmation of this with its skewing of the 0 order reflection far to the low-energy side of the oxygen line that is dominant in the detector's spectrum. *Right*: The PHD of just the slightly-blended +2 order oxygen and +1 order carbon lines. The carbon line skews the PHD toward the low-energy end of the spectrum, peaking at bin 7 rather than $12 - 13$ for the +1 order oxygen PHD.

2.6.5 Directional field of view tests

Proper testing of the full system (as with just the collimators) should include tests with a partially-blocked aperture; these test were not conducted due to limitations placed by the launch schedule. Restricting photons not just to a location but to an angle of incidence would measure the contribution of different angles to a spectrum. The central graze angle of the gratings is 4.4°, but lower-energy photons can reflect at a greater angle and higher-energy photons will be much more efficiently reflected at a lower angle. Since CODEX does not have any focusing optics, the position of detection has no bearing on the angle of incidence of the photon (equivalent to saying that the spectrograph cannot distinguish between an on-axis and an off-axis source in the field of view by x and y positions alone). Although this can be modeled with a ray trace, design and assembly tolerancing mandates empirical testing for proper calibration of the instrument.

2.6.6 Integration

CODEX was only the payload of sounding rocket flight 36.274, and it had to be attached to the many components (motors, guidance, recovery) supplied by NASA's Wallops Flight Facility (Figure 2.45).

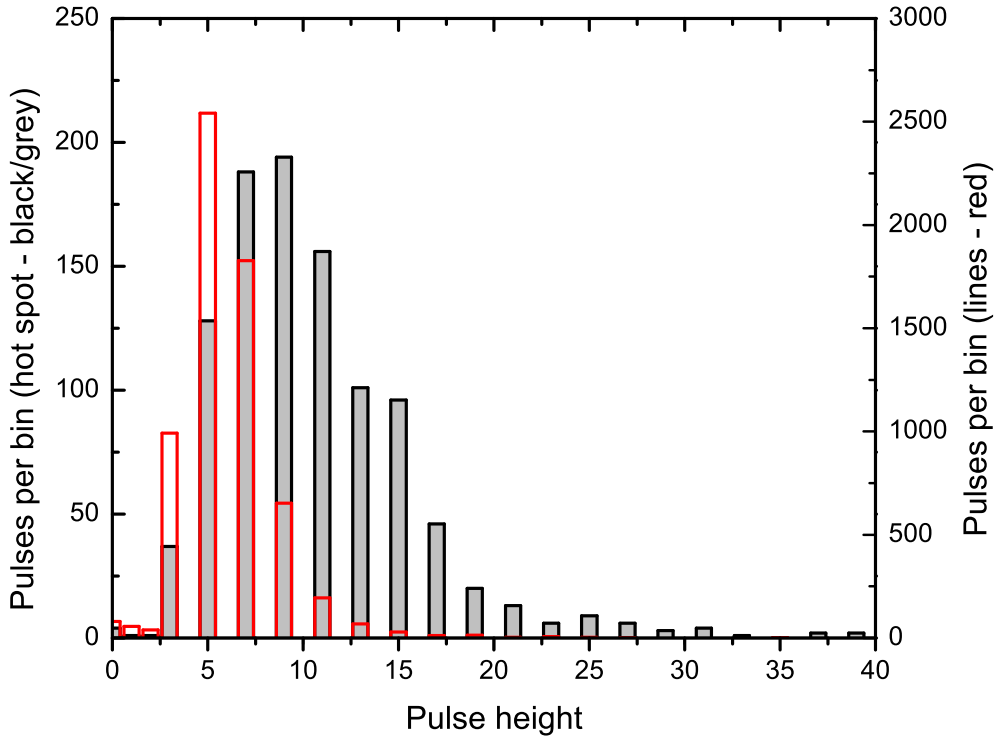

Figure 2.44 A comparison PHD of the hot spot in the 13.3 psia detector image in Figure 2.37 to the spectral lines in it. The oxygen spectral lines (red) can be easily distinguished from the higher-energy hot spot, although there is enough overlap that the PHD information is not enough to provide sound statistics if data genuinely overlap. Adding 0.3 psi to the operating pressure of the detector has decreased the gain of the +1 order oxygen line by a factor of ∼2.

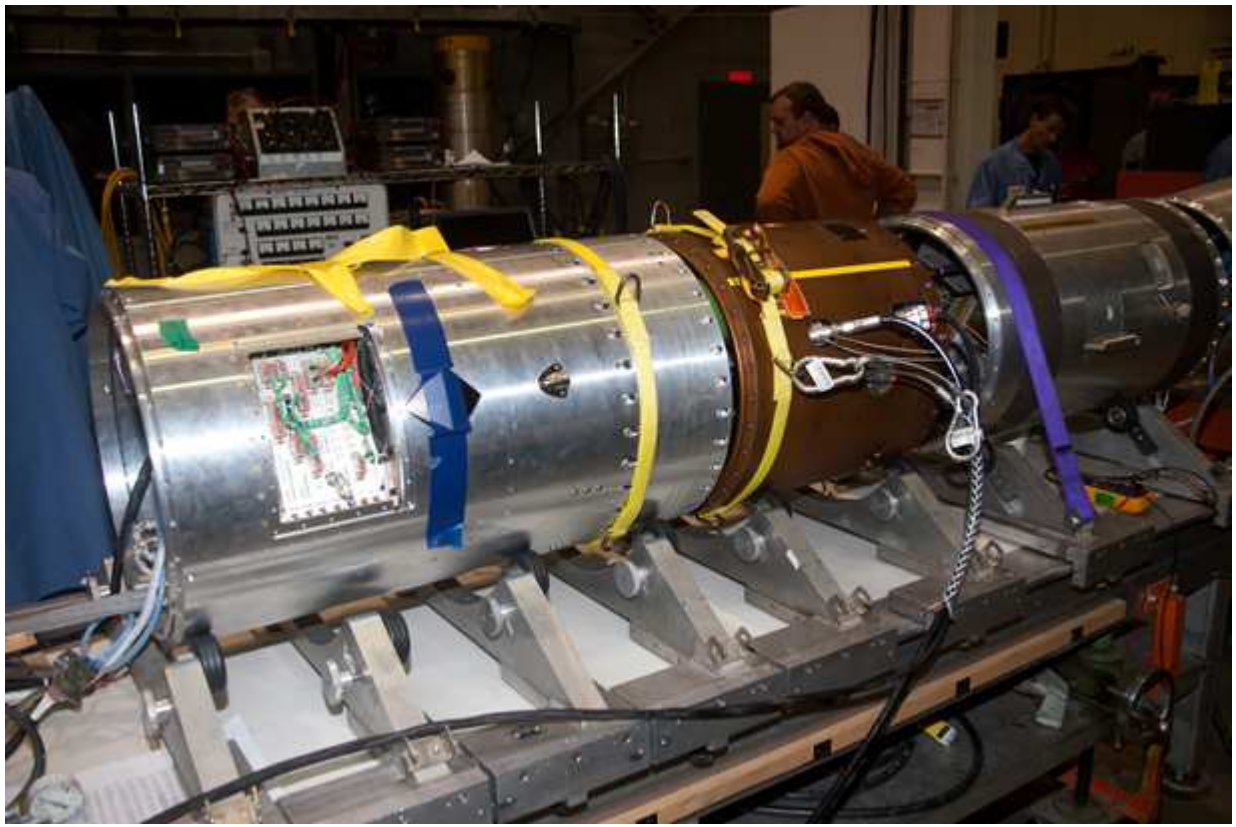

Figure 2.45 Integration with NASA's sections of the rocket. The electronics section of the payload is just entering at image right, with the telemetry, S-19L guidance system, and ACS sections laid out above it. The ACS gas bottles, ORSA recovery (parachute) system, and nose cone lie off-camera to image left.

After construction and testing at the University of Colorado, we carried it in a U-haul truck to the White Sands Missile range for integration with the rest of the rocket, final testing, and launch. Preflight tests included numerous simulations of launch countdowns, manual triggering of pressure switches and timers, and checks of data passing through the system. Vibration testing again revealed harmonic modes in the sheer panels of the collimators, which emitted an unnerving whine but no damage. The panels had already debuted this symphony in earlier shake tests of just the collimators. The payload's weight, bending, and moments of inertia were tested, and no mechanical troubles were found.

We were able to identify several flaws during the first few days at White Sands, once the rush of trying to resolve all of the show-stopping troubles had subsided. One was a leak in one of our detector windows, which kept the payload pressure high enough that tests under vacuum hovered on the edge of damaging coronal discharges. We covered each of its 26.5 mm square window supports with Kapton® tape. The tape bulged in sections where there was a leak, and a quick dose of ethanol on the window identified the leak location. In two sections the ethanol bubbled, and in one a geyser shot more than 30 cm into the air. All of the holes were patched with arathane, creating small dark regions in the detector but affecting less than 1% of the active area of the window.

A second problem was only partially solved. During one of the countdown simulations, an AC power line from the wall outlet to telemetry computers crossed the lines from our ground system electronics (GSE). The line provides control over payload functions (turn on detectors, monitor payload and detector pressures, etc.) but does not directly interact with signal lines, nor does it pass the signal from the payload to the observer. The crossed lines are noteworthy because a signal was seen in the telemetered data. A series of four discrete points appeared along the $x = y$ line. Noise on the power and control lines, not actually interacting with the signal except through power to the signal processing electronics and through the common chassis ground, produced a signal. If a signal generated in the power lines could lead to a data signal, then noise from the NASA electronics (or our own) could lead to spurious signals, and a random noise rather than a regular

AC pulse might swamp the detector with continuum noise. However, the electronics section of the payload and the Wallops-supplied telemetry and other electronics were nearly identical to what flew on CyXESS and EXOS, as well as University of Colorado payloads for the past two and a half decades. None of these payloads reported issues with noise pickup from the power lines (an AC wall outlet has a very strong signal relative to the power lines in the rocket), so this was deemed an anomalous situation that should be remembered but not worrisome enough to delay the launch. The problem was quickly and superficially solved: the lines were un-crossed.

A third issue came when testing with a ^{55}Fe source. Testing to ensure that a signal was being passed properly from the detectors through our electronics and through Wallops's telemetry system, the radioactive iron was placed in front of the long wavelength detector. After the full countdown sequence, the detectors turned on and saw nothing. Of the two detectors, the long wavelength one is the more difficult to access after complete assembly, and with the payload mostly sealed, it was difficult to tell if the source was positioned properly for the detector. In a second attempt, the ^{55}Fe source was placed in front of the short wavelength detector, and the signal passed through perfectly (Wallops flips x and y relative to laboratory tests, but that is a trivial change in the software used for data processing). I should have tried again to place the source in front of the other detector to verify that it was working properly, but at the time the test was only to pass data. I did not recheck the long wavelength detector, and that detector did not work in flight. The problem might have been caught pre-flight, although we would have opted to launch with a single detector rather than slip for a year to figure out and repair the problem (which was likely fused GEM plates, which would require a month lead time from SciEnergy in Japan) and adequately test the solution, with a launch window that would close in mid-March. The exact possibility of launching with only one detector was discussed a week prior to delivering the payload to White Sands, when CODEX still only had one working detector.

The last notable event from the integration was a launch delay of a week. The payload was loaded onto the rail roughly a week before the scheduled launch (Figure 2.46), then on the scheduled launch date the forecast for the wind turned forbidding. The launch was delayed, and

the payload had to sit on its launch rail for another week, sheltered by a rolling garage with a controlled temperature. A day before the actual launch date, we once again tested the ^{55}Fe source, but again in front of the more convenient detector. This might have been another chance to catch the faulty detector, if it had indeed failed prior to flight.

Figure 2.46 Full configuration for sounding rocket flight 36.274, carrying the CODEX payload, on the launch rail at the White Sands Missile Range. CODEX is housed in the thicker skin toward the nose of the rocket.

2.7 Flight plan

Although not traditionally part of the design of the hardware, the flight plan is a part of the design of the experiment. Sounding rockets get roughly 300 s of flight time above 150 km, where the atmosphere is thin enough to transmit x-rays. CyXESS and EXOS both targeted the Cygnus Loop for the duration of their flights, and the former flight was swamped with discharge noise while the latter detected a strong continuum signal. Disentangling a continuum from noise is difficult, relying on features from the detector window and the (very low resolution) pulse height information from the detectors. CODEX sacrificed ∼40% of its flight time to ensure that the continuum was real: it switched between the Vela SNR (one of the brightest soft x-ray sources in the sky) to a region 5° N of the Vela pointing, a region where the only emission is from the soft x-ray background, a factor of ∼50 below the Vela SNR's 1/4 keV flux.

The CODEX flight plan could be changed on the fly by the Command Uplink System (CUS), providing real-time control of the attitude control system (ACS). Real-time readout of the data onto on oscilloscope (voltage along two channels corresponding to x and y coordinates) as well as numerical count rate data allowed for evaluation of in-flight performance. There was no cure for an unexpectedly low count rate, as the ballistic trajectory of the payload does not allow for an increased flight time. A high count rate could indicate problems with the detectors, specifically arcing internal to the detectors or across the front of the detectors, both of which were experienced in the EXOS and CyXESS flights. The payload had two sets of flight plans, one for basic acquisition of data if the CUS failed, and one for the optimal case.

The optimal case called for a quick targeting of the dark target to confirm that the detectors had a low background. After 25 s, CODEX would slew onto the Vela SNR and watch the count rate climb. The 0 order line should be brilliant in either a line or a continuum emission scenario. Moving off-target again after 100 s on the SNR would show the count rate to drop to background levels, then climb again when CODEX returned to the SNR after another 25 s on the dark sky. The nominal times are listed in Table 2.4. Times were chosen to ensure that the background value

Table 2.4. Targeting cadence

Target	Time [s][a]	Expected count rate [Hz][b]
Dark sky (08h41m40s, $-39°00'00''$, 90° roll angle)	25.0	$0-1$
Vela SNR (08h41m40s, $-44°08'00''$, 0° roll angle	100.0	10-50
Dark sky	25.0	$0-1$
Vela SNR	70.8	10-50
True dark (shutter door closed)	2.0	0

[a]Times do not sum to the full flight time because of the 30 s overhead per slew.

[b] Expected count rates do not include the ∼14 Hz detector stim rates.

would be statistically significant from the expected signal value. The estimates were conservative because the slew time of the telescope is ∼30 seconds, yet most of that is in the settling time of the telescope, so for targets significantly larger than the field of view (the telescope could be off by $>20'$ without affecting the expected signal by more than 10%), the slew time is only a few seconds and it could be reasonably considered "on target" least 20 seconds before the star tracker considers itself to have arrived at the target. Pointing was manually controlled by the CUS, so times were variable based on performance. The nominal plan has a large fraction of time near the apex of the flight devoted to slewing to and dwelling on the dark target (Figure 2.47). While the apex offers the best observing conditions, the upleg and downleg provide variable optical depths through the atmosphere, providing yet another check that any received signal was astronomical in nature, and the 30 s overhead per slew prevents rapid switching of targets.

If the detectors turned on with a high background (arcing can produce count rates of >1 kHz, two orders of magnitude above the expected count rate on the dark sky), CODEX would stay on the dark sky longer, until the detectors calmed down. The remaining schedule would be compressed accordingly.

A contingency flight plan assumed that two major failures occurred (both of the two correctable failures that would affect desirable targeting):

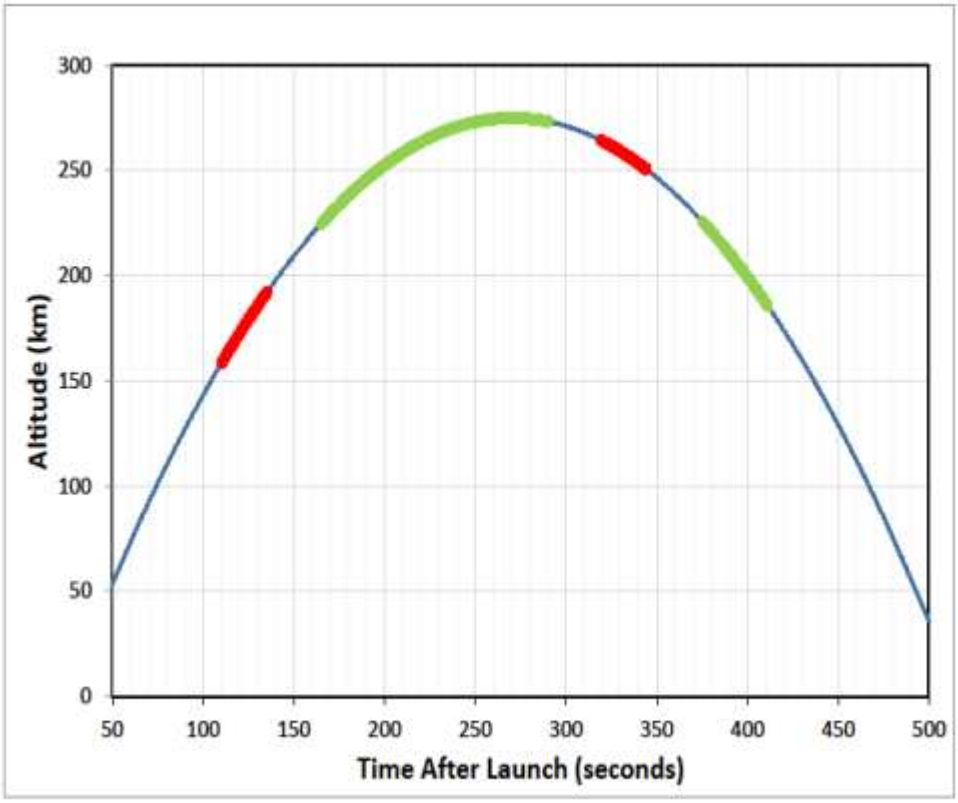

Figure 2.47 Plot of the expected targeting cadence versus time and altitude. Red is the dark target; green is the Vela SNR. See Table 2.4 for precise times. Image credit: C. Murphy, NASA/WFF.

(1) The CUS failed, preventing real-time control of the rocket. Since targeting relied on commands sent to the rocket from the ground station, a failure of the CUS would mean, without a backup system, that the rocket would stay on its first target the entire time. The first target was the dark sky.

(2) The detectors misbehaved. GEM detectors that have a historical record of arcing events, usually close to the turn-on of the detectors. If the flight plan included only a quick targeting of the dark sky before moving to the Vela SNR, CODEX might be swamped with noise from detector arcs and effectively lose all off-target data.

The backup plan was a timer-based system that would keep the telescope on the dark target for 125 s to give the detectors a chance to settle down in case of arcing, then move to the Vela SNR and sit there for the remainder of the flight. The scientific data would lose some of its elegance since the Vela SNR observations would not be neatly alternated with dark sky images, but the plan would allow for scientific success of the mission even with significant hardware failures. Since the backup system was timer-based, dwelling on the dark sky for 125 s (in the case of high detector noise, where a CUS signal was not sent to move to the SNR), the timers would kick in and require the payload to move to the SNR. They could be overridden by a CUS command, although there were no foreseeable circumstances under which we would have overridden the timers because, at that point, only half of the flight would remain to observe the SNR.

A schedule of the important non-targeting events during the CODEX flight is listed in Table 2.5.

Table 2.5. Important events of the 36.274 launch

Event	Time [s]	Nominal/2σ low altitude [km]	Velocity [m/s]
Launch	0.0	0.0/0.0	0.0
Rail exit	0.6	0.0/0.0	43.2
Black Brant ignition	12.0	3.0/3.0	573.6
Black Brant burnout	45.9	6.0/5.9	2079.7
Low voltage power on	47.0	45.0/44.2	2068.6
Despin	62.0	77.1/75.4	1923.1
Shutter door open	80.0	110.0/107.4	1752.5
High voltage on (detectors)	104.5	149.9/146.0	1523.3
150 km upleg	104.5	150.0/146.0	1523.3
150 km upleg (2σ low)	107.2	...[a]/150.0	...
1st target acquisition	110.0	158.1/153.9	1472.3
Apogee	270.7	274.9/262.0	165.7
Shutter door close	421.6	.../150.0	...
150 km downleg (2σ low)	421.6	.../150.0	...
150 km downleg	436.8	150.0/127.1	1523.3
Power off	466.0	101.7/77.0	1796.9
Parachute deploy	606.5	4.9/...	92.5
Impact	912.6	0.0/0.0	8.5

[a]Ellipses denote values that were not reported by NASA.

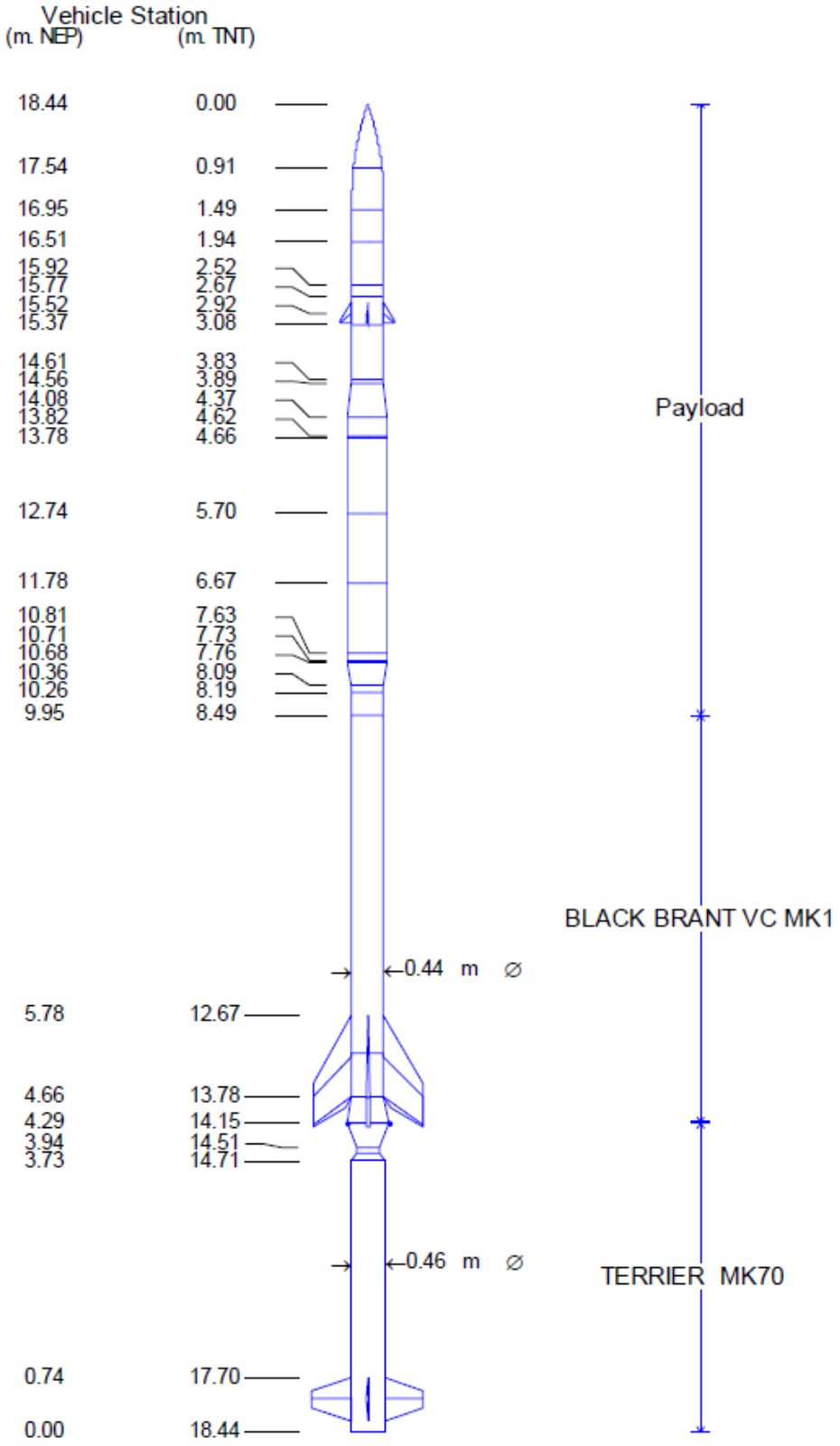

Figure 2.48 Station heights in inches of the 36.274 rocket, measured from the tip of the nose cone. CODEX was the longest payload ever flown by NASA with the Black Brant IX rocket configuration.

Figure 2.49 10 Dec 2011, CODEX took flight.

Chapter 3

Launch

We can lick gravity, but sometimes the paperwork is overwhelming.

-- W. von Braun[1]

After a week's weather delay, CODEX launched from the White Sands Missile Range (WSMR) at 04:00 local time (GMT +07:00) on 10 December 2011. The only apparent hitch during the flight was a failure of the star tracker to acquire its target on the Vela SNR. It was successful with its target acquisition on the dark target, which was the first and third target, allowing the star tracker to update the attitude and control system (ACS) software for precise control by gyroscopes. Post-flight analysis of the star tracker video feed by Wallops Flight Facility ACS personnel indicated that the payload pointed within $20''$ of the nominal SNR target, and the SNR and CODEX field of view are both large enough that targeting was not an issue. The gyroscope pointing data are shown in Figure 3.1. The Anomaly Investigation Board later determined that the failure to acquire the target was due to an improved star tracker CCD that increased the sensitivity but had issues with bleeding, resulting in most of the stars of magnitude 4 to 8 — which are the only ones considered by the star tracker software — being unusable for determining pointing.

Count rates on the SNR were $\sim$30 Hz initially, and slowly climbing to the $40-50$ Hz range — close to the lower end of the expected $50-100$ Hz range. We did not have a way of distinguishing

[1] Launius (2003)

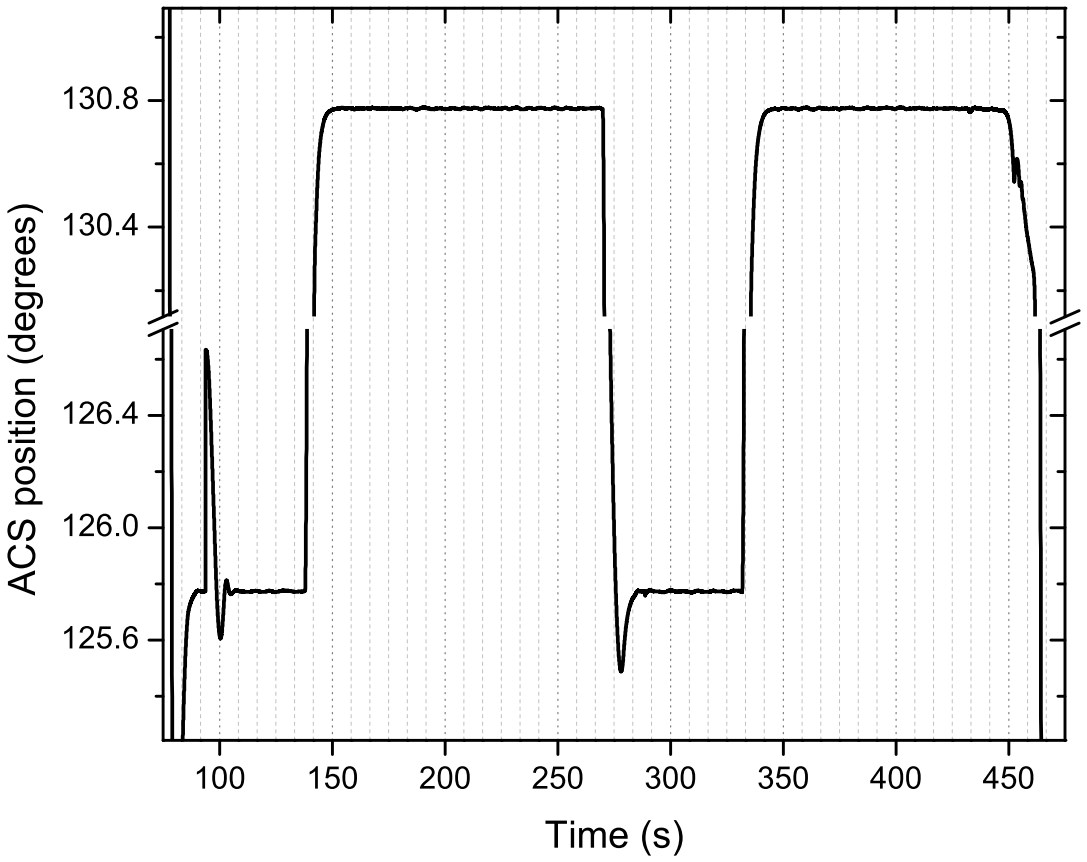

Figure 3.1 ACS pointing according to the on-board gyroscopes (not the star tracker) showing the rate of target acquisition. The four pointings of the payload are identifiable by the plateaus, with the high one being the Vela SNR and the low one being the dark region; the y axis scaling is correct, but its origin is arbitrary as far as the experiment is concerned. Within the resolution of CODEX, it takes 15 s to arrive on target, although the fine guidance of the rocket does not actually settle until about 30 s after the repointing begins.

the two detectors in real time aside from the rotation of spectral lines; both the count rate monitor and an oscilloscope set to display real-time data of the detector images summed both detectors. There were two apparent problems:

(1) The count rate from the detectors did not change appreciably when CODEX was pointed off-target rather than at the Vela SNR. After subtracting the $14 - 16$ Hz background and stim rate, the count rates should have differed by a factor of 50 (including the stim counts, the count rate should have changed from $\sim$15 to $50 - 100$).

(2) Specular reflection (0 order light) should have produced a strong signal, and one stronger than any other spectral line. Although gain variations on the detectors created the appearance of a line, there was no clear 0 order signal or other spectral lines.

Both of these dampened enthusiasm on launch night, but there was some hope that a signal could yet be pulled from the noise.

An additional problem was discovered when we recovered the payload the next morning: the payload had acquired a kink of $\sim 1.2^\circ$ at some point before coming to its final rest (Figure 3.2). If it happened on the way up, the kink would have affected the optical alignment and might explain the lack of counts, but the most jarring impact happens on landing. It landed in soft mud that made no impact on its crush bumper, and the kink was on the wrong side of the payload to have happened due to landing, but at no other point should it have been impacted with enough force to bend the skin. The bent skin was overmachined by the Wallops machine shop, missing 0.040 inches in thickness from the 0.125 inch standard, but it had passed all pre-flight tests. Regardless of when it happened, it could affect alignment during post-flight calibration. Fortuitously, the kink affected alignment perpendicular to the dispersion axis, minimizing its effect. (Pre-flight and post-flight spectra showed no discernible difference.)

Figure 3.2 CODEX, after its return to the University of Colorado, displaying the kink it acquired on launch night. The horizontal red line is aligned with the top of the left section of the payload; the horizontal white line is aligned with the top of the right section; and the vertical black line marks the kink. The collimator and the gratings lie in the left third of the visible payload, while the optics bench comprises the right two-thirds with the detectors on the right edge of the photograph. The relative angle of the optics and the detectors — due to the kink — is 1.2°, corresponding to a shift of the detectors of 4 cm perpendicular to the dispersion of the spectrograph (along the *unfocused* direction of the spectrum, where the spectral lines are long). The internal optics are not directly connected to the external skin, and the actual shift is under 2 cm. Due to the coarse nature of the spectrograph, however, we could not accurately measure the internal shift. For future payloads, a mirror placed on the detector bulkhead would have allowed for such a measurement using a theodolite. There is no good explanation of the cause of the kink.

Figure 3.3 What goes up must come down, but it doesn't always look the same when it gets back. The Black Brant sustainer section is not designed to be recoverable, but it hit in soft mud and demonstrated why lawn darts are now illegal.

Chapter 4

Data analysis

``In cases of major discrepancy it's always reality that's got it wrong.''

-- Douglas Adams, The Hitchhiker's Guide to the Galaxy

4.1 Arc

CODEX telemetered down 182,244 counts. The data, with only the requisite image processing of converting parallel bits into detector position values and swapping the x and y dimensions to make the NASA format match laboratory testing axes, are shown in Figure 4.1. Several things are immediately notable in the raw data:

(1) Window bars are very apparent, meaning that the dominant signal came from outside of the detectors rather than from internal electronics noise. This is good.

(2) Both stims show up on the shorter wavelength detector; only one stim shows very weakly on the longer wavelength detector. The electronics are configured such that each should have one pulse and one pulse only, but in practice $90 - 100\%$ of the stim bleeds from the longer wavelength detector to the shorter one. Detector identification is made by the least significant bit of the charge pulse data, so the bleeding implies either an unstable bit or that the stim signal is correlated with noise from both detector lines, so that a charge pulse arrives from both detectors. In general, this does not imply a problem because, although

the stim bleed rate is >90%, the data bleed rate was <10% in laboratory tests. The 10% bleed rate is significantly more than ideal, but it is tolerable. Post-flight testing identified a faulty amplifier as the culprit of the cross-talk. The reason the stim would bleed at a different rate from the data is unclear, but the pulse profiles of the data and the stim differ significantly and the explanation might lie therein.

(3) The active area extends in a ghostly fashion to nearly the limits of the detector readout. The ghostly image includes the shadows of the window bars, indicating that they are real counts that came from outside of the detector but were aliased vertically or horizontally. They were not actually detected in this region, since the anode only extends underneath the darkest 4×4 region. This is bad and indicative of a garbled signal in the electronics, but at first glance it is a relatively small fraction of the counts in most parts of the detector. Aliasing has been witnessed in the laboratory, but only with extreme count rates from the 6 keV ^{55}Fe source.

(4) There are common features on both detectors, such as the hot spot at $(x, y = 2250, 2250)$ and the signal decrement in the upper left corner. Since these features are unlikely to occur identically on both detectors, they are a strong indication that many counts bled from one detector to the other. An additional note about the hot spot: when $x = y$, there is a decent chance that it is generated by radio-frequency (RF) noise picked up on the signal lines.

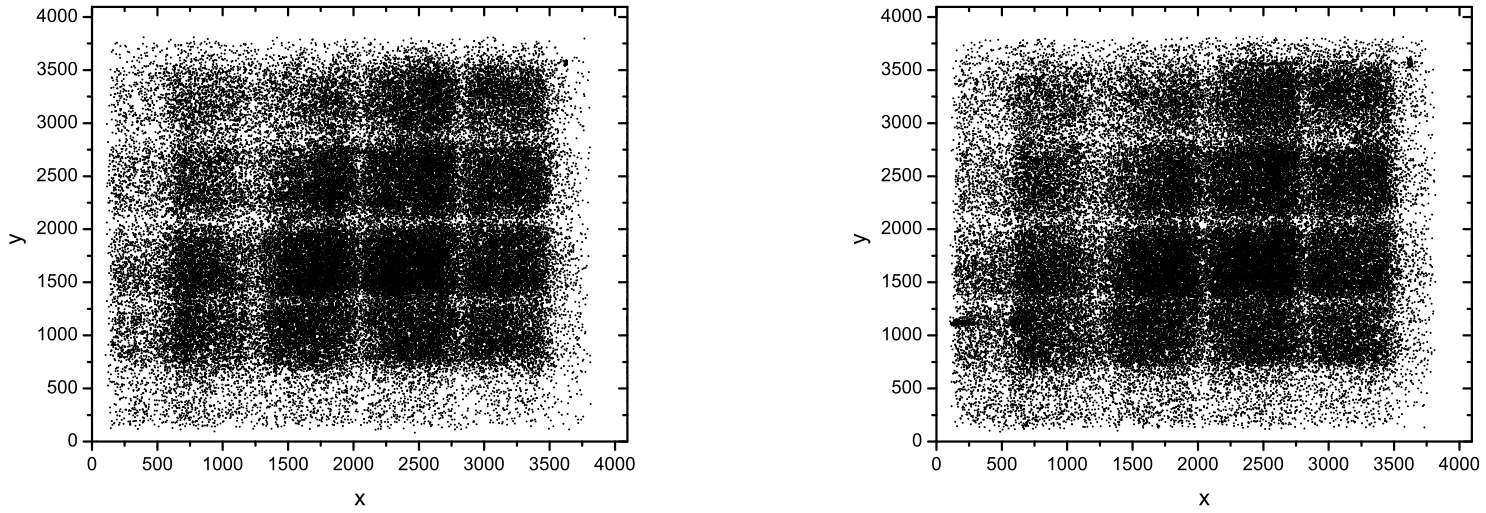

Figure 4.1 Raw flight data, summed from the time that the detectors turned on to when they turned off without discriminating by source and including an arc at the end of the flight.*Left*: Data from the long wavelength detector. The detector registered 87,339 counts, and it displays only a very weak stim signal in the upper right. Although the signal has clearly been distorted beyond the active area of the detector (the darkest 4×4 rectangular grid), the noise does not extend all of the way to the limit of the signal position bits, which span 0 to 4,095, as it would for uniform electronics noise. *Right*: Data from the short wavlength detector. 0 order should show around bin ∼1,500. Note the strong stim signals from both detectors present in the lower left and upper right of the image. The image contains 94,905 counts.

Monitoring the data in real time during the flight, CODEX detected a count rate that started at 30 Hz and climbed to $40 - 50$ Hz over $\sim$300 s, as mentioned above. For about two seconds at the end of the flight and arcing event produced count rates of nearly 1 keV after closing the shutter door and before the high voltage power to the detectors was cut. The $40 - 50$ Hz count rate was well within the range of expected count rates from the Vela SNR, but overall that accounts for only $\sim$5% of the detected signal. The electronics section of the rocket has survived flights since the mid-1980s with modifications for different detector technologies, and in earlier testing (>10 years ago), it was found that the electronics would generate duplicate counts (same time, position, and charge) when faced with extraordinarily high count rates; a quick test of the data showed that this was not the case for CODEX's flight.

The second and simpler check of the excess counts looks at their rate of detection, looking for the bunching of data from arcing events because CODEX clearly did not receive a continuous high signal level. The data in Figures 4.2 and 4.3 were binned by timestamp to show the counts that arrived per second. All time axes in this section are set to launch as the temporal origin to allow for easy comparison to flight plans. The culprit of the high counts is readily apparent.

The detectors turned on at 104.5 s. Arcing occurred across the front of the detector about 5 s after the shutter door was closed, generating the vast majority of counts received during flight. The shadow definitively shows that the arcing was external because the stainless steel mesh supporting the polyimide window is clearly visible. The detectors have a constant low-level flow of gas out of the semi-permeable polyimide window, and quickly after the shutter door was closed this gas raised the internal pressure from the operating pressure of a few hundred μTorr to the mTorr regime. The higher pressure allowed the high voltage windows of the detectors to arc to the "grounded" (still in space, but attached to the chassis of the rocket) detector bulkhead.

The count rate plots (Figures 4.2 and 4.3) show three things of immediate interest:

(1) The vast majority of counts on both detectors came at the end of the flight, when the shutter door closed and gas pressure built up in the detector. This arcing event was known

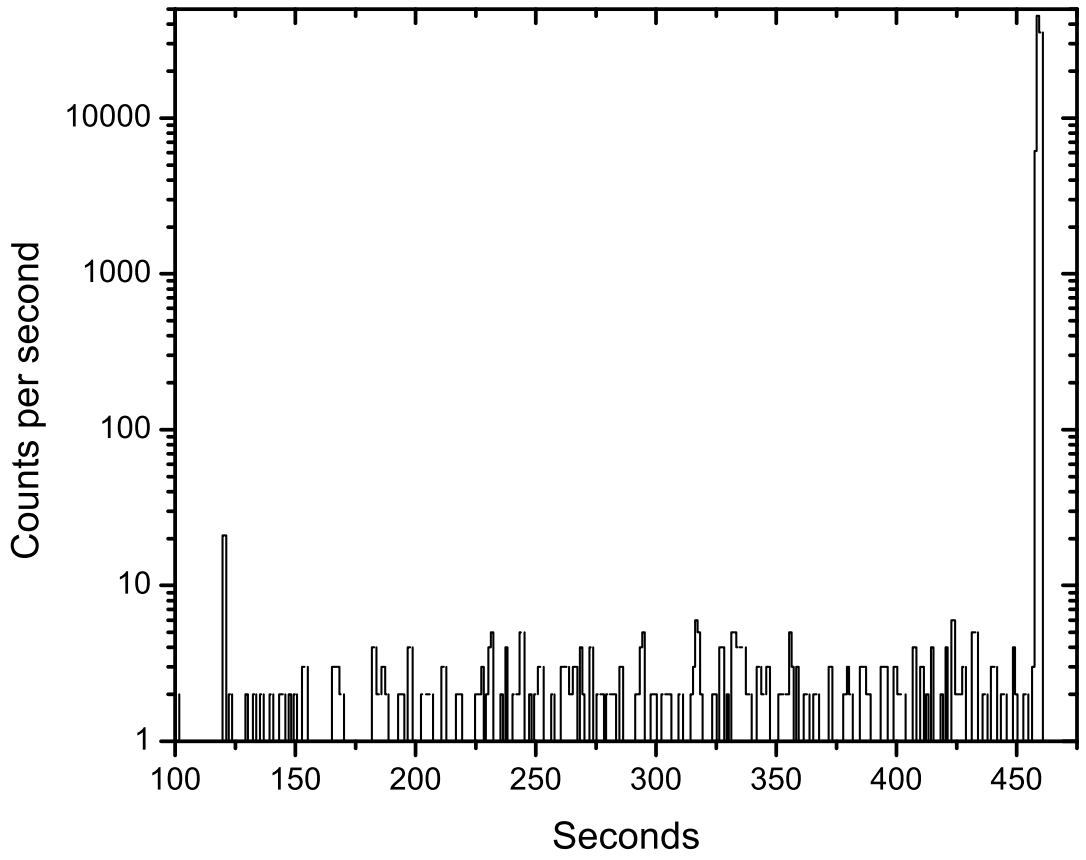

Figure 4.2 Timestream of data from the long wavelength detector. The spike at the far right, an arcing event produced by the climbing pressure in the payload after closing the shutter door, is a convenient reference point: it ended when the high voltage was turned off. The detector turned on at 104.5 s.

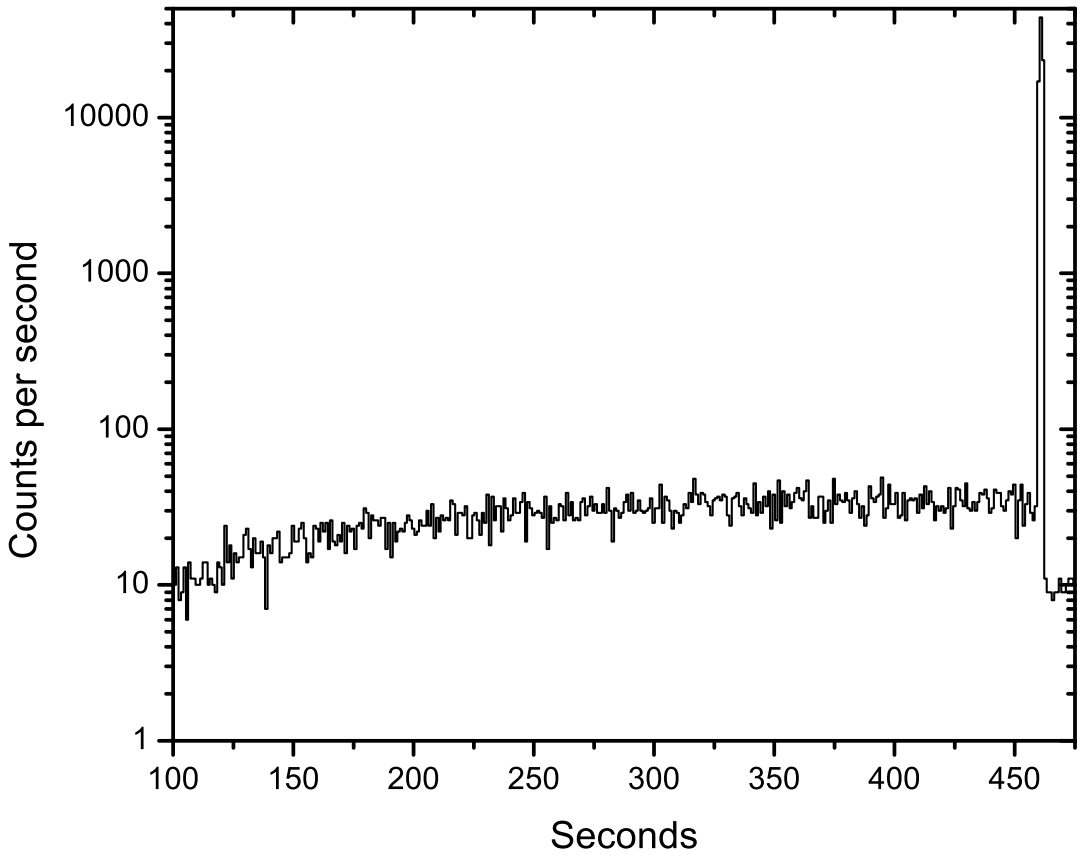

Figure 4.3 Data from the shorter wavelength detector. Note the spike to the far right, indicative of an arcing event, and the slow rise of counts to $30 - 40$ Hz. The slow rise might indicate that the counts are from ions in the payload, which would slowly rise with altitude. The ionic theory is challenged, however, by the lack of a decrease of count rate after reaching the apex of the flight (or a delay from the apex, corresponding to the ion drift rate). Given the slow rise ($\sim$275 s from turn-on before the count rate peaks), it is possible that the increase in counts is due to the drift of ions from the ionosphere through the payload, and on the descent the pressure outside is increasing and not flushing ions from the payload, so it reaches a maximum and does not appreciably decline. A χ^2 fit of a parabola (inspired by the rocket flight through the ionosphere) to the data above, from 50 s to 200 s, gives a peak at 210(70) s ($\chi^2_\nu = 1.03$; 150 data points), easily encompassing the apogee of the rocket flight at 270 s. Fits to regions beyond 200 s, where the time stream begins to fail the eyeball test of being parabolic and levels off, are poorly fit with a parabolic arc. The detector was turned on for 338.5 s before the start of the arc, and most damning of all is that the shutter door obscured the collimators at least partially for 10 s before the arc, and fully for at least 4 s and probably closer to 7 s. The detector turned on at 104.5 s, but the stim counts at 12-14 Hz create the lower bound on the count rate. (Laser-etched GEM plates should not have a warm-up time, although this was taken as read and not explicitly tested; Tamagawa et al. 2009)

and expected but larger than anticipated. The in-flight real-time readout reported 1 kHz for the $1-2$ seconds that the arcing took place, but was probably overwhelmed by the signal. The arc is not a problem; the count rate plots merely show that the last pieces of data, when the shutter door was closed anyway, must be excised. The signals were also remarkably similar, showing comparable count rates and gain across the faces of the detectors, as well as several spots of intense or weaker signal. It seems likely that the arcing overwhelmed the electronic readout, causing detector identification to be lost during the arcing because the charge pulse, which identifies the detector, travels separately and delayed from the signal pulse, allowing for an overlap of signal pulses with charge pulses from the other detector during times of very high count rates. At lower count rates this is not a significant issue (again, cross-talk is <10% for laboratory tests with count rates up to several kHz).

(2) The longer wavelength detector did not work in flight. The count rate is consistent with just the stim pulse — most of which bled onto the other detector — and not with an external signal. In short, that is bad. This issue will be addressed later. The data from both detectors will still be treated as though it were legitimate, despite this preliminary evidence to the contrary, to ensure that this interpretation is correct.

(3) The count rate of the shorter wavelength detector is not constant in time but it is still smooth. It displays a parabolic climb and then flat count rate, suggestive of the parabolic trajectory of the flight filling the payload with ions, then failing to discharge them as the pressure increased again after the apex of the flight. Additionally, there is no clear distinction between the several pointings of the payload. CODEX changed targets three times, starting on a dark target, moving onto the Vela SNR, moving back to the dark target, and finally returning to the Vela SNR. The count rate of the pointings was expected to differ by a factor of nearly 50 (after subtracting the baseline $\sim 14-16$ Hz of stim and normal background noise). There is no indication of those pointings in the data. This is a

strong indication that the data from this detector are not astronomical. It is unlikely that CODEX proved that x-rays are not of astronomical origin, but there is a chance that the electronics misbehaved.

(4) Since the count rate did not descend with the parabolic trajectory of the payload itself, one hypothetical source of the noise can be readily cut out: that it is due to RF pickup on the signal lines between the detectors and the amplifiers. This was considered a possible source of noise, since the electronics are enclosed with all of the NASA telemetry, ACS, and other hardware in a large section of the skin, with nothing to block noise from propagating along the length of it. Essentially, it could operate as a large resonance chamber for RF noise. CODEX electronics use single-shielded wires (RS316) for the signal lines to the detectors, while the NASA sections use double-shielded SMA signal lines; thus there is possibility for pickup on CODEX lines that the NASA electronics would not otherwise see. The CODEX wiring standard is consistent with decades of rockets from the University of Colorado that have not had issues with RF pickup on the signal lines, but the detector electronics have only flown previously on the EXOS and CyXESS payloads. If the noise were constant or directly related to the pressure of the electronics section, which was monitored, then it would be a strong indication of the source of the noise. The pressure monitor in the electronics section (Figure 4.4) shows the pressure monotonically dropping as the payload outgasses into the vacuum of space during flight.

Oakley (2011) uses a larger arc during the EXOS flight to generate a gain map; CODEX arc data has not been treated similarly because the gain due to the arc is qualitatively different from laboratory gain maps (Figure 2.41), indicating that the arc data is not a response to soft x-ray photons and thus not a meaningful gain map. The arc is of no scientific interest and was expected (the intrinsic gas leak rate into the payload from the detectors rapidly puts the payload into a coronal region where the -4 kV windows arc to the grounded chassis), so counts arriving during the arc will be cut without further ado. This drops the longer wavelength detector to 478 counts,

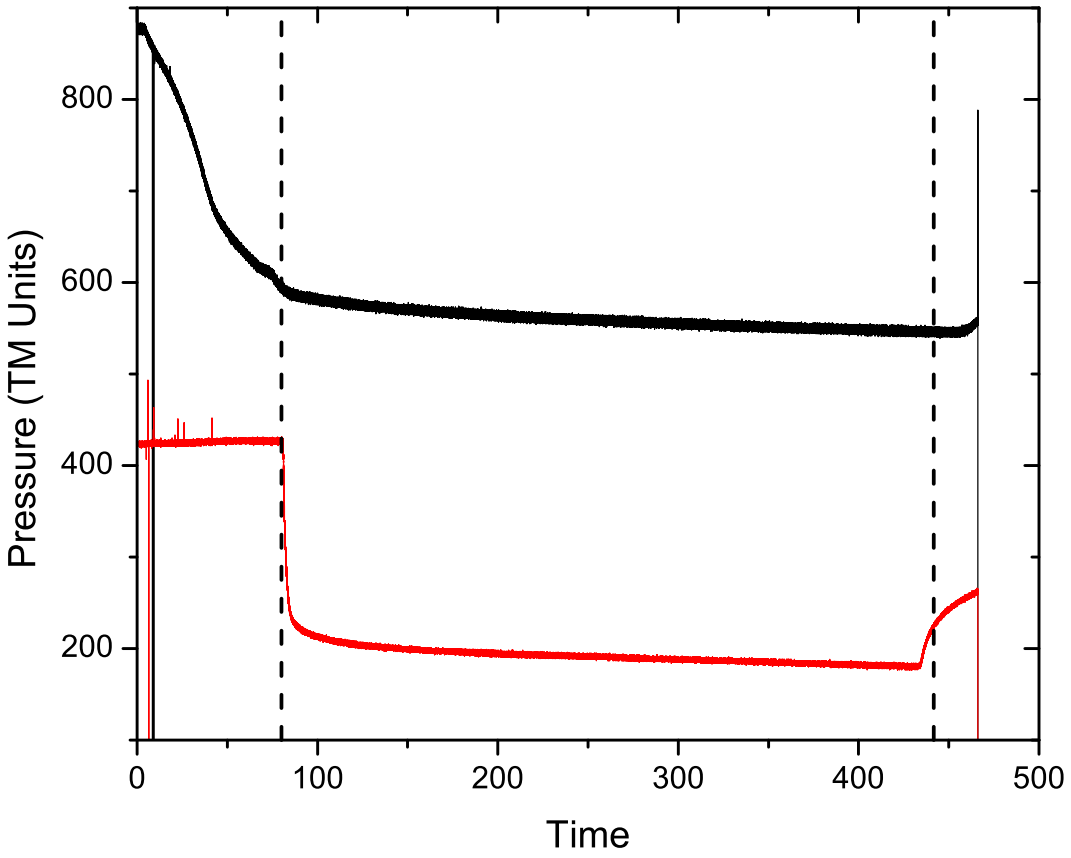

Figure 4.4 Payload pressure as a function of time, measured with MicroPirani 925C vacuum transducers. The red line is the internal pressure, measured next to the detectors. The black line is the pressure in the electronics section, which is not launched under vacuum or sealed from the atmosphere. The two dashed lines indicate the opening of the shutter door at 80 s and the location of the arc at 441.8 s, shortly after the shutter door closed (the start of the rise of the red line). Pressure units are logarithmic (100 TM units = 10× pressure), with atmospheric pressure equal to ∼900 and the payload pressure, during operation, in the mid-10^{-4} Torr range. Note how terrifyingly close the pressure at detector turn-on (104.5 s) is to the pressure that caused the arc after the shutter door closed; fortunately, functionality lies just on the sane side of terror and there was no arcing at the start of the flight.

concentrated in the middle and in the stim pulse, while the shorter wavelength detector is left with 9,741. The factor of 20 difference between the detectors is consistent with zero signal on the long wavelength detector and electronic cross-talk passing some signal from the short wavelength detector as though it were from the other one. The arc occurred 336.5 s after turning on the detectors and $5 - 8$ s after the shutter door was fully closed. The pre-arc detector images, along with their associated pulse height distributions, are shown in in Figures 4.5 and 4.6. For comparison, the charge signal generated by the arcing event is shown in Figure 4.7. Since the count rate plots showed no distinction by source, these figures are full-flight (sans arc) to maximize any signal, either from the shadow of the window bars or from astronomical lines.

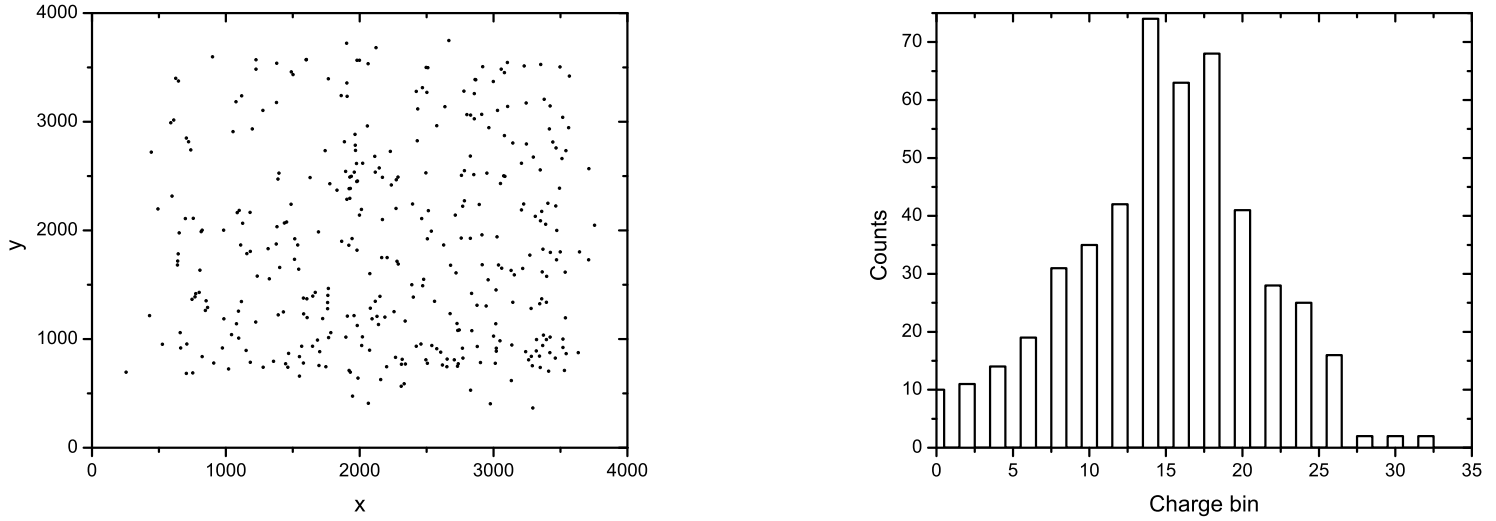

Figure 4.5 *Left*: Full-flight long wavelength detector image (sum of both targets and slewing events), after excising the arcing event. Since the payload has no spatial resolution, it only detects motion and different targets as the rising or falling of intensity of spectral lines; the lines will not smear. *Right*: Histogram of the charge pulses received on that detector. There are no counts with a charge greater than 35.

It is clear from Figures 4.5 and 4.6 that the long wavelength detector failed, as its counts are consistent with cross talk from the short wavelength detector, the pulse height distribution does not qualitatively match an astronomical signal, and the charge signal is centered on a charge bin of wavelength ∼20 Å, which is not in the long wavelength spectrograph's bandpass. Henceforth, data discussions will be constrained to the short wavelength detector.

The remaining counts on the short wavelength detector do not show any sign of the window bars, although they are confined better to the active area of the detector than the arcing signal. Likewise, there is no sign of the 0 order specular reflection, which should fall around $x = 1,500$ at a $-6.2°$ angle. Before dismissing the photons for their lack of effort, however, they deserve proper analysis: transform the 2-D image into a 1-D spectrum, rotate the image to match the dispersion axis, and sum it onto the dispersion axis as a spectrum. Trimming it to the reasonable charge bins ($1 - 25$, corresponding to $\sim 0.1 - 1.5$ keV, beyond CODEX's nominal bandpass but including the full and broad line width from ∼1.0 keV) gives the spectrum in Figure 4.8.

The first hunt in the data should be for its brightest (expected) feature: the 0 order specular reflection should be 0.24 times the sum of all real counts from a flat continuum source with a spectrum extending only over the bandpass of the detector (Figure 4.9). The signal is not evident in Figure 4.8, indicating that a large fraction of the received signal is actually noise. One method to extract signal from noise is offered by the charge resolution of the GEM detectors. The noise signal *might* be more concentrated in charge space than will be the signal. Attempts to extract the signal via analysis of the pulse height distribution is shown in Figure 4.10. There is no sign of an astronomical signal in any of the various charge bins.

There still is no sign of 0 order reflection. However, options have not yet been exhausted, as this has been a search for evidence that some data are valid, regardless of the actual astronomical source of origin. The signal has been analyzed according to time of arrival (smooth, despite changing targets) and pulse height (no apparent signal), but not as a function of target. The full processing will follow this outline:

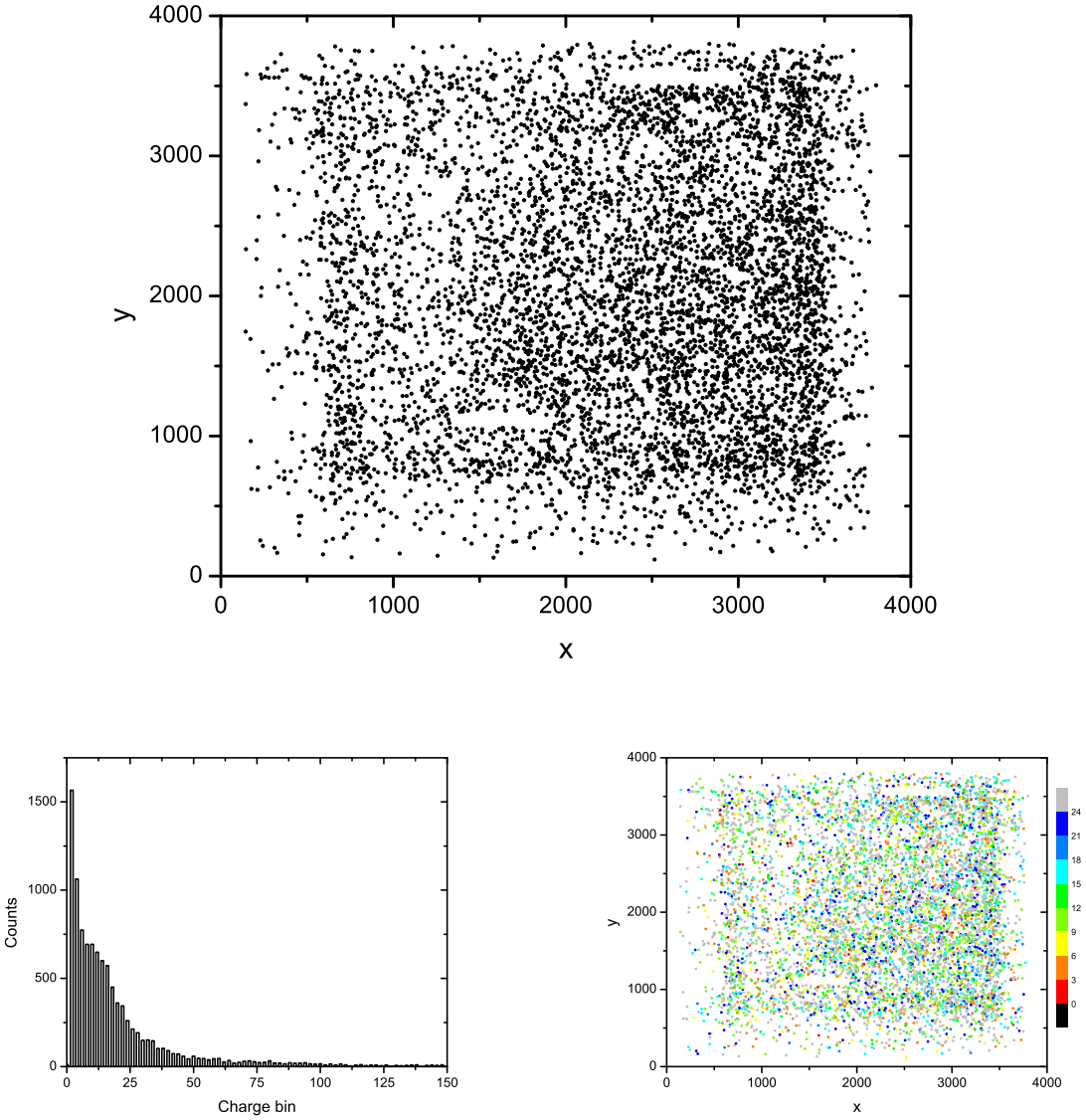

Figure 4.6 *Top*: Full-flight short wavelength detector image (sum of both targets and slewing events), after excising the arcing event. The white regions are where the stim pulse (with its bleeding) have been blanked from the data. *Left*: Histogram of the charge pulses received with the counts in the above images. Note the long high-energy tail, and compare it to the arcing event charge distribution below in Figure 4.7. *Right*: An alternative visualization of the other two plots, combining into one. The color scale describes the charge associated with each pulse, while the axes describe the position of detection. At least to eye, there is no clumping of particular energies of counts aside from a low-gain region around $x = 1,000$.

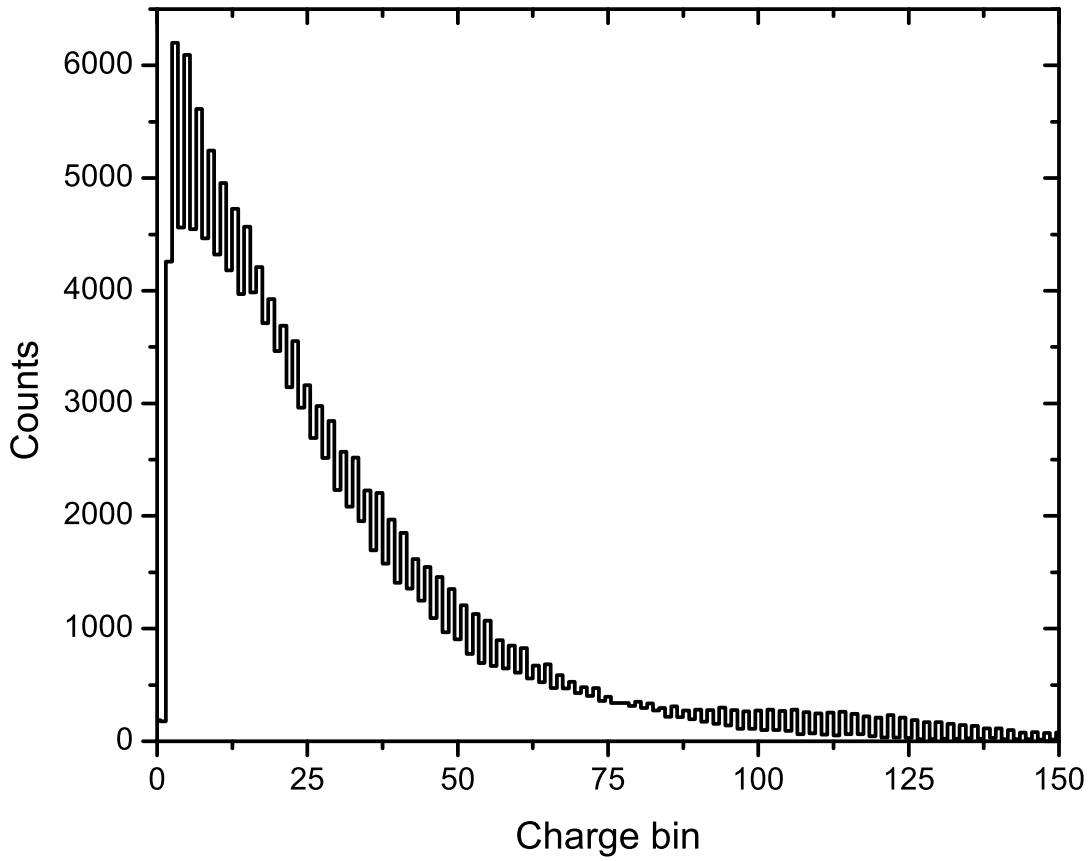

Figure 4.7 Charge pulse height distribution from the entire flight, dominated by the arcing event at the end of the flight (95% of the counts). It has a long tail similar to the non-arc charge distribution above in Figure 4.6, but lacks the low-energy "bump" around bin 15, where the long wavelength detector's charge histogram also peaks. Pre-flight tests put the oxygen peak (22.6 Å) at bin ∼ 8.5, giving this plot a hypothetical range up to ∼6.5 keV (assuming a linear response to very high energies, which was never tested), although photons of that energy would not reflect off of the 4.4° gratings.

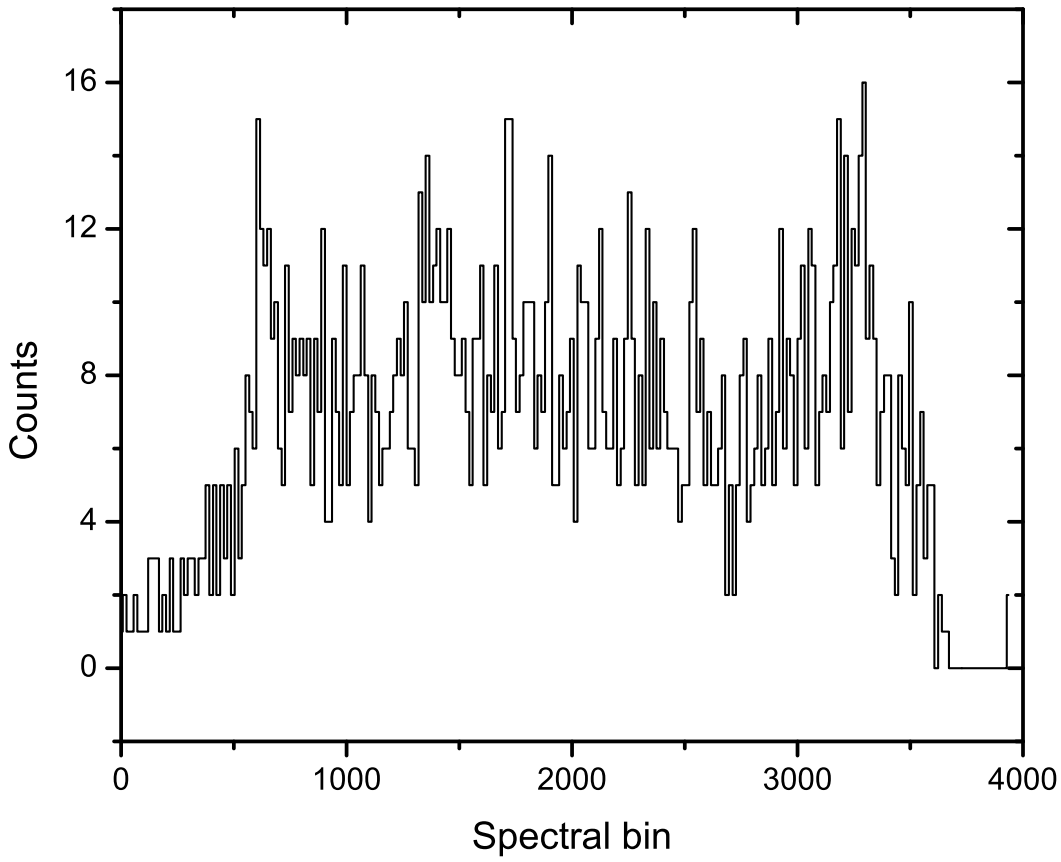

Figure 4.8 The final cut of data from the short wavelength detector used for model fitting, using data from charge bins $1-25$. Specular reflection should create a $3-4$ pixel wide feature centered on spectral bin 1,534; the tempting feature at bin ∼1,350 is 0.5 cm out of position and twice the width of that (expected) signal. The kink in the payload would not deflect the spectrum in this direction, and post-flight tests showed that the spectrum had not shifted significantly.

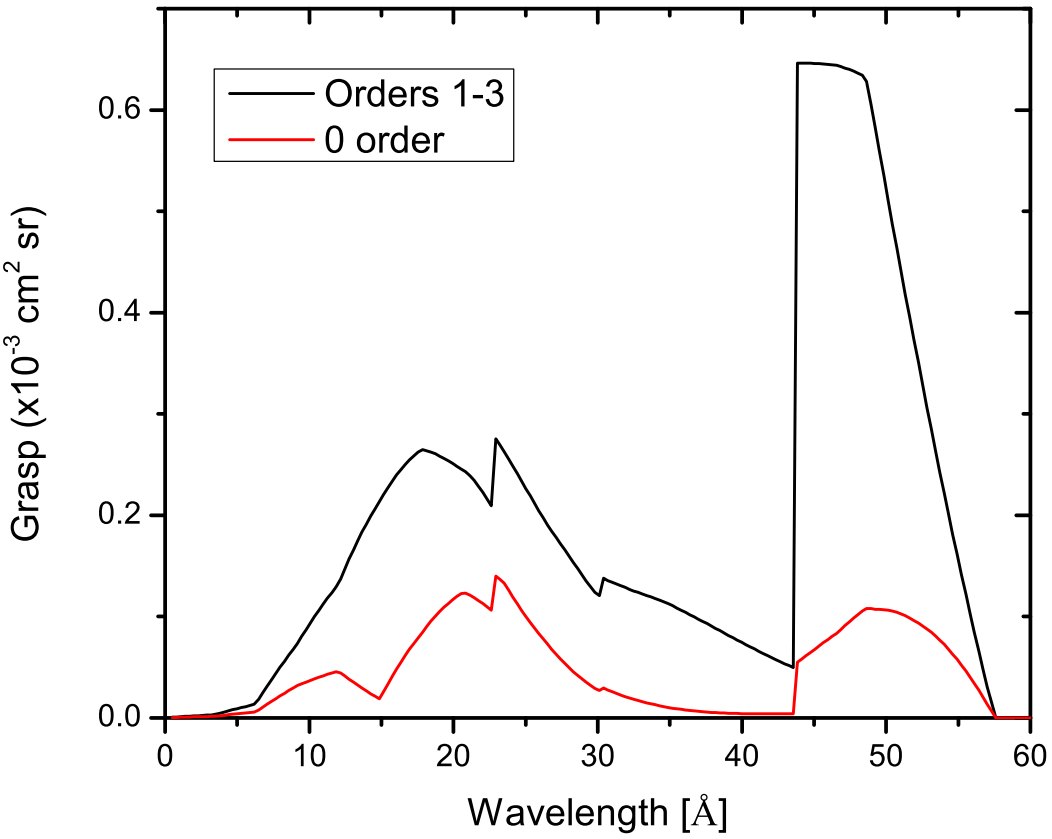

Figure 4.9 Throughput (theoretical) for the short wavelength spectrograph. 0 order is the sum of all values of the red line for all incident photons, while the diffracted photons (black lines) will be positioned according to the dispersion of the gratings.

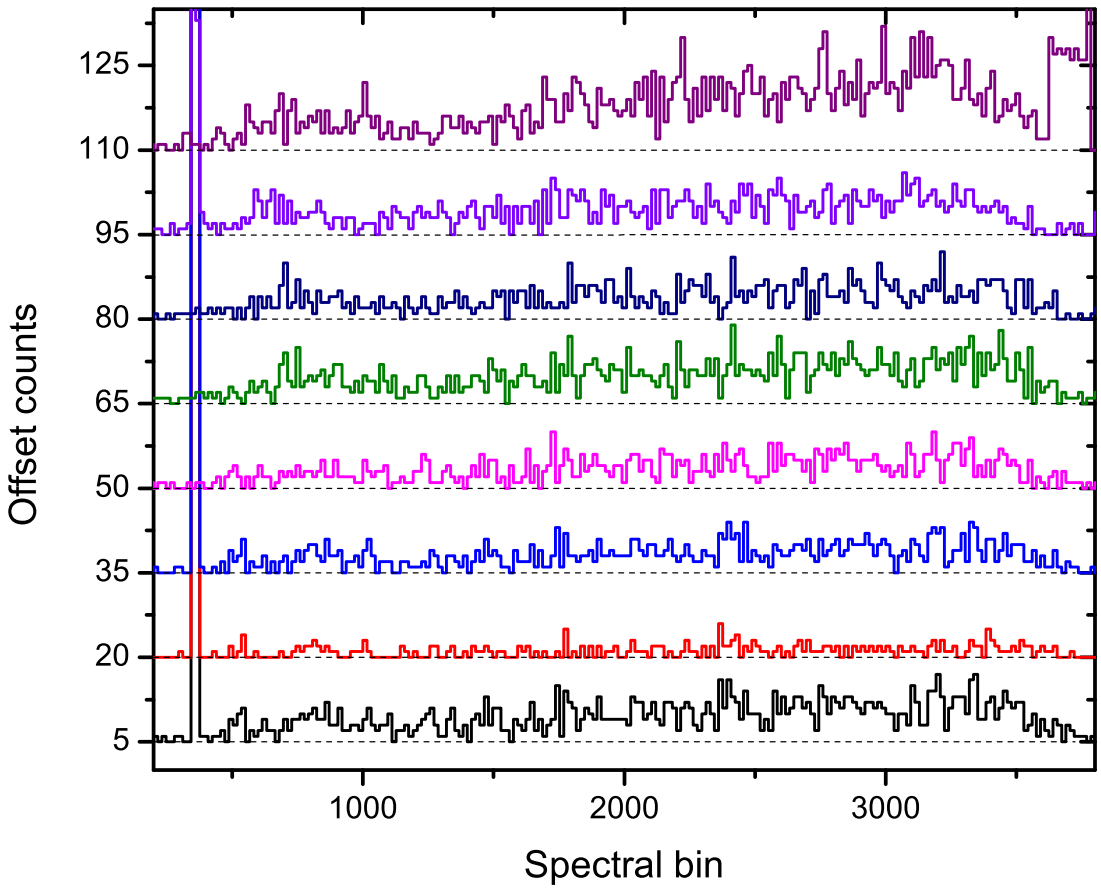

Figure 4.10 Spectra of the CODEX rocket flight from the short wavelength detector, separated by detector energy resolution (y offset, no scaling) as well as the spectrograph's spatial dispersion (x axis). 0 order was expected to center on bin 1,534 with a 56 bin FWHM, and it should receive a large fraction of light from all parts of the CODEX bandpass (Figure 4.9) as well as from spectral lines beyond the nominal CODEX bandpass. From bottom to top, the charge bins represented are (unweighted square bins: 1 count anywhere in the bin = 1 count) $3-12$, $0-6$, $3-9$, $6-12$, $9-15$, $12-18$, $15-21$, and >25. Due to overlapping sampling functions, the counts represented do not sum to the counts received during flight. The width of the square wave was chosen to match the FWHM (in charge bins) of a spectral line. The y axis for each charge bin has a zero value that is offset by 15 (beginning at 5 at the lowest), but it is otherwise unscaled. The large feature at the left of all of the spectra is renegade bit of stim pulse that did not fit neatly into the excising criteria applied, but it should not be considered real data. Since no spectral model has been constructed to assign photons to wavelength bins, the instrument response has not been deconvolved from these data and it has been left in "bins" instead of converting to more transferable wavelength or energy units.

(1) Convert bits to position and charge information.

(2) Split the data into on-target and off-target data sets.

(3) Trim the data to charge bins $1-25$ (approximately $0.1-1.5$ keV by laboratory calibrations, although the wide FWHM in charge space could spread 1.0 keV photons to the 1.5 keV bin).

(4) Divide both spectra by the gain map (Figure 2.41). This is a linear operation and can be after further processing, as well, but it is most convenient to do it here. The gain map removes most gain variations in the y dimension of the detectors; gain calibration of the x dimension is not available. Places where the gain is $<1\%$ (relative to the peak of the gain map) are taken as zero gain. Since the time-dependent increase in count rate cannot be pinned to a detector gain increase as opposed to noise, no effort has been made to apply a temporally-dependent gain factor.

(5) Rotate spectra $-6.206°$ for the short wavelength detector (and $+36.0$ for the long wavelength one, if it were still relevant) to make the dispersion axis a nice horizontal line.

(6) Sum the data perpendicular to the dispersion axis to generate spectra of on- and off-target observations. The results are shown in Figure 4.11.

(7) Scale the off-target data to account for the time difference between on and off pointings ($2.46\times$ more time was spent on the Vela SNR than on the dark off-target region).

(8) Rebin the spectra by a factor of 16 to reduce the noise.

(9) Subtract the two spectra from each other. Differencing the spectra should remove most systematic noise signals, although it will increase the statistical noise by $\sqrt{2}$. Since the off-target observations were of a dark target, differencing should not affect the Vela spectrum significantly. The difference spectrum is shown in Figure 4.12.

(10) Scale the spectrum by the relative amounts of the detector devoted to each region of it, since the detector is rotated relative to the focus and the dispersion. This emphasizes the outer regions of the spectrum, where the detector collecting area is lowest, as seen in Figure 4.12.

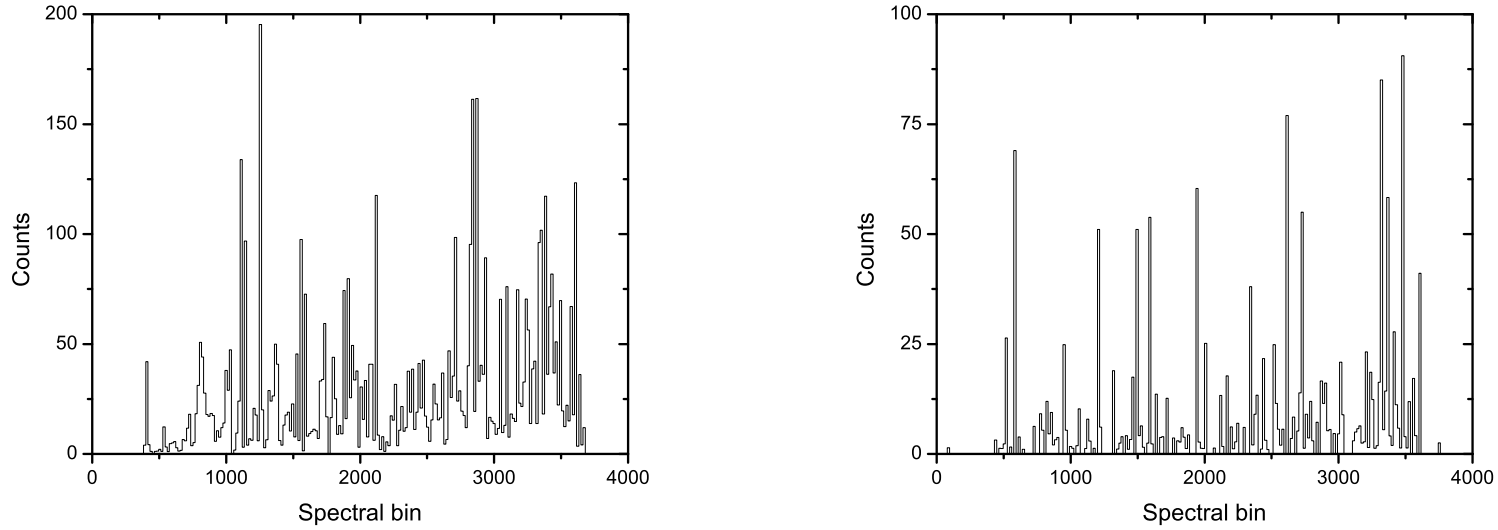

Figure 4.11 *Left*: The final flight data from the two pointings at the Vela SNR with charge pulses between values of 1 and 25, after applying the gain map (Figure 2.41). Data have been rebinned such that a single datum represents 16 raw detector bins. *Right*: The final flight data from the two pointings at dark region north of the Vela SNR, processed identically to the Vela SNR data. Time spent on the dark target was 2.46× less than the time spent on the Vela SNR.

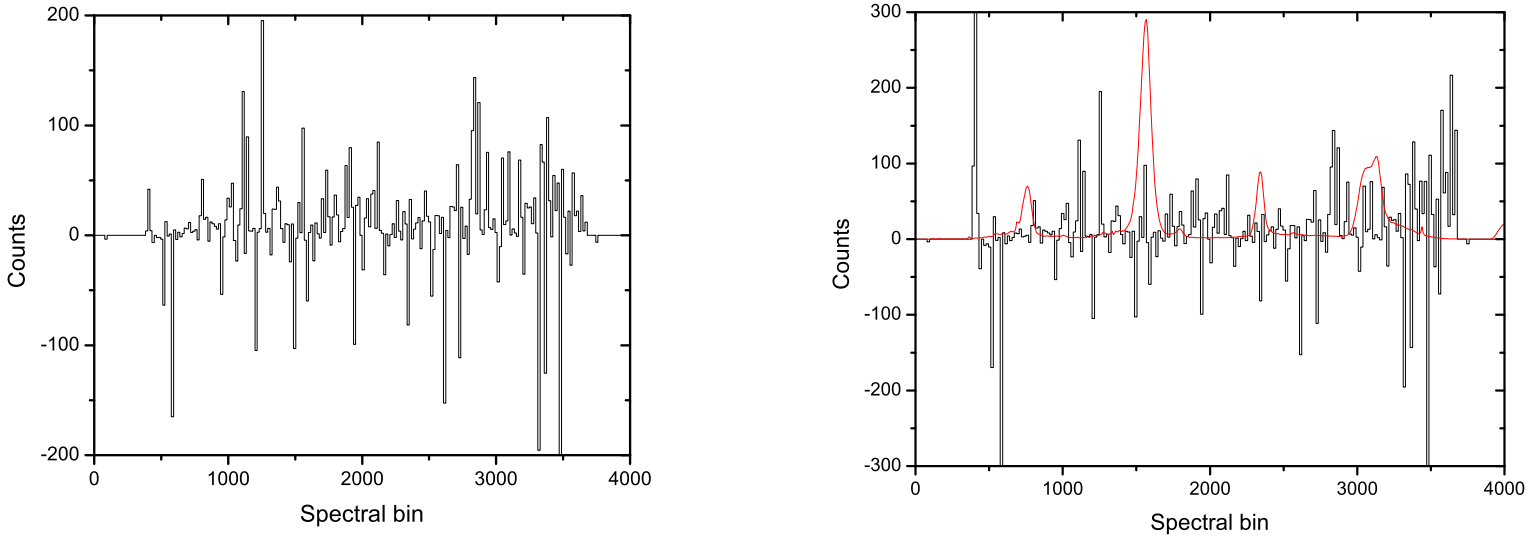

Figure 4.12 *Left*: The difference between the on- and off- target spectra (Figure 4.11), after scaling for the time difference (a factor of 2.46) and rebinning with 16 detector bins per bin. 0 order should be a 56-pixel Gaussian line centered on bin 1,534 if there is a signal in the data. If there is no signal, the sum of the spectrum should be zero. No significant spike is seen in the expected 0 order bin, but the spectrum sums to 1,901. The mean value is 7.4, 2.3σ above the 0 ± 3.2 expected if there is no signal (error is from the standard deviation of the above dataset). Although it is tempting to declare this as significant, a 2.3σ signal is still quite weak and it lacks any other characteristics of an astronomical signal. *Right*: The final spectrum, with a geometric gain factor applied to the spectrum at left to account for the detector rotation relative to the spectrum. Overlaid in red is a laboratory calibration spectrum (Manson source with a magnesium anode, with four peaks from left to right: -1 oxygen, 0, $+1$ oxygen, blended $+2$ carbon/$+1$ oxygen orders) to guide the eyeball. Although there is a positive feature beneath the 0 order peak, if summed over the expected line width (56 bins), the value is consistent with 0. The geometric factor scales the outer 11.5% on each side of the spectrum, merely amplifying what appears to be noise. The increase in noise raises the full-spectrum standard deviation from the 42 counts bin^{-1} in the spectrum at left to 63 counts bin^{-1}; the interior (bins 700-3200) has a standard deviation of 41 counts bin^{-1}. The spectrum has 2,764 counts, dominated by pixels that get severely over-amplified due to their small areas on the detector.

Oxygen has been detected in the Vela remnant, as well as a thermal continuum (Kahn et al. 1983). The expected signal should look like a series of lines (at least an oxygen line or two, which have been detected previously), with a continuum that is either purely thermal or a mix of thermal and non-thermal. If it is synchrotron emission, then a continuum spectrum makes sense aside from a minor detail: as discussed above, a quarter of the flux from all wavelengths (including those well beyond the range of the short wavelength detector) is undiffracted and should still produce a very strong 0 order line — much stronger relative to spectral lines than laboratory calibrations, even, because lab tests used the spectra of only one or two elements. The actual signal is uniform (including a lack of a 0 order line) and concentrated solely on the short wavelength detector, which raises several questions, addressed below:

(1) What happened to the long wavelength detector?

(2) What is the uniform noise on the short wavelength detector?

(3) Why are there no window bars?

(4) Where is the signal from the Vela SNR? And particularly, why is there no 0 order line?

4.1.1 Long wavelength spectrograph

The collimator and gratings are not likely to be at fault for causing the signal to disappear, as they are mechanically coupled to the other spectrograph for support and the spectrographs are mechanically identical. Post-flight testing of the short wavelength detector showed no appreciable change from pre-flight tests. The long wavelength detector did not work post-flight, even when presented with an ^{55}Fe source.

The detectors have several fundamental modes of failure: loss of operating voltage or gas pressure, fusing of GEM plates, and damaged signal cables/connections/anode preventing the passage of data. The power supply and gas voltage were both monitored in flight (Figure 4.13); the latter options are more difficult to detect.

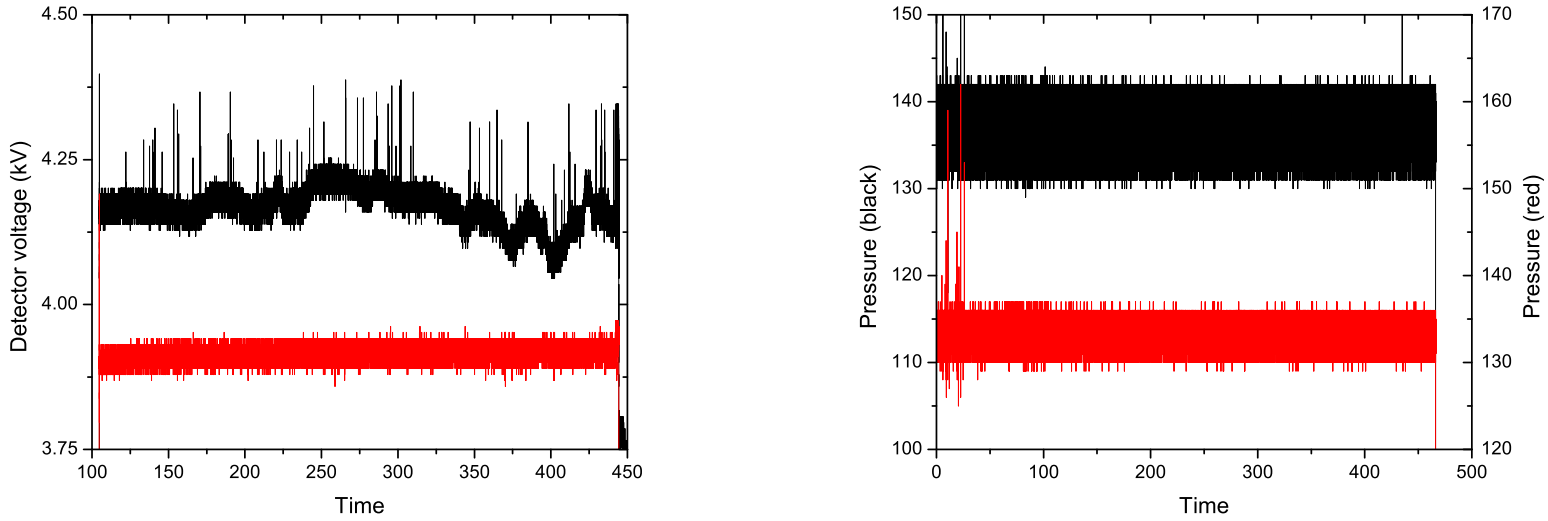

Figure 4.13 *Left*: Detector voltage monitors, sampled at 892 Hz. Despite their appearances about quality, the black line is the short wavelength detector that worked at least to some extent in flight. Red is the long wavelength detector which shows no appearance of flight functionality. They were deliberately set to different voltages per optimization tests described above. *Right*: Detector pressure as a function of time, sampled at 892 Hz. The telemetry pressure units are approximately 10 TM units per unit psia, but scaling is not exact (both flew at 13.0 psia; the difference lies in the voltage dividers prior to the telemetry section and not in the actual pressure). To distinguish the two lines, the black pressure line is scaled on the left, and the red one is scaled on the right. The red line corresponds to the short wavelength detector; the black one corresponds to the long wavelength one. The polyimide window burst pressure is in the 80+ psia range.

It is tempting to blame the power supply for the detector failure, since one can clearly see that a power supply's monitoring voltage fluctuated by about 100 V peak to peak (<3%), not counting transient noise. The monitoring current comes from the primary power supply of each detector, while the detectors were each supplied by independent high voltage supplies with a backup power supply set 50 V below the primary and combined through a diode mixer such that the higher power supply should always dominate. Power supply stability was not explicitly tested in laboratory testing beforehand. Post-flight reviewing of the pre-launch tests at White Sands show that the variation occurred during tests on the ground as well. However, the power supply that looks faulty supplied the detector that looks good. The bad detector had a rock solid voltage, and thus power is not the cause of the failure.

Detector pressure is also clearly not an issue: both detectors maintained their nominal pressures (Figure 4.13). The detector pressures were continuously monitored by the proportional valves that feed them from the gas reservoir. The pressures were measured downstream of the controlling valve and thus reflect the true detector pressures.

Post-flight testing conducted by Thomas Rogers to study the bleeding of the signal from one detector to the other showed that an amplifier on the long wavelength detector was inverting the stim pulse. Simply replacing the amplifier resulted in data being passed through from the detector, although at a lower efficiency than for the short wavelength detector. The amplifier worked when CODEX shipped to the White Sands Missile Range, but it did not work in flight or afterward. Apparently it failed; where, when, and why it failed (pre-flight, in-flight, post-flight; power fluctuations, bad components, etc.) has not been determined.

4.2 Short wavelength detector

4.2.1 Source of noise on the short wavelength detector

The short wavelength detector picked up significant signal, but it does not look astronomical. It does not even look as though the signal came from outside of the detectors, since an external

signal should be imprinted with the shadows of the window bars. On the other hand, it does not look as though the signal was created by RF noise on the signal lines, since the signal is confined to the active area of the detector (as opposed to the laboratory RF pickup in Figure 2.28). The TDC can process data outside the active area, evidenced by the biasing seen in the end-of-flight arcing event. Somehow, a uniform signal was generated across the entire interior of the detectors. Additionally, in its raw form and summed along the y axis of the detector, CODEX made a startling "confirmation" of the raw data from the EXOS flight, despite being shifted along the spectral access and looking at a different object (Figure 4.14). The characteristics of the noise and the similarity of the data sets indicate that the signal in both flights was dominated by a background intrinsic to the detectors.

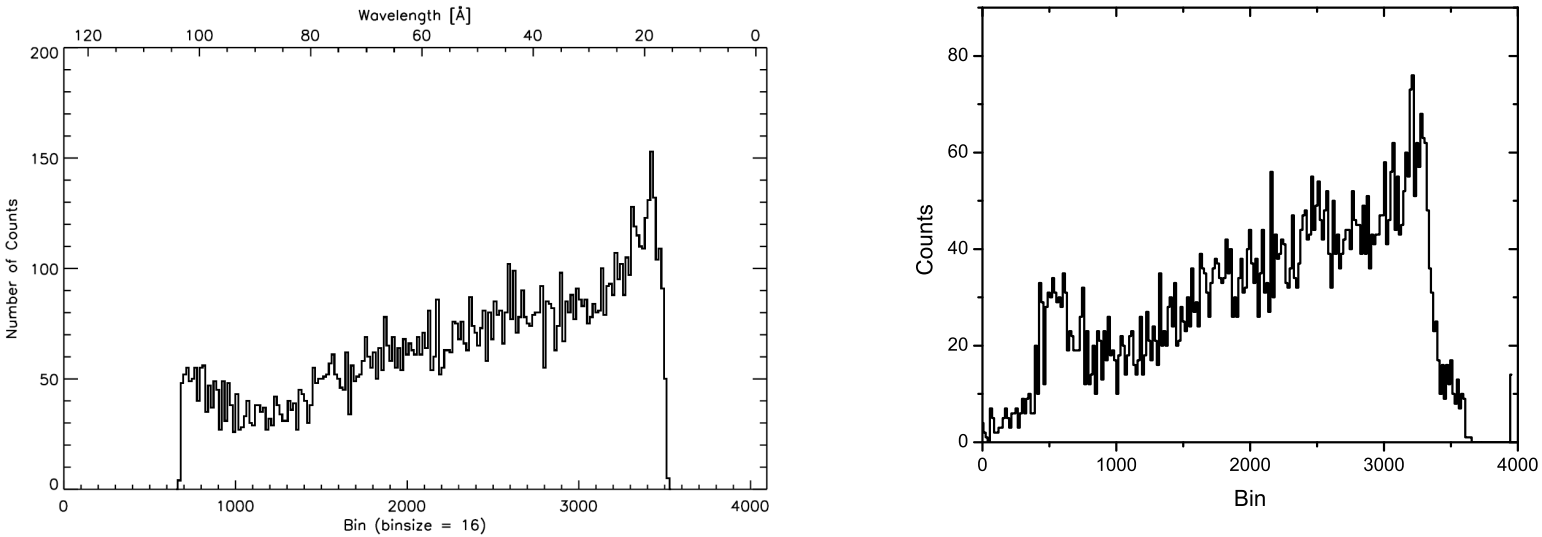

Figure 4.14 *Left*: Spectrum from the EXOS flight. Data are entirely unprocessed, aside from summing the 2-dimensional detector image into a 1-dimensional spectrum and removing the stim and hot spots (Oakley 2011). *Right*: Pseudo-spectrum from CODEX, as received along the y axis (nearly orthogonal to the dispersion axis, and unfocused) without applying any gain calibration or rotation to align the detector with any astronomical signal passed from the collimators, and summed over the entire flight prior to the arcing event. Data have been rebinned with 16 detector bins per bin. The poor definition of the edges of the CODEX spectrum is due to the biasing of counts off of the active area of the detector, but other than that the two images are hauntingly similar despite looking at different parts of the spectrum and at different regions of the sky, suggesting that the commonality is due to an intrinsic background common to the observations (detectors, noise, or ion environment) rather than a confirmation of the results. Aside from the blip around bin 600 in the CODEX data, the "spectrum" is fit very well by a linear slope of 2.2. The y axis is approximately radial in both payloads, suggestive that the position of the detector is relevant to its noise, but this hypothesis not been confirmed.

The time-dependent noise signal appears to increase nearly parabolically until the apogee of the flight. Coinciding with that rise is the (unmeasured) density of atmospheric ions in the payload. The density of ions would not fall appreciably as the payload descended back into the atmosphere because the increase of atmospheric density during descent will not evacuate the ions. Tests in the laboratory often require tens of minutes or more for an ionic background to die down.

The detectors each have a -4 kV window exposed to the interior of the payload: positively-charged ions will be attracted to these windows. This is a design flaw, but again not one detected (although perhaps it was seen and not identified) by EXOS and CyXESS. It can be corrected by adding an ion repeller grid in front of the detectors. However, this is not assuredly the correct interpretation of the noise, since laboratory tests indicate do not clearly show that ions could produce such a signal.

I attempted to duplicate the observed signal with a Varian Vacuum Technologies' Eyesys mini-IMG, an active vacuum gauge that produces large quantities of ions (generally just called an "ion gauge" by lab rats). I conducted tests with the ion gauge in several different locations, attempting to create a signal that duplicated the flight signal either from proximity, diffusion throughout the payload, or diffusion down the collimators. The configurations are described below.

(1) Ion gauge on the detector bulkhead in place of the passive MicroPirani 925C vacuum gauge (so the ion gauge face was parallel to and facing away from the detectors): produced a strong signal but also strong shadows of window bars. Temporally, the signal also corresponded very closely with the turning on and off of the ion gauge.

(2) Ion gauge inside the optics bench but between the detectors and the optics: similar results, casting shadows of the window bars while illuminating the entirety of the detectors, and doing so only when the ion gauge was turned on.

(3) Ion gauge in front of the collimators and facing the detectors: weak window bar shadows and a discernible spike around 0 order even though ions and photons in this test must reflect off the 4.4° graze angle of the gratings to hit the detector. The signal is still originally the

product of the ions generated by the gauge, and these have varying drift distances through the collimator (a mean free path is just a statement of probability of collisions). At some point, most ions will collide with a neutral particle and emit a photon while neutralizing. The photons are generated inside the collimator, having already passed through some of the metal grids, so the collimator is incapable of blocking all paths for the light and the light is poorly collimated when it hits the detectors. (Ions themselves should not reflect off the gratings, since they would induce a negative charge on the metallic surface and stick to the gratings.) Thus, it forms a poor focus. The results of the test are shown below in Figure 4.15.

(4) Ion gauge in front of the optics but facing away from the payload produced no discernible signal. This is reasonable, since the signal would spread out too much to be detectable.

The test results, though not definitive, suggest that the ion hypothesis is on the right track. It also has a few differences from the flight signal. The most notable results are listed below:

(1) 0 order is readily apparent. The laboratory signal was therefore generated within the collimator or at least was shaped by it. There are several other paths (requiring at least one redirection no straight path) that ions might take in the payload to avoid collimation, but a signal that drifts into the collimators still comes out collimated.

(2) The signal bleeds onto the dysfunctional detector at a low level, peaking in charge bins $15 - 20$, similar to what was seen in flight.

(3) Window bars are readily apparent, although their shadows are muted. Their muting inspires optimism that the ion tests are on the right path. The ion gauge is (approximately) an ion point source, while in contrast, every aperture in CODEX is a source of ions in flight. As mentioned above, there are several such apertures on the grating bulkhead to facilitate the evacuation of the payload, which also allows ion passage into the payload. The pumpout holes are baffled, with $>1/2$ of the aperture obscured on each side of the bulkhead. There

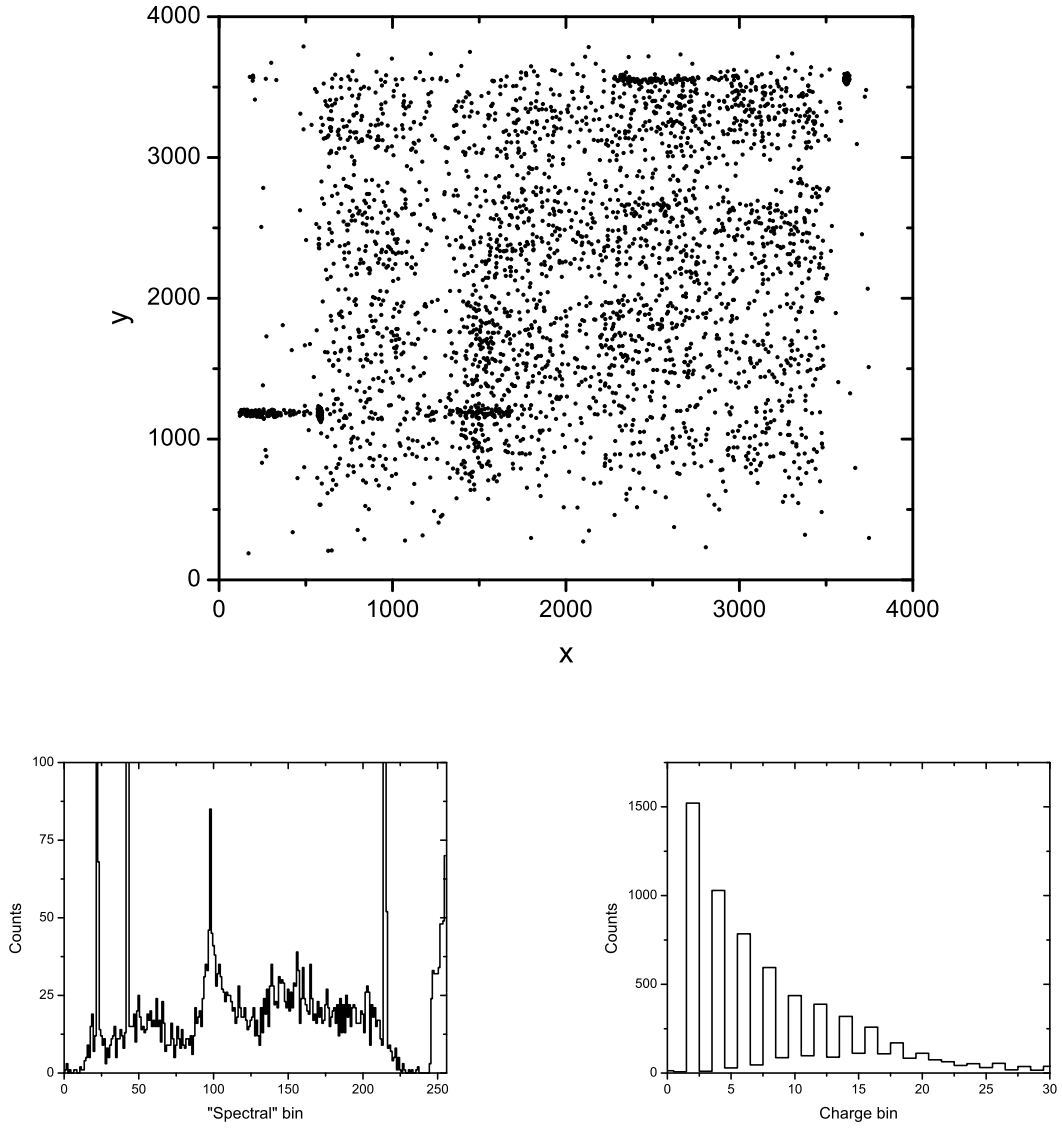

Figure 4.15 Ion gauge-generated signal as received by the detectors. The ion gauge was placed in front of the collimators, roughly 10 cm from the aperture. *Top*: The detector image, showing the window bars despite our best efforts to create an ion source that would mimic flight data. The window bars create decrements of a factor of $2-3$ below the continuum not as filled as the flight image, but not as empty as pure photon tests. *Bottom left*: The "spectrum" of the ion gauge as it fell on the 0 order detector, including the 6.2° rotation of the collimator axes relative to the detector axes. Although there is no sign of a dispersed spectrum, the peak near bin 1,500 is the specular reflection. Although the baseline is much more structured than for tests using the Manson x-ray source, it does not (by eye) mimic the baseline seen in flight. This could be due to a different ion population or to a significant photonic contribution from the ion source. No effort was made to remove the stim signals. *Bottom right*: The pulse height distribution for the image. Note the cross-talk: the detectors are identified by an odd or an even charge, so the odd values that peak around bin 15 are carried over onto the other detector (these images comprise data from both detectors). Also notable is the high-energy tail, similar to what is seen in the flight data.

is no direct path from outside of the optics bench to the detectors, but they still present a large aperture to allow gas to escape the payload (this prevents an internal gas buildup near the detectors that could cause arcing similar to what was seen at the end of the flight). Getting an ion to the detectors without passing through the collimators requires at least one redirection of the ion's path.

(4) Positioning the ion source close to the detectors can skew the image significantly because the GEMs are 3-dimensional detectors. Laboratory tests with the radioactive ^{55}Fe (6 kV) source have shown that placing the source close to the detector creates a severe pincushion distortion of the window bars such that two sources placed on opposite sides of a window bar would make the bar's shadow indiscernible. Uniformly filling the payload with ions could be similar to placing one of those radiation sources (scaled down in intensity) or an ion gauge at every point in the detector. The penetration depth of the photons or ions would wash out any shadows before an electron cascade could begin and localize the impact. This does not definitively identify the source of the noise in flight, but it does lend some credibility to the ionogenic hypothesis. Further testing is necessary before these detectors fly again, since the received noise was comparable to the expected signal and a continuum signal — like that sought by CODEX — would be very difficult to discern from noise. (CODEX's on/off differencing scheme was laid out with this in mind; otherwise the signal, aside from the missing 0 order, might have been interpreted as astronomical data.)

The ion test fails to duplicate the flight data in one crucial aspect in addition to producing a 0 order line: the gain of the detector is very uniform. Also, the spectrum does not show the gain distribution observed in the flight data. The lack of a similar gain map for the ion test could be due to the energies of the incident particles, as higher energies should penetrate farther into the Ar/CO_2 gas mixture than lower energy ones before they collide and begin the shower of electrons toward the anode. These tests were conducted with a convenient laboratory ion source and not matched to atmospheric ion populations or to the observed pulse height distribution. If

the flight noise were generated by lower energy particles that could not travel far enough through the detector to start a viable electron cascade, then a region of slightly lower gain might develop. This argument is supported by the distribution of counts during the arcing event and laboratory tests beforehand (Figures 4.1 and 2.41), where the two time periods have drastically different distributions determined primarily by the energy of the incident particle.

Cosmic rays can be ruled out as the source of the noise, although they plague many detectors in space. The count rate persisted without any change when the shutter door was closed. Additionally, the cosmic ray hypothesis cannot explain why the count rate would rise and then remain constant until the arcing event. While one could argue for the rise on the grounds of opacity of the upper atmosphere, it should then fall again after the apogee, unlike the ion rate, which stays roughly constant after apogee. But then, the ion hypothesis is suspicious when one notices that the counts climb from $\sim$0, even though the detector voltage turns on effectively instantly. In testing with the ion gauge, there was no delay (at least not a measurable one, with a finger on the power switch and an eyeball on the clock) between powering the gauge and receiving the signal.

4.2.2 Lack of window bar shadows

The lack of window bars is conveniently described by the ion hypothesis (§4.2.1) as a product of ions and the three-dimensional detector body. Any other explanation would require either a mechanism for getting photons to arrive at the same location on the detector at vastly different angles to wash out the shadow, or would require that the noise be generated inside the detector and in a fashion where it increases over time after turning the detectors on. It does not require the detector to actually pick up ions, but could be the result of de-excitation processes producing photons within the 2 m optics bench, where there are no optics to block scattered light.

Processes entirely internal to the detector have never produced internal noise of that magnitude (there is a several Hz background signal that is uniform, but it is a full order of magnitude below the detected noise signal). The detectors have never been tested shortly after a launch-vibration simulation because the shake tests were conducted under vacuum, but not at a low enough pressure

to safely operate the detectors. Vacuum pumps are not stable enough under launch vibrations, and would have to be added after shake tests. The addition of pumping equipment placed a minimum shake-to-operation test separation at 2 hr, while in flight it was 60 s from the end of vibrations to the high voltage turn-on. It is unlikely that vibrations could cause a signal, though, and particularly not a noise signal that increases with time from the vibration and turn-on events.

Since the window bars are generally one of the clearest indications of an external signal, it is worth looking for them. Without the arcing event, the full signal does not show any indication of the window bars, and to go more in-depth requires the third dimension of the detector signal — the charge pulse height — to see if a region of that dimension shows characteristics of an astronomical signal. Preflight testing showed pulse height distributions peaking in the $5-20$ range with FWHM of $4-6$ charge bins. Accordingly, cuts were taken through the pulse height data at three-bin interals with a square sampling function with a width of six charge bins. Furthermore, to increase the chance of finding the bars, the 2-D images were summed horizontally because a dispersed spectrum should be approximately vertical ($-6.2°$ from vertical, so the window bar shadows should be most apparent in the horizontal direction). The cuts are shown in Figure 4.16, and they show no evidence of window bars.

Figure 4.16 also shows a spillover of counts, broader than the window bars and beyond the active area of the detector, evident in the small y bins. Whether wayward astronomical signal or pure noise, that level of spreading would have blended out any window bars. The effect on a spectra line would differ from that on a shadow: a shadow gets filled in by diffuse light, while a positive signal must be statistically overwhelmed by the additional photon-like signal around it. The most likely place for an ion to generate a signal is either through an impact with the detector or impacting gas particles or metal structures between the gratings and the detectors, where there is no dispersive optic to constrain the system. On the chance that the lines would have been broadened by increased angles of incidence, however, the spectra were smoothed by powers of 2 up to 28 (giving 16 bins across the entire detector, equivalent to expecting a 6 mm-wide line). Regardless of the amount of smoothing, no window bars were found, indicating that the signal that

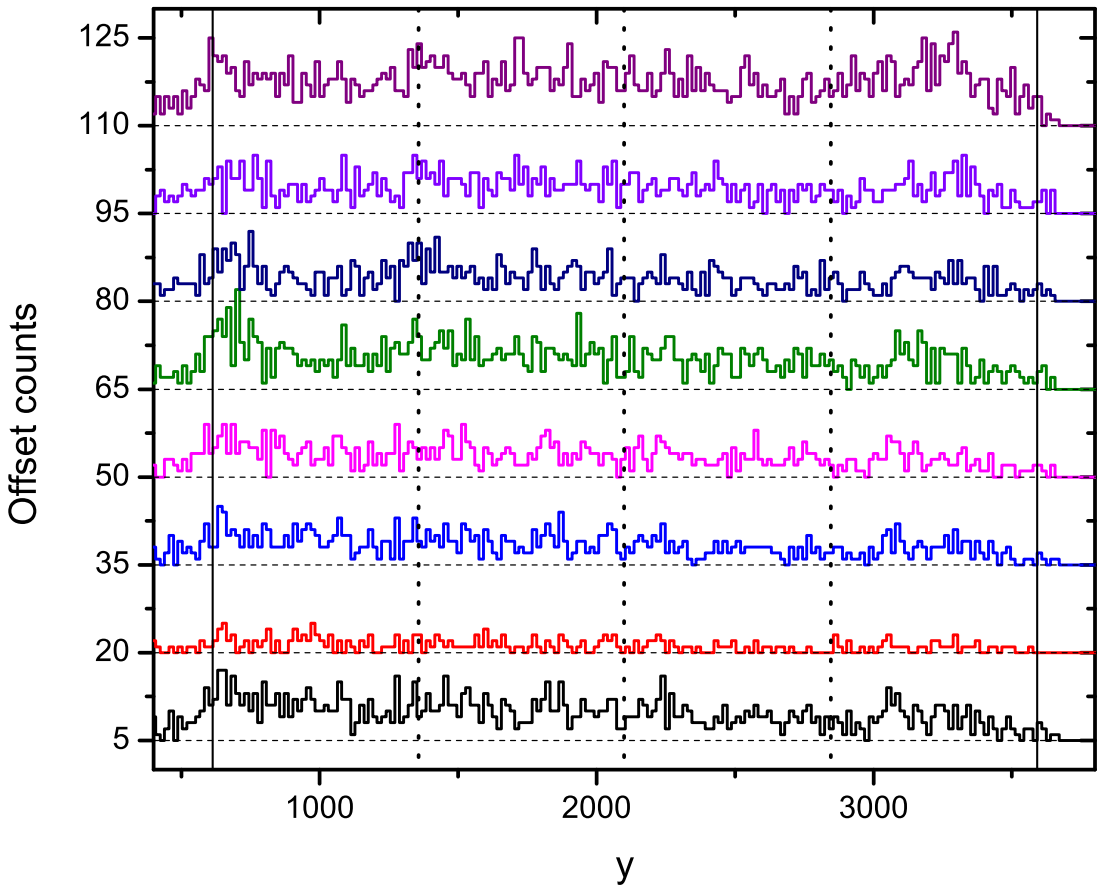

Figure 4.16 Horizontally-summed "spectra" (since a real astronomical signal passed though the optics would be nearly orthogonal to these) of the flight data. These are not true spectra, but they are created from the (low) energy resolution of the GEM detectors. From bottom to top, the charge bins represented are $3-12$, $0-6$, $3-9$, $6-12$, $9-15$, $12-18$, $15-21$, and >25. Figure 4.10 explains the reasoning for these bins. Count rates are offset by 15 (from 5 at the lowest), but otherwise unscaled. Horizontal dashed lines demark the zero point for each line; vertical solid lines mark the edge of the detectors, and the vertical dotted lines guide eyeballs to where the window bar shadows "should" appear. Data have been spatially rebinned by a factor of 16 to increase the signal-to-noise ratio.

Table 4.1. Tests of flight data

Test	All data (including arc)	Non-arc data
Window bars apparent	Pass	Fail
Increase of counts when on target	...	Fail
Pulse height data resembling soft x-rays	Fail	Fail
0 order line (or other spectral lines)	Fail	Fail
Count rate consistent with expected astronomical signal	Fail	Pass
Stim pulses showing electronic functionality	Pass	Pass
Symmetric on either side of 0 Order	Pass	Pass
Signal confined to the active area of the detector	Fail	Pass

washed out the shadows was sufficiently strong and diffuse to overwhelm any signal that would have produced shadows.

4.2.3 Astronomical signal

CODEX targeted one of the brightest diffuse soft x-ray sources in the sky. If it functioned anywhere near to its design, it would have seen an astronomical signal, yet no analyses have shown that any astronomical signal passed through the detectors.

The noise signal even has a curveball to throw: since CODEX collected data on- and off-target, analyses included a difference spectrum (Figure 4.12). The difference spectrum has ∼2,000 counts (depending on treatment of the edges of the detector), a 12 Hz count rate. Normally, this would be an indication of a positive signal from the Vela SNR. However, if times are taken only after apogee, the sum of the difference becomes statistically insignificant ($<1\sigma$, assuming Poisson noise). Similarly, removing a baseline noise level fit to the data (linear fit) produces a spectrum consistent with zero photons.

For a summary of tests of the data, see Table 4.1.

4.2.4 What if it were real?: Fitting the data.

Nonetheless, there is a chance that a signal is hidden in the noise.

The 0 order line is at least comparable to the other orders for most monochromatic light sources (see Figure 4.9): 0 order steals a considerable amount (often $10 - 40\%$) from every wavelength that passes through the system (including from photons that would normally fall outside of the CODEX bandpass). As such, the lack of a 0 order line can constrain (in an upper-limit fashion) the continuum contribution.

The mean value of the final spectrum is 11.8(33) counts bin^{-1}, with a standard deviation of 40.2 in any single bin. Across the central bins ($600 - 3304$), there are 1806 counts — remarkably similar to the predicted count rate for the Vela SNR. The response function of the short wavelength spectrograph drops 0.24 of all counts from a uniform continuum (counts per wavelength spanning only the bandpass of this spectrograph) into 0 order. That distribution corresponds to 433 counts, a 10.8σ outlier above the mean, and the counts in the actual 0 order bins sum to -2.5. For all practical purposes, that is a certain nondetection and a continuum can be ruled out as the cause of the signal. The significance drops if a continuum is present but dominated by noise, but no defining characteristics of differing populations of photon events have been found, so any distinction between signal and noise in the continuum is arbitrary and the lack of a 0 order line still argues against any continuum. The 10.8σ outlier estimate is highly conservative, however: although the long wavelength spectrograph did not work and the short wavelength detector was not positioned to detect photons longward of 57 Å, long wavelength photons from beyond the nominal diffracted bandpass are still included in the 0 order specular reflection (and more efficiently than short wavelength photons).

If, instead of assuming a uniform continuum only spanning the detector as was done above, we assume a rather flat synchrotron spectrum ($\alpha = 0.5$, as motivated by Green 2009, a steeper index will increase the contribution of longer-wavelength photons) across the entire bandpass of CODEX, then the 0 order reflection has 23 times more photons than the combined signal captured by the rest of the short wavelength spectrograph. A simulated image of this scenario is shown in Figure 4.17.

If the detected signal is assumed to be dominated by noise and the noise is removed via

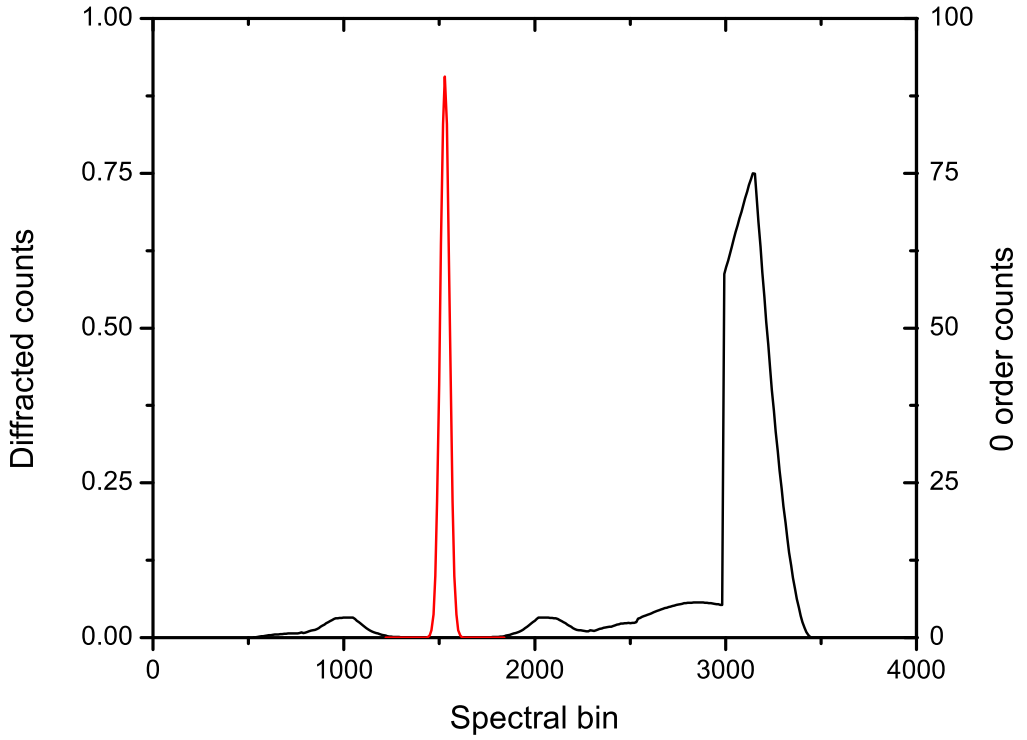

Figure 4.17 Simulated noiseless synchrotron image ($\alpha = 0.5$) for the short wavelength detector, including the contributions of photons whose diffracted light falls beyond the bandpass of the spectrograph, with energies ranging from $0.1 - 2$ keV. The 0 order reflection contains 23 times the counts of the rest of the image. Steepening the spectrum increases that ratio because most of the photon flux comes from longer wavelengths and will be deposited into 0 order without contributing to the short wavelength spectrum. The structure in this image comes from the full response function of the CODEX payload aside from the detector gain map. The y axes has an arbitrary linear scaling, although the scaling between the 0 order (red) and diffracted (black) signal is maintained.

subtraction of a linear fit from the central channels of the data (intercept = 11.35; slope = -4.0×10^{-4}), the total counts drop to -7×10^{-3} (essentially 0), with a mean value of -4×10^{-5}, an error on the mean of 3.3 and a standard deviation of 43.1. At this level (0 counts), one cannot expect any 0 order signal from a continuum. Assuming the linear slope is an adequate description of the noise (the fit is not particularly good, with $\chi^2_\nu = 3.1$ for 168 degrees of freedom), there is no statistical reason to expect a 0 order line at all.

If subtracting the noise leaves behind spectral lines, both those lines and 0 order would have a consistent structure that would push them above the noise. In a line-dominated case, the 0 order signal will still be stronger than any single line. The laboratory calibration tests (Figures 2.35 and 2.36) mimic this scenario. The lack of a 0 order feature (dominant in any model, thermal or not) prevents any plasma model from fitting the data with any reasonable statistical significance.

Chapter 5

Discussion and conclusions

‘‘Somewhere in here there’s truth. You care to take me to it?’’

-- Cmdr. William Adama, *Battlestar Galactica*

5.1 Instrument performance

No tests have yet indicated that CODEX saw anything but noise. The data were of insufficient quality to determine the contribution of synchrotron emission to the soft x-ray bandpass of Vela SNR, and the timescale question of how long DSA can persist remains unanswered. The main conclusions of the flight pertain to how the technology could have failed. Namely, where did the noise come from and why was there no signal? The former is addressed in §4.2, and although inconclusive because comparable noise could not be generated in the laboratory, the most probable explanation seems to be that ions in the payload are to blame for the noise. Laboratory testing is required before declaring a repeller grid to be the solution to the noise level. For the latter, the lack of a signal, there are a limited number of options when taken on a large scale:

(1) Pointing. The star tracker could not acquire its target on the Vela SNR. However, comparisons of the video feed from the star tracker to star maps show that its pointing was good to $20''$. To miss the Vela SNR by enough to drop the count rate by 50%, pointing would need to be $>1^\circ$ off. Pointing is not at fault.

(2) Alignment. The payload bent at some point, and even without that, optics could have shifted due to launch vibrations. Since the CODEX collimators block rather than focus light, an alignment shift along the collimators results in lost throughput rather than defocusing, while an alignment shift between the gratings and the collimators and the detectors will shift the spectrum. Comparison of pre- and post-flight tests showed the short wavelength spectrograph to be unchanged by flight.

(3) Grating losses. Time or contamination could have changed the grating reflectivity and dispersion efficiency. As with item [2] on this list, the flight itself did not change the efficiency, but the gratings could have degraded since the CyXESS and EXOS flights. Comparisons to those payloads will be discussed further below.

(4) Detector failure. Gas pressure and voltage do not appear to have been issues during flight. The short wavelength detector worked as calibrated before and after flight (discussed below). The long wavelength detector had an amplifier fail.

(5) Electronics failure. That signal was confined to the active area of the detector indicates both that RF pickup or other electronics noise was not responsible for the noise on the detector and that signal picked up by the detector was passed through the electronics. The electronics worked in both pre- and post-flight tests under vacuum comparable to its space environment.

The only glaring potential for a loss of signal is in poor calibration of the gratings and the detectors. All calibrations were done in a relative sense, in terms of line strengths and wavelength calibration, and compared to the previous and successful CyXESS and EXOS flights using many of the same components (McEntaffer and Cash 2008; Oakley 2011). The gratings were calibrated at the carbon K-line at 44.8 Å more than half of a decade before the CODEX flight (McEntaffer 2007); they have not been recalibrated since. The detector calibration history is even more specious. At their creation, they were calibrated at Sensor Sciences, LLC, to a ^{55}Fe source such that a 6 keV photon produced a 2.5 V signal. They were never calibrated absolutely.

CODEX gain calibration was limited to a relative calibration to previous payloads and to its own optimal conditions (detectors were optimized independently and the results were compared to calibration measurements from EXOS). The pre-flight comparison was non-rigorous — just a quick comparison of signal-to-noise and raw strength of the signal. Rigorous comparison to EXOS would have raised red flags about either the consistency of the Manson source being used for calibration or about the potential for the GEM detectors to be well below 100% quantum efficiency (by several orders of magnitude). The Manson soft x-ray source is reported by its manufacturer as being reliable to $5 - 10\%$ for a clean anode, but the anode might not have been cleaned in previous tests or the differing configurations (voltage losses across lines, biases in the control electronics that changed with time) could have affected the accuracy of the calibration source. The CODEX gain map itself indicates an upper limit to its quantum efficiency in the range of 45%, and several conservative steps were taken in creating the map that make even that limit probably well above the actual value. CODEX compares favorably to both the EXOS and CyXESS calibration, as shown in Figure 5.1 and Table 5.1, yet results from both payloads were consistent with each other. Table 5.1 does not challenge their results, but rather makes it all the more perplexing that CODEX behaved well before and after flight but failed to detect an astronomical signal.

Table 5.1. Calibration data from the CyXESS, EXOS, and CODEX payloads

Payload	Manson settings			t_{int} [s]	Full image count rate [Hz][a]	Peak line strength [Hz][b]	Line/continuum
	Anode	kV	mA				
CODEX	Mg	1.0	0.1	494	2942	97.9	20-300
EXOS	Mg	1.0	0.1	523	191	1.7	3-5
CODEX	Mg	2.5	0.2	297	19178	397.0	23-85
CyXESS	Mg	2.5	0.2	60	702	9.5	3.8-6.3

[a]These numbers do not include the distance to the photon source. Although the EXOS and CODEX tests were comparable, the CyXESS test positioned the source 6.0 m from the detectors, compared to CODEX's 3.9 m. The closeness increased the flux of CODEX by ∼2.4 relative to CyXESS. All data were rebinned by a factor of 8 to increase the signal-to-noise ratio.

[b] Data are from peak channels within a line and not from a Gaussian fit, since a misaligned collimator could produce a non-Gaussian focus. CODEX's peak line is the 0 order reflection, even for (nearly) monochromatic spectra; EXOS and CyXESS did not have this line in their bandpasses.

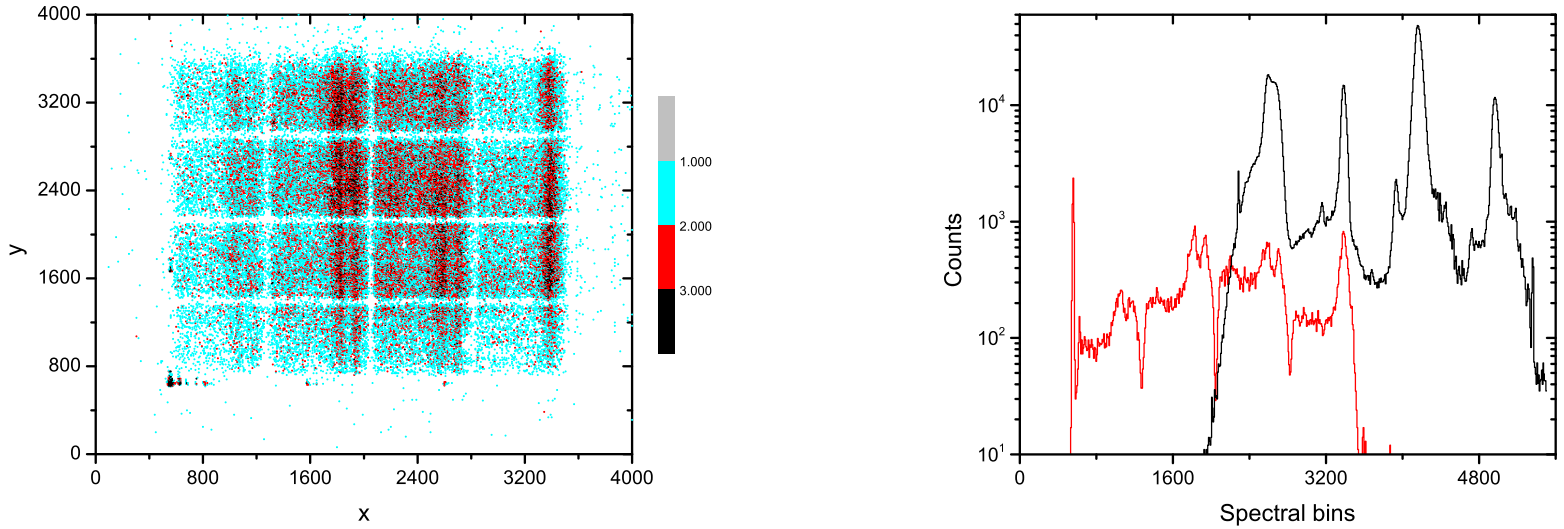

Figure 5.1 A comparison of the EXOS and CODEX calibration data from the images summarized in Table 5.1. *Left*: The EXOS calibration image. Data have been rebinned by a factor of 8 to reduce noise (the image is 512×512 in pixels but plotted on its original scale). The color scale marks the number of detections in each bin. The comparable CODEX image is 2.40. *Right*: Comparison of the two calibration spectra (EXOS in red and CODEX in black). The spectral bin axis has an arbitrary zero point, with the CODEX data inverted from elsewhere in this thesis to match the direction of the EXOS dispersion. 0 order is the largest of the peaks, with repeating orders of oxygen dominating the spectrum. +2 order oxygen is significantly broadened by the +1 order carbon line. These spectra have not been scaled to account for differences in time or in geometry (the CODEX detectors are angled with respect to the spectrum; the EXOS detector was aligned with the spectrum). Also unaccounted for is the distance to the Manson source, although like the geometry, this only alters the resuts by <20%. The CODEX test positioned the source 3.9 m from the detectors; the EXOS test was close to that but the exact distance is not recorded. Both spectra were rebinned by a factor of 8 to increase the signal-to-noise ratio but replotted on the original axis for consistent scaling with spectra elsewhere in this thesis. CODEX was designed with a bandpass that would have stretched beyond the left edge of the EXOS spectrum, as well, but that was on the dysfunctional longer wavelength detector.

The concurrent problems of low signal and high noise that are to blame for a lack of a signal are likely (but not definitively) identified as a high ion background and low quantum efficiency of the detectors. Both of these problems are curable now that they have been identified. Absolute calibration requires a diffuse absolute calibration source. Calibrating the diffuse soft x-ray source (§2.1) with a proportional counter will serve this purpose to $5 - 10\%$. The latter, ion pickup, requires a hardware solution in flight, with a charged repeller grid placed in front of the detector to block ions. This will lower the efficiency of the system slightly but reduce the noise significantly. The ion hypothesis still begs laboratory calibration before a repeller grid becomes an unequivocal solution.

5.2 Bremsstrahlung or synchrotron emission?

Since no viable signal could be extracted from the data, the question that motivated CODEX — whether synchrotron emission comprises a large fraction of the energy budget of the Vela SNR — is still unanswered. Answering it will require a clean, high resolution soft x-ray spectrum of a large fraction of a nearby supernova remnant (Cygnus Loop, Vela, or possibly the North Polar Spur or the Monogem Ring). If an experiment can acquire such a spectrum, it will provide a window to understanding the cooling mechanisms in the hot shock fronts and interior of supernova remnants as they evolve and approach the stage where they blend with the ISM. Thus the data would have implications beyond just SNRs and into the state of the majority of the volume of galaxies. Having identified some of the major issues impeding this payload from acquiring good spectra, the payload that follows will hopefully have more success when it targets the Vela SNR again in 2014.

CODEX, when functioning properly, is still capable of science that no other instrument can do.

Chapter 6

TEST Pilot

``Without dreams, man is a bird without wings.''

-- S. Korolev (1957)

CODEX has been passed on to the University of Iowa to fly as the OGRESS payload, where the lessons learned from CODEX can be applied to help the payload design achieve its full potential. It will again target the Vela SNR, and again offer the potential of answering the emission question that motivated CODEX.

The University of Colorado and the National Institute of Standards and Technology-Boulder submitted a joint proposal in response to the NASA APRA NNH11ZDA001N-APRA call for proposals (PI: W. Cash), planning to build a new diffuse soft x-ray imaging spectrograph. The instrument, dubbed TEST Pilot (Transition Edge Sensor Telescope Pilot program), will be a very different payload than CODEX, using focusing optics and detector energy resolution rather than a passive collimator and a dispersive grating array. The optics will be an array of flat mirrors in a Kirkpatrick-Baez configuration to make a rather poor focus of $3'$ on an array of transition edge sensor microcalorimeters. After a test flight, the system will be scaled from a $3'$ to a $6'$ field of view and with an array of 1,024 detectors, being the first flight testing of a kilopixel microcalorimeter array that will be the standard for the next generation of x-ray telescopes.

The detectors will present new challenges, since they operate by holding a superconductor at the "transition edge" between superconductor and normal conductivity, in the mK regime. Any

energy (n.b., a photon) heats the superconductor and increases the resistance, with the amount of energy being a capable non-dispersive spectrometer. TEST Pilot will fly a cryogenic system, and even with that, the power that is required to run the detectors and their amplifiers would overheat the system if care were not taken to read out the detectors in an efficient manner. Kent Irwin at NIST has recently developed a "code-domain multiplexing" scheme whereby a matrix of bias values applied to the readout allows for simultaneous sampling of all pixels without running an unfortunate amount of power into the cooled section of the instrument. TEST Pilot will be the first x-ray telescope to demonstrate this new technology.

As another diffuse-object soft x-ray spectrograph, it is capable of doing somewhat similar science as what CODEX was designed to do. The smaller field of view, however, is optimal for smaller targets: galaxy clusters, comets, and compact SNRs.

The microcalorimeters require mK temperatures to operate, so TEST Pilot would fly a cryogenic system, and even with that, the low power that is required to run the TESes and their amplifiers would overheat the system if care were not taken to read out the detectors in an efficient manner.

The NIST detectors will approach the theoretical limit for that type of detector, achieving sub-eV resolution in the soft x-ray bandpass for a resolution of $\sim 10^3$ in an imaging spectrograph. Although more complex and expensive than the GEM technology flown on CODEX, their vast improvement over the GEMs' spectral resolution allows them to operate as their own spectrograph — Porter et al. (2000) used a microcalorimeter array to study the soft x-ray background across a steradian of sky by merely exposing these pixels to space with no intervening optics — or coupled behind a dispersive optic akin to the grating arrays flown on CODEX.

Although the TEST Pilot proposal was turned down on the first submission, it has been improved (its major failing was the status of the detectors, and they will have another year of development before the next proposal cycle). The rocket has potential to expand the field of soft x-ray astronomy and to get high resolution spectra of supernova remnants and galaxy clusters that could validate the hypotheses that CODEX flew (and ultimately failed) to resolve.

Bibliography

Aharonian, F. A. and Atoyan, A. M.: 1999, A&A **351**, 330

Aschenbach, B.: 1998, Nature **396**, 141

Aschenbach, B., Egger, R., and Trümper, J.: 1995, Nature **373**, 587

Aschenbach, B., Iyudin, A. F., and Schönfelder, V.: 1999, A&A **350**, 997

Badenes, C., Maoz, D., and Draine, B. T.: 2010, MNRAS **407**, 1301

Baring, M. G.: 1997, in Y. Giraud-Heraud and J. Tran Thanh van (eds.), Very High Energy Phenomena in the Universe; Moriond Workshop, p. 97

Baring, M. G. and Summerlin, E. J.: 2005, in G. Li, G. P. Zank, and C. T. Russell (eds.), The Physics of Collisionless Shocks: 4th Annual IGPP International Astrophysics Conference, Vol. 781 of American Institute of Physics Conference Series, pp 207–212

Blümer, J., Engel, R., and Hörandel, J. R.: 2009, Progress in Particle and Nuclear Physics **63**, 293

Bohm, D.: 1949, The characteristics of electrical discharges in magnetic fields, McGraw-Hill, New York

Briel, U. G. and Pfeffermann, E.: 1985, NASA STI/Recon Technical Report N **87**, 11649

Caprioli, D.: 2012, JCAP **7**, 38

Caraveo, P. A., De Luca, A., Mignani, R. P., and Bignami, G. F.: 2001, ApJ **561**, 930

Cash, W., Malina, R., and Stern, R.: 1976, ApJ **204**, L7

Cha, A. N., Sembach, K. R., and Danks, A. C.: 1999, ApJ **515**, L25

Cox, D. P.: 2005, ARA&A **43**, 337

Cruddace, R. G., Friedman, H., Fritz, G., and Shulman, S.: 1976, ApJ **207**, 888

Crutcher, R. M.: 1982, ApJ **254**, 82

Diehl, R., Halloin, H., Kretschmer, K., Lichti, G. G., Schönfelder, V., Strong, A. W., von Kienlin, A., Wang, W., Jean, P., Knödlseder, J., Roques, J.-P., Weidenspointner, G., Schanne, S., Hartmann, D. H., Winkler, C., and Wunderer, C.: 2006, Nature **439**, 45

Dodson, R., Legge, D., Reynolds, J. E., and McCulloch, P. M.: 2003, ApJ **596**, 1137

Ellison, D. C., Decourchelle, A., and Ballet, J.: 2004, A&A **413**, 189

Fermi, E.: 1949, Physical Review **75**, 1169

Ferrière, K. M.: 2001, Reviews of Modern Physics **73**, 1031

Freyberg, M. J. and Egger, R.: 1999, in B. Aschenbach and M. J. Freyberg (eds.), Highlights in X-ray Astronomy, p. 278

Frisch, P. C.: 1981, Nature **293**, 377

Ghavamian, P., Raymond, J., Smith, R. C., and Hartigan, P.: 2001, ApJ **547**, 995

Giacconi, R., Gursky, H., Paolini, F. R., and Rossi, B. B.: 1962, Physical Review Letters **9**, 439

Green, D. A.: 2009, Bulletin of the Astronomical Society of India **37**, 45

Haffner, L. M., Reynolds, R. J., Tufte, S. L., Madsen, G. J., Jaehnig, K. P., and Percival, J. W.: 2003, ApJS **149**, 405

Huxley, T. H.: 1894, Collected Essays, Vol. 8: Discourses: Biological & Geological, Vol. 8, Macmillan & Co., London

Iyudin, A. F., Schönfelder, V., Bennett, K., Bloemen, H., Diehl, R., Hermsen, W., Lichti, G. G., van der Meulen, R. D., Ryan, J., and Winkler, C.: 1998, Nature **396**, 142

Kahn, S. M., Brodie, J., Bowyer, S., and Charles, P. A.: 1983, ApJ **269**, 212

Koyama, K., Kinugasa, K., Matsuzaki, K., Nishiuchi, M., Sugizaki, M., Torii, K., Yamauchi, S., and Aschenbach, B.: 1997, PASJ **49**, L7

Koyama, K., Petre, R., Gotthelf, E. V., Hwang, U., Matsuura, M., Ozaki, M., and Holt, S. S.: 1995, Nature **378**, 255

Large, M. I., Vaughan, A. E., and Wielebinski, R.: 1969, Nature **223**, 1249

Launius, R. D.: 2003, The Oral History Review **30**, 111

Levenson, N. A., Graham, J. R., and Snowden, S. L.: 1999, ApJ **526**, 874

Lu, F. J. and Aschenbach, B.: 2000, A&A **362**, 1083

Masai, K.: 1994, ApJ **437**, 770

McEntaffer, R. L.: 2007, Ph.D. thesis, University of Colorado at Boulder

McEntaffer, R. L. and Cash, W.: 2008, ApJ **680**, 328

Melrose, D. B. and Crouch, A.: 1997, PASA **14**, 251

Miceli, M., Bocchino, F., Maggio, A., and Reale, F.: 2005a, Advances in Space Research **35**, 1012

Miceli, M., Bocchino, F., Maggio, A., and Reale, F.: 2005b, A&A **442**, 513

Miller, E. D., Tsunemi Hiroshi, Bautz, M. W., McCammon, D., Fujimoto, R., Hughes, J. P., Katsuda, S., Kokubun, M., Mitsuda, K., Porter, F. S., Takei, Y., Tsuboi, Y., and Yamasaki, N. Y.: 2008, PASJ **60**, 95

Miroshnichenko, A. P.: 2010, Radio Physics and Radio Astronomy **1**, 93

Miyata, E., Tsunemi, H., Aschenbach, B., and Mori, K.: 2001, ApJ **559**, L45

More, L.: 1934, Isaac Newton: a biography, Charles Scribner's Sons, New York

Morlino, G. and Caprioli, D.: 2012, A&A **538**, A81

Morrison, R. and McCammon, D.: 1983, ApJ **270**, 119

Neviere, M., Maystre, D., and Hunter, W. R.: 1978, Journal of the Optical Society of America (1917-1983) **68**, 1106

Oakley, P. H. H.: 2011, Ph.D. thesis, University of Colorado at Boulder

Oakley, P. H. H., McEntaffer, R. L., and Cash, W.: 2011a, Experimental Astronomy **31**, 23

Oakley, P. H. H., McEntaffer, R. L., and Cash, W.: 2011b, Experimental Astronomy **31**, 23

Oppermann, N., Junklewitz, H., Robbers, G., Bell, M. R., Enßlin, T. A., Bonafede, A., Braun, R., Brown, J. C., Clarke, T. E., Feain, I. J., Gaensler, B. M., Hammond, A., Harvey-Smith, L., Heald, G., Johnston-Hollitt, M., Klein, U., Kronberg, P. P., Mao, S. A., McClure-Griffiths, N. M., O'Sullivan, S. P., Pratley, L., Robishaw, T., Roy, S., Schnitzeler, D. H. F. M., Sotomayor-Beltran, C., Stevens, J., Stil, J. M., Sunstrum, C., Tanna, A., Taylor, A. R., and Van Eck, C. L.: 2012, A&A **542**, A93

Palmieri, T. M., Burginyon, G., Grader, R. J., Hill, R. W., Seward, F. D., and Stoering, J. P.: 1971, ApJ **164**, 61

Parizot, E., Marcowith, A., Ballet, J., and Gallant, Y. A.: 2006, A&A **453**, 387

Plucinsky, P. P., Smith, R. K., Edgar, R. J., Gaetz, T. J., Slane, P. O., Blair, W. P., Townsley, L. K., and Broos, P. S.: 2002, in P. O. Slane and B. M. Gaensler (eds.), Neutron Stars in Supernova Remnants, Vol. 271 of Astronomical Society of the Pacific Conference Series, p. 407

Porter, F. S., Almy, R., Apodaca, E., Figueroa-Feliciano, E., Galeazzi, M., Kelley, R., McCammon, D., Stahle, C. K., Szymkowiak, A. E., and Sanders, W. T.: 2000, Nuclear Instruments and Methods in Physics Research A **444**, 175

Racusin, J. L., Park, S., Zhekov, S., Burrows, D. N., Garmire, G. P., and McCray, R.: 2009, ApJ **703**, 1752

Raymond, J. C., Ghavamian, P., Sankrit, R., Blair, W. P., and Curiel, S.: 2003, ApJ **584**, 770

Reichley, P. E., Downs, G. S., and Morris, G. A.: 1970, ApJ **159**, L35

Reville, B., Bell, A. R., and Gregori, G.: 2012, ArXiv e-prints

Reynolds, S. P.: 1998, ApJ **493**, 375

Rudnick, L. and Brown, S.: 2009, AJ **137**, 145

Rybicki, G. B. and Lightman, A. P.: 2004, Radiative Processes in Astrophysics, Wiley-VCH, Weinheim

Salter, C. J.: 1983, Bulletin of the Astronomical Society of India **11**, 1

Sankrit, R., Blair, W. P., and Raymond, J. C.: 2003, ApJ **589**, 242

Seward, F. D., Burginyon, G. A., Grader, R. J., Hill, R. W., Palmieri, T. M., and Stoering, J. P.: 1971, ApJ **169**, 515

Shipley, A., Gleeson, B., McEntaffer, R., and Cash, W.: 2006, in Society of Photo-Optical Instrumentation Engineers (SPIE) Conference Series, Vol. 6273 of Society of Photo-Optical Instrumentation Engineers (SPIE) Conference Series

Shipley, A., Zeiger, B. R., and Rogers, T.: 2011, in Society of Photo-Optical Instrumentation Engineers (SPIE) Conference Series, Vol. 8076 of Society of Photo-Optical Instrumentation Engineers (SPIE) Conference Series

Siegmund, O. H. W., McPhate, J. B., Vallerga, J. V., Tremsin, A. S., Jelinsky, S. R., Frisch, H. J., and LAPPD Collaboration: 2011, Nuclear Instruments and Methods in Physics Research A **639**, 165

Siemieniec-Ozieblo, G.: 2004, Acta Physica Polonica B **35**, 2131

Simon, F., Azmoun, B., Becker, U., Burns, L., Crary, D., Kearney, K., Keeler, G., Majka, R., Paton, K., Saini, G., Smirnov, N., Surrow, B., and Woody, C.: 2007, IEEE Transactions on Nuclear Science **54**, 2646

Slane, P., Gaensler, B. M., Dame, T. M., Hughes, J. P., Plucinsky, P. P., and Green, A.: 1999, ApJ **525**, 357

Slane, P., Hughes, J. P., Edgar, R. J., Plucinsky, P. P., Miyata, E., Tsunemi, H., and Aschenbach, B.: 2001, ApJ **548**, 814

Slavin, J. D. and Cox, D. P.: 1993, ApJ **417**, 187

Snowden, S. L., Egger, R., Freyberg, M. J., McCammon, D., Plucinsky, P. P., Sanders, W. T., Schmitt, J. H. M. M., Truemper, J., and Voges, W.: 1997, ApJ **485**, 125

Sushch, I., Hnatyk, B., and Neronov, A.: 2011, A&A **525**, A154

Tamagawa, T., Hayato, A., Asami, F., Abe, K., Iwamoto, S., Nakamura, S., Harayama, A., Iwahashi, T., Konami, S., Hamagaki, H., Yamaguchi, Y. L., Tawara, H., and Makishima, K.: 2009, Nuclear Instruments and Methods in Physics Research A **608**, 390

Taylor, G.: 1950, Royal Society of London Proceedings Series A **201**, 175

Tsunemi, H. and Katsuda, S.: 2006, New Astr. Rev. **50**, 521

Vink, J.: 2012, A&A Rev. **20**, 49

Vink, J., Bleeker, J., van der Heyden, K., Bykov, A., Bamba, A., and Yamazaki, R.: 2006, ApJ **648**, L33

Vink, J. and Laming, J. M.: 2003, ApJ **584**, 758

Werner, N., de Plaa, J., Kaastra, J. S., Vink, J., Bleeker, J. A. M., Tamura, T., Peterson, J. R., and Verbunt, F.: 2006, A&A **449**, 475

Willingale, R., Hands, A. D. P., Warwick, R. S., Snowden, S. L., and Burrows, D. N.: 2003, MNRAS **343**, 995

Wolleben, M.: 2007, ApJ **664**, 349

Yamaguchi, H. and Katsuda, S.: 2009, ApJ **696**, 1548

Yoshii, R., Yamaguchi, H., Katsuda, S., Tamagawa, T., and Hiraga, J.: 2010, in 38th COSPAR Scientific Assembly, Vol. 38 of COSPAR Meeting, p. 2785

Zeiger, B. R., Shipley, A., Cash, W., and McEntaffer, R.: 2010, in Society of Photo-Optical Instrumentation Engineers (SPIE) Conference Series, Vol. 7732 of Society of Photo-Optical Instrumentation Engineers (SPIE) Conference Series

Zeiger, B. R., Shipley, A., Cash, W., Rogers, T., Schultz, T., McEntaffer, R., and Kaiser, M.: 2011, in Society of Photo-Optical Instrumentation Engineers (SPIE) Conference Series, Vol. 8076 of Society of Photo-Optical Instrumentation Engineers (SPIE) Conference Series